Julia Langer, Dipl.-Ing.

Towards the Understanding of Li^+ Diffusivity in Ionic Conductors: Jump Rates and Pathways in 2D and 3D Energy Materials

DISSERTATION

zur Erlangung des akademischen Grades

Doktorin der technischen Wissenschaften (Dr. techn.)

eingereicht an der

Technischen Universität Graz

Betreuer

Univ.-Prof. Dr. Martin Wilkening

Institut für Chemische Technologie von Materialien

Graz, Oktober 2015

Affidavit

I declare that I have authored this thesis independently, that I have not used other than the declared sources/resources, and that I have explicitly indicated all material which has been quoted either literally or by content from the sources used. The text document uploaded to TUGRAZonline is identical to the present doctoral dissertation.

Eidesstattliche Erklärung

Ich erkläre an Eides statt, dass ich die vorliegende Arbeit selbstständig verfasst, andere als die angegebenen Quellen/Hilfsmittel nicht benutzt, und die den benutzten Quellen wörtlich und inhaltlich entnommenen Stellen als solche kenntlich gemacht habe. Das in TUGRAZonline hochgeladene Textdokument ist mit der vorliegenden Dissertation identisch.

Date / Datum	Signature / Unterschrift

Abstract

Electrochemical energy storage affects our daily life to a great extent. Many electronical devices such as laptops, tablets, digital music players or cell phones rely on secondary Li-ion batteries. In order to keep up, however, with advancing technology for mobile and portable devices new ways have to be found to improve performance and safety in Li-based batteries. In this context, the field of materials science plays a main role in the development of high-performance energy materials and in providing the necessary means for their in-depth characterization. Ion dynamics, *i.e.,* Li self-diffusion in particular, determine the applicability of solid ion conductors as electrodes or electrolytes in batteries, or other technical systems. To more closely examine self-diffusion a variety of complementary methods can be employed on a microscopic and macroscopic length scale.

The following dissertation, is directed towards studying fast and slow Li ion diffusivity in different classes of ionic conductors with the help of solid-state nuclear magnetic resonance and impedance spectroscopy as well as dynamic mechanical analysis. Diffusion in layer-structured compounds, *i.e.,* $Li_{0.17}SnS_2$ and LiC_6, is governed by motional confinement within the interlayer. Li diffusion parameters in LiC_6 were assessed by spin-lattice relaxation NMR techniques in a temperature range relevant for their practical application in batteries. Self-diffusion at room temperature (T= 295 K) is characterized by $D \approx 10^{-15}\,m^2\,s^{-1}$. The study of Li ion dynamics in lithium-intercalated tin disulfide ($Li_{0.17}SnS_2$) revealed the existence of both fast and slow diffusion by going from microscale down to nanoscale materials. With the introduction of more defects and disorder overall diffusivity could be enhanced via ball-milling, indicated by a shift of the relaxation rate peak, with however considerable influence of correlation effects. Ultraslow and heterogeneous ion dynamics were found for Li_2SnO_3 characterized by $D \approx 9 \times 10^{-20}\,m^2s^{-1}$ at T = 297 K. Via high-resolution ^{6}Li NMR two unexpected out-of-plane diffusion pathways were identified with Li exchange rates in the order of 1 s^{-1}. A fundamental study of $LiAlO_2$ revealed slow Debye-like ion motion in a highly ordered single crystal over a broad temperature and frequency range. This study is a rare example which probes Li motion via the application of electrical and mechanical relaxation techniques. As a fast conducting solid garnet-type Al-, Ga-doped LLZO proves to be a promising candidate for the application as solid electrolyte. Influence of Al and Ga doping on the Li sub-lattice in terms of site occupation was investigated via ^{27}Al and ^{71}Ga MAS NMR. Increased Li-diffusivity of the Ga-doped samples compared to its Al-doped analogues can be attributed to an increase in the unit cell parameter a_0, rather than a blocking effect associated with the Al:Ga ratio.

Keywords: Li ion dynamics, self-diffusion, NMR, dimensionality, nanostructured materials

Kurzfassung

Die elektrochemische Energiespeicherung nimmt heutzutage großen Einfluss auf unseren Alltag. Zahlreiche elektronische Geräte wie Laptops, Tablets, Multimedia-Player oder Mobiltelefone sind auf Lithium-Ionen-Batterien angewiesen. Um mit dem Voranschreiten auf dem Gebiet der technischen Entwicklung von mobilen und portablen Geräten mithalten zu können, müssen neue Wege gefunden werden, um die Leistungsfähigkeit und Sicherheit von Speichersystemen zu gewährleisten, die auf der Lithium-Ionen-Technologie basieren. Bei der Entwicklung hochleistungsfähiger Speichermaterialien spielt vor allem das Forschungsgebiet der Materialwissenschaften eine große Rolle. Hier ist insbesondere die Charakterisierung der Ionendynamik, speziell der Lithium-Ionendynamik, bedeutend, welche die praktische Anwendbarkeit von festen Ionenleitern in Batterien oder anderen technischen Systemen bestimmt. Um diese Aufgabe zu erfüllen, steht eine Vielzahl an Methoden zur Verfügung, die eine Betrachtung der Lithium-Selbstdiffusion auf einer mikro- und makroskopischen Längenskala ermöglichen.

Die folgende Dissertation beschäftigt sich mit den grundlegenden Studien von schnellen und langsamen Transportprozessen in verschiedenen festen Lithium-Ionenleitern basierend auf der Untersuchung mittels Festkörper-NMR, Impedanzspektroskopie und dynamisch-mechanischer Analyse. In schichtstrukturierten Ionenleitern, in diesem Fall: $Li_{0.17}SnS_2$ und LiC_6, wird die Li-Diffusion in einem großen Ausmaß durch die eingeschränkte Bewegungsmöglichkeit in den Zwischenschichten dominiert. Für das Anodenmaterial LiC_6 wurden über einen weiten Temperaturbereich Lithium-Diffusionsparameter anhand von Spin-Gitter-Relaxationszeitmessungen bestimmt. Die für ein Elektrodenmaterial eher langsame Selbstdiffusion wird durch einen Koeffizient von $D \approx 10^{-15}\,m^2\,s^{-1}$ (bei Raumtemperatur) verdeutlicht. Messungen an der Lithium-Interkalationsverbindung $Li_{0.17}SnS_2$ zeigten das Auftreten zweier unterschiedlich schneller Diffusionsprozesse bei Vergleich von nano- mit mikrokristallinen Proben. Weiters konnten durch Hochenergie-Kugelmahlen zusätzliche Defekte und strukturelle Unordnung in Zinndisulfid eingebracht werden, welches sich in einer Verschiebung des ^{7}Li-NMR-Ratenpeaks äußerte. Dadurch lässt sich, unter Berücksichtigung von Korrelationseffekten, auf eine Erhöhung der Li-Diffusivität schließen. Die diamagnetische Verbindung Li_2SnO_3 zeichnet sich durch eine ultralangsame und heterogene Ionendynamik aus, beschrieben durch $D \approx 9 \times 10^{-20}\,m^2s^{-1}$ bei 297 K. Mittels hochauflösender ^{6}Li NMR konnten zwei unerwartete Diffusionspfade für Ionenaustausch entlang der kristallographischen *c*-Achse identifiziert werden. Die Sprungraten für langsamen Li-Austausch liegen in der Größenordnung von 1 s^{-1}. An einem strukturell hochgeordnetem System, in der Form eines γ-$LiAlO_2$-Einkristalls, konnten durch

elektrische und mechanische Relaxationsmessungen ein Debye-ähnliches Bewegungsverhalten beobachtet werden. Diese Grundlagenstudie stellt ein seltenes Beispiel dar wo Diffusionsprozesse komplementär mit dynamisch-mechanischer-Analyse und Impedanzspektroskopie in einem breiten Temperatur- und Frequenzbereich untersucht wurden. Kubisches Al-, Ga-dotiertes $Li_7La_3Zr_2O_{12}$ ist ein Beispiel für einen schnellen Lithium-Ionenleiter, und somit ein Kandidat für die Anwendung als Festkörperelektrolyt. In der entsprechenden Studie wurde der Einfluss der Dotierung mit Al- und Ga-Ionen auf die Besetzung der kristallographischen Li-Plätze mittels ^{27}Al und ^{71}Ga NMR bei 21 T untersucht. Dabei zeigte sich bei beiden Ionensorten ein ähnliches Verhalten bezüglich der Besetzung der tetraedrischen 24*d*- und 96*h*-Plätze. Die Erhöhung der Li-Diffusivität von Ga-dotierten Proben gegenüber den Al-dotierten Analoga wird mit einer Erhöhung der Gitterkonstante a_0 in Zusammenhang gebracht werden und weniger mit einem Blockierungseffekt bedingt durch das Al:Ga-Verhältnis.

Stichworte: Lithium-Ionendynamik, Selbstdiffusion, NMR, Dimensionalität, nanostrukturierte Materialien

Contents

1. Introduction

There is no doubt that a steadily growing consumption of energy leaves its mark on the environment. Indeed, the effects of humankind on climate change are estimated to have increased to more than 50% since the onset of industrialization. The intensive use of fossile resources and the resulting increase in CO_2 emissions in particular led to atmospheric enrichment of greenhouse gases.

Amongst other effects, global warming is considered to be linked to extreme weather events such as floods or droughts, the steady rise of the sea levels, shrinkage of glaciers and polar caps, or the loss of global biodiversity. As the environmental impact was shown to be irreversible, mitigation strategies have to be found to ensure that the changes remain manageable [1]. In terms of energy supply key mitigation strategies demand a switch from fossil-based resources towards increasing use of renewable energy, *i.e.,* hydro-, solar-, wind-, geothermal- and bioenergy-based sources [2]. However, variable renewable resources, *e.g.,* solar or wind power, are challenging to incorporate into the energy supply chain, as they cannot be scheduled to produce energy in specific amounts at specific times. Thus, with the help of *storage systems* energy can be stored in either mechanical, electrochemical, chemical, electrical and thermal form and, thus, facilitate the conversion and deployment when the need arises.

In the field of electric automobiles and portable appliances, such as cell phones or notebooks, secondary *lithium ion batteries* are the most important energy storage technology due to their high cell voltage levels up to 3.7 V, their high gravimetric energy density and their high efficiency in the range of 95% - 98% [3]. However, many metal oxide electrodes are thermally unstable and tend to decompose at elevated temperatures. Additionally the usage of volatile and flammable liquid electrolytes presents a serious safety issue. These facts provide the motivation for ongoing research in Li ion battery technology with a special focus on the development of *solid electrolytes* and improvement of electrode materials. In an *all-solid-state battery* volatile and toxic organic electrolytes are replaced by a fast ion-conducting solid. Compared with conventional Li ion batteries an all-solid-state system features superior longevity and thermal stability and offers increased safety [4]. The engineering of electrodes and electrolytes either involves synthesis of new energy materials or can also be achieved by improving the Li transport properties of known ones. This can be accomplished, for example, via high-energy

ball-milling of crystalline, highly-ordered structures, which results in nano-sized, defect-rich materials with enhanced Li diffusivity [5–7]. In general, ionic transport in solids is strongly governed by structural disorder, defects and particle size. Understanding the relation between these factors allows a specific tuning of the Li ion transport in solids for their application as battery materials.

An in-depth knowledge on Li-ion diffusion can be gained by applying complementary methods that characterize Li hopping on a large time and length scale. *Solid-state NMR spectroscopy* provides a wide array of techniques which are sensitive to *short-* and *long-range jumps* from sub-Hz to GHz, over a scale of more than ten orders of magnitude. *In concreto*, diffusion-induced relaxation of Li ions is accessible via ^{6,7}*Li spin-lattice relaxation (SLR) NMR measurements*. Ideally, temperature-dependent measurements probe a so-called relaxation rate peak. Here, the rate maximum contains dynamical parameters such as the *Li jump rate*, *activation energy* and *self-diffusion coefficient*. Further information on *correlation effects* and *dimensionality* of the diffusion process are provided by *frequency-dependent* spin-lattice NMR measurements. *Stimulated-echo* experiments set the lower limit for NMR spectroscopy and can provide *direct access* to the jump rate of a single spin [8–11].

The overall aim of this work is to qualitatively and quantitatively study Li^+ transport in ion conductors, primarily via solid-state NMR. Qualitatively, in terms of site occupation, diffusion pathways and dimensionality of Li motion – quantitatively, in terms of accessing Li diffusion parameters along with site-specific Li exchange rates. Furthermore these dynamical parameters and mechanisms are considered are related with structure and morphology of the compounds.

A broad spectrum of materials is characterized: *viz.* (i) layer-structured intercalation compounds (LiC_6, $Li_{0.17}SnS_2$), (ii) ultraslow ion conductors (Li_2SnO_3, $LiAlO_2$) and (iii) solid electrolytes ($Li_{7-3(x+y)}Ga_xAl_yLa_3Zr_2O_{12}$).

This thesis is organized as follows: At first a short introduction into the *basics and principles of diffusion* is provided in section 2.1. along with an overview on *diffusion measurement* in 2.2. It is followed by the section on *solid-state NMR* (2.3) providing information on the fundamentals, interactions and different NMR techniques applied in the framework of this thesis. Experimental results are presented in a cumulative form of published (and peer-reviewed) papers, and paper drafts in chapter 3. All findings are briefly summarized in 4). Supplemental information concerning the papers, along with a description of the experimental setup and NMR pulse sequences can be found in the Appendix.

2. Solid-State Diffusion

2.1 Basics and Principles of Diffusion

A complete description of the diffusion concept is beyond the scope of this thesis. Only the most basic principles mechanisms are discussed in order to understand the experimental findings presented in chapter 3. The interested reader is referred to the works of Mehrer [12], Murch [13], serving as the basis of the following introduction.

The term *diffusion* describes the flux of atoms or molecules against a concentration gradient, which is driven by the temperature-dependent Brownian motion. In the liquid or gas phase the motion can be described as passive and unspecific, *i.e.,* random and undirected motion. Statistically the particles are distributed homogeneously, as seen over a certain period of time. In the case of a difference in concentration the equalizing movement of atoms and molecules leads to a stationary equilibrium. The tendency to return to the thermodynamic equilibrium is always driven by an increase in entropy due to the diffusion process. Hence, the particle flux j_x in an isotropic medium along an arbitrary direction, *e.g.* in *x*-direction can be described with Fick's first law:

$$j_x = -D\frac{\partial c}{\partial x} \tag{2.1}$$

where D denotes the diffusion coefficient (also known as diffusivity)and $\partial c/\partial x$ the concentration gradient in *x*-direction, which is the driving force of the equalizing movement. If we consider the general case of diffusion in all three dimensions equation (2.1) is expressed via vector quantities:

$$\boldsymbol{j} = -D\nabla c \tag{2.2}$$

With $\boldsymbol{j}$ representing the particle flux in *x*-, *y*- and *z*-direction and the symbol *nabla* ∇as the vector differential operator describing a *stationary* concentration gradient, *i.e.* the gradient is

constant with time or can be seen as quasi-constant for a very slow diffusion process. As D is dependent on the direction of the concentration gradient it is represented by a tensor. However, regarding transport phenomena in polycrystalline solid samples, where we find many crystalline orientations and no macroscopic orientation, an average diffusion coefficient suffices to describe diffusion $D \equiv \langle D \rangle$.

We assume that the number of diffusing particles is conserved. The combination of the *equation of continuity* and (2.2) gives

$$\frac{\partial c}{\partial t} = -\nabla j \tag{2.3}$$

With equation (2.2) yields Fick's second law, also known as the diffusion equation:

$$\frac{\partial c}{\partial t} = \nabla(D \nabla c) \tag{2.4}$$

This partial differential equation yields non-numerical solutions if the diffusivity depends on the concentration. For the opposite case, if D is independent of the concentration, *i.e.* in a chemically homogeneous material, we obtain a time- and location-independent diffusion coefficient. For given initial and boundary conditions the equation can be solved via Laplace-transformation: $(\Delta \equiv \nabla^2 \equiv \partial^2/\partial x^2 + \partial^2/\partial y^2 + \partial^2/\partial z^2)$

$$\frac{\partial c}{\partial t} = D \nabla^2 c \equiv D \Delta c \tag{2.5}$$

We obtain the diffusivity by fitting the experimental concentration profile $c_{exp}(x, t)$ with the analytical solution of (2.5). For further information see the works of Murch [13] and Mehrer [12].

The diffusion coefficient has been empirically found to show Arrhenius behavior:

$$D = D_0 \exp\left(\frac{\Delta H}{-k_B T}\right), \tag{2.6}$$

With D_0 representing the pre-exponential factor, ΔH the activation enthalpy, k_B Boltzmann's constant and T the absolute temperature. For solid-state matter, ΔH equals the activation energy E_A[1], provided constant pressure and negligence of the activation volume term.

$$D = D_0 \exp\left(\frac{E_A}{-k_B T}\right) \tag{2.7}$$

Depending on the experimental situation we can distinguish between various types of diffusion coefficients. Here, the discussion will be limited to the type, which is most relevant for our study of bulk diffusion in binary systems.

Tracer diffusion coefficient

Tracer diffusion differentiates between two cases: the first one, referred to as *self-diffusion*, uses diffusing tracers that are chemically the same as the host, while the second one uses a different species (*impurity diffusion coefficient*). Here, suitable tracers are either labelled by radioactivity or their isotopic mass and are present only in tiny amounts within the material. While the prerequisite of a concentration gradient is still fulfilled, the tracer concentration is very low in order not to change the chemical composition and exclude interaction with other tracer atoms. Tracer diffusion is adequate to describe the self-diffusion of matrix atoms, *e.g.*, migration of atoms in a pure metal. It also can be applied for more complex situations, *e.g.*, in ionic crystals, when we study a mobile species in an immobile matrix [12].

The bridge between the macroscopic *self-diffusion coefficient* D^T and the microscopic view of diffusion can be built with a relation referred to as the *Einstein-Smoluchowski* equation [14–16]

$$D^T = \frac{\left\langle \boldsymbol{r}^2 \right\rangle}{2d\Delta t} \tag{2.8}$$

$\left\langle \boldsymbol{r}^2 \right\rangle$ denotes the *mean square displacement* of a given particle during the time Δt, taking the dimensionality d of the diffusion process into account. In order to describe discrete jumps in solid matter equation (2.8) reads:

$$D^{uc} = \frac{a^2}{2d\tau} \tag{2.9}$$

[1] With the expression $\Delta H = \Delta E + p\Delta V$; in the following ΔE is referred to as E_A.

The jump length a corresponds to the distance between the lattice sites, whereas τ represents the mean residence time of the particle on the lattice site, or τ^{-1} the jump rate. Note that this expression holds for uncorrelated motion, *i.e.* the jumps are independent of their prior positions. If diffusion in a crystal is not solely caused by the interstitial mechanism, correlation effects have to be taken into account via the correlation factor f for the range $0 < f \leq 1$.

$$D^T = f \cdot D^{uc} \tag{2.10}$$

Diffusion and defects

As a prerequisite for diffusion *per se*, existence of defects and vacancies is needed. Even every "perfect" crystal in the state of thermodynamic equilibrium contains defects at $T > 0$ K. *Zero*-dimensional defects, also called *point defects*, are atomic defects in an ionic crystal. These point defects move through the crystal via different mechanisms (see below) and mediate atomic diffusion. They can be further distinguished between i) *intrinsic and structural defects* and ii) *extrinsic or chemical defects* [17].

Intrinsic *Frenkel-* or *anti-Frenkel*-defects can be formed when cations or anions (anti-disorder) move onto an interstitial site, leaving vacancies on the regular site Defects of the *Schottky*-type are formed by both cation and anion moving onto interstitial sites, leaving vacancies in both sub-lattices in order to preserve charge neutrality (*cf.* Figure 1a), b)).

Extrinsic disorder can be introduced by *homo-* or *heterovalent* impurity atoms. While homovalent doping will merely lead to a distortion in the crystal lattice, heterovalent impurities are the driving force for the additional formation of vacancies in order to preserve charge neutrality.

Line-shaped, *one-dimensional defects* often occur in the form of *edge* and *screw* dislocations. This type of defects can delete vacancies and interstitials, or can create new ones. So-called planar defects occur in the form of *stacking faults* in the lattice or as grain boundaries [12,18,19]. The boundaries are the interfaces between crystallites with different orientations. Such grain boundaries are often found to exhibit higher diffusivity compared to the bulk material. For the sake of completeness, three-dimensional disorder exists in the form of voids/pores and precipitates which are clusters of vacancies or and impurities forming inclusions of a different phase.

Diffusion mechanisms

The position and migration path of atomic particles is restricted by the crystal lattice. The jump mechanism of the diffusing atom is strongly influenced by the host crystal structure, size and chemistry of the diffusing atom and by which kind of defects it is mediated. If diffusion is not

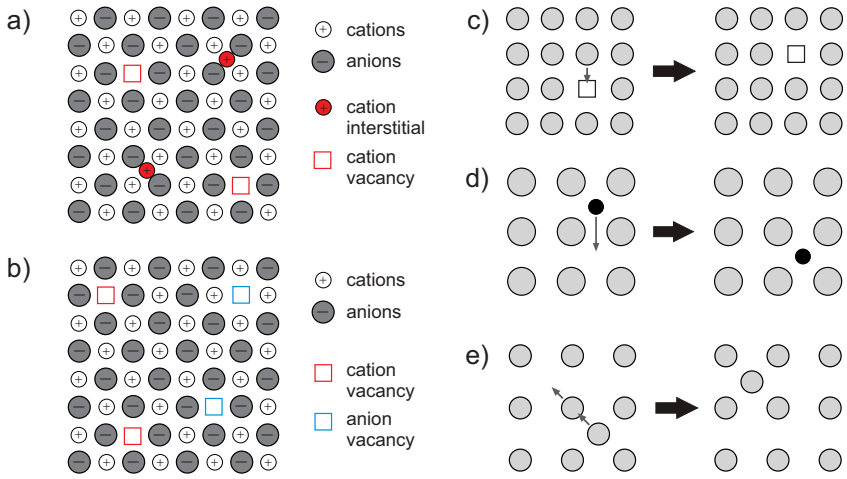

Figure 1: Structural defects of the a) cationic Frenkel-type, b) Schottky-type along with schematic representations of the most common diffusion mechanisms: c) the vacancy mechanism, d) the interstitial mechanism, e) the interstitialcy mechanism. Adapted from references [12,13].

just mediated by interstitial atoms correlation effects are inevitable. It shows how atomic jump probabilities depending on the direction of the previous jump. In the following, only a brief description is given for the most important mechanisms (*cf.* Figure 1c)-e)). More detailed information is available in the literature [12,13]:

The *vacancy mechanism* occurs preferentially for matrix and solute atoms in metals and alloys. Here, the atom jumps from its regular lattice site onto a vacancy, *i.e.* we find an atomic jump coupled with vacancy movement into the opposite direction. Diffusion via the vacancy-mechanism is mostly influenced by the mobility and availability of vacancies.

Interstitial mechanism (*direct interstitial mechanism*) denotes atomic movement only along interstitial sites, which works without the help of defects and thus results in enhanced diffusivity. This mechanism is favored by particles much smaller than the atomic building blocks of the lattice, i.e. they can be seen as solute atoms forming a solid solution with the host lattice.

If an atom occupying a regular lattice site is displaced by an interstitial atom the mechanism is called *indirect interstitial mechanism* or *intersticialcy* mechanism. This jump mechanism is important if the atomic particle is about the same size as the lattice atoms.

2.2 Measurements of Diffusion Parameters

There are different ways in order to classify methods for the determination of diffusion coefficients either by the length of the diffusion range, *viz.* as *microscopic* and *macroscopic* methods, or if they depend on the solutions of Fick's laws, *i.e. direct* and *indirect* methods. Addtionally, we differentiate between nuclear and non-nuclear methods. Figure 2 provides an overview of established techniques. As the detailed description of each method exceeds the frame of this introduction, only those techniques most relevant for this work are briefly described below and in the case of nuclear magnetic resonance spectroscopy (NMR) in a more exhaustive form in chapter 2.3.

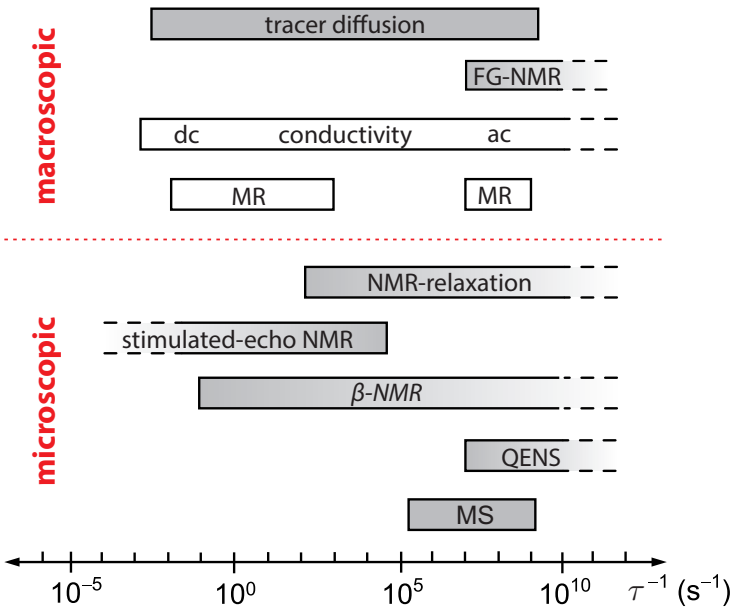

Figure 2: Overview on the dynamic range of microscopic and macroscopic methods for the measurement of self-diffusion parameters in solids (Adapted from [11]). Nuclear methods are marked with grey colors; non-nuclear methods in white. (FG-NMR: Field-gradient NMR, MR: Mechanical relaxation, QENS: quasi-elastic neutron scattering, MS: Mössbauer spectroscopy)

Macroscopic, direct methods are directly based on Fick's law and involve the recording of concentration profiles in solids, by radio tracer experiments [18]. Direct measurement of *macroscopic, i.e., long-range* diffusion may also be achieved by static or pulsed field-gradient nuclear

magnetic resonance (NMR)spectroscopy [20]. In contrast, indirect techniques generally study phenomena which are caused by diffusion. With the help of specific atomic models self-diffusion coefficients can be extracted, along with information on correlation effects. These values, extracted from micro- or macroscopic models, are necessarily approximations of D, as obtained by direct means.

DC-conductivity measurements [21] and mechanical relaxation spectroscopy both provide a non-nuclear access, whereby the latter is best suited to study mixed-ionic transport phenomena of glassy systems [22] In the frame of this PhD work we successfully applied this technique for the study of the monocrystalline Li ion conductor $LiAlO_2$ and compared macroscopic diffusion parameters with those obtained from dc-conductivity. (See section 3.2.2.)

Microscopic techniques can access microscopic parameters such as activation energy E_A and jump rates τ^{-1} on an atomic length scale. Nuclear methods involve the broad spectrum of NMR relaxometry in the laboratory and rotating frame of reference, β-NMR [8,23–25], quasi-elastic neutron scattering (QENS) [26], and Mössbauer spectroscopy [27]. With these indirect methods relaxation times or linewidths are measured and correlated with mean residence times, or jump rates. Via the *Einstein-Smoluchowski* equation (*cf.* equations (2.9) and (2.10)), they can be transformed into *self-diffusion* coefficients.

As shown in Figure 2, a broad time scale can be covered with NMR and conductivity measurements, *i.e.* impedance spectroscopy, depending on the measurement frequency. In order to gain information on long- and short-range diffusion characteristics it is necessary to combine complementary methods and techniques covering a broad time and length scale. The upper and lower limit of diffusion measurements via NMR are given by relaxometry in the laboratory frame of reference, where we can probe ionic motion up to the GHz-range and stimulated echo NMR techniques being sensitive to sub-Hz jumps. These, and other selected techniques are discussed in greater detail in the next chapter.

2.3 Solid-State Nuclear Magnetic Resonance

In the following section the fundamental properties of nuclear spin systems in an NMR experiment are explained via the classical vector model. Strictly speaking this model only applies to uncoupled spin systems; but it helps to illustrate the effects of pulsed NMR and understand key NMR experiments. However, a complete understanding can only be achieved with the help of quantum mechanics. As soon as we consider nuclear spin interactions, the dynamics of the system can only be described with quantum mechanical models.

Here, the basics of NMR and relevant magnetic and electric interactions are briefly outlined along with essential techniques for probing nuclear interactions. Ultimately, correlations of jump diffusion and NMR relaxation are explored on a micro- and macroscopic timescale. The following books provide extensive and detailed information on (solid-state) NMR spectroscopy [28–32] and were used along with references [7,33–36].

2.3.1 Basics of NMR

2.3.1.1 The Vector Model of Pulsed NMR

The phenomenon of nuclear magnetic resonance is based on interaction of a nucleus with a magnetic field. Certain types of nuclei appear to have a source of an angular momentum, which is referred to as the *nuclear spin angular momentum* $\boldsymbol{I}$, a vector quantity with both a direction and magnitude. Nuclei with $\boldsymbol{I} \neq 0$, often simply referred to as spins, possess a magnetic (dipole) moment $\boldsymbol{\mu}$. The magnetic moment describes each nucleus individually with the so-called gyromagnetic (also magnetogyric) ratio:

$$\boldsymbol{\mu} = \gamma \cdot \boldsymbol{I} \tag{2.11}$$

The spin angular momentum $\boldsymbol{I}$ is determined by the *spin quantum number I*, which can only possess discrete values. The absolute value is given by the relation

$$|\boldsymbol{I}| = \sqrt{I(I+1)}\hbar \tag{2.12}$$

with half-integer and integer values of I and $\hbar$ as the reduced Planck constant.

In the presence of a static magnetic field $\boldsymbol{B}_0$, a magnetic moment $\boldsymbol{\mu}$ experiences a torque $\boldsymbol{T}$. This causes a time-dependence of the spin precessing around B_0.

$$\boldsymbol{T} = \boldsymbol{\mu} \times \boldsymbol{B}_0 = \frac{d\boldsymbol{I}}{dt} \tag{2.13}$$

Together with equation (2.11) the classical equation of motion for the magnetic moment is given as:

$$\boldsymbol{\mu} \times \boldsymbol{B}_0 = \frac{1}{\gamma} \frac{d\boldsymbol{\mu}}{dt} \tag{2.14}$$

Thus, $\boldsymbol{\mu}$ precesses with an *angular frequency* ω_0, which is also referred to as *Larmor frequency*. (See Figure 3a)).

$$\omega_0 = \gamma \cdot B_0 \tag{2.15}$$

Zeeman Splitting

The energy of the nuclear dipole depends on the value of the magnetic moment $\boldsymbol{\mu}$ the static, uniform magnetic field $\boldsymbol{B}_0$ and the angle θ, between the spin momentum and the magnetic field. In order to describe the discrete energy states of the spin angular momentum we look at the projection of $\boldsymbol{I}$ (*cf.* equation (2.12)) onto the *z*-axis, *i.e.*, I_z, leading to discrete energy levels as:

$$I_z = m_I \hbar \tag{2.16}$$

with m_I denoting the magnetic quantum number: $m_I = I, I - 1, \ldots, -I$. According to the rules of quantum mechanics the orientation quantization of the magnetic moment leads to $2I + 1$ energy eigenvalues E_m of the nuclear spin vector:

$$E_\mathrm{m} = -\mu_z B_0 = -\gamma m_I \hbar B_0 \tag{2.17}$$

The splitting of the spin energy levels occurs as a result of the presence of a magnetic field $B_0 \neq 0$; the energy levels are equidistant and their absolute values are field-dependent (*cf.* Figure 3b)). This effect is known as *Zeeman splitting*. Upon irradiation with electromagnetic waves with the appropriate energy values the spins can cross over between the Zeeman levels, given that the condition $\Delta m = \pm 1$.[2] For the transition the required frequency ν depends on the gyromagnetic ratio γ and the field strength, which can be deduced from the angular frequency ω_0. (see also equation (2.15))

[2] Quantum mechanical selection rules for electromagnetic transitions involving a photon spin S=1 allow transitions between the energy levels for $\Delta m = \pm 1$, fulfilling the conservation of angular momentum.

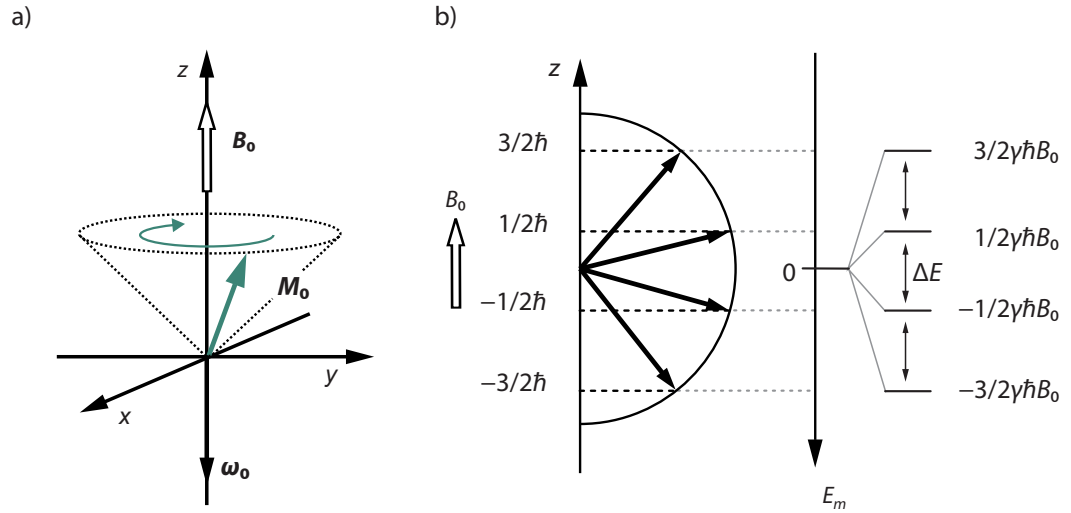

Figure 3: a) Larmor precession of the magnetization vector $\boldsymbol{M_0}$ in a static field $\boldsymbol{B_0}$. The angular frequency is given as $\boldsymbol{\omega}_0 = -\gamma \boldsymbol{B}_0$. b) Zeeman-splitting shown for a nucleus with I =3/2, *e.g.* ^{7}Li, in a static field B_0: For the projection of the spin angular momentum $\boldsymbol{I}$ onto the z-axis we find four possible orientations of I_z, due to the orientation quantization of the magnetic moment, as described in equation (2.16). Accordingly, the potential energy E_m splits into $2I$+1 equidistant energy levels. (Adapted from reference[11]).

$$\omega_0 = 2\pi\nu = |\gamma| B_0 \tag{2.18}$$

Therefore the NMR resonance condition can be written as:

$$\Delta E = \hbar |\gamma| B_0 = \hbar\omega_0 = h\nu \tag{2.19}$$

Occupation numbers $N_{m,m-1}$ of the two Zeeman levels are temperature-dependent and follow a Boltzmann distribution in the thermodynamic equilibrium state, *i.e.* a relaxed spin system.

$$\frac{N_{m-1}}{N_m} = \exp\left[\frac{-(E_{m-1} - E_m)}{k_B T}\right] = \exp\left[\frac{-\gamma\hbar B_0}{k_B T}\right] \tag{2.20}$$

Influence of RF Pulses

In an NMR experiment we observe a macroscopic net magnetization $\boldsymbol{M}$ of N nuclear spins in the field $\boldsymbol{B}_0$, which can be described as the vector sum of the magnetic moment $\boldsymbol{\mu}_i$ in the unit volume V.

$$\boldsymbol{M} = \frac{1}{V}\sum_{i=1}^{N}\boldsymbol{\mu}_i \tag{2.21}$$

Thus the equation of motion described for $\boldsymbol{\mu}$ in expression(2.14) can be expressed as:

$$\frac{d\boldsymbol{M}}{dt} = \gamma\cdot(\boldsymbol{M}\times\boldsymbol{B}_0) \tag{2.22}$$

Note, at thermal equilibrium $\boldsymbol{M}= \boldsymbol{M}_0$ is given by the sum of the z-components of $\boldsymbol{\mu}_i$ and thus $\boldsymbol{M}_z = \boldsymbol{M}_0$ and $\boldsymbol{M}_x = \boldsymbol{M}_y = 0$. During an NMR experiment the thermal equilibrium is disturbed by a radiofrequency (rf) field $\boldsymbol{B}_1$ perpendicular to the orientation of $\boldsymbol{B}_0$, generated by an electromagnetic coil in the xy-plane of the coordinate system, enabling the energy level cross-over of the spins. Such a time-dependent linearly oscillating magnetic field $\boldsymbol{B}_1$ can be described as

$$\boldsymbol{B}_1 = B_1\cos(\omega t)\cdot\boldsymbol{e}_x \tag{2.23}$$

with $\boldsymbol{e}_x$ as the unit vector in x-direction in the laboratory coordinate system. A linearly polarized field can also be described with the help of two *counter rotating* fields rotating around the z-axis clockwise and counterclockwise.

$$\boldsymbol{B}_1 = \frac{1}{2}B_1\cos(\omega t)\boldsymbol{e}_x + \frac{1}{2}B_1\sin(\omega t)\boldsymbol{e}_y + \frac{1}{2}B_1\cos(-\omega t)\boldsymbol{e}_x + \frac{1}{2}B_1\cos(-\omega t)\boldsymbol{e}_y \tag{2.24}$$

As the second term rotates in the opposing direction to the precessing magnetization it has no significant influence and can therefore be ignored in the following. Consequently, under the influence of a time-dependent field $\boldsymbol{B}_1$ the equation (2.22) of motion can be written as

$$\frac{d\boldsymbol{M}}{dt} = \gamma\boldsymbol{M}\times(\boldsymbol{B}_0 + \boldsymbol{B}_1(t)). \tag{2.25}$$

The motion of magnetization is easier to describe in a *rotating coordinate system* which removes the time-dependence of the RF field. It rotates with the *same* frequency as $\boldsymbol{B}_1$ along the direction of $\boldsymbol{B}_0$, *i.e.* the z-axis. Viewed in this frame the magnetization appears stationary. By switch-

ing from the laboratory to the rotating coordinate system an additional term is introduced into equation (2.22) which now reads as:

$$\left(\frac{d\boldsymbol{M}}{dt}\right)_{rot} = \gamma\cdot(\boldsymbol{M}\times\boldsymbol{B}) - (\boldsymbol{\omega}\times\boldsymbol{B}) = \gamma\cdot\left[\boldsymbol{M}\times\left(\boldsymbol{B}+\frac{\boldsymbol{\omega}}{\gamma}\right)\right] = \gamma\cdot\left(\boldsymbol{M}\times\boldsymbol{B}_{\text{eff}}\right) \tag{2.26}$$

As a result of switching to the rotating frame we now find an effective magnetic field $\boldsymbol{B}_{\text{eff}}$.

$$\boldsymbol{B}_{\text{eff}} = \boldsymbol{B} + \frac{\boldsymbol{\omega}}{\gamma} \tag{2.27}$$

Expressed with the unit vectors in the rotating frame $\boldsymbol{e}_{x'}$ and $\boldsymbol{e}_{z'} = \boldsymbol{e}_z$ it reads:

$$\boldsymbol{B}_{\text{eff}} = (B_0 - B_\omega)\cdot\boldsymbol{e}_{z'} + B_1\cdot\boldsymbol{e}_{x'} \quad \text{with} \quad B_\omega = -\frac{\omega}{\gamma} \tag{2.28}$$

B_ω represents the *reduced field* in the rotating frame. If $\omega = \omega_0$ the z-component vanishes and $B_{\text{eff}} = B_1$. This means that B_1 determines the motion of the magnetization, even though $B_1 \ll B_0$. As a result the magnetization precesses with $\omega_1 = \gamma\cdot B_1$. As an example: if B_1 is switched off as $\boldsymbol{M}$ rotates in the $x'y'$-plane, this is referred to as a 90°-pulse. In this case the magnetization precesses in the xy-plane around B_0 in the stationary coordinate system and induces a characteristic "answer" in the form of a voltage $U(\mathrm{t})$, *i.e.* the free induction decay (FID), in the magnetic coil. The manipulation of the magnetization by the angle θ depends on the pulse length and is defined by:

$$\theta = \omega_1\tau_{\text{p}} = \gamma B_1\tau_{\text{p}} \tag{2.29}$$

Thus, the direction of the magnetization can be tuned by the duration of B_1. Manipulation of $\boldsymbol{M}$ represents a perturbation of the thermodynamic equilibrium. The result of a 90° ($\pi/2$) pulse are equally populated the spin energy levels, whereas a 180° pulse leads to an occupation inversion with the magnetization aligned along the ($-z$)-direction. The system relaxes back to equilibrium via different relaxation mechanisms, characterized by the time constants T_1 and T_2 which can be described as follows:

$$\frac{\mathrm{d}M_{z=z'}}{\mathrm{d}t} = \frac{M_0 - M_{z=z'}}{T_1}, \tag{2.30}$$

$$\frac{dM_{x'}}{dt} = -\frac{M_{x'}}{T_2} \quad \text{and} \quad \frac{dM_{y'}}{dt} = -\frac{M_{y'}}{T_2} \tag{2.31}$$

Transversal relaxation time or *spin-spin relaxation* time denotes the relaxation of $\boldsymbol{M}$ in the $x'y'$-plane. The decay of the transversal magnetization is an entropy process; the spin level occupation and the total energy of the spin system remain constant. Instead phase coherence between the nuclear sites is lost, which is mainly caused by field inhomogeneities and locally different environments of the nuclear spins. Additionally the decay of M_{xy} can be influenced by localized spin-spin interactions, flip-flop processes and longitudinal relaxation due to diffusive motion of atoms and molecules.

$$M_{y'}(t) = M_0 \exp\left(-\frac{t}{T_2^*}\right) \tag{2.32}$$

T_2^* includes all above mentioned contributions to the dephasing of the spins. "Pure" spin-spin relaxation times can be measured with so-called spin-echo NMR techniques, applying a sequence of 90° and 180° pulses, as described in more detail in chapter 2.3.4.
The time-dependent decay of M_{xy} is reflected in the exponential decrease of an alternating voltage:

$$U(t) = U_0 \exp\left(-\frac{t}{T_2^*}\right) \tag{2.33}$$

This "free induction decay" is translated into the frequency range via Fourier transformation, yielding the NMR spectrum.

Longitudinal relaxation or *spin-lattice relaxation* (SLR) describes the relaxation of the magnetization in z-direction of the coordinate system, parallel to B_0 and is characterized by the spin-lattice relaxation time T_1 It is associated with the time which is required to transfer the energy that the spin system acquired during the rf pulse back to the lattice.[3] This relaxation process is sensitive to molecular and ionic motion if the timescale is in the order of the inverse Larmor frequency. Motion of the nuclei can be seen as fluctuation of local fields at the nuclear sites that induce the transition of the spin system back to equilibrium. Diffusion induced-relaxation is mainly caused by homo- and heteronuclear dipole-dipole interactions or interactions of nuclei

[3] The term "lattice" is used to describe a so-called "reservoir of energy"; here it is molecular motion. Hence spin-latttice relaxation can understood as energy flow between spins and molecular motion.[37]

with a quadrupole momentum with electric field gradients (*cf.* section 2.3.1.2) Other internal fluctuating fields can result from resulting from the spin interaction with i) conducting electrons in metals (Korringa relaxation), ii) electrons of surrounding atoms (chemical shift), iii) phonons or iv) localized fluctuations due to paramagnetic impurities [11]. With the help of temperature- and frequency-dependent NMR techniques the separation of diffusive from non-diffusive contributions is attempted. Further information on the SLR NMR techniques and the relation between spin-lattice relaxation and diffusion can be found in chapter 2.3.3.

2.3.1.2 Nuclear Spin Interactions

In the previous chapter the interaction of a single spin with the static magnetic field B_0 and a magnetic field due to rf pulses, B_1, has been presented. However, in order to describe the internal interaction between the spins a quantum mechanical approach is required. Interactions between the nuclei and internal electric and magnetic fields can be described with the help of *wavefunctions* and *operators*. Mathematically, wavefunctions are functions that entail the complete description of the system with appropriate operators extracting the information by acting on functions to produce new functions. Operators thus determines the *observables*, *e.g.* energy. The energy operator is called *Hamilton operator*, or *Hamiltonian* $\hat{H}$ with the "hat" indicating its use as an operator.

For a more detailed description and quantum mechanical basics in the context of NMR see the excellent textbooks of Levitt [30]and Duer [31]. In the following only the most important magnetic interactions are described, *viz.*, *chemical shielding*, *dipolar coupling* and *quadrupole coupling*.

The general representation of the interaction between a nuclear spin $\boldsymbol{I}$ and any field $\boldsymbol{B}$ can be described by the following Hamiltonian:

$$\hat{H} = -\gamma \hat{\boldsymbol{I}} \cdot \boldsymbol{B} = -\gamma (\hat{I}_x B_x + \hat{I}_y B_y + \hat{I}_z B_z) \tag{2.34}$$

$\hat{\boldsymbol{I}}$ represents the spin operator with its respective *x*-, *y*- and *z*-components $\hat{I}_x$, $\hat{I}_y$, $\hat{I}_z$ along with the components of the magnetic field. For the description of the whole spin system we need to take internal and external magnetic fields, *i.e.* the static field B_0 and the high frequency field B_1 into account:

$$\hat{H}_{\text{tot}} = \hat{H}_{\text{ext}} + \hat{H}_{\text{int}} \quad \text{mit} \quad \hat{H}_{\text{ext}} = -\gamma \cdot \hat{I} \cdot (B_0 + B_1(t)) \tag{2.35}$$

Interactions represented by $\hat{H}_{\text{int}}$ arise from internal sources, *viz.* local fields, as a result of the interaction with other spins or due to chemical shielding. Any local magnetic field can be expressed as:

$$\boldsymbol{B}_{\text{loc}} = \boldsymbol{A}_{\text{loc}} \cdot \boldsymbol{J}. \tag{2.36}$$

$\boldsymbol{A}_{\text{loc}}$ denotes the coupling tensor, representing the nuclear spin interaction and its orientation dependence, with the vector $\boldsymbol{J}$ describing the ultimate source of the local field, *viz.*, another nuclear spin in the case of dipole-dipole coupling, or B_0 itself in the case of chemical shielding.

Chemical Shift and Chemical Shift Anisotropy (CSA)

The electrons surrounding the nuclear spin react to the influence of the magnetic field applied in the NMR experiment inducing circular electric currents in the electron shell. This produces a secondary magnetic field opposed to B_0 which, in return, interacts with the nucleus. The electron density at the nuclear site is influenced by the chemical environment, *i.e.* chemical bonding and polarization effects of the spin ensemble. This so-called shielding interaction is the source of the frequency shift observed in an NMR spectrum, and thus enables structural analysis via NMR. If the chemical shielding is influenced by diamagnetic effects, the effective field at the nuclear site is decreased. On the other side paramagnetic effects support the applied field and tend to de-shield the nucleus, resulting in a magnetic field larger than B_0. Therefore, in accordance with the general form proposed in equation (2.36) the corresponding interaction Hamiltonian can be written as

$$\hat{H}_{cs} = -\gamma \hat{\boldsymbol{I}} \cdot \boldsymbol{\sigma} \cdot B_0 \tag{2.37}$$

with B_0 as the ultimate source of shielding and the second-rank tensor $\boldsymbol{\sigma}$ describing the chemical shielding. In liquids translational and rotational motion lead to an averaging of the anisotropic magnetic contributions, which is why solely an isotropic shielding value σ_{iso} is determined. In the solid state the electron distribution around the nucleus is highly anisotropic, and thus the chemical shifts of the nuclei strongly depend on the orientation of B_0. The tensor $\boldsymbol{\sigma}$ contains the isotropic chemical shift σ_{iso}, the anisotropy $\Delta\sigma$ and the asymmetry parameter η. In solids the increasing influence of the anisotropic and asymmetric parameters $\Delta\sigma$ and η leads to broad powder spectra. For the NMR experiment the secular part of the Hamiltonian opera-

tor describing the chemical shift is relevant. It considers the interactions in the *z*-direction with respect to B_0.[4] The corresponding matrix elements are defined as follows:

$$\begin{aligned} \sigma_{\text{iso}} &= \frac{1}{3}(\sigma_{xx} + \sigma_{yy} + \sigma_{zz}) \\ \Delta\sigma &= \sigma_{zz} - \sigma_{iso} \\ \eta &= \left(\sigma_{xx} - \sigma_{yy}\right) / \Delta\sigma \end{aligned} \tag{2.38}$$

Following equation (2.36) and (2.37) the Hamiltonian for the chemical shift reads[31]:

$$\hat{H}_{\text{CS}} = \gamma \hat{I}_z B_0 \left[\sigma_{\text{iso}} + \frac{1}{2}\Delta\sigma\left(3\cos^2\theta\right) - 1 - \eta\sin^2\Theta\cos 2\phi) \right] \tag{2.39}$$

The polar coordinates describe the orientation of B_0 with respect to the principal axis frame of the chemical shift tensor, which is determined by the electronic structure of the molecule. The resulting NMR powder pattern represents a sum of the different orientations of the structural element under investigation. In the case of fast isotropic motion only σ_{iso} is detected, as the angle-dependent contributions are averaged. In order to obtain a field-independent isotropic chemical shift $\delta_{\text{CS}} = -\sigma_{\text{iso}}$, the respective resonance frequency ν_{iso} is related to a reference substance with the frequency ν_{ref}.

$$\delta_{\text{CS}} = \frac{\nu_{\text{iso}} - \nu_{\text{ref}}}{\nu_{\text{ref}}} \cdot 10^6 \left[\text{ppm}\right] \tag{2.40}$$

Dipolar interactions

Due to their magnetic moment, nuclear spin generate a magnetic field and interact with each other; this is referred to as *direct dipolar coupling* or *dipole-dipole coupling*. Note that indirect dipole-dipole coupling (scalar (*J*-) coupling), which is mediated through electrons but negligible in the case of solids. Dipolar coupling in solution is averaged due to molecular tumbling. In solid-state spectra, on the other hand, it is a major source for the broadening of the resonance

[4] In general, for all internal interactions described here, only the secular part of the corresponding Hamiltonian suffices to describe the interaction given that the external interaction, *i.e.*, Zeeman-interaction $\hat{H}_Z$ is much larger than the internal one.

line and relaxation processes. The interaction energy of two point-magnetic dipoles μ_1 and μ_2, separated by the internuclear distance r is:

$$U = \left\{ \frac{\mu_1 \mu_2}{r^3} - 3\frac{(\mu_1 \cdot \boldsymbol{r})(\mu_2 \cdot \boldsymbol{r})}{r^5} \right\} \frac{\mu_0}{4\pi} \tag{2.41}$$

with $\boldsymbol{r}$ denoting the vector between the point-magnetic dipoles and μ_0 as the vacuum permeability. From a quantum mechanical point of view the magnetic moment operator of the spin $\boldsymbol{I}$ is given by the relation $\hat{\boldsymbol{\mu}} = \gamma \hat{\boldsymbol{I}}$. Therefore the interaction Hamiltonian for dipolar coupling between two spins i and j is obtained as follows:

$$\hat{H}_{\mathrm{D}} = \frac{\mu_0}{4\pi} \frac{\gamma_i \gamma_j}{r_{ij}^3} \left(\hat{\boldsymbol{I}}_i \hat{\boldsymbol{I}}_j - 3\left[\left(\hat{\boldsymbol{I}}_i \boldsymbol{e}_{ij} \right) \left(\hat{\boldsymbol{I}}_j \boldsymbol{e}_{ij} \right) \right] \right) \tag{2.42}$$

With respect to equation (2.42) r_{ij} denotes the distance and $\boldsymbol{e}_{ij}$ represents the unit vector between both spins. By expanding the scalar products equation (2.42) can be expressed with the help of polar coordinates [29]:

$$\hat{H}_{\mathrm{D}} = \frac{\mu_0}{4\pi} \frac{\gamma_i \gamma_j}{r_{ij}^3} (A + B + C + D + E + F) \tag{2.43}$$

where:

$$\begin{aligned}
A &= \hat{I}_i^z \hat{I}_j^z (1 - 3\cos^2 \theta_{ij}), \\
B &= -\frac{1}{4} \left(\hat{I}_i^+ \hat{I}_j^- + \hat{I}_i^- \hat{I}_j^+ \right) \left(1 - 3\cos^2 \theta_{ij} \right), \\
C &= -\frac{3}{2} \left(\hat{I}_i^+ \hat{I}_j^z + \hat{I}_i^z \hat{I}_j^+ \right) \sin\theta_{ij} \cos\theta_{ij} e^{-i\phi_{ij}}, \\
D &= -\frac{3}{2} \left(\hat{I}_i^- \hat{I}_j^z + \hat{I}_i^z \hat{I}_j^- \right) \sin\theta_{ij} \cos\theta_{ij} e^{+i\phi_{ij}}, \\
E &= -\frac{3}{4} \hat{I}_i^+ \hat{I}_j^+ \sin^2 \theta_{ij} e^{-i2\phi_{ij}}, \\
F &= -\frac{3}{4} \hat{I}_i^- \hat{I}_j^- \sin^2 \theta_{ij} e^{+i2\phi_{ij}}.
\end{aligned} \tag{2.44}$$

$\hat{I}^{+}_{i(j)}$ and $\hat{I}^{-}_{i(j)}$ are the respective raising and lowering operators for spins *i* and j. In fact, the terms C to F can be neglected [29] and therefore the secular Hamiltonian takes the following form, depending on the nature of the dipolar interaction, *i.e.*, homonuclear ($\gamma_i = \gamma_j = \gamma_I$),

$$\hat{H}_{\mathrm{D}}^{\mathrm{homo}} = -\frac{1}{2}\frac{\mu_0}{4\pi}\frac{\gamma_I^2}{r_{ij}^3}\left(\hat{\boldsymbol{I}}_i\hat{\boldsymbol{I}}_j - 3\hat{I}_i^z I_j^z\right)\left(1-3\cos^2\theta_{ij}\right) \tag{2.45}$$

or heteronuclear ($\gamma_i \neq \gamma_j$), where only the term A contributes [29]:

$$\hat{H}_{\mathrm{D}}^{\mathrm{hetero}} = \frac{\mu_0}{4\pi}\frac{\gamma_i\gamma_j}{r_{ij}^3}\hat{I}_i^z\hat{I}_j^z(1-3\cos^2\theta_{ij}) \tag{2.46}$$

Due to the strong dependence on nuclear spin distance ($\propto r_{ij}^3$) dipolar coupling usually needs to be considered for the spins in the nearest neighborhood.

Quadrupolar Coupling

All nuclei with a spin $I \geq 1$ are quadrupolar, *i.e.* they possess a quadrupole moment eQ with e being the proton charge. This quadrupole moment is independent of the chemical environment of the respective nucleus and constant for each type of nucleus. The quadrupolar coupling arises from the interaction with an electric field gradient (EFG) at the nuclear site. Such an electric field gradient arises at sites with non-cubic symmetry and is influenced by local distribution of other nuclei and electrons, *i.e.* the electronic charge distribution around the nucleus differs from spherical symmetry and takes an ellipsoid form. Thus, the nucleus does not only interact with the applied magnetic field and local magnetic fields, but with any EFG present at this site. As a result the Zeeman levels are shifted. Similarly to the other nuclear interactions as described above the quadrupolar interaction Hamiltonian is given as:

$$\hat{H}_{\mathrm{Q}} = \frac{eQ}{2I(2I-1)\hbar}\hat{\boldsymbol{I}}\cdot\boldsymbol{V}\cdot\hat{\boldsymbol{I}} \tag{2.47}$$

$\boldsymbol{V}$ represents the traceless EFG tensor[5], which allows the description of the field gradient via two parameters: the quadrupole coupling constant C_{Q} and the asymmetry parameter η_{Q}. These parameters can be calculated using the diagonal entries of the EFG tensor expressed in its principal axis frame, *viz.* V_{XX}, V_{YY}, V_{ZZ}.

[5] traceless: sum of the matrix main diagonal equals zero, *i.e.*, $V_{XX} + V_{YY} + V_{ZZ} = 0$.

$$C_Q = \frac{e^2 qQ}{\hbar} \text{ with } eq = V_{ZZ} \tag{2.48}$$

$$\eta_Q = \frac{V_{XX} - V_{YY}}{V_{ZZ}} \tag{2.49}$$

If the Zeeman interaction outweighs the quadrupolar contribution, *i.e.* $\|\hat{H}_Z\| \gg \|\hat{H}_Q\|$ or rather $\omega_0 \gg \omega_Q$, also only the secular part of the Hamilton operator is required to calculate the quadrupole coupling. The polar coordinates θ and ϕ describe the orientation of the EFG with respect to the external magnetic field.

$$\hat{H}_Q = \frac{C_Q}{8\hbar I(2I-1)}\left(3\hat{I}_Z^2 - \hat{\boldsymbol{I}}^2\right)\left(3\cos^2\theta - 1 + \eta_Q \sin^2\theta\cos 2\phi\right) \tag{2.50}$$

The energy by which the Zeeman levels are shifted can be determined with the help of the time-independent Schrödinger equation.

$$E_Q^m = \hbar\frac{C_Q}{8I(2I-1)}\left(3m_I^2 - I(I+1)\right)f(\theta,\phi) \tag{2.51}$$

Here, the angular dependence is given by the relation $f(\theta,\phi) = 3\cos^2\theta - 1 - \eta\sin^2\theta\cos 2\phi$. Nuclei with an integer spin number give spectra composed solely of satellite transitions, whereas in the case of half-integer spins (*e.g.*, $I = 3/2$) a central line is obtained, flanked symmetrically by the satellite transitions. For half integer spins the transition frequency for the transition $m = +1/2 \rightarrow -1/2$ (central transiton) remains unaffected by quadrupolar anisotropy to first order, while transition frequencies for $m = +3/2 \rightarrow +1/2$ and $m = -1/2 \rightarrow -3/2$ (satellite transitions) are raised or lowered by the quadrupole frequency ω_Q. The satellite transitions are removed differ from the Larmor frequency by the quadruopole splitting:

$$\omega_Q = \frac{3e^2 qQ}{8I(2I-1)}((3\cos^2\theta - 1) + \eta_Q \sin^2\theta\cos 2\phi) \tag{2.52}$$

So for non-integer spins we observe one central line and $2I - 1$ satellite resonances. In solid powders a distribution of EFG can be found due to the random orientation of the crystallites, resulting in a quadrupole powder pattern as shown in the example spectrum depicted in Figure 4. As the satellites are removed from the central transition ω_Q can be directly read out from the spectrum with $C_Q = 2\omega_Q$. Satellites under the influences of an asymmetric EFG tend to smear out, as can be seen on the righthand side of Figure 4. However, note that these equations are

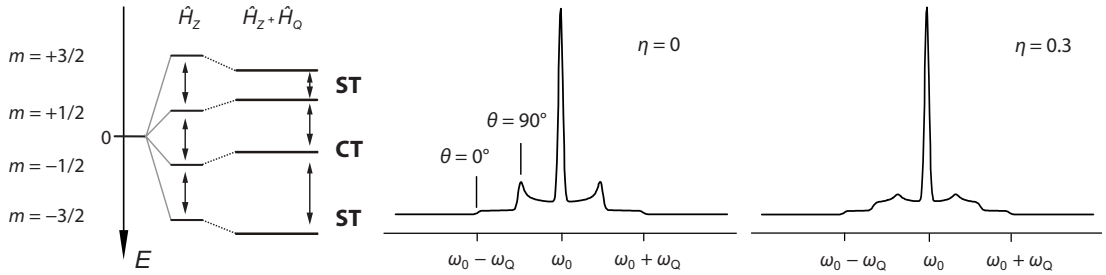

Figure 4: *left*: Energy level splitting with and without the influence of quadrupole interaction for a spin-3/2 nucleus. *right*: simulations of the corresponding static powder spectra $(I = 3/2)$ for a symmetric $(\eta = 0)$ and asymmetric EFG $(0 \leq \eta \leq 1)$. (Adapted from reference [11]).

only suitable if the quadrupole coupling is weak compared to the Zeeman interaction. For nuclei with large quadrupole coupling moments and low symmetry of the electronic environment the calculation via the secular part of the Hamiltonian is inadequate; as a matter of fact an angular dependence is also given for the central transition.

The magnitude of the quadrupolar interaction can also significantly contribute to nuclear relaxation processes, in addition to dipolar coupling, as mentioned above. Also, if the sample is rotated with respect to the magnetic field the orientation-dependent quadrupolar interaction changes. This is feature is useful in magic-angle spinning (MAS) NMR.

2.3.2 High-Resolution Magic-Angle Spinning NMR

Nuclear spin interactions affect solid-state NMR, as they are all orientation-dependent, *i.e. anisotropic*. In particular for solid powder samples, which can be described as crystallites with random orientations, this results in many different molecular orientations, or rather frequencies. Because of that, we obtain so called powder patterns. For many crystallite orientations, however, these powder patterns do overlap and are additionally broadened by dipolar coupling of the spins. In the liquid state, anisotropic interactions as chemical shift anisotropy, dipole or quadrupole coupling are barely observed due to fast isotropic tumbling of the molecules. In other words: the rate of the orientation change exceeds the magnitude of these spin interactions. For solid samples, the application of magic-angle spinning (MAS) NMR provides the necessary means to average anisotropic parts of the interaction. This chapter describes how high-resolution NMR spectra can be achieved with this technique, hereby revealing structural or dynamical information on the material under investigation. For further reading on the theoretical background of the MAS technique see references [31,32,37], which were extremely useful in the conceptualization of the following section.

Historically, MAS NMR is one of the first techniques for narrowing dipolarly broadened lines but it can also eliminate chemical shift anisotropies and first order quadrupolar splitting[6]. All the (interaction) operators introduced above contain an angular-dependent factor $(1-3\cos^2\theta)$, with the angle θ describing the orientation of the spin interaction tensor. In a powder sample the orientation of θ takes all possible values. If the sample is spun around an axis which is inclined to the applied field B_0 under a certain angle θ_R, the molecular orientation varies with time. This powder-averaged orientation dependence (as indicated by the brackets $\langle ... \rangle$) is given as:

$$\left\langle 1-3\cos^2\theta \right\rangle = \frac{1}{2}\left(1-3\cos^2\theta_R\right)\left(1-3\cos^2\beta\right) \tag{2.53}$$

with β as the angle between the principal z-axis of the shielding tensor and the rotation axis of the sample (*cf.* Figure XX). By choosing θ_R = 54.74° the condition $1-3\cos^2\theta_R = 0$ is satisfied and the orientation dependence equals zero. Further, a sufficient magnitude of the spinning rate has

[6] The molecular orientation dependence is influenced by second-rank rotation matrix terms of the quadrupole coupling tensor, leading to a removal of the first-order quadrupolar interaction through MAS, whereas the second-order effects depend on the second- *and* fourth-rank rotation matrices and are not averaged here. For a more detailed description see [31].

to be provided so that all orientations are averaged rapidly compared with the interaction anisotropy. If the spinning rate is too slow we can observe so-called spinning sidebands in addition to the isotropic chemical shift. These sharp sidebands appear to the left and right side of the isotropic line, separated by a distance equal to the spinning rate. Note that the isotropic line is not necessarily the most intense spectral line, but the only one that does not change position with the spinning rate. Nowadays spinning rates up to 50 kHz can be achieved in small rotors with diameters of 1.2 mm, but usually by spinning the sample at 30 kHz only few sidebands are obtained. However, for nuclei with a large CSA, *i.e.*, with a large number of electrons such as ^{195}Pt, ^{207}Pb ^{117,119}Sn, we see many spinning sidebands. As the CSA is proportional to the magnetic field strength it gets worse at higher fields. As mentioned above, magic-angle spinning only averages the first order quadrupole broadening of satellite transitions, and in most cases the spinning cannot be fast enough to achieve full averaging, resulting in an array of sidebands. But in fact, we can analyze the spinning bands to extract interaction parameters that are otherwise masked if only the isotropic line is obtained at high spinning rates. The expected spectrum is calculated with different values for anisotropy and asymmetry values and compared with the experimental pattern until it agrees. Note, that if the spinning speed is not large enough to average the dipolar coupling between nuclei additional sidebands appear. Consequently, this leads to an inaccurate fitting, and thus, erroneous determination of CSA.

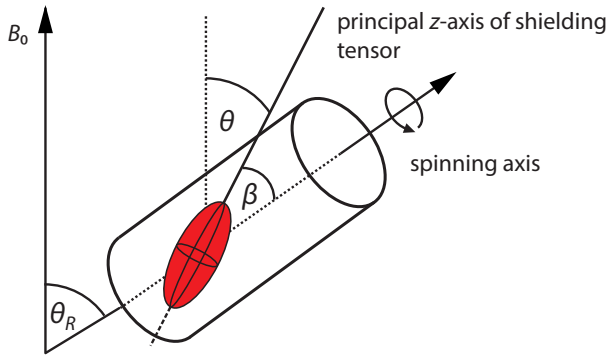

Figure 5: Principle of magic-angle-spinning: If the sample is spun rapidly about an axis inclined about the angle θ_R = 54.74° to the applied static field B_0 the effects of chemical shielding and heteronuclear dipolar coupling are removed. (θ and β denote the angle between the principal z-axis of the tensor with B_0 and the spinning axis, respectively. Here, the ellipsoid shielding tensor represents a randomly oriented molecule in a powder sample.) Adapted from reference [31].

Concerning the quadrupolar interaction, first-order effects are averaged to zero through spinning for the central transition. However, second and higher-order effects are not fully averaged by MAS NMR and an anisotropic pattern remains.

Nonetheless, MAS NMR can be used to investigate the structural features and the environment of the nucleus, as it enhances the signal resolution of magnetically inequivalent nuclear sites that only differ minimally by their chemical shift. With the help of advanced pulse sequences we can selectively induce or suppress interactions between the nuclei under investigation.

Two-Dimensional NMR (following reference [37])

The development of 2D NMR techniques has made structure determination much easier, and thus allows more complex problems to be resolved. Where in conventional 1D NMR spectra we find the intensity plotted versus the frequency domain, 2D spectra entail intensities versus two frequency domains, *i.e.*, that each peak has one intensity and two frequency coordinates. Generally speaking, in most types of experiments the positions of these peaks show a correlation between two quantities. Hereby, it can be distinguished between 2D experiments whether the transfer of magnetization occurs through scalar coupling or through relaxation processes, *e.g*, such as the *Nuclear Overhauser Effect* (NOE) or cross-correlation and, and for studying dynamics, the transfer through *chemical exchange*. During the *preparation period* (also: *evolution period*) the equilibrium magnetization is transformed into a type of *coherence*[7] that evolves during the variable preparation time t_p (also referred to as evolution time). Preparation might occur through a simple 90° pulse ($\beta_1 = \pi/2$) inducing transverse magnetization (single-quantum coherence) or through a more complex series of pulses and delays, which for example, create so-called multiple-quantum coherences or generate the transfer of magnetization from another type of nucleus (INEPT-style) [37]. The preparation time is varied systematically in a series of experiments without observing the evolving coherences. In the next step the coherence is transferred into an observable signal during the mixing time t_m, involving the transfer of magnetiza-

[7] Coherence is the reason for the generation of transverse magnetization of the spins. At equilibrium we observe no (bulk) magnetization in *x*- and *y*-direction, thus the z-magnetization can be regarded as a polarization along the *z*-axis. Due to the interaction with an RF pulse the polarization along *z* is rotated to the *y*-direction and the coherence in the sample is simply generated by all the spins experiencing the same RF field. Sometimes the term coherence is used in the sense of an "alignment of spins." However, the pulse does not create an alignment or alter the phases of the spins; it just rotates the polarization of the *z*-magnetization to another direction.

tion from one spin to the other. Here, the form of the mixing time determines the type of experiment. This experiment is concluded by the detection period t_2.

MQ-MAS NMR

High resolution NMR experiments for spin numbers $I > 1/2$, *i.e.*, on nuclei with a quadrupole moment, require elaborate techniques where second and higher-order quadrupolar effects can be eliminated. Besides double rotation (DOR) and dynamic-angle spinning (DAS), the multiple-quantum magic-angle spinning (MQ-MAS) NMR experiment proves to be a feasible technique to increase the resolution of quadrupolar spectra and enables the detection of previously unseen structural species. This is especially significant for NMR studies on disordered materials, *i.e.*, glasses [38]. In the following, a brief description is given only for MQ-MAS NMR which has been applied in our studies on Al- and Ga-containing solid electrolytes. For a more comprehensive description see references [31,39–45]. Developed by Frydman and Harwood in 1995 [39,41], this method has become the primary technique for the study of half-integer quadrupolar nuclei for major reasons. In contrast to DAS and DOR, MQ-MAS experiments can be achieved with ordinary MAS probeheads and are easier to implement as the sample spins at just one angle throughout the experiment. The DOR technique averages the (second-order) quadrupolar broadening through rotating the sample around two axes, while during DAS experiments the rotating angle is changed, which both involves a lot of experimental effort. In the MQ-MAS experiment the sample is spun at the (fixed) magic-angle through the whole experiment in order to remove the effects of first-order quadrupolar coupling as well as other first-order effects like dipolar or chemical shift anisotropies. The spins evolve during two periods of time t_1 and t_2 under the influence of two different transition orders m_1 and m_2. During the first pulse multiple quantum coherences are formed. The choice of this order m_1 depends on the spin number I (for $I = 3/2$ only $m_1 = 3/2$ is available; for $I = 5/2$ $m_1 \leq 5/2$, *etc.*) The order of the coherence that evolves during t_1 is changed to a single-quantum coherence ($m_2 = ½$) and an echo is recorded in t_2. Second-order driven anisotropies are refocused at times fulfilling the condition:

$$t_2 = \left\{ \frac{\left| C_4^S(m_1) \right|}{C_4^S(1/2)} \right\} t_1 \tag{2.54}$$

with

$$C_4^S(m) = 2m\left[18I(I+1) - 34m^2 - 5\right] \tag{2.55}$$

Consequently, in a 2D representation of t_2 versus t_1 we find the signal intensities on a straight line with the slope 42/54 for $m_1 = 3/2$.
Via Fourier transformation of the time-domain data followed by a shearing transformation yields a representation with ν_1 (1Q domain) containing the distorted MAS line shape and ν_2 describing the isotropic dimension where the signals are highly resolved and electrically inequivalent sites can be distinguished.

Chemical Exchange as Seen via 2D Exchange and 1D Selective Inversion NMR
As the study of chemical exchange in NMR is an exhaustive topic, a comprehensive description would go beyond the scope of this introduction; it is only briefly discussed in the context of the NMR techniques used in the framework of this thesis. The reader is referred to the following references: [37,46,47].

When we look for evidence of exchange we will see that the NMR spectrum depends on the exchange rate constant and the frequency difference of the two observed environments. Fast exchange means that the rate constant is larger than the frequency separation of the NMR peaks, and accordingly for slow exchange the rate is much smaller than the frequency difference. Let us consider the case of exchange between site A and B: With no exchange present one peak shows at the position of A and one at the position of B, well separated and both of same intensity, given that both sites are equally populated. As the exchange rate k_{ex} increases, the peak intensity decreases, and line broadening sets in before the signals finally overlap and a single merged peak evolves. The position of this *coalescence* peak always depends on the population of the sites involved. With A and B having equal populations the shift of the merged line can be found in the middle between A and B. In the limit of fast exchange, where the rate constant is much larger than the frequency separation, the line narrows again and has the same width as in the absence of exchange. This phenomenon is called *exchange narrowing*, whereas *exchange broadening* describes the increase of the linewidth due to slow exchange. Note that the line broadening can be additionally influenced by magnetic field inhomogeneities and other mechanisms. Thus, instead of estimating the exchange rate solely from the line broadening, measuring the effects of chemical exchange on the spin-lattice relaxation rate provides a better access to the rate constant. If we invert the magnetization of the spin through a 180° RF pulse, it

relaxes back to equilibrium via the relaxation mechanisms as described above (see section 2.3.1.1). For a two-site system the spin may undergo a site exchange during relaxation.

2D Exchange NMR

The *2D exchange spectroscopy* technique (EXSY)[46,47] is widely used to study slow chemical exchange. In principle, the pulse sequence is the same as in the NOESY (Nuclear Overhauser Effect Spectroscopy) experiment that takes advantage of the dipolar relaxation between spins. (See, *e.g.*, p. 33 in Ref. [47]) After the first $\pi/2$-pulse the magnetization evolves in the transverse x',y'-plane during t_p. Here, the initial conditions are frequency-labelled in order to get a correlation between the initial conditions and the observed signal. This means that the relaxation rate of one site depends on the initial state of the other site (as a function of the evolution time t_p). The second $\pi/2$-pulse tips the magnetization into the $-z$-direction allowing the system to relax during the mixing time t_m via exchange and longitudinal relaxation before the signal is made observable through a third non-selective $\pi/2$-pulse. A 2D-Fourier transformation yields a spectrum with cross-peaks revealing exchange (during t_m) between the respective sites that are involved, with the main intensities of the 1D spectrum along the diagonal. For a two-site jump process we can determine an actual exchange rate τ_{ex} from the ratio between the intensities of the cross-peak and the diagonal-peak:

$$\frac{I_c}{I_d} = \left[1 - \exp\left(-\frac{t_m}{\tau_{ex}}\right)\right], \text{ or } \tau_{ex} = -\frac{t_m}{\ln\frac{I_d - I_c}{I_d}} \tag{2.56}$$

With I_d and I_c as the respective diagonal and cross-peak intensities. Another, however, time-consuming way is measuring the cross-peak intensities in a series of experiments with different mixing times [48,49]. The slope of the resulting line directly represents the exchange rate. The rate constant can be directly transformed into a Li self-diffusion coefficient using the Einstein-Smoluchowski relation (*cf.* equation(2.9)). Note that other correlation effects, like the NOE, also lead to appearance of cross-peaks. The NOE is caused by dipolar cross-relaxation between spatially close nuclei. In order to suppress cross-relaxation in favor of exchange, the nuclei species under investigation has to be present in a diluted form, *i.e.* with its neighbor far away. In the case of ^{6}Li the NOE is usually not a problem, due to the low natural abundance of this isotope. Otherwise, unwanted effects contributing to off-diagonal intensities can be eliminated through appropriate phase cycling.

1D Selective Inversion NMR

Although 2D EXSY draws a comprehensive picture of distinct chemical exchange processes, quantitative analysis often requires significant amount of spectrometer time in order to extract information on the timescales and energy barriers of slow exchange processes. 1D selective inversion NMR experiments have been found to show a more efficient way of quantifying exchange in two- and multisite systems [50–54] by considering the complete course of exchange and relaxation. Following the selective inversion of the magnetization of a single spin, its relaxation towards equilibrium, *i.e.* via spin-lattice relaxation and exchange, is monitored over a series of mixing times in one experiment.

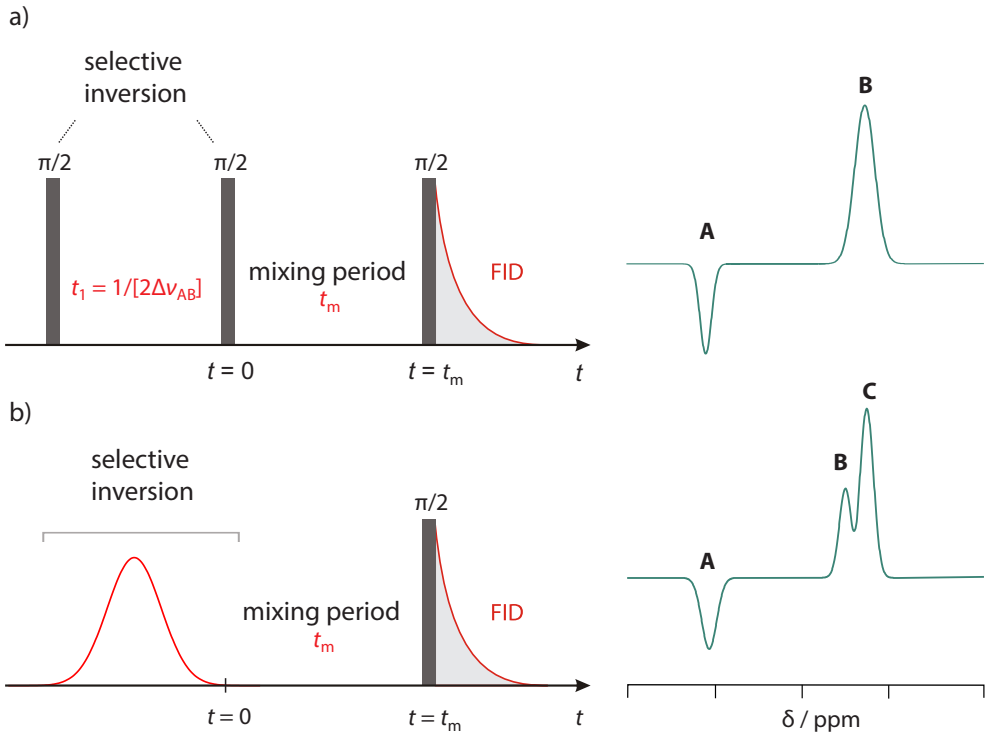

Figure 6: a) illustrates the schematic pulse sequence for a 1D EXSY experiment .This technique cannot be extended beyond a 2-site, 1-exchange process system. b) Selective inversion with a Gaussian-shaped (180°) pulse can be applied for the selective excitation of one site undergoing multiple exchange processes. Corresponding 1D inversion spectra are shown on the right.

The pulse sequence follows the scheme of Figure 6 where the first $\pi/2$-pulse is on-resonance with one site of the exchange pair and brings both into the transverse plane. Here the time period t_1 is set to $1/2\Delta\nu_{ab}$, where ν_{ab} is the frequency difference of the exchange pair A and B under the condition of no exchange. As a result the off-resonance spins will precess to the opposite side of the $x'y'$-plane, creating a maximum difference of magnetization. The second pulse transfers the on-resonance spin *selectively* onto the $-z$-direction whereas the exchange partner is placed along the $+z$-direction. Experiments are carried out as a function of the mixing time, with the longest t_m ensuring full relaxation of the inverted spin.[8] As the evolution time depends on the spectral distance between the two spins involved, the 1D EXSY technique is sensitive to the single exchange process taking place between two sites.[50,51] For studying more complex system, involving multiple ion exchanges *selective inversion* experiments using shaped pulses were successfully applied both in liquid [54–57] and solid systems [50–53,58] The 90° - t_1 - 90° sequence is replaced with a 180° - t_m - 90° sequence, where the first pulse is applied in the form of a soft Gaussian-shaped pulse [48,55] with t_m denoting the mixing time which is stepped over a series of experiments (Figure 6). Here, tuning the bandwidth of the pulse to selectively excite the inversion of only one spin and monitor the relaxation back towards equilibrium for more (than one) non-inverted spins, provided a sufficient resolution in the 1D MAS spectrum exists [55]. Increase of the transient well depth, *e.g.* with increasing temperature, can be traced back to an increase of the exchange rate. The temperature-dependence of the rates further allows the calculation of energy barriers for the hopping process [50–53,58]. More information on this technique, in particular for the mathematical deconvolution of the selective inversion spectra, see references [46,54].

2.3.3 NMR Relaxation and Diffusion

During the NMR experiment the thermal equilibrium of a spin system can be disturbed by resonant RF pulses altering the population of the Zeeman states. The *relaxation* of the system back to thermal equilibrium is mediated by temporal fluctuations of local fields. These temporal fluctuations can be due to interactions of the spins with the "lattice", *i.e.* their surroundings, *viz.* conducting electrons (in metals), electrons of their nearest neighbors, as well as phonons or localized fluctuations induced by paramagnetic centra, or localized motional processes. Diffu-

[8] In order to determine a suitable range for t_m, ensuring full longitudinal relaxation, $1/T_1$, the corresponding rate constant is determined in a second, non-selective inversion recovery experiment. Strictly speaking, the value for the rate constant is influenced by exchange, but it suffices for the evaluation of the selective inversion data.

sion-induced spin-lattice relaxation is, however, caused by dipolar and quadrupolar interactions of spins with neighboring spins with electric field gradients. If the jump rate of the nuclei is in the order of the Larmor frequency, transitions between the Zeeman levels can be induced effectively. Thus, the nuclear magnetic relaxation rate can be used to characterize diffusion processes in solids.

Referring to the orientation of the external magnetic field we can distinguish between two different relaxation processes: *longitudinal relaxation* or *spin-lattice relaxation* with the characteristic time T_1, occuring in the direction of the applied field, and relaxation perpendicular to the field, *i.e.* transversal or spin-spin relaxation expressed via the relaxation time T_2.

Relaxation and Spectral Density Functions

Relaxation processes can ultimately be described via *spectral density functions* $J(\omega)$. The spectral density function is the Fourier transform of the *autocorrelation function* $G(t)$ describing an ensemble average of the transitions between the spin states $|i\rangle$ and $|j\rangle$.

$$G_{ij}(\tau) = \overline{\langle i|\hat{H}_1(t-\tau)|j\rangle\langle j|H_1(t)|i\rangle} \tag{2.57}$$

$\hat{H}_1$ denotes the perturbation Hamiltonian characteristic for the interaction, *i.e.* with fluctuations induced by (direct) dipole-dipole coupling and, for spins with $I \geq 1$, with electric field gradients. The autocorrelation function is a measure of the correlation of the local field at the time τ with the field at $\tau = 0$. The mean time between these (transition inducing) fluctuations is quantified by the correlation time τ_c. Consequently the spectral density function J is given as:

$$J_{ij}(\omega) = \int_{-\infty}^{+\infty} G_{ij}(\tau)\exp(-i\omega\tau)d\tau \tag{2.58}$$

The spectral density is related to the spin-lattice relaxation rate via $1/T_1 \propto J(\omega_0)$, which means that the relaxation is induced at $\omega = \omega_0$. Thus, in the case of *longitudinal* relaxation in the laboratory frame the relaxation rates can be calculated as [28,29].

$$T_{1,\mathrm{D}}^{-1} \equiv R_{1,\mathrm{D}} = \frac{3}{2}\gamma^4\hbar^2 I(I+1)\left[J_{\mathrm{D}}^{(1)}(\omega_0) + J_{\mathrm{D}}^{(2)}(2\omega_0)\right], \tag{2.59}$$

$$T_{1,\mathrm{Q}}^{-1} \equiv R_{1,\mathrm{Q}} = \frac{9}{128}\left(\frac{eQ}{\hbar I}\right)^2 \frac{2I+3}{2I-1}\left[J_{\mathrm{Q}}^{(1)}(\omega_0) + J_{\mathrm{Q}}^{(2)}(2\omega_0)\right] \tag{2.60}$$

The spectral densities $J^{(q)}$ describe the spin transitions with $\Delta m = \pm q$, where q denotes the change in total angular momentum, hereby describing single or multiple quantum transitions. For nuclei with $I > ½$ quadrupolar relaxation is more effectively induced than dipolar. Here, eQ denotes the electric quadrupole moment. Generally, both contributions add to a total relaxation rate. Similarly to R_1 the spin-spin relaxation rates $R_2 = 1/T_2$ are given as:

$$T_{2,\mathrm{D}}^{-1} = \frac{3}{8}\gamma^4\hbar I(I+1)\left[J_{\mathrm{D}}^{(0)}(0) + 10J_{\mathrm{D}}^{(1)}(\omega_0) + J_{\mathrm{D}}^{(2)}(2\omega_0)\right]. \tag{2.61}$$

$$T_{2,\mathrm{Q}}^{-1} \equiv R_{2,\mathrm{Q}} = \frac{9}{128}\left(\frac{eQ}{\hbar}\right)^2\left[J_{\mathrm{Q}}^{(0)}(0) + 10J_{\mathrm{Q}}^{(1)}(\omega_0) + J_{\mathrm{Q}}^{(2)}(2\omega_0)\right] \tag{2.62}$$

Note, that these descriptions for R_2 are only adequate in the so-called *motional narrowing regime* (see below for further information). In this regime, the jump rate is in the order of the inverse spin-spin relaxation rates. This means that different local fields are averaged due to diffusive motion of the spins. In the *rigid-lattice regime*, where $J^{(0)}\tau_c \gg 1$ we obtain a constant R_2:

$$R_2 = R_{20} \equiv \sqrt{\left\langle \Delta\omega^2 \right\rangle} \tag{2.63}$$

with $\left\langle \Delta\omega^2 \right\rangle$ describing the second moment [24,29,31].

Relaxation in the Rotating Frame of Reference

Spin-locking NMR provides the necessary means to record ionic motion which is too slow to be captured by conventional spin-lattice relaxation measurement with jump rates on the MHz scale, but rather by spectral density functions in the kHz range [59–61]. The static external field B_0 is formally replaced by a weak locking field B_1, which is in the order of about 10^{-4} T [11]. During the locking pulse the magnetization is polarized along B_1 in the x',y'-plane of the rotating frame. The magnetization M_ρ is therefore locked to the axis of the applied pulse; its decay is characterized by the spin-lattice relaxation rate R_2 [59,62]. The expression takes the form[63]:

$$T_{1\rho,\mathrm{D}}^{-1} \equiv R_{1\rho,\mathrm{D}} = \frac{3}{2}\gamma^4\hbar^2 I(I+1)\left[J_{\mathrm{D}}^{(0)}(2\omega_1) + 10J_{\mathrm{D}}^{(1)}(\omega_0) + J_{\mathrm{D}}^{(2)}(2\omega_0)\right] \tag{2.64}$$

$$T_{1\rho,\mathrm{Q}}^{-1} \equiv R_{1\rho,\mathrm{Q}} = \frac{9}{640}\left(\frac{eQ}{\hbar}\right)^2\frac{2I+3}{2I-1}\left[J_{\mathrm{Q}}^{(0)}(2\omega_1) + 10J_{\mathrm{Q}}^{(1)}(\omega_0) + J_{\mathrm{Q}}^{(2)}(2\omega_0)\right] \tag{2.65}$$

with $\omega_1 = \gamma B_1$ as the locking frequency.

BPP-Model for Isotropic Three-Dimensional Diffusion

Spectral densities are obtained when the time-dependence of the correlation function is known. It can be determined with the help of suitable models, such as the one proposed by Bloembergen, Purcell and Pound [64]. This phenomenological model describes *uncorrelated* jump diffusion via a single exponential decay of the correlation function:

$$G^{(q)}(\tau) = G^{(q)}(0)\exp\left(-|t|/\tau_c\right) \tag{2.66}$$

Thus the corresponding spectral density functions can be described by Lorentzian-shaped functions of the form.

$$J^{(q)}(\tau) = G^{q}(0)\frac{2\tau_c}{1+\left(\omega\tau_c\right)^2} \tag{2.67}$$

SLR becomes effective when $J(\omega)$ has contributions at the resonance frequency ω_0. Assuming an isotropic distribution of the spins we obtain the following ratio of the autocorrelation functions: $G^{(0)}(0) : G^{(1)}(0) : G^{(2)}(0) = 6 : 1 : 4$. The spin-lattice relaxation rates in the laboratory and rotating frame of reference can be written as:

$$R_1 = C_1'\left[J^{(1)}(\omega_0) + 4J_Q^{(1)}(2\omega_0)\right], \tag{2.68}$$

$$R_2 = C_2'\left[6J^{(1)}(0) + 10J^{(1)}(\omega_0) + 4J^{(1)}(2\omega_0)\right], \tag{2.69}$$

$$R_{1\rho} = C_{1\rho}'\left[6J^{(1)}(2\omega_1) + 10J^{(1)}(\omega_0) + 4J^{(1)}(2\omega_0)\right] \tag{2.70}$$

Combination of equation (2.67) with (2.68)-(2.70), and conflating all the respective prefactors C_n' into C_n (n = 1, 2, ρ) via the relation $C_n = 2G^{(1)}(0)C_n$' yields the following expressions:

$$R_1 = C_1\left[\frac{\tau_c}{1+\left(\omega_0\tau_c\right)^2} + \frac{4\tau_c}{1+\left(2\omega_0\tau_c\right)^2}\right], \tag{2.71}$$

$$R_2 = C_2\left[6\tau_c + \frac{10\tau_c}{1+\left(\omega_0\tau_c\right)^2} + \frac{4\tau_c}{1+\left(2\omega_0\tau_c\right)^2}\right], \tag{2.72}$$

$$R_{1\rho} = C_{1\rho}\left[\frac{6\tau_c}{1+\left(2\omega_1\tau_c\right)} + \frac{10\tau_c}{1+\left(\omega_0\tau_c\right)^2} + \frac{4\tau_c}{1+\left(2\omega_0\tau_c\right)^2}\right]. \tag{2.73}$$

The correlation time τ_c is of the same order of magnitude as the mean residence time of the diffusing atom, *i.e.* the time between two successive jumps [65]. Its temperature dependence is given as:

$$\tau_c^{-1} = \tau_{c0}^{-1} \exp\left(\frac{-E_A}{k_B T}\right). \tag{2.74}$$

τ_0^{-1} describes the pre-exponential factor, k_B Boltzmann's constant and E_A denotes the activation energy of the diffusion process. At a given Larmor frequency ω_0 the relaxation rate increases with temperature and reaches a maximum value at T_{max}, as shown in Figure 7. In this figure the relationship of the relaxation rate with the temperature T and frequency is illustrated for R_1, R_2 and $R_{1\rho}$. In the so-called low-T limit, where $\omega_0 \tau_c \gg 1$ holds, we observe a proportionality of

$$R_1 \propto \tau_c^{-1} \omega_0^{-2} \text{ for } \omega_0 \tau_c \gg 1, \tag{2.75}$$

whereas at $T > T_{max}$ (high-T limit), *i.e.* where the correlation rate is much greater than the Larmor frequency $\omega_0 \tau_c \ll 1$, R_1 is independent of the frequency, as illustrated in Figure 7 for different frequencies $\omega_0(1) > \omega_0(2) > \omega_0(3)$.

$$R_1 \propto \tau_c \text{ for } \omega_0 \tau_c \ll 1 \tag{2.76}$$

At the rate maximum ($T = T_{max}$) the atomic jump rate is in the order of the resonance frequency.[9]

$$\omega_0 \tau_c \approx 1 \tag{2.77}$$

In an Arrhenius representation the slopes of the flanks left and right to the rate maximum provide a direct access to the activation energy of diffusion process (*cf.* Figure 7).

[9] In fact $\omega_0 \tau_c = 0.62$, taking the complete expression of equation (2.71). $\omega_0 \tau_c = 1$ is valid if only the first summand is considered.

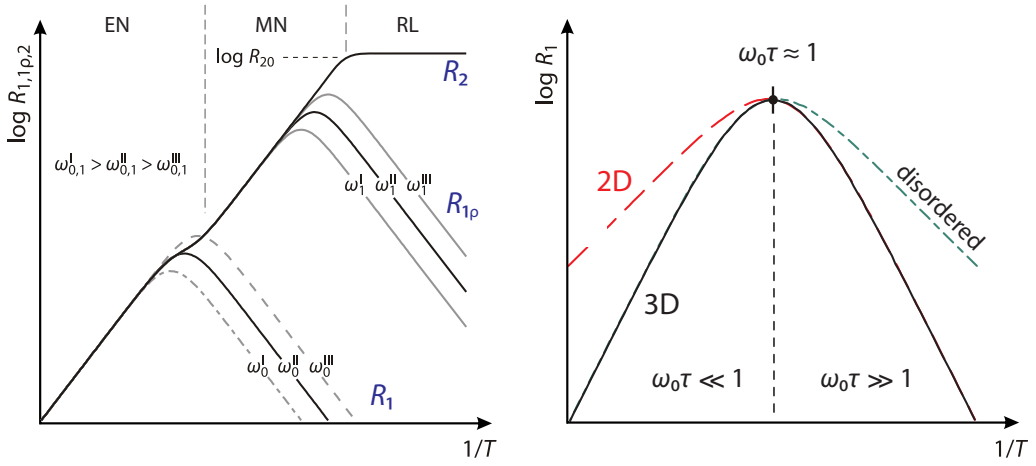

Figure 7: *left:* Temperature-dependence of the spin-lattice and spin-spin relaxation rates R_1, $R_{1\rho}$ and R_2,along with the frequency dependence of R_1 and $R_{1\rho}$ in the low-T limit $\omega_0\tau_c \gg 1$. If the resonance frequency ω is lowered the rate maximum shifts towards lower temperatures. (EN: extreme narrowing; MN: motional narrowing and RL: rigid lattice describe the regimes of the narrowing of the spectral line width. *Right:* Deviations from uncorrelated, 3D BPP-type behavior decrease the slope of the rate peak: for 2D motion in the high-T limit, for the influence of structural disorder and correlation effects at $T < T_{max}$. (Taken and adapted from references [25,33].)

The same behavior is seen for the rates in the rotating frame of reference. Using locking frequencies in the order of kHz the corresponding rate peak is shifted towards lower temperatures. Compared to R_1, diffusion processes are probed on a much longer time (and length) scale. According to equation (2.73) the maximum condition in the rotating frame of reference is fulfilled at $\omega_1\tau_c = 0.5$.

As already stated above, we see a linear progression for R_2 only in the motional narrowing regime, whereas for higher temperatures τ_c the rates are limited by the NMR linewidth. (*cf.* equation(2.63).) The expression for R_2 as shown in equation (2.69) is valid only in the case of extreme motional narrowing.

However, NMR experiments capture a more complex dynamical behavior resulting in an asymmetric rate peak, where the high-T and low-T flank of the rate peak yield $E_{A,\,high\text{-}T} \neq E_{A,\,low\text{-}T}$. This behavior is often seen for structurally disordered materials, such as glasses. Here, the interplay of amorphous and defect-rich structures leads to ion dynamics that cannot be described as isotropic and random. But also in structurally ordered materials correlation effects lead to

asymmetric rate peaks [66]. In this case a modified BPP-model can be employed to account for the influence of correlated jump diffusion.

$$J(\omega)=G(0)\frac{2\tau_c}{1+(\omega\tau_c)^{\beta}} \tag{2.78}$$

In the ideal case the correlation parameter β equals 2 whereas a distribution of jump correlation times leads to $1 < \beta < 2$. Accordingly the expression for R_1 can be rewritten as:

$$R_1=C_1\left[\frac{\tau_c}{1+(\omega_0\tau_c)^{\beta}}+\frac{4\tau_c}{1+(2\omega_0\tau_c)^{\beta}}\right] \tag{2.79}$$

While the high-T limit is not influenced by the correlation parameter, the slope and frequency dependence of the low-T flank is altered:

$$R_1 \propto \tau_c \text{ for } \omega_0\tau_c \ll 1, \tag{2.80}$$

$$R_1 \propto \tau_c^{1-\beta}\omega_0^{-\beta} \text{ for } \omega_0\tau_c \gg 1 \tag{2.81}$$

As already mentioned above the alteration of the slope leads to two different activation energies:

$$E_{\text{A, low-}T}=(\beta-1)E_{\text{A, high-}T} \tag{2.82}$$

These different values can be interpreted in terms of the length scales of diffusion: The lower activation energy is characteristic for short-range motion at low temperatures, while the high-T flank for long-range dynamics. For anisotropic diffusion, the slopes in the limit $\omega_0\tau_c \ll 1$ are influenced by dimensionality effects in a characteristic way. Spatially confined motion, *viz.* 1D and 2D diffusion, leads to a smaller slope of the high-T flank than that predicted for isotropic diffusion. Further, the spin-lattice relaxation rates depend on the magnetic field, or rather the frequency ω_0.

Semi-empirical Model of Richards for Two-Dimensional Diffusion

For layer-structured materials we can often find ionic motion confined to two dimensions which results in the divergence of the spectral densities for $\omega\tau_c \rightarrow 0$. As the low-$T$ limit of the relaxation rate peak describes ionic motion on a short length scale, the spatial dimension has

little influence on the rates, or rather spectral densities. However at temperatures $T > T_{max}$, which is characteristic for long-range motion, anisotropy effects influence the high-T flank of the rate peak. According to Richards [67] it can be described as follows:

$$\begin{aligned} J^{2D}(\omega,\tau_c) &\propto \tau_c \ln(1/\omega\tau_c) \quad \text{for } \omega\tau_c \ll 1 \\ J^{2D}(\omega,\tau_c) &\propto \tau_c^{-1}\omega^{-2} \qquad \text{for } \omega\tau_c \gg 1. \end{aligned} \tag{2.83}$$

Both expressions can be combined in the spectral density function:

$$J^{2D}(\omega,\tau_c) \propto \tau_c \ln\left(1+\frac{1}{(\omega\tau_c)^2}\right), \tag{2.84}$$

and consequently, with the expression for the spin-lattice relaxation rates in the laboratory and rotating frame of reference:

$$R_1^{2D} = C_1^{2D}\left[\tau_c \ln\left(1+\frac{1}{(\omega_0\tau_c)^\beta}\right)+4\tau_c \ln\left(1+\frac{1}{(2\omega_0\tau_c)^\beta}\right)\right] \tag{2.85}$$

$$R_{1\rho}^{2D} = C_{1\rho}^{2D}\left[6\tau_c \ln\left(1+\frac{1}{(2\omega_1\tau_c)^\beta}\right)+10\tau_c \ln\left(\frac{1}{(\omega_0\tau_c)^2}\right)+4\tau_c \ln\left(\frac{1}{(2\omega_0\tau_c)^2}\right)\right]. \tag{2.86}$$

The influence of correlation effects can again be accounted for by a correlation parameter β [36,68]. Overall, dimensionality affects the low-frequency limit (high-T limit), whereas the high-frequency behavioris affected by correlation effects and structural disorder (*cf.* Figure 7). Note, that the combination of both effects can result in a symmetric rate peak, and thus mimic BPP-behavior. However, if R_1 is measured at constant T as a function of the resonance frequency ω_0 we can easily distinguish between isotropic and anisotropic motion through the frequency-dependence of R_1 in the high-T range.

NMR Diffusion Coefficient

Probing the relaxation rate peaks we can calculate a microscopic diffusion coefficient through the maximum condition. Independent of the applied model the correlation rate is in the order of the jump rate, *i.e.* $\tau^{-1} \approx \omega_0$ in the laboratory frame and $\tau^{-1} \approx 2\omega_1$ in the rotating frame. Consequently, the jump rates are transformed into the NMR self-diffusion coefficient D_{NMR} via the Einstein-Smoluchowski relation (equation (2.9)).

2.3.4 Stimulated-Echo NMR

As described in the sections above, diffusion parameters can be obtained from relaxometry measurements in the laboratory and rotating frame of reference covering a jump rates in the range of 10^8 – $10^4 s^{-1}$ (see Figure 2). Jump rates can be *directly* accessed only via the rate maximum, whereas in the limits $\omega_0\tau \ll 1$ and $\omega_0\tau \gg 1$ a suitable diffusion model is required. Also, the slopes of the relaxation rate peak can be considerably influenced by correlation and the dimensionality of the motional process, which make it difficult to determine the "true" value of the activation energy. Furthermore, the investigated sample can be the limiting factor: Usually the SLR rate maxima can be probed at temperatures much larger than room temperature, also in the rotating frame. In some cases often only part of the low-T flank is accessible which excludes the measurements of slow and ultraslow motion in the kHz and sub-Hz range. Apart from the experimental limitations given by the standard NMR probeheads (450 K – 150 K), temperature-sensitive samples might undergo structural changes such as phase transitions or even crystallite growth due to temperature increase.

Here, *stimulated-echo* or *spin-alignment echo* (SAE) NMR is an alternative to relaxometry measurements, as it provides a *direct* access to *single-spin* motional correlation functions. This method was first applied by Spiess et *al.* [69,70] for the study of rotational and translational motion of deuterons and then extended to study slow Li^+, Be^+ or Ag^+ dynamics [71]. The SAE technique takes advantage of the interaction of the quadrupolar moment of the nucleus with an EFG: the site-specific quadrupole frequency is correlated at two different points of time; which, if monitored as a function of time yield, ideally, Li jump rates as the echo amplitude is damped due to diffusive motion. Thus, the ionic hopping between *electrically* inequivalent sites can be used to extract Li jump rates, similarly to 1D and 2D exchange experiments [72–74]. The dynamics of this process can be captured by recording the decay of a spin-alignment echo with the Jeener-Broekart pulse sequence [75]:

$$\left(\beta_1\right)_{\phi_1} - t_\mathrm{p} - \left(\beta_2\right)_{\phi_2} - t_\mathrm{m} - \left(\beta_3\right)_{\phi_3} - t \tag{2.87}$$

This sequence consists of three pulses with different pulse lengths β_i and ϕ_i which are separated by the preparation (evolution) time t_p and the mixing time t_m. The quadrupolar spin-alignment state is generated by the first two pulses containing the phase information, built during t_p.

$$\hat{T}_{10} \xrightarrow[\text{phasecycling}]{\beta_1\hat{I}_{\phi_1},\,\hat{H}_\mathrm{Q}t_\mathrm{p},\,\beta_2\hat{I}_{\phi_2}} -\frac{1}{2}\sqrt{\frac{3}{2}}\sin\beta_1\sin 2\beta_2\sin\left(\omega_\mathrm{Q}t_\mathrm{p}\right)\hat{T}_{20} \tag{2.88}$$

with:

$$\hat{H}_{\mathrm{Q}} = \frac{1}{\sqrt{6}}\omega_{\mathrm{Q}}\hat{T}_{20} \text{ and } \hat{T}_{20} = \frac{1}{\sqrt{6}}\left[3\hat{I}_z^2 - I(I+1)\right] \tag{2.89}$$

$\hat{T}_{10}$ and $\hat{T}_{20}$ denote spherical tensor operators, where the initial state (thermal equilibrium), expressed as $\hat{T}_{10}$ transforms into the quadrupolar state by the first two pulses of the Jeener-Broekart sequence, with $\left|\phi_1 - \phi_2 = 90^\circ\right|$. $\hat{H}_{\mathrm{Q}}$ is the corresponding quadrupolar Hamiltonian, obtained via first order perturbation theory. The aforementioned quadrupole frequency can be described as:

$$\omega_{\mathrm{Q}} / 2\pi = \frac{1}{4}C_{\mathrm{Q}}\left(3\cos^2\theta - 1 - \eta^{\mathrm{Q}}\sin^2\theta\cos(2\phi)\right) \tag{2.90}$$

taking the quadrupole coupling constant and the asymmetry parameter (*cf.* (2.48), (2.49))into account. During the mixing time t_{m} the nucleus under investigation "visits" electrically inequivalent sites and is thus marked with differing ω_{Q}. Accordingly, the phase information is encoded in the term $\sin\left(\omega_{\mathrm{Q}} t_p\right)$. Further, a phase cycling is applied to the pulse sequence in order to eliminate unwanted coherences due to inaccurate pulse lengths and phases. After the mixing time t_{m} the third pulse, *i.e.* a detection pulse, transforms the longitudinal phase information into the (*x*, *y*)-plane, with the spin-echo showing up at $t = t_p$.

$$\begin{aligned} &-\frac{1}{2}\sqrt{\frac{3}{2}}\sin\beta_1\sin 2\beta_2\sin\left(\omega_{\mathrm{Q}} t_{\mathrm{p}}\right)\hat{T}_{20} \xrightarrow[\text{phasecycling}]{\beta_3\hat{I}_{\phi_3},\hat{H}_{\mathrm{Q}}t} \\ &\frac{9}{20}\sin\beta_1\sin 2\beta_2\sin 2\beta_3\sin\left(\omega_{\mathrm{Q}} t_{\mathrm{p}}\right)\sin\left(\omega_{\mathrm{Q}} t\right)\hat{I}_{\phi_3} \end{aligned} \tag{2.91}$$

The spin-echo amplitude is maximal if $\beta_1 = 90°$, $\beta_2 = \beta_3 = 45°$ and can described as the following two-times hopping correlation function for a single spin. Again, the notation $\langle ... \rangle$ is used to mathematically describe a powder average.

$$S_2\left(t_{\mathrm{p}}, t_{\mathrm{m}}, t\right) = \frac{9}{20}\left\langle \sin\left[\omega_{\mathrm{Q}}(0)t_{\mathrm{p}}\right]\sin\left[\omega_{\mathrm{Q}}(t_{\mathrm{m}})t\right]\right\rangle. \tag{2.92}$$

Here, the decay of the echo amplitude, reflecting the diffusive motion of the spins, should be governed by quadrupolar relaxation. However, spin-spin and spin-lattice relaxation processes have to be considered. The echo is damped by the simple exponential decay of R_1 and R_2, *i.e.* the transversal decay during t_{p} and the longitudinal decay of R_1 influencing the spin-alignment. At

sufficiently low temperatures echoes can also be damped by the influence of spin-diffusion [76,77].

$$S_2\left(t_\mathrm{p}, t_\mathrm{m}, t\right) = \frac{9}{20}\left\langle \sin\left[\omega_\mathrm{Q}(0)t_\mathrm{p}\right]\sin\left[\omega_\mathrm{Q}(t_\mathrm{m})t\right]\right\rangle \exp\left(-\frac{2t_p}{T_2}\right)\exp\left(-\frac{t_m}{T_1}\right) \qquad (2.93)$$

The correlation function describing the quadrupolar decay can be usually described with a stretched exponential with the stretching factor $0 < \gamma \leq 1$ yielding the respective SAE decay rate $1/\tau_{\mathrm{SAE}}$. This rate is independent of the quadrupole frequency. As a result SAE time constants are not influenced by the strength of the magnetic field.

SAE Correlation Function and Residual Correlation

The dynamics and timescale of motion is obtained by variation of t_m at constant t_p, yielding spin-alignment echoes recorded at $t = t_\mathrm{p}$ and directly accessing the correlation time $\tau_c \approx \tau_{SAE}$. Here, t_p is chosen to be as small as possible, with $t_\mathrm{p} \rightarrow 0$ in order to generate *quadrupolar* states only. As can be seen in Figure 8, S_2 decays in two steps, with a plateau value of B in between. While the first exponential decay is caused by the diffusive process, the remaining residual correlation is reduced towards $S_2 = S_0 = 0$ via a relaxation process. For the overall expression of $S_2(t_\mathrm{p}, t_\mathrm{m}, t)$ it can be written:

$$S_2\left(t_\mathrm{p}, t_\mathrm{m}, t\right) = S_0 + \left(A\exp\left(-\left(t_\mathrm{m}/\tau_{SAE}\right)^{\gamma_1}\right) + B\right)\cdot\exp\left(-\left(t_\mathrm{m}/T_1\right)^{\gamma_2}\right) \qquad (2.94)$$

with the stretching factors $0 < \gamma_{1,2} \leq 1$. Equation (2.94) describes a stretched exponential decay of S_2 with a residual correlation given as $S_\infty = B/(A+B)$ which is damped by the second term $\exp\left[-(t_m/T_1)^{\gamma_2}\right]$, representing either a relaxation process or another (isotropic) motional process towards $S_2 = S_0 = 0$. In the second case, where we observe exchange between (electrically) equivalent positions or no exchange at all, the decay of S_2 is induced by spin-lattice relaxation. The third example shows isotropic motion where S_2 is governed by the correlation part, with $S_2 = 0$ for $t_\mathrm{m} \rightarrow \infty$.

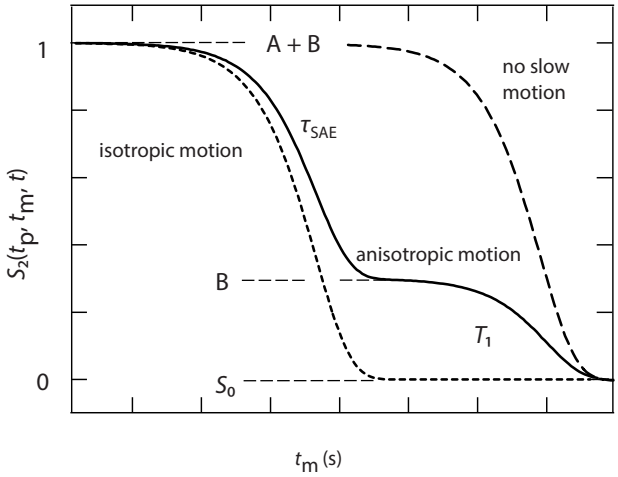

Figure 8: S_2 (t_m, t_p, t) transient for variable t_m and fixed t_p. B denotes residual correlation in the case of anisotropic motion while for the isotropic case a single decay step towards 0 is observed. See text for further information.

While the variation of t_m gives access to the timescale and dynamics, the variation of t_p provides information on the geometry of diffusion. Through the oscillating term $\sin\left[\omega_Q(t_m = 0)t_p\right]$ the sensitivity towards phase differences and ω_Q can be enhanced for $t_p \rightarrow 0$. For $t_p \rightarrow 0$ the number of visited, *i.e.* electrically inequivalent sites, can be determined:

$$\lim_{t_p \rightarrow \infty} S_\infty(t_p) = 1/N \tag{2.95}$$

with S_∞ as the final state correlation factor which is related to the strength of the quadrupolar coupling.(For more information see ref. [78].)

$$S_\infty(t_p) = \frac{S_2(t_p, t_m \rightarrow \infty, t_p)}{S_2(t_p, t_m \rightarrow 0, t_p)} \tag{2.96}$$

Equation(2.95) is adequate for equal site populations where we have a limited amount of inequivalent sites, and thus, a limited amount of possibilities for the jumping nucleus. Otherwise the relative site occupation has to be considered and S_∞ is constituted by the sum of the squares of the corresponding weighting factors w_i of the sites i.

$$\lim_{t_p \to \infty} S_\infty(t_p) = \sum_i^N w_i^2 \tag{2.97}$$

In the case of an inifinite number of electrically inequivalent sites, *e.g.* amorphous materials the correlation function S_2 tends towards zero, and as a result the limiting value of S_∞ equals zero.

SAE Spectra and Dipolar Coupling

SAE spectra, which are obtained after Fourier-transformation of the echo (appearing at $t = t_p$), also contain the time constant $1/\tau_{SAE}$. As a result we can also determine jump rates from the decay of the quadrupolar satellite intensities as a function of the mixing time. Particularly, if $\omega_Q > \omega_D$[10] sharp signals are obtained which allow for a separation of different satellite pairs, *i.e.* transitions with different ω_Q [11,79]. In another approach, modulating the satellite intensities by variation of t_p enables the masking of satellite pairs. As a result, the selective recovery of the satellite intensity during t_m directly reflects the exchange rate.

Now, if we look at a spin system with *two* spins *a* and *b* we observe the influence of dipolar coupling on the alignment experiment. Approximately, the dipole-dipole interaction only affects the central transition [79]. As a result we see additional intensities in the SAE spectrum, apart from those at $\pm\omega_Q^a$ and $\pm\omega_Q^b$ at

$$\begin{aligned} &\pm(k\omega_D/2 - \omega_Q^a) \quad \text{and} \quad \pm(k\omega_D/2 - \omega_Q^b), \\ &\pm(5\omega_D/2 - \omega_Q^a) \quad \text{and} \quad \pm(5\omega_D/2 - \omega_Q^b)\left(5\omega_D/2 - \omega_Q^b\right) \end{aligned} \tag{2.98}$$

With the factor $k = 1.3$. In the case of $\omega_D = 0$ the "pure" quadrupolar alignment spectrum is obtained. However, even weak dipolar coupling leads to the appearance of a central line in the spectrum. For a powder sample the following holds: by increasing t_p the intensity of the "central transitions" add up at $\omega = \omega_0$, whereas the quadrupolar satellites spread over a broader frequency range, due to the angular dependence of the interaction itself. Also, under the influence of $\omega_D \neq 0$, the (quadrupolar) echo still appears at $t = t_p$ (see above) for the case $\omega_D \ll \omega_Q$. Each "pure" quadrupole signal amounts to 9/20 (0.45) of the total amplitude, while dipolar contributions to less than 0.02 [35]. In analogy to the correlation function described in equation (2.92) the dipolar correlation is given as:

[10] The dipole frequency is given as $\omega_D = -\frac{\mu_0}{4\pi}\hbar(\gamma^2/r^3)\frac{1}{2}(3\cos^2\theta - 1)$, for further explanation see equations(2.42) - (2.46).

$$S_2(t_p,t_m) \propto \left\langle \sin\left[k\omega_D(0)t_p\right]\sin\left[k\omega_D(t_m)t_p\right]\right\rangle \tag{2.99}$$

If $\omega_D(0) \neq \omega_D(t_m)$a time constant $1/\tau_D$ can be extracted. Although the dipolar interaction of spins *a* and *b* is coded in terms of a two-spins-correlation function it has been found that $1/\tau_D$ is in the same order as $1/\tau_{SAE} = 1/\tau_Q$, by monitoring the intensities of the satellites and central transition as a function of the mixing time [79].

It has been shown that separation of dipolar and quadrupolar contributions can be achieved via so-called "cross-measurements" [35,71,79,80]. The echo amplitude is recorded as a function of the preparation time at fixed value of t_m. Note that this is only possible for $t_m \rightarrow 0$, without the influence of dynamics. In order to suppress dipolar contributions short preparation times (t_p < 20 μs) have to be applied. The attempt to separate dipolar and quadrupolar contributions of the spin-alignment echoes recorded for Li_2SnO_3 is described in the form of a paper manuscript (see section 3.2.1).

3. Results

The experimental work and results of all studies on Li ion conductors are presented in this chapter in the following form: Most results exist as articles which were submitted to or published in peer-reviewed journals (at the time being). The articles are organized and grouped in relation to their contents, or rather, classes of materials, *viz. layer-structured* Li ion conductors (section 3.1), *ultraslow* Li ion conductors (section 3.2) and *garnet-type* Li ion conductors (section 3.3). Each section provides a brief introduction and background information, and contains, in some cases, additional experimental results not included in the article.

At first studies on the layer-structured materials $Li_{0.17}SnS_2$ and LiC_6 are presented: Paper 1 (**P1**) with the title *"Diffusion-induced ^{7}Li NMR relaxation of layer-structured tin disulphide – Li diffusion along the buried interfaces in $Li_{0.17}SnS_2$"* presents a fundamental NMR study on the characteristics of Li ion transport in chemically intercalated *microcrystalline* SnS_2. These findings are then discussed in the context of similar ^{7}Li NMR studies on a *nanocrystalline* and *nanosized, defect-rich* $Li_{0.17}SnS_2$ in an additional subsection **M1**.

This is followed by **P2** where we looked upon the elementary steps of Li hopping in the ordered graphite intercalation compound LiC_6, taking advantage of microscopic and macroscopic NMR techniques covering a broad Li hopping time scale. Using ^{7}Li SLR and SSR NMR techniques, we were able to gain insight into Li self-diffusion at ambient conditions in the paper *"Lithium motion in the anode material LiC_6 as seen via time-domain ^{7}Li NMR"*.

In section 3.2 an array of methods, nuclear and non-nuclear, are presented to measure diffusion parameters in the *ultraslow* Li ion conductors Li_2SnO_3 and $LiAlO_2$ using 1D and 2D NMR techniques, conductivity spectroscopy and dynamical mechanical relaxation analysis (DMA). Li exchange between the three distinct Li sites in the stannate Li_2SnO_3 can be described with a 3-site, 2-exchange model for motion along the crystallographic *c*-axis. This is discussed in detail in the manuscript *"An unexpected pathway—^{6}Li exchange NMR points to vacancy-driven out-of-plane Li ion hopping in crystalline Li_2SnO_3."* (**M2**).

Then, employing static ^{7}Li spin-lattice relaxation measurements in combination with mixing time-dependent spin-alignment echo NMR we can directly access dynamical parameters, *viz.* mean Li jump rates, associated energy barriers along with the measurement of the Li self-diffusion coefficient. At room temperature slow Li motion is characterized by $D \approx 9 \times 10^{-20}$ m^2s^{-1}. Along with these parameters SAE NMR also provides insights into dipolar and quadrupolar contributions constituting the stimulated echo as a function of the evolution and mixing time. The manuscript *"Long-range Li^+ diffusion in Li_2SnO_3 studied by two-time ^{7}Li spin-alignment echo NMR in combination with ^{7}Li NMR relaxometry"* (**M3**) corroborates the slow and heterogeneous dynamics as found via ^{6}Li exchange NMR in M2.

Another ultraslow Li ion conductor, $LiAlO_2$, has already been the subject of earlier NMR and impedance spectroscopic studies [81–83]. Here we report on the application of dynamic mechanical analysis/spectroscopy on single-crystal lithium aluminate in comparison with high-T conductivity measurements. The corresponding article is listed as "*Mechanical detection of ultraslow, Debye-like Li-ion motions in $LiAlO_2$ single crystals*" (**P3**).

The last section contains the article "*Site Occupation of Ga and Al in Stabilized Cubic $Li_{7-3(x+y)}Ga_xAl_yLa_3Zr_2O_{12}$ Garnets as Deduced from ^{27}Al and ^{71}Ga MAS NMR at Ultrahigh Magnetic fields*"(**P4**). This contribution stands alone as it is rather focused on the study of the site preference of Al and Ga in the mixed-doped solid electrolyte LLZO rather than on the quantification of Li diffusion parameters. Still, new insights are given on the relation between site occupancy and the resulting influence on Li diffusivity. Synthesis and characterization of the garnet samples via XRD diffraction was conducted by D. Rettenwander (University of Salzburg) while ^{7}Li dynamics were investigated by W. Schmidt (Graz University of Technology).

In all our studies we mainly applied NMR spectroscopy as a universal method to characterize *microscopic* and *macroscopic* ionic motion and the influence of *structural* features on ion dynamics. Spin-lattice relaxation and stimulated-echo NMR were primarily used to look at the *self-diffusion* parameters and dimensionality of Li ion motion. Furthermore, preferred diffusion pathways of Li ions, or site occupation preferences can be investigated. Together with complementary non-nuclear measurement techniques, *viz.* conductivity and mechanical relaxation measurements, dynamical parameters are probed on different length scales.

3.1 Layer-structured Li Ion conductors[84]

Intercalation materials are a special class of solid ion conductors that are based on the reversible insertion of a molecular or atomic species into a host-lattice, given that the structure of the host material is preserved. Such materials have to provide an adequate free volume and appropriate geometry to host the guest species, such as frameworks, layers, chains with cavities and channel-like structures. Here, layer-stuctured materials are most common as the interlayer space can be easily accessed by the mobile guest species. Types of materials that consist of a layered structure are clays, transition metal oxides, chalcogenides and graphite.

Insertion by electrochemical electron transfer has received much attention for the design of electrode material in secondary batteries. For application in batteries the intercalation reaction has to be highly reversible and continuous over the whole composition range of the material. Layered dichalcogenides, *i.e.* sulfides or selenides of Ti, Mo, W, Zr, Ta, Nb, V and Cr can dissolve alkali metal ions via insertion in between the chalcogenide layers. In particular, for lithium-intercalated layered disulfides a high electrochemical activity and reversibility was found [85], making them feasible to be used as electrodes in secondary batteries that exhibit both ionic and electronic conductivity. The basic features of the insertion process are described for TiS_2, the most prominent representative of layered chalcogenide cathode materials. Basically, the layers of the host material are bound by van- der- Waals forces, *i.e.*, by induced electric dipoles. In the hexagonal modification of TiS_2, the tin layer is sandwiched between sulfur layers. Hence, the shielded Ti atoms interact with the sulfur atoms of the next TiS_2-sandwich. During the intercalation of one Li ion into the van-der-Waals gap, Ti(IV+) is reduced to Ti(III+) in order to preserve charge neutrality: $x\mathrm{Li} + \mathrm{TiS_2} \rightleftharpoons \mathrm{Li}_x\mathrm{TiS_2}$.

As a result of that, the weak van-der-Waals forces are replaced by coulombic interactions along with an expansion of the lattice along the *c*-axis. The lattice expansion can be reversed chemically or electrochemically. In the interlayer, Li can occupy octahedral and tetrahedral interstitial sites. Occupation of octahedral sites is usually energetically more favored, reaching a maximum occupation of one Li atom per formula unit, while the hexagonal phase persists over the whole intercalation range. However, Li diffusion mechanisms also involve the interlayer tetrahedral sites in their diffusion pathway[11].

This is where NMR comes into play. Layer-structured materials, such as TiS_2 and NbS_2 are well studied by NMR [36,68,86–93] as they offer the possibility to study the effects of *confined*, *i.e. anisotropic* ionic motion within the van- der- Waals gap. As described in section 2.3.3, the diffusion-induced relaxation rate peak does not only entail dynamical parameters, *i.e.*, Li ion

jump rates and activation energies, but its shape is influenced by many factors such as correlation effects, structural disorder, geometry of ionic jump process. In the case of a host lattice which is composed of commensurate layers, the inserted Li ions are prone to preferably diffuse in two-dimensions as diffusion perpendicular to the layers is energetically unfavorable. For 2D diffusion the expression by Richards (*cf.* equation (2.83)) predicts a characteristic frequency-dependence in the high-temperature limit. Thus, by repeating the NMR experiment at different resonance frequencies, *i.e.*, at different field strengths, 2D motion can be distinguished elegantly from isotropic 3D motion. In practice, however, a complex behavior is found frequently, depending on the sample history.

The amount and distribution of defects and vacancies, as a prerequisite for diffusion in the ionic crystal, are strongly influenced by the synthesis condition and particle size. Nanomaterials are a class of great interest in material research as optical and mechanical material properties, as well as chemical reactivity, can be tuned via the particle size. Nanocrystalline materials can be synthesized starting from their atomic or molecular building blocks via established gase phase procedures or from the other extreme where a polycrystalline material is mechanically treated. Established methods of the former type include chemical/physical vapor deposition/condensation (CVD, PVD, CVC) and condensation under inert gas where, in principle, the material is evaporated and precipitated on a cooling finger and then compacted under high pressure (up to 5 GPa)[25]. Starting from the polycrystalline side the grain size can be reduced by high-energy ball milling, tuning the size through the duration of the milling process. Due to the excessive impact force exerted a defect-rich atomic arrangement is obtained, particularly in the form of grain boundaries.

Insertion materials are usually dominated by their ordered stacking of host and guest layers. However, on a nanoscale level an assembly of randomly oriented crystallite grains and interfacial regions is found. In order words, nanocrystalline materials combine the features of crystalline regions together with defective interfacial regions. For that reason, the ionic motion of guest species in *nanocrystalline insertion materials* is predisposed to differ from its microcrystalline counterpart.

This interesting feature is studied via ^{7}Li NMR spectroscopy in the next section for different morphologies of lithium-intercalated SnS_2. In the following section, the characteristics of Li ion transport in the van- der- Waals layers of *microcrystalline* $Li_{0.17}SnS_2$ are discussed in **P1**. This is followed by NMR studies on *nanocrystalline* $Li_{0.17}SnS_2$, as prepared from a gas phase synthesis,

and ball-milled, *nano-sized* $Li_{0.17}SnS_2$ prepared from its molecular constituents.[11] The results are presented in a comparative form, in the context with the findings deduced from the study on microcrystalline $Li_{0.17}SnS_2$. The second subsection presents a fundamental Li diffusion study of the graphite intercalation compound LiC_6. More background information is provided at the beginning of the section 3.1.2.

[11] Note that the different synthesis methods apply for the prepraration of the host material SnS_2. The intercalated form is obtained via chemical intercalation with *n*-Butyllithium in solution for all three samples. For further information see P1 and M1.

3.1.1 Lithium-Intercalated Tin Disulfide: $Li_{0.17}SnS_2$

Tin disulfide SnS_2 crystallizes in the hexagonal CdI_2-type lattice, in analogy to the aforementioned TiS_2. The layers consist of SnS_6 octahedra with sulfur atoms above and below the planes with an interlayer gap of about 3.6 Å [94]. Different stacking periodicities result in a large number of polytypes. We find the basic types of hexagonal (2H, 4H) and rhombohedral symmetry (18R) with the 2H- and 18R-type being the most common ones. Upon insertion Li can occupy vacant lattice sites within the layer (intralayer) and in between the SnS_2 layers. For *n* units of SnS_2 we find *n* octahedral (Oh1) and 2*n* tetrahedral (Td2) sites in the interlayer and 2*n* tetrahedral vacancies (Td1) in the intralayer. Insertion into the interlayer octahedral and tetrahedral sites is favored over occupation of Td1 sites where the inserted Li is surrounded by four tin and three sulfur atoms. Occupation of the interlayer octahedral vacancies seems most likely with the neighboring Sn atoms far away [94,95].

Chemical insertion of Li into SnS_2 yields Li_xSnS_2, where the intercalation degree *x* can take different values, *e.g.* $x = 0.17, 0.49, 0.65, 1.22$, without disrupting the host structure. If one lithium atom is inserted per six tin atoms, *i.e.,* $Li_{0.17}SnS_2$, preferred insertion should occur in the interlayer only. Lithium insertion is mainly achieved via chemical or electrochemical insertion. In the following studies Li was intercalated chemically with *n*-Butyllithium, as described in detail in **P1**. Progress of the intercalation reaction can be monitored optically, as shown in Figure 9.

The amount of lithium ions inserted can considerably influence the ion dynamics, such as diffusion mechanism, Li hopping rates, jump activation energies and dimensionality of diffusion. For that reason we chose the *lowest possible* intercalation degree of $x = 0.17$ where Li only occupies sites in the van-der-Waals gap, in order to look at diffusion in the *ab*-plane and rule out *intralayer* hopping parallel to the *c*-axis. With the help of ^{7}Li spin-locking NMR, being sensitive to slower Li motions, a superposition of two diffusion-induced rate peaks was found for microcrystalline $Li_{0.17}SnS_2$. These rate peaks represent two different Li jump processes, which can be approximated with models for 3D and 2D motion. The occurrence of two distinct diffusion processes in interlayer-intercalated $Li_{0.17}SnS_2$ is discussed in the first article **P1** along with the irreversible change of diffusion behavior after the sample is exposed to 573 K. These surprising results are discussed with respect to the vacant octahedral and tetrahedral lattice sites both between and within the SnS_2-layers, also considering the possibility of Li clustering as a result of chemical intercalation.

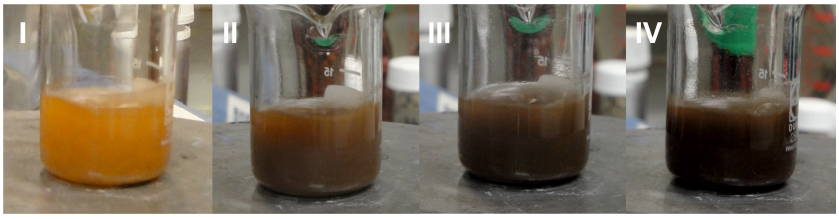

Figure 9: (I) SnS_2 before lithiation, (II) upon addition of n-BuLi, (III) reaction time: 10 min, (IV) reaction time: 60 min

Another aspect of our studies on lithium-intercalated SnS_2 was the comparison of Li diffusivity between micro- and nanocrystalline SnS_2 and between nano-sized, defect-rich SnS_2 which was synthesized via ball-milling. The relaxation rates, in particular the low-T slope, is influenced by background relaxation, correlation effects or localized Li hopping. In this sense it provides information on the influence of particle size and structural environment on Li diffusion. In the manuscript **M1** ^{7}Li NMR spectra and results from spin-lattice relaxation measurements in the rotating frame of reference of all three morphologies are compared.

P1: (pp. 55–60)

Diffusion-induced ^{7}Li NMR relaxation of layer-structured tin disulphide – Li diffusion along the buried interfaces in $Li_{0.17}SnS_2$

Julia Langer, Viktor Epp, Michael Sternad, and Martin Wilkening
Solid State Ionics **276**, 56, (2015)

Solid State Ionics 276 (2015) 56–61

Contents lists available at ScienceDirect

Solid State Ionics

journal homepage: www.elsevier.com/locate/ssi

Diffusion-induced ^{7}Li NMR relaxation of layer-structured tin disulphide — Li diffusion along the buried interfaces in $Li_{0.17}SnS_2$

Julia Langer *, Viktor Epp, Michael Sternad, Martin Wilkening *

Institute for Chemistry and Technology of Materials, NAWI Graz, Graz University of Technology, Stremayrgasse 9, 8010 Graz, Austria
DFG Research Unit 1277, Graz University of Technology, Stremayrgasse 9, 8010 Graz, Austria

ARTICLE INFO

Article history:
Received 14 July 2014
Received in revised form 30 March 2015
Accepted 30 March 2015
Available online 14 April 2015

Keywords:
Nuclear magnetic resonance
Self-diffusion
Lithium ion conductors
Layered structures

ABSTRACT

^{7}Li NMR relaxation has been used to study lithium-ion diffusion in layer-structured SnS_2. Keeping the Li intercalation degree in Li_xSnS_2 below $x = 0.49$, the Li ions preferentially occupy sites in the van der Waals gap between the SnS_2 sheets. In contrast to conventional NMR spin-lattice relaxation (SLR) rate measurements in the laboratory frame of reference, which are sensitive to rather fast Li exchange processes, with the help of spin-locking SLR NMR slower Li motions were extracted from characteristic diffusion-induced rate peaks. The latter contain information on both Li^+ activation energies E_a and Li ion jump rates τ^{-1} characterizing the elementary steps of Li^+ hopping. Our results point to two different diffusion processes (E_a(I) = 0.38 eV; E_a(II) = 0.28 eV), a slower and a faster one, observable directly after chemical Li insertion. Interestingly, the diffusion behaviour irreversibly changes when the sample has been exposed to temperatures as high as 573 K. Diffusion-induced NMR rates and corresponding line shapes are discussed with respect to an inhomogenous distribution of Li ions in SnS_2, which seems to be present directly after Li intercalation.

1. Introduction

Layer-structured materials, which are the key materials that made rechargeable (secondary) lithium-ion batteries alive [1], provide fast 2D diffusion pathways [2] along their inner surfaces [3,4]. In many cases Li ions are quite mobile in the van der Waals gap [3,5] between the sheets that are usually composed of a transition metal (*e.g.*, Ti, Co or Nb) coordinated six-fold by oxygen or sulphur [6]. Dichalcogenides, such as the prominent TiS_2 [7,8], ensure facile and highly reversible Li insertion and de-insertion [1]. This results in an extremely long cycle life because the host structure is considerably robust against structural degradation. Admittedly, the *open structure* of the hosts also allows larger solvent molecules of the commonly used liquid electrolytes to co-intercalate [1].

Besides the classic TiS_2 [3,5,7,8,9], or the recently investigated NbS_2 [10], tin dichalcogenide serves as another very interesting model systems to study the spatially confined Li motion within a rigid host structure. Compared to TiS_2, earlier diffusion studies by, *e.g.*, Pietrass et al. [11], indicate a more complex Li dynamics for the Sn analogue. In the present contribution, we studied the microscopic Li diffusivity in Li_xSnS_2 in detail with the help of time-domain methods such as nuclear magnetic resonance (NMR) spin-lattice relaxation (SLR) performed in the so-called rotating frame of reference [12,13]. The method is sensitive to Li jump processes with rates in the order of 10^5 s^{-1}. Indeed, the NMR relaxation results obtained so far are quite different from those reported for the layered polymorph of Li_xTiS_2 [3].

Like TiS_2 the Sn analogue crystallizes with the CdI_2 type lattice (space group *P*3*m*1 [14], see Fig. 1). It consists of commensurate layers where each Sn atom is octahedrally coordinated by six sulphur anions [11]. In this structure several vacant lattice sites prove to be feasible for Li insertion. In $Li_{0.17}SnS_2$, which is the compound studied here, lithium ions are anticipated to only occupy octahedral (Oh1) and tetrahedral (Td2) vacancies in the interlayer space, whereas the intralayer tetrahedral sites (Td1) tend to be filled up only with increasing degree of intercalation [11,15]. To our knowledge, this is, in general, in contrast to the situation in the trigonal (1T) form Li_xTiS_2 where Li ions preferentially occupy interlayer sites over the whole range of composition *x* [7,16]. Even if we keep *x* in Li_xSnS_2 rather small, *i.e.*, well below $x = 0.2$, to rigorously avoid the occupation of any intra-layer sites, the possibility to occupy two distinct sites in the van der Waals gap, as compared to TiS_2, as well as the fact that Sn^{4+} is preferentially reduced to Sn^{2+} (and Sn^0 at larger values of *x* [15]) seems to leave its mark on the NMR rates recorded. For $x = 0.16$ no noticeable distortion of the SnS_2 structure should occur; Mössbauer spectroscopy has shown that part of the Sn^{4+} ions is reported to be completely reduced to Sn^{2+} [15].

In the present study we used ^{7}Li NMR line shape measurements and time-domain ^{7}Li NMR spin-lattice relaxometry, performed in both the laboratory and the rotating frame of reference, to follow short- and long-range Li ion dynamics in Li_xSnS_2 with $x = 0.17$. The sample was prepared by chemical lithiation of SnS_2 with a solution of *n*-butyllithium in hexane.

* Corresponding authors.
E-mail addresses: julia.langer@tugraz.at (J. Langer), wilkening@tugraz.at (M. Wilkening).

http://dx.doi.org/10.1016/j.ssi.2015.03.039
0167-2738/

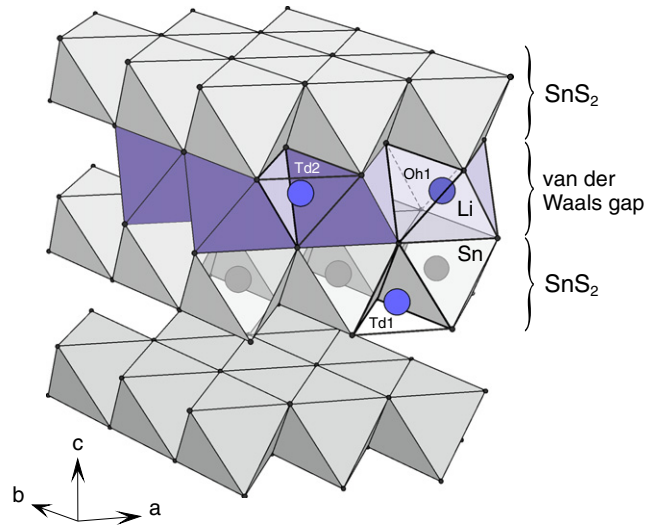

Fig. 1. Crystal structure of layer-structured SnS_2. Circles in blue show Li ions occupying octahedral, Oh1 (or tetrahedral, Td2, Td1) sites in the van der Waals gap or within the SnS_2 sheets. Most likely, the octahedral sites are energetically favoured.

The advantage of spin-locking SLR NMR measurements is that relatively slow motions can be probed as mentioned above. Hence, considering fast and moderate lithium ion conductors, the desired diffusion-induced rate peaks, from which the Li jump rate can be deduced, are passed through at temperatures expected to be much lower than 500 K. In particular, this enables the investigation of heat-sensitive materials.

2. Experimental

Chemical lithiation of phase pure 2H-SnS_2, which was prepared by chemical vapour transport from the elements, was carried out in an Ar-filled glovebox. The microcrystalline sample was dispersed in anhydrous hexane (98%, Aldrich) and treated with an equivalent amount of *n*-butyllithium (1.6 M, Aldrich) to form $Li_{0.17}SnS_2$. Intercalation of Li into the host material is accompanied by the immediate change of colour from gold to a dark-brownish tone. After stirring the suspension for another 24 h at room temperature the sample was filtered, rinsed several times with hexane and dried.

The exact amount of lithium inserted, here $x = 0.17$, was determined by atomic absorption spectroscopy after eluting in deionized water at 333 K for 24 h. Compared to the amount of *n*-butyllithium used, this proves that the complete amount of lithium has been inserted into the Sn-bearing host.

For our ^{7}Li NMR experiments the dry powder was fire-sealed in Duran glass tubes (4 mm in diameter, 3 cm in length) under vacuum. The structure of SnS_2 might be slightly distorted after chemical intercalation with *n*-butyllithium, as the Li ions are likely (*i*) to enter the van der Waals gap in an inhomogenous manner in such a way that clusters are formed or (*ii*) to aggregate on or near the crystallite surfaces. Thus, at first, all investigations were performed on the so-called "pristine" (non-annealed) $Li_{0.17}SnS_2$ sample. Afterwards, in order to study any homogenization effects by NMR as has been done recently for Li_xNbS_2 [10], the sample was annealed inside the closed NMR glass tube in an oven at 573 K for 5 days.

Variable-temperature ^{7}Li NMR relaxation measurements were carried out on a Bruker Avance III spectrometer connected to a shimmed cryomagnet. The nominal magnetic field was 7 T; this corresponds to a ^{7}Li resonance frequency of $\omega_0/2\pi = 116$ MHz. A commercial high-temperature probe (Bruker Biospin) was used to measure line shapes and NMR SLR rates, allowing π/2 pulse lengths between 2.3 and 2.9 μs. Measurements were performed at temperatures ranging from 221 K to 593 K. This was monitored and adjusted using a Eurotherm temperature controller in combination with a type T thermocouple.

^{7}Li NMR SLR rates $1/T_1$ ($\equiv R_1$) were recorded in the laboratory frame of reference with a saturation recovery pulse sequence: $10 \times \pi/2$–t_d–π/2–acquisition (acq.). Here, the initial ten pulses, separated by 80 μs, were used to destroy any longitudinal magnetization M_z prior to recording its recovery as a function of the delay time t_d.

In addition, rotating-frame ^{7}Li SLRρ NMR rates $1/T_{1\rho}$ ($\equiv R_{1\rho}$) [17] were acquired with the spin-lock technique introduced first by Ailion and Slichter [18,19]: π/2p (t_{lock})–acq. using an angular locking frequency $\omega_1/2\pi$ of approximately 20 kHz. The locking pulses were varied from $t_{lock} = 56$ μs to $t_{lock} = 100$ ms. In order to ensure full longitudinal relaxation between each scan, the recycle delay was set to at least $5 \times 1/R_1$. Note that in both types of experiments the corresponding magnetic transients $M_z(t_d)$ and $M_\rho(t_{lock})$ can be best described by stretched exponentials only, *i.e.*, we have used $M_z(t_d) \propto 1 - \exp[-(t/T_1)^\gamma]$ and $M_\rho(t_{lock}) \propto \exp[-(t_{lock}/T_{1\rho})^{\gamma\rho}]$, respectively.

Static ^{7}Li NMR spectra were obtained by Fourier transformation of the free induction decay (FID). They were recorded under static conditions in a single pulse experiment using the same recycle delays as for the SLRρ NMR measurements.

3. Results and discussion

3.1. Static ^{7}Li NMR spectra and their motional narrowing

3.1.1. Local electronic structures

Selected static ^{7}Li NMR spectra of $Li_{0.17}SnS_2$ as prepared and after annealing, are shown in Fig. 2 a) and e). In general, the lines recorded at low temperatures are broadened by dipolar interactions of the ^{7}Li spins [20], resulting in a Gaussian-type shape. In the so-called *rigid lattice* regime, that is, at temperatures well below 200 K, Li exchange processes are too slow to affect the spectral line width.

At elevated temperatures, however, motional narrowing (MN) of the NMR line sets in as dipole–dipole interactions are averaged due to drastically increased Li exchange processes typically resulting in a Lorentzian shape (Fig. 2 a) and d)) [21]. A closer look at the NMR central lines reveals that at intermediate temperatures the lines heterogeneously narrow; this indicates a distribution of Li^+ jump rates. Interestingly, this effect is also observed after annealing and could be related to an intrinsic heterogeneous Li dynamics in Li_xSnS_2 (see Fig. 2 e)).

In the case of annealed $Li_{0.17}SnS_2$ so-called quadrupole satellite intensities emerge, which appear to be more pronounced at $T \leq 295$ K and tend to lose in intensity as temperature is increased. Such quadrupole (powder) patterns originate from the electric interaction of the quadrupole moment of ^{7}Li (spin-quantum number $I = 3/2$) with a non-vanishing electric field gradient (EFG) at the nuclear site [22]. The spectra show a relatively well defined overall powder pattern (see Fig. 2 b) and c)); the pattern may represent a single site with an asymmetric EFG ($\eta_Q \neq 0$) or multiple sites; already two different Li sites with different EFGs and asymmetry parameters η_Q would give a rather complex powder pattern. Nevertheless, this observation indicates that after annealing the Li ions represented by the satellite intensities seem to occupy a large number of electrically equivalent insertion sites, The corresponding quadrupole coupling constants, defined by $C_Q = e^2qQ/h$, can be determined from the first-order singularities [23]. Here, *e* is the elementary charge, *eq* represents the principal component of the EFG at the Li site, *Q* denotes the electric quadrupole moment of ^{7}Li and *h* is Planck's constant. In the present case, the associated site-specific quadrupole coupling constants C_Q are estimated to range between 40 and 80 kHz at temperatures 221 K $\leq T \leq$ 373 K.

For comparison, less distinct quadrupole signals were found for the non-annealed $Li_{0.17}SnS_2$ sample. They seem to be of low intensity and smeared out over a broad frequency range indicating a larger

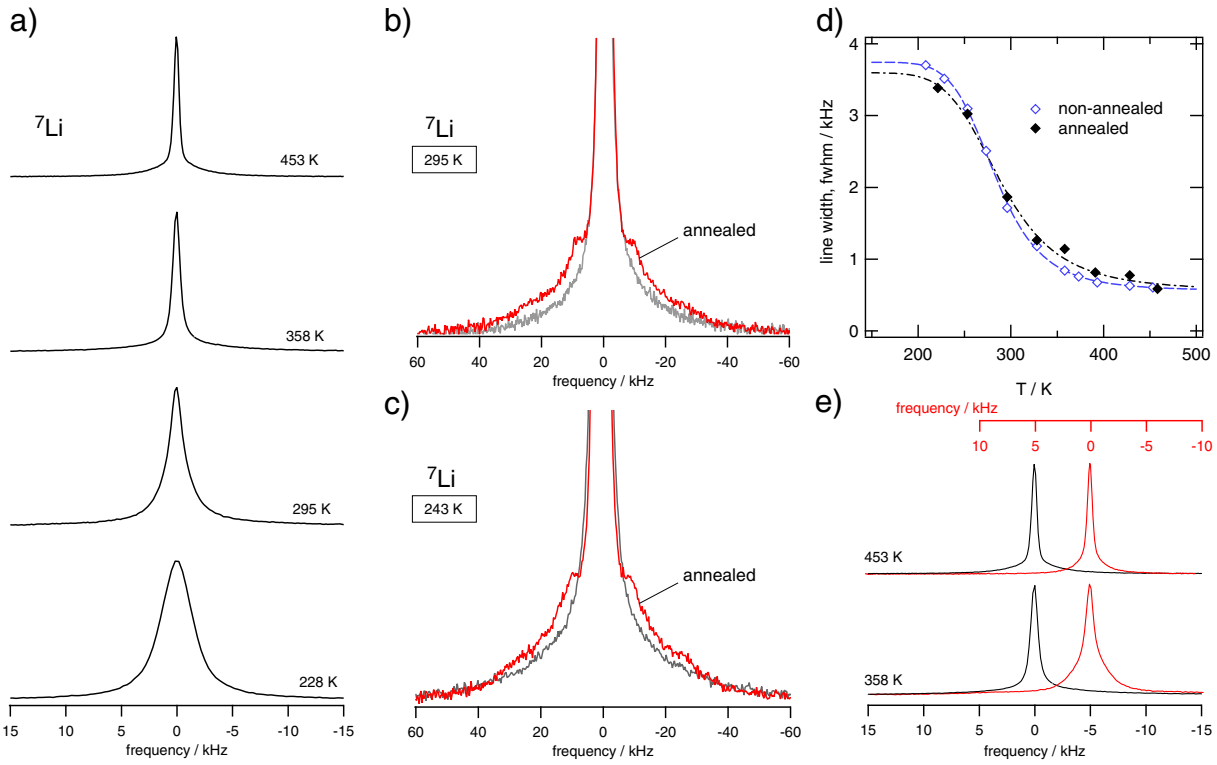

Fig. 2. a) Evolution of the ^{7}Li NMR spectra of non-annealed polycrystalline Li_xSnS_2 (with $x = 0.17$) with increasing temperature. b) and c) magnification of the quadrupole foot of the spectra recorded before (in grey) and after annealing (in red). d) Motion-induced narrowing of the width of the central Li NMR line as a function of temperature. e) Comparison of the ^{7}Li NMR spectra recorded before and after annealing (red) of the sample studied.

distribution of (slightly different) EFGs sensed by the Li spins as it is found after annealing. This difference between the two sets of spectra points towards a less homogeneous occupation of possible Li sites or clustering of Li spins in $Li_{0.17}SnS_2$ right after chemical intercalation. Hence, the quadrupole pattern of the annealed sample indicates that the Li ions are distributed in a more ordered fashion after heat treatment.

Interestingly, Pietrass et al. [11] report on a two-component ^{7}Li central transition and, correspondingly, on two different quadrupolar coupling constants for chemically intercalated $Li_{0.17}SnS_2$. In contrast to our study, their ^{7}Li NMR measurements were performed under magic angle spinning (MAS) conditions; they found $C_Q = 20$ kHz for the narrow component and $C_Q = 60$ kHz for the broader one. The two contributions were assigned to Li ions occupying the interlayer octahedral (Oh1) and tetrahedral sites (Td2) in the van der Waals gap.

In the mechanistic Li insertion study of Lefebvre-Devos et al. [15] it was proposed that at first Li ions are inserted in the octahedral voids of the van der Waals gap without noticeable change of the host structure. With increasing Li content x (>0.17), however, the ions occupy both the interlayer octahedral *and* tetrahedral sites; finally, at even higher levels of intercalation ($x = 0.49$, 1.21, see ref. [15]) also the *intra*layer sites within the SnS_2 sheets are occupied. Then the SnS_2 structure will be stressed. Here, in agreement with Pietrass et al. [11] we tend to interpret the spectra of the annealed sample such that they mainly reveal those Li ions residing on the crystallographic (octahedral) sites within the van der Waals sheet. For small values of x, the Li ions introduce only weak structure perturbations [15].

3.1.2. Diffusion-initialized line narrowing

A quantitative analysis of the NMR lines allows an estimation of Li jump rates τ_{MN}^{-1} and (jump) activation energies $E_{a,MN}$. In Fig. 2 d) the full width at half maximum (fwhm) of the central transition $\Delta\nu$ is plotted as a function of temperature. The line widths of $Li_{0.17}SnS_2$ do not change significantly after the annealing step. This indicates both (*i*) comparable dipole–dipole interactions between the ^{7}Li spins before and after Li intercalation, as well as (*ii*) no drastic influence on Li self-diffusion. As we will see below, SLR NMR will give a more precise picture on the elementary hopping processes before and after the annealing step at elevated T; it points to different diffusion processes and reveals the influence of annealing on Li hopping in SnS_2.

To estimate Li jump rates from MN, at the inflection point of the MN curve ($T \approx 280$ K, see Fig. 2 d)) the jump rate is roughly given by $\tau_{MN}^{-1} = 2\pi \times \Delta\nu_{RL}$, where $\Delta\nu_{RL}$ denotes the line widths at extremely low T, *i.e.*, in the so-called rigid lattice regime. For both, the annealed and non-annealed $Li_{0.17}SnS_2$ it lies in the order of 10^4 jumps per second if we use $\Delta\nu_{RL} \approx 3.7$ kHz (see Fig. 2). Moreover, the semi-empirical expression of Waugh and Fedin [24] relates the onset temperature of line narrowing with an activation energy according to $E_{a,MN}$ (eV) $= 1.62 \times 10^{-3} \cdot T_{onset}$(K) [25]. Using $T_{onset} \approx 233$ K this yields $E_a = 0.38$ (9) eV for Li diffusion process in the pristine sample; a similar result was obtained for the annealed one. The model of Hendrickson and Bray [26,27], however, points to slightly lower activation energies of $E_a = 0.27(2)$ eV before heat treatment and $E_a = 0.23(4)$ eV after. These values (see also Table 1) have to be taken as rough estimations. SLR NMR, especially when diffusion-induced rate peaks are analysed with appropriate models, provides a more accurate access to Li ion self-diffusion parameters such as absolute hopping rates and activation energies.

3.2. ^{7}Li NMR relaxometry using spin-locking

^{7}Li spin-lattice relaxation rates, recorded in both the laboratory frame (R_1) and the rotating frame of reference ($R_{1\rho}$), are shown as a function of the inverse temperature in Fig. 3. The Arrhenius plot compares results from the as prepared (black, unfilled symbols) with the annealed sample (black, filled symbols) to investigate the effect of

Table 1
Activation energies and pre-factors deduced from both NMR line shapes and SLR measurements performed at 166 MHz and 20 kHz; activation energies from $T_{1\rho}$ measurements were deduced from BPP-type fits.

Method	Sample	E_a (eV)	τ_0^{-1} (s^{-1})
MN (Waugh–Fedin)	Pristine	≈0.39	
	Annealed	≈0.38	
MN (Hendrickson–Bray)	Pristine	0.27(2)	
	Annealed	0.23(4)	
T_1 (116 MHz)	Annealed[b]	0.10(1)	
$T_{1\rho}$ (20 kHz) BPP fits[a]	Pristine:		
	(Low-T peak)	0.38(4)	$\approx 1 \times 10^{11}$
	(High-T peak)	0.28(9)	$\approx 3 \times 10^{8}$
	Annealed:		
	(Low-T peak)	0.38(5)	$\approx 1 \times 10^{11}$
	(High-T peak)	0.275(50)	$\approx 4 \times 10^{8}$

[a] The parameter β has been restricted to values smaller than or equal to 2; with $\beta = 2$ the best fits were obtained.
[b] Only the low-T flank was accessible.

heat treatment on Li ion dynamics in $Li_{0.17}SnS_2$. At first we will consider the relaxation rates measured at 116 MHz.

The rates R_1 of the non-annealed sample weakly increase with T until they reach a plateau at ca. 358 K. One might interpret this plateau as a shallow rate maximum. As it is obvious from Fig. 3, the overall relaxation process slows down after heat treatment. As a result of this annealing process from the slope of $R_1(1/T)$ an *apparent* activation energy of $E_a = 0.10(1)$ eV can be determined from the linear fit shown. This value, since it is deduced in the low-T limit of a diffusion-induced rate peak, reflects short range Li ion dynamics being predominant in this T range. The result is in good agreement with the activation energy reported by Pietrass et al., E_a (T_1) = 0.155(20) eV, for a sample with the same chemical composition ($x = 0.17$) [11].

In order to probe a full diffusion-induced SLR rate peak including the high-T flank we recorded $R_{1\rho}$ rates with the spin-locking technique. SLR NMR in the rotating frame of reference is *per se* sensitive to much slower diffusion processes compared to SLR in the laboratory frame of reference. This is because the spins relax in the presence of a spin-lock field B_1 that is much smaller than the external one B_0. While γB_0 corresponds to a Larmor frequency ω_0 in the MHz range, $\omega_1 = \gamma B_1$, with B_1 determined by the radio-frequency spin-lock pulse, is given by frequencies in the kHz range. Hence, the rate maximum of $R_{1\rho}(1/T)$ is shifted towards much lower T; it shows up when $\omega_1 \tau_c = 0.5$ is fulfilled where $\tau_c^{-1} = f(T)$ is the motional correlation rate being of the same order of magnitude as the Li jump τ^{-1} [17,28]; usually the difference between τ_c and τ is less than a factor of, say, 5.

To extract the rates $R_{1\rho}$, we parameterized the corresponding magnetization transients with stretched exponentials. Compared to the R_1 experiments the stretching factors turned out to be somewhat smaller; for comparison, they are shown in the upper part of Fig. 3 a). The $R_{1\rho}$ rates of the sample before annealing reveal a complex temperature behaviour and can be best fitted with a sum of two rate peaks,

$$R_{1\rho} = R_{1\rho}{}' + R_{1\rho}{}''.$$

The rate $R_{1\rho}$ is proportional to the spectral density functions $J(\omega_1)$ and $J(\omega_0)$ describing the temporal magnetic dipolar (and electric quadrupolar) fluctuations being responsible for spin-lattice relaxation in the spin-lock field. For $R_{1\rho}{}'$ we have [17]

$$R_{1\rho}{}' = C_\rho{}'(J'(2\omega_1) + 5/3\, J'(\omega_0) + 2/3\, J'(2\omega_0)).$$

The same is valid for $R_{1\rho}{}''$ but with $C_\rho{}'$ and J' replaced by $C_\rho{}''$ and J'', respectively. For three-dimensional diffusion (BPP-type [29]) the spectral density function reads in general [12,30] :

$$J^{3D}\left(\alpha, \omega_{1(0)}\right)_{\alpha=1,2} \propto \tau_c / \left[1 + \left(\alpha \times \omega_{1(0)} \tau_c\right)^{\beta}\right]$$

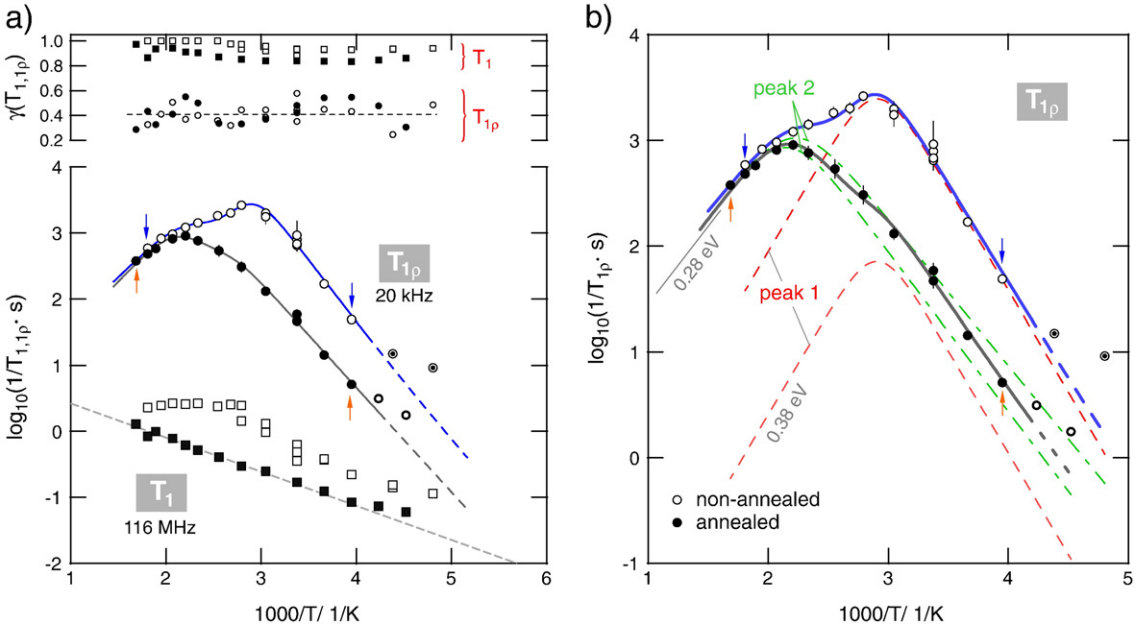

Fig. 3. a) Temperature dependence of the ^{7}Li NMR relaxation rates of $Li_{0.17}SnS_2$ recorded before and after annealing; data were sampled at two different frequencies, *viz.* 20 kHz and 116 MHz. The upper graph shows the corresponding stretching exponents used to fit the transients with stretched exponentials. Filled symbols refer to the annealed sample, unfilled ones reflect the results before annealing. The solid lines show fits with a sum of two BPP-type Lorentzians. The temperature behaviour of the rates R_1 after annealing points to relaxation of the Li spins due to coupling with conduction electrons. b) Magnification of the overall rotating-frame relaxation fit of the data $R_{1\rho}$ recorded for the annealed and non-annealed sample. The (red) dashed lines (peak 1) and the (green) dashed-dotted lines (peak 2) show the individual relaxation rate peaks. Arrows mark the range of data points used for the fit (see also a)). The low-T data points marked with circles were excluded from the analysis since they are governed increasingly by so-called non-diffusive background relaxation with a much weaker temperature dependence than expected for translational ion hopping.

with β being equal to 2 or smaller. $\beta = 2$ reflects uncorrelated motion (see below). Since only the first terms of the corresponding relaxation functions contribute significantly to $R_{1\rho}'$ and $R_{1\rho}''$, the restriction to the first term serves a good approximation for $R_{1\rho}'$ (and $R_{1\rho}''$):

$$R_{1\rho}^{3D} = C_\rho \tau_c / \left[1 + (2\omega_1\tau_c)^\beta\right].$$

The correlation time τ_c can be described with an Arrhenius law :

$$\tau_c^{-1} \approx \tau^{-1} = \tau_0^{-1} \exp(-E_a/(k_B T)).$$

By combining the latter relations, a fitting function can be constructed containing the pre-factor τ_0^{-1}, the asymmetry parameter β, and the activation energy E_a that is governed by long-range Li ion motion. Its value is identical with the activation energy which would be obtained from the slope of the high-T flank of a diffusion-induced NMR SLR rate peak. As shown explicitly in Fig. 3 b), each of the data sets can be approximated with a joint fit; hereby linking the parameters $C_\rho{}'^{(\prime\prime)}$, $\tau_0{}'^{(\prime\prime)-1}$, $\beta'^{(\prime\prime)}$, and $E_a{}'^{(\prime\prime)}$. The dashed and dashed-dotted lines represent single fits of the two rate peaks at low-T and high-T, respectively; the solid lines represent the sum of both relaxation functions.

Both samples investigated, the annealed and the non-annealed ones, reveal at least two relaxation rate peaks. The relaxation rate peak showing up at the lower temperature, $T_{low} = 346$ K, before annealing the sample is characterized by an activation energy $E_a(I)$ of 0.38(4) eV. The peak shifted towards higher T, showing up at $T_{high} = 446$ K is best described with $E_a(II) = 0.28(9)$ eV.

Worth noting, the exponent β, which reflects the asymmetry of the NMR rate peak, encloses information on correlation effects such as structural disorder and/or Coulomb interactions [31,32]. In the presence of correlation effects asymmetric rate peaks are expected with the slope of the low-T flank being much smaller than that in the high-T limit. Here, in the case of the non-annealed sample β equals 2 for both rate maxima ($\beta' = \beta''$); this results in a symmetric shape of the rate peak. Hence, correlation effects in the sense of Ref. [31] seem to be almost negligible for the description of the shape of the rate peaks in the present case.

Surprisingly, after heat treatment, the rate $R_{1\rho}$ still reveals the two-peak profile; the two rate maxima occur at the same temperatures as for the non-annealed, pristine sample (see above). In addition, the joint fit mentioned above of the data sets yields almost the same jump activation energies $E_a(I)_{annealed} = 0.38(5)$ eV and $E_a(II)_{annealed} = 0.275(50)$. Likewise, no correlation effects seem to influence the NMR rates; the best overall fit is obtained if we chose $\beta'^{(\prime\prime)} = 2$. Thus, the rate peaks can be well described with classical BPP-type relaxation behaviour for which a quadratic frequency dependence $R_{1\rho}^{3D} \propto \omega_1^{-2}\tau_c^{-1}$ is a characteristic [29].

After the annealing procedure, however, the second rate peak, which leads to the maximum at T_{high}, predominates while the rate peak at lower T is almost fully superimposed by the second one. This means that overall Li diffusivity is slowed down after annealing. Remarkably, the opposite behaviour has recently been found for Li diffusion in Li_xNbS_2 [10].

The low-T peak could represent localized Li hopping processes. One might suppose that Li ions directly after insertion with *n*-butyllithium form 'local clusters'. This could involve both interlayer octahedral and tetrahedral sites and, to a small extent, also Li sites within the SnS_2 layers. Clearly, the latter suffer from huge Coulomb repulsion between Li^+ and Sn^{4+} or Sn^{2+}. Such clustering between the SnS_2 layers might be directly related to the redox behaviour, *i.e.*, the different oxidation states available of Sn. In contrast to, *e.g.*, $Ti^{3+/4+}$ in Li_xTiS_2, it is reduced from Sn^{4+} to Sn^{2+} and, at much larger values of x, further to Sn^0 as it has been evidenced by Mössbauer studies [15]. Hence, one may suppose that initially the Li ions seem to be located near the positions of the initially reduced Sn atoms. The dissolution of such small agglomerates *via* Li diffusion is expected to be coupled with the transfer of electrons between the Sn atoms.

The activation energies associated with hopping processes perpendicular to the layers, however, are expected to be much larger than those for interlayer Li diffusion. Most likely, annealing at elevated T causes homogenization of the Li^+ (and Sn^{2+}) distribution and facilitates long-range ion transport. Thus, with increasing temperature this leads to a more uniform and ordered occupation of the interlayer octahedral sites that we assume to persist even after annealing. The emergence of quadrupole satellite intensities underpins this interpretation (see above). Ultimately, (*in situ*) neutron diffraction is necessary to work out which sites the Li ions definitely occupy under which conditions and to shed light on the question whether also the opposite is true, that is, to investigate whether the Li ions become increasingly trapped on, *e.g.*, the interlayer tetrahedral sites Td2 after annealing. Let us, however, mention that for the high-T peak a rather small pre-factor is found (see Table 1). It might be a characteristic of and, thus, directly related with the low-dimensional (2D) diffusion process involving octahedral voids within the van der Waals gap of Li_xSnS_2.

The occupation of both octahedral (Oh1) and tetrahedral voids (Td2) within the van der Waals gap may give rise to different hopping processes manifesting themselves in a complex $R_{1\rho}(1/T)$ behaviour. Annealing is expected to shift this behaviour towards a single diffusion process involving in the simplest case crystallographically equivalent sites, most likely the octahedral ones [15] as it is the case in Li_xTiS_2. The latter, however, does not rule out that Td2 sites participate in Li hopping between the van der Waals gap. In Li_xTiS_2 the interlayer tetrahedral voids are temporarily occupied when Li ions jump between two octahedral sites [3,33].

Assuming 2D diffusion between the SnS_2 sheets for the prevailing transport mechanism, we analysed the rates recorded with appropriate

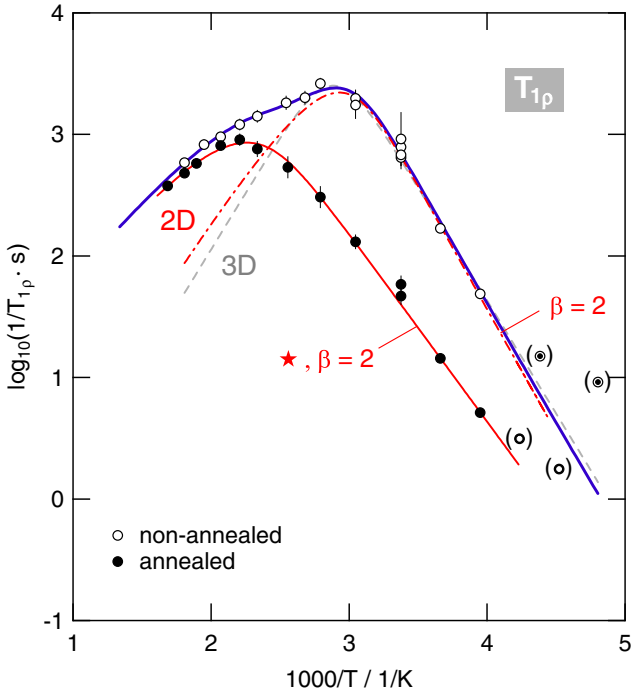

Fig. 4. ^{7}Li NMR $R_{1\rho}$ relaxation rates (20 kHz) recorded before and after annealing, taken from Fig. 3. In contrast to Fig. 3, however, the bold line represents an overall fit which is a combination of two so-called 2D-fits. The dashed-dotted line and the solid line (marked with a stark) represent the two peaks 1 and 2. For comparison, if peak 1 is approximated with a BPP-type (3D) spectral density function, this results in a rate peak represented by the dashed line; it has no large effect on the fit of peak 2. Reasonable fits were only obtained if $\beta = 2$ is chosen. Note that the fit for the annealed sample is not shown. The peak represented by the solid line (and marked with a star) coincides with the data points representing the relaxation behaviour after annealing.

Table 2
Activation energies and pre-factors deduced from the $T_{1\rho}$ measurements if we analyze the data in terms of 2D diffusion [34]; the results refer to the non-annealed sample.

Method	Kind of fit	E_a (eV)	τ_0^{-1} (s^{-1})
$T_{1\rho}$ (20 kHz) 2D fits[a]	Low-T peak, 2D	0.40(5)	$\approx 4 \times 10^{10}$
	High-T peak, 2D	0.31(12)	$\approx 2 \times 10^{8}$
	Low-T peak, 3D	0.37(2)	$\approx 6 \times 10^{9}$
	High-T peak, 2D	0.30(12)	$\approx 2 \times 10^{8}$

[a] As for the 3D fits, with $\beta = 2$ the best fits were obtained.

2D spectral density functions $J^{2D}(\omega_1)$. The solid line in Fig. 4 shows a fit with a combination of two terms of $R_{1\rho}^{2D}$ based on the semi-empirical expression of Richards [34] to analyze 2D diffusion processes *via* NMR relaxation.

$$R_{1\rho}^{2D} = C_\rho \tau_c \ln\left[1 + 1/(2\omega_1\tau_c)^\beta\right]$$

The dashed dotted and the solid lines (in red) represent the two individual peaks $R_{1\rho}'$ and $R_{1\rho}''$. The quality of the overall fit $R_{1\rho}^{2D} = R_{1\rho}' + R_{1\rho}''$ is comparable to that shown in Fig. 3. Interestingly, peak 2 (*cf.* the red (solid) line in Fig. 4) coincides with the data points obtained after annealing; this situation does not change if we use a BPP-type 3D ansatz for $R_{1\rho}'$ (see the dashed line in Fig. 3).

Compared with the results presented in Table 1, the activation energies turn out to be quite similar, the low-T rate peak points to 0.4 eV, whereas the high-T peak can be best represented with a fit using an activation energy of approximately 0.3 eV (see Table 2). These values can be regarded as those representing the hopping barrier of the elementary steps of hopping in Li_xSnS_2. They are much larger than those deduced from low-T R_1 measurements being influenced to a larger extent by correlation effects and/or strictly localized (forward–backward) Li hopping rather than by long-range ion transport along the (buried) interfaces in Li_xSnS_2.

Once again, a relatively low pre-factor is obtained for the peak showing up at high temperatures. For a last comparison, activation energies estimated from line narrowing agree relatively well with those from SLR measurements. This indicates at least that the same diffusion processes were probed by line shape analysis and SLR measurements. Most likely, a uniform distribution of Li ions among the octahedral sites (Oh1) is reached after annealing, as mentioned above.

Besides the possibility that all the Li ions solely occupy interlayer sites, one might think about surface effects having an impact on the NMR results presented. However, since we deal with a polycrystalline material with μm-sized crystallites, such effects, as found for nanocrystalline materials with a large fraction of interfacial regions [4,27,35], are negligible.

Finally, if we use the maximum condition being valid for SLR measurements in the rotating frame of reference, $\omega_1\tau_c = 0.5$ [21], Li^+ self-diffusion coefficients D can be estimated for the two rate peaks according to $D = \ell^2/(2d \cdot \tau_c)$ where ℓ is the jump distance and d the dimensionality of the jump process ($d = 2$ for 2D diffusion). If we use $\ell = 3$ Å, that is the Li–Li distance for octahedral occupation of interlayer sites, this yields, for the high-T peak, 5.7×10^{-15} m^2 s^{-1} at approximately 446 K; for comparison, the low-T peak shows up at 346 K, as mentioned above.

For comparison, the diffusion-induced $R_{1\rho}$ rates of Li_xNbS_2 ($x = 0.7$), which have been recorded also at a locking frequency of 20 kHz, pass through a rate maximum at 320 K [10], *i.e.*, at a lower temperature. The same is true for Li_xTiS_2 ($x = 0.7$), for which the maximum of a log $R_{1\rho}(1/T)$-plot appears at 260 K (10 kHz locking frequency) [3,9]. The activation energies obtained for $Li_{0.7}TiS_2$ and $Li_{0.7}NbS_2$ are quite similar, approximately 0.4 eV. Thus, even if the latter two samples show higher Li contents, roughly speaking, the Li^+ diffusivities, if temperatures around ambient are considered, are seen to increase in the following order: $D(Li_xSnS_2) < D(Li_xNbS_2) < D(Li_xTiS_2)$.

4. Summary and conclusion

Li_xSnS_2 serves as an interesting model system to study Li diffusion in a layer-structured material that also offers Li diffusion pathways perpendicular to the SnS_2 planes. By means of ^7Li NMR relaxation, performed in the rotating frame of reference using spin-locking, we were able to deduce microscopic Li diffusion parameters and to elucidate the effect of annealing on a sample with the composition $Li_{0.17}SnS_2$.

The characteristic diffusion-induced SLR NMR rate peaks obtained entail information on absolute hopping rates and activation energies for the elementary steps of hopping. For the non-annealed sample two overlapping rate peaks show up between 450 K and 600 K, if the rates are measured at a locking frequency of 20 kHz. Analysing the two peaks in terms of 2D relaxation models yields activation energies ranging from 0.3 to 0.4 eV. It turned out that after annealing the relaxation behaviour changes and Li diffusion slows down a bit. This is reflected by the disappearance of the low-T rate peak. We tend to interpret this behaviour as a thermally initiated re-distribution of the Li ions among the various crystallographic sites, most likely the octahedral voids, located between the SnS_2 sheets as suggested by theoretical investigations [15].

Acknowledgement

We thank the Deutsche Forschungsgemeinschaft for the financial support (Research Unit 1277, grant no.: WI 3600 2-2.)

References

[1] M.S. Whittingham, Chem. Rev. 104 (2004) 4271.
[2] V. Epp, M. Wilkening, Phys. Rev. B 82 (2010) 020301.
[3] M. Wilkening, P. Heitjans, Phys. Rev. B 77 (2008) 024311.
[4] P. Heitjans, M. Wilkening, Mater. Res. Bull. 34 (2009) 915.
[5] M. Wilkening, W. Küchler, P. Heitjans, Phys. Rev. Lett. 97 (2006) 065901.
[6] W. Müller-Warmuth, R. Schöllhorn (Eds.), Progress in Intercalation Research, Springer, Netherlands, 1994.
[7] M.S. Whittingham, Prog. Solid State Chem. 12 (1978) 41.
[8] C. Prigge, W. Müller-Warmuth, R. Schöllhorn, Z. Physik. Chem. 189 (1995) 153.
[9] W. Küchler, P. Heitjans, A. Payer, R. Schöllhorn, Solid State Ionics 70-71 (1994) 434.
[10] V. Epp, S. Nakhal, M. Lerch, M. Wilkening, J. Phys. Condens. Matter 25 (2013) 195402.
[11] T. Pietrass, T. Francis, P. Lavela, J. Olivier-Fourcade, J.-C. Jumas, J. Phys. Chem. B 101 (1997) 6715.
[12] A. Kuhn, S. Narayanan, L. Spencer, G. Goward, V. Thangadurai, M. Wilkening, Phys. Rev. B 83 (2011) 094302.
[13] M. Wilkening, W. Iwaniak, J. Heine, V. Epp, A. Kleinert, M. Behrens, G. Nuspl, W. Bensch, P. Heitjans, Phys. Chem. Chem. Phys. 9 (2007) 6199.
[14] B. Palosz, W. Steurer, H. Schulz, Acta Crystallogr. Sect. B: Struct. Sci. 46 (1990) 449.
[15] I. Lefebvre-Devos, J. Olivier-Fourcade, J.C. Jumas, P. Lavela, Phys. Rev. B 61 (2000) 3110.
[16] J.R. Dahn, W. McKinnon, R. Haering, W. Buyers, B. Powell, Can. J. Phys. 58 (1980) 207.
[17] P. Heitjans, J. Kärger (Eds.), Diffusion in Condensed Matter — Methods, Materials, Models, Springer, Berlin, Heidelberg, 2005.
[18] D.C. Ailion, C.P. Slichter, Phys. Rev. Lett. 12 (1964) 168.
[19] C.P. Slichter, D.C. Ailion, Phys. Rev. 135 (1964) A1099.
[20] M. Wilkening, V. Epp, A. Feldhoff, P. Heitjans, J. Phys. Chem. C 112 (2008) 9291.
[21] V. Epp, Ö. Gün, H.-J. Deiseroth, M. Wilkening, J. Phys. Chem. Lett. 4 (2013) 2118.
[22] A. Abragam, The Principles of Nuclear Magnetism, Oxford University Press, Oxford, 1999.
[23] T. Bredow, P. Heitjans, M. Wilkening, Phys. Rev. B 70 (2004) 115111.
[24] J.S. Waugh, E.I. Fedin, Sov. Phys. Solid State 4 (1963) 1633.
[25] M. Wilkening, A. Kuhn, P. Heitjans, Phys. Rev. B 78 (2008) 54303.
[26] J.R. Hendrickson, P.J. Bray, J. Magn. Reson. 9 (1973) 341.
[27] M. Wilkening, D. Bork, S. Indris, P. Heitjans, Phys. Chem. Chem. Phys. 4 (2002) 3246.
[28] H. Buschmann, J. Dölle, S. Berendts, A. Kuhn, P. Bottke, M. Wilkening, P. Heitjans, A. Senyshyn, H. Ehrenberg, A. Lotnyk, V. Duppel, L. Kienle, J. Janek, Phys. Chem. Chem. Phys. 13 (2011) 19378.
[29] N. Bloembergen, E.M. Purcell, R.V. Pound, Phys. Rev. 73 (1948) 679.
[30] A. Kuhn, M. Kunze, P. Sreeraj, H.-D. Wiemhöfer, V. Thangadurai, M. Wilkening, P. Heitjans, Solid State Nucl. Magn. Reson. 42 (2012) 2.
[31] M. Meyer, P. Maass, A. Bunde, Phys. Rev. Lett. 71 (1993) 573.
[32] K. Funke, Prog. Solid State Chem. 22 (1993) 111.
[33] A. van der Ven, J.C. Thomas, Q. Xu, B. Swoboda, D. Morgan, Phys. Rev. B 78 (2008) 104306.
[34] P. Richards, Solid State Commun. 25 (1978) 1019.
[35] M. Wilkening, S. Indris, P. Heitjans, Phys. Chem. Chem. Phys. 5 (2003) 2225.

M1: Micro- vs. Nanocrystalline $Li_{0.17}SnS_2$

Experimental

Phase-pure, nanocrystalline SnS_2 as the precursor for $Li_{0.17}SnS_2$, was synthesized according to the same procedure as described for the microcrystalline form. This can be found, along with the description of the chemical intercalation process and chemical analysis via atomic absorption spectroscopy, in **P1**. Additonally, nano-crystalline SnS_2 was prepared by high energy ball-milling from the elements using stoichiometric amounts. The powders were ground at 600 rpm for 100 min in a high-energy planetary ball mill (Fritsch Pulverisette 7, premium line). Li intercalation and chemical analysis was performed, accordingly in **P1**. All materials were investigated using the same NMR equipment, experimental setup and pulse sequences as described in **P1**.

Results

A clear difference can be seen between micro- and nanocrystalline $Li_{0.17}SnS_2$. At low temperatures (T = 193 K) a dipolarly (and quadrupolarly) broadened peak is observed with a width of roughly 6 kHz (*cf.* Figure 10). With increasing temperature a narrow peak evolves on the top of the broad one, starting below ambient temperature. This second contribution indicates fast Li motion as lines are subsequently narrowed due to increased mobility of Li ions. In contrast, the width of the broad signal only starts to significantly narrow at elevated temperatures, around 400 K. This behavior is also reflected by the motional narrowing curve where the full width at half maximum is plotted against the temperature. In order to extract the line width the shape of the two-component peaks could be fitted best with a Gaussian for the broad and a Lorentzian fit for the narrow contribution. For neither "species", which can be referred to as "spin reservoir", the full motional narrowing curve (*cf.* Figure 11) was recorded. Li diffusion is observed in the rigid-lattice regime for the slow "species" of Li ions in the temperature regime covered in these experiments. For the fast diffusion process the lines seem to be fully narrowed with values ranging between 0.6 and 1 kHz.

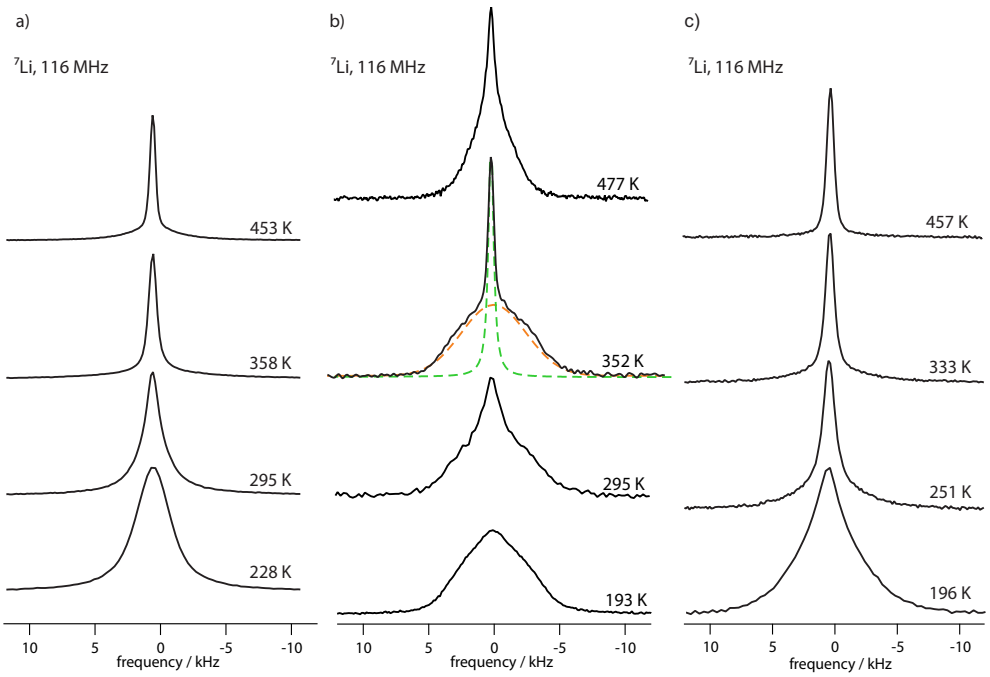

Figure 10: a) Temperature-dependent ^{7}Li spectra of non-annealed microcrystalline $Li_{0.17}SnS_2$, b) Evolution of the ^{7}Li NMR lines for nanocrystalline $Li_{0.17}SnS_2$ showing a two-component line shape, c) ^{7}Li spectra of nano-$Li_{0.17}SnS_2$ as synthesized via ball-milling. (See text for further explanations.)

Note that the occurrence of two-component line shape is a reversible process. After being subjected to high temperatures during the first "run" of NMR experiments, the re-measured line shapes proved to be identical to the original ones. This indicates that, the existence of two contributions in the ^{7}Li NMR spectra of the nanocrystalline Li might not be attributed to an inhomogeneous Li distribution that can be cured by thermal treatment. Consequently, the extraordinary behavior observed for nanocrystalline $Li_{0.17}SnS_2$ might stem primarily from the size and morphology of the crystals. In fact, high-resolution TEM images indicate nanocrystals embedded in an amorphous matrix which is why we tend to assign the different Li spin reservoirs to Li ion diffusing in crystalline grains and in amorphous interfacial regions. As the sharp ^{7}Li NMR line (*cf.* Figure 10b)) attributed to the fast Li spins in $Li_{0.17}SnS_2$ resembles that of the microcrystalline sample, it can be concluded that Li ions in within the nanocrystalline grains move faster than those situated in the amorphous regions. On the contrary, a similar phenomenon was observed in the study of micro- and nanocrystalline Li_2O:Al_2O_3 composites [96]. Yet, the

interpretation is completely the opposite: slow dynamics was seen for the crystalline regions (in micro- and nanocrystalline Li_2O) and fast Li motion in the amorphous nano-interfaces.

For comparison, nano-$Li_{0.17}SnS_2$ was also prepared via mechanochemical synthesis of SnS_2, followed by a chemical intercalation in solution according to the procedure described in **P1**. The corresponding ^{7}Li NMR spectra are shown in Figure 10c). At temperatures below 333 K, the NMR signal also appears to be constituted by two different contributions, however, not as pronounced as in the spectra shown in Figure 10b). With increasing temperature the broad contribution is narrowed with one sharp contribution dominating in the regime T >251 K indicating enhanced Li diffusivity for the nano-sized, defect-rich $Li_{0.17}SnS_2$ which was prepared by high-energy ball-milling, compared to the nanocrystalline form.

A two-component behavior is also observed by recording spin-lattice relaxation rates in the rotating frame of reference via the spin-locking technique. By taking advantage of locking frequencies in the kHz-range this technique is more sensitive towards slow Li ion motion, compared to conventional spin-lattice relaxation NMR. Corresponding $T_{1\rho}$ magnetization transients show a two-step decay behavior, which can be approximated by a double exponential fit yielding two characteristic time constants for both diffusion processes. As can be seen in Figure 11, the relaxation rates of the fast and the slow contribution differ by more than two orders of magnitude at low temperatures between 204 K and 250 K. With increased Li mobility at higher temperatures $R_{1\rho,(s)}$ approaches $R_{1\rho,(f)}$.

For the slow diffusing Li ions (*cf.* Figure 11, "S") a diffusion-induced rate maximum could not be probed in the experimental temperature range. In the low temperature regime up to $T \approx$ 250 K the constant relaxation rate values can be attributed to non-diffusive relaxation mechanisms, such as localized jumps or interaction of Li nuclei with conducting electrons. The rates start to gradually increase showing a "dent" around T = 308 K. This "dent" is also observable in the motional narrowing curve with the linewidths increasing from roughly 6 kHz to 7 kHz before decreasing due to the onset of motional narrowing. The "dent" observable in the Arrhenius and motional narrowing representation could be caused by a homogenization process concerning the distribution of Li ions directly after intercalation. Considering the nano-size of the crystallites this might take place already at lower temperature values, if compared with the microcrystalline sample. However, repeating the temperature-dependent experiments yields the same course for both $R_{1\rho,(s)}$ and $R_{1\rho,(f)}$. Subsequently, the onset Li motion induces the steep increase for $R_{1\rho,(s)}$ at T > 337 K, with the rate maximum expected at $T \gg 500$ K.

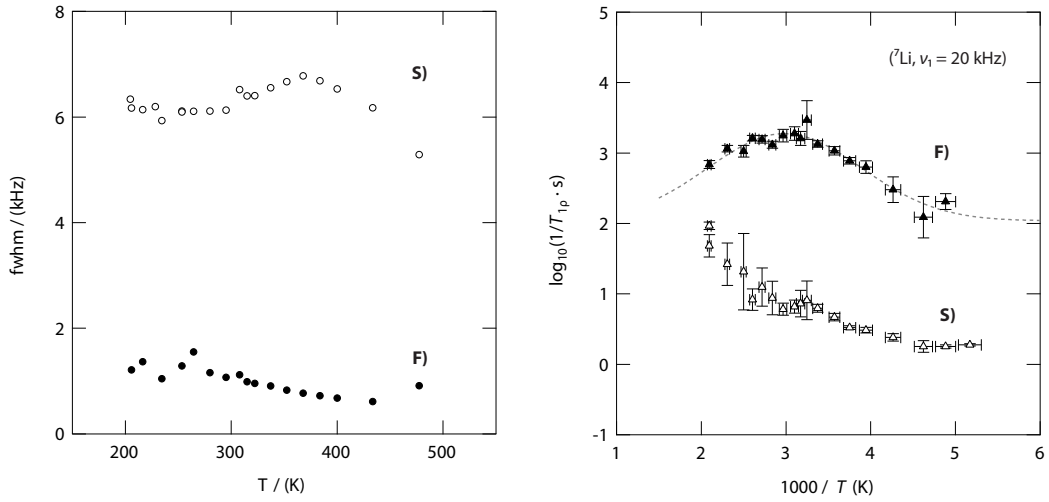

Figure 11: *left:* ^{7}Li NMR linewidths of both slow and fast Li ions (Line shapes were obtained via approximation with Gaussian- (S) and Lorentzian-type (F) functions. For (S) we observe a rigid-lattice linewidth up to about 400 K, while the lines corresponding to (F) are already motionally narrowed. *Right:* SLR_ρ magnetization transients (recorded at a locking frequency ν_1 = 20 kHz) show a two-step decay behavior which, parametrized with stretched exponentials, yield relaxation rates for the fast and the slow spin reservoir.

Interestingly, a shallow rate peak is probed for the fast spin reservoir (*cf.* Figure 11 "F"). If $R_{1\rho,(f)}$ is recorded between 250 K < T < 478 K, the maximum condition $\omega_1\tau_c \approx 0.5$ is fulfilled at $T \approx$ 320 K, roughly corresponding to a mean Li jump rate of $\tau \approx 2.5 \times 10^{-5}$ s^{-1}. The high- and low-T flanks of the rate peak are to a great extent influenced by correlation effects or localized jumps, *i.e.* non-random Li motion, which makes it impossible to the determine a value for the activation energy via NMR relaxometry.

In order to obtain a clear picture of the difference in Li diffusivity in all three morphologies of $Li_{0.17}SnS_2$ a comparison of the $R_{1\rho}$ maxima is shown in Figure 12. In accordance with the ^{7}Li line shape analysis a high Li mobility is observed for Li-intercalated, nano-sized SnS_2, prepared via the mechanochemical synthesis route. Materials synthesized via these methods generally exhibit a defect-rich structure due to the high mechanical impact exerted during the synthesis. Such defects can be thermally cured; however they leave a characteristic signature in the structure, manifesting itself in the mobility of the diffusing ion.

In this case, the features of a less-ordered and defect-rich structure in nano-sized $Li_{0.17}SnS_2$ enables fast Li hopping, as shown by the appearance of a weak rate maximum well below room

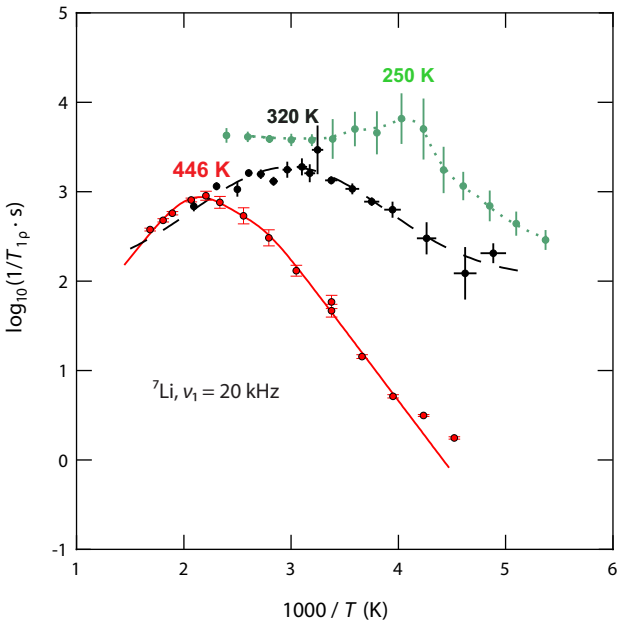

Figure 12: Arrhenius representation of spin-lattice relaxation rates for microcrystalline (red), nanocrystalline (black) and "nano-ballmilled" $Li_{0.17}SnS_2$. The shift of the rate peak towards lower temperatures indicates an increased Li diffusivity as defects, disordered and amorphous regions are introduced for the nano-sized compounds.

temperature, at $T \approx 250$ K. However, the shallow maximum of the SLRρ rate peak reflects, to the most extent thermally activated localized hopping, rather than diffusion-induced Li motion.

Li diffusion in nanocrystalline $Li_{0.17}SnS_2$ takes place in the crystalline, layer-structured grains and in amorphous interfacial regions. While Li diffusivity is low within an amorphous disordered environment it increases in the crystalline SnS_2 layers. Still, Li motion is greatly influenced by correlation effects, resulting in a broad rate maximum. Correlated jumps, *i.e.* non-random jumps, could be the result of Li clusters causing an inhomogeneous distribution of Li ions in octahedral and tetrahedral voids of the crystalline layers, as a result of the chemical intercalation process.

Eventually, only for microcrystalline $Li_{0.17}SnS_2$ purely diffusion-induced relaxation rate peaks were probed, describing uncorrelated Li motion in the van-der-Waals gap (see **P1**). Here, the complex SLRρ behavior was, in a first explanation, also ascribed to the formation of local Li clusters both in inter- and intralayer of SnS_2. After thermal annealing only one process with a rate maximum at 446 K dominates. Taking the ^{7}Li spectra before and after annealing, as well as

theoretical considerations into account, it can be assumed that thermal treatment has caused a *re-destribution* of Li ions among both the octahedral and tetrahedral voids in the interlayer, facilitating long-range Li transport.

Studying the effect of thermal annealing was attempted for both nanomaterials, in order to homogenize the Li distribution and dissolve local clusters formed after chemical intercalation. Unfortunately, this led to an irreversible change caused by structural transformations (for the ball-milled sample) and decomposition (for the nanocrystalline samples).

3.1.2 Lithium-Intercalated Graphite: LiC_6

In the past years lithium-intercalated graphite compounds (Li-GICs) have attracted considerable attention due to their application as negative electrode materials in secondary Li ion batteries [97–99,85]. Electrical charge/discharge behavior, as well as rate capability and stability of the electrode are connected with the intercalation and deintercalation of Li ions in between the graphene layers. Properties of practical interest, such as ionic and electronic transport as well as magnetic properties can be tailored by the amount of intercalated Li [100].

Lithium is intercalated preferentially between graphite layers that are already occupied with atoms; this effect is referred to as "staging". Not every interlayer is necessarily occupied by Li in Li-GIC. In so-called stage-1-compounds, graphite layers and intercalated layers alternate and in stage-2-compounds, two graphite layers alternate with an intercalated layer [101]. Compounds up to stage-4 are known, whereas, Li-diffusivity has been studied only for the stage-1/-2 compounds LiC_6 and LiC_{12} [25,26,102–104]. In the past, Li self-diffusion parameters in the stage-1-compound were mostly determined via nuclear techniques such as quasi-elastic neutron scattering (QENS) and β-radiation detected ^{8}Li NMR (β-NMR). Both techniques report low-dimensional diffusion in the *ab*-plane of LiC_6, characterized by activation barriers of 1.0 eV (QENS)[102] and 0.6 eV (*β*-NMR)[103]. Moreover, recent theoretical investigations deal with the diffusion mechanisms in this material, underline the great interest and need for in-depth studies of Li diffusion in LiC_6 [105–107]. Thinius *et al.* [107] studied Li migration with different density functional theory (DFT) methods. By comparing vacancy and interstitial diffusion mechanism, they found a slight preference for the latter (E_a = 0.42 - 0.56 eV) in the *ab*-plane. According to their studies, motion along the *c*-axis, *i.e.*, along hexagonal channels, seems to be kinetically prohibited, and thus highly improbable. The above mentioned diffusion parameters determined by QENS and β-NMR have both been studied in the high-temperature regime, *i.e.* 630 – 675 K (QENS) [102] and between 373 K – 453 K for ^{8}Li β-NMR [103].

However, from an application-oriented point of view, it is necessary to obtain Li self-diffusion parameters in the lower temperature regime down to ambient temperature and below. Therefore alternative NMR techniques were applied. In the following article **P2** we studied Li motion via temperature-dependent ^{7}Li spin-spin and spin-lattice relaxation NMR in the laboratory and rotating frame of reference which allowed us to access much slower Li motion down to 200 K and evaluate the geometry of Li diffusion. Li hopping rates show an almost linear Arrhenius behavior over a broad temperature range between 250 K and 670 K, taking the results from QENS and *β*-NMR into account. From these results, a mean Li-self diffusion coefficient could be deduced for T = 295 K.

P2: (pp. 71–79)

Lithium motion in the anode material LiC_6 as seen via time-domain ^{7}Li NMR

J. Langer, V. Epp, P. Heitjans, F. Mautner, and M. Wilkening
Phys. Rev. B **88**, 094304, (2013)

Lithium motion in the anode material LiC_6 as seen via time-domain ^{7}Li NMR

J. Langer,[1,*] V. Epp,[1,†] P. Heitjans,[2] F. A. Mautner,[1] and M. Wilkening[1,‡]

[1]*Christian Doppler Laboratory for Lithium Batteries, and Institute for Chemistry and Technology of Materials, Graz University of Technology, Stremayrgasse 9, 8010 Graz, Austria*

[2]*Institute of Physical Chemistry and Electrochemistry, Leibniz University Hannover, Callinstraße 3-3a, 30167 Hannover, Germany*

(Received 28 June 2013; revised manuscript received 28 August 2013; published 16 September 2013)

Since the commercialization of rechargeable lithium-ion energy storage systems in the early 1990s, graphite intercalation compounds (GICs) have served as the number one negative electrode material in most of today's batteries. During charging the performance of a battery is closely tied with facile Li insertion into the graphite host structure. So far, only occasionally time-domain nuclear magnetic resonance (NMR) measurements have been reported to study Li self-diffusion parameters in GICs. Here, we used several NMR techniques to enlighten Li hopping motions from an atomic-scale point of view. Li self-diffusion in the stage-1 GIC LiC_6 has been studied comparatively by temperature-variable spin-spin relaxation NMR as well as (rotating frame) spin-lattice relaxation NMR. The data collected yield information on both the relevant activation energies and jump rates, which can directly be transformed into Li self-diffusion coefficients. At room temperature the Li self-diffusion coefficient turns out to be 10^{-15} m^2 s^{-1}, thus, slightly lower than that for layer-structured cathode materials such as $Li_{x\approx0.7}TiS_2$.

DOI: 10.1103/PhysRevB.88.094304 PACS number(s): 66.30.−h, 76.60.−k, 82.56.−b

I. INTRODUCTION

The stage-1 graphite intercalation compound, LiC_6, belongs to one of the most fascinating application-oriented materials which is widely used as an anode in secondary lithium-ion batteries.[1–3] Most of the various electronic devices of our daily life such as notebooks or cell phones rely on the insertion and deinsertion of lithium ions into graphite-based negative electrodes.[4] In particular, the charge/discharge performance and thus the rate capability of an anode is closely related to self-diffusion of lithium ions inside the crystalline host. Moreover, if models are to succeed in simulation of the electrochemical processes in batteries, precisely measured data such as diffusion parameters are required.

Surprisingly, only a few studies can be found in the literature which directly deal with the in-depth investigation of Li diffusion parameters in crystalline, phase-pure LiC_6. Despite the relatively simple, but fascinating, structure of LiC_6 research is yet far away from drawing a comprehensive picture on diffusive Li motion. Apart from earlier studies[5] applying quasielastic neutron scattering (QENS)[6] or taking advantage of β-radiation detected nuclear magnetic resonance (β-NMR) measurements of spin-polarized ^{8}Li ($t_{1/2} = 0.8$ s) nuclei produced *in situ* by polarized neutron capture,[7–9] classical NMR measurements[9–13] on the stable Li isotope ^{7}Li have rarely been utilized for this purpose. *En passant*, the results obtained from ^{7}Li pulsed NMR as yet turned out to be less conclusive with respect to Li diffusion parameters.[14] This is because mainly spin-lattice relaxation (SLR) measurements in the so-called laboratory frame of reference have been performed. Compared to other time-domain NMR techniques, those measurements are sensitive to Li jump rates with values in the MHz range.[10] However, in order to probe Li motional processes in the temperature range where the structurally ordered LiC_6 phase does exist, i.e., at ambient temperature, alternative NMR techniques have to be applied which are able to access much slower Li motions. For example, this is possible by recording SLR rates R_1 in the rotating (ϱ) frame of reference via the so-called spin-lock technique introduced by Ailion and Slichter.[11,13,15–18] If ^{7}Li SLR takes solely place in the presence of a controllable magnetic field with resonance frequencies on the order of a few kHz instead of some MHz,[19] the desirable diffusion-induced rate peak $R_1(1/T)$ shows up at much lower temperatures T.[11,18] In general, the peak entails valuable information on both short-range and long-range motions[9,13,18] as well as correlation effects.[20,21]

Here, layer-structured LiC_6 (see Fig. 1) served as an excellent model system to probe Li dynamics with spatially confined migration pathways; it is the most prominent anode host material with applications in energy storage technology. The stage-1 compound consists of commensurate layers of carbon and lithium; Li resides in the central site below and above each third hexagon formed by C atoms. The stacking sequence is AαAα with a periodicity of 3.71 Å; A denotes the graphite basal plane and α the intercalate layer. The carbon host structure of LiC_6 allows in-plane jump diffusion and, because of the open channels parallel to the hexagonal c

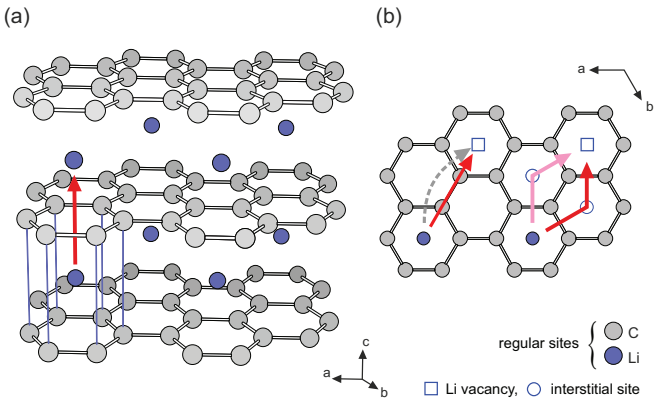

FIG. 1. (Color online) Illustration of the crystal structure of ordered LiC_6 with AαAα stacking sequence. (a) View along the *ab* plane; (b) view along the *c* axis. Arrows roughly indicate possible Li^+ migration pathways, that is, in-plane diffusion (b) vs motion along the open channels parallel to the hexagonal axis (a). A detailed description of possible migration pathways can be found in Ref. 22.

axis and the small size of the Li ion, it has been argued that also diffusion normal to the graphite plane cannot be ruled out *a priori* as in the case of the heavy alkalis.[23] In the present contribution, the results from various ^{7}Li NMR measurements investigating both (local electronic) structure and Li ion dynamics of polycrystalline LiC_6 will be presented and compared with those deduced from previous β-NMR[7,8] and QENS studies,[5] in particular. While β-NMR results were obtained on highly oriented pyrolytic graphite (HOPG) at temperatures around 373 K, results from QENS being sensitive to Li correlation times in the ns to ps range, were collected at much higher T, i.e., in a range with sufficiently fast Li motion.

II. EXPERIMENT

The synthesis procedure to obtain polycrystalline stage-1 LiC_6, shining like gold, is described in the classical paper by Guérard and Hérold.[24] After preparation, the sample (approximately 300 mg) was sealed in a quartz ampoule (3 cm in length, 5 mm in diameter) and stored for several months at room temperature; we anticipate almost full lithium homogenization, i.e., a homogenous distribution of the Li ions between the layers. The sample consists of LiC_6 crystallites with diameters less than 500 μm. Phase purity was checked by x-ray powder diffraction (XRPD). XRPD revealed a small volume fraction of the stage-2 compound LiC_{12} formed. By NMR, however, it was very difficult to detect this minor phase (see below and Fig. 2). The same sample was used for all measurements presented below.

^{7}Li NMR measurements were carried out using two different high-performance digital Bruker Avance III spectrometers in connection with shimmed cryomagnets with nominal magnetic fields of 7 T and 11 T, respectively. This corresponds to ^{7}Li Larmor frequencies of $\omega_0/2\pi = 116$ MHz and $\omega_0/2\pi = 194$ MHz, respectively. Both a commercial high-temperature probe (Bruker Biospin) and a probe designed for temperatures up to 453 K were employed to measure line shapes and NMR relaxation rates. Typically, the $\pi/2$ pulse lengths ranged from 6 to 9 μs. The measurements were performed at temperatures ranging from 203 K to 450 K; here, a Eurotherm temperature controller in combination with a type T thermocouple was used.

^{7}Li NMR SLR rates $1/T_1 = R_1$ were acquired with the saturation recovery pulse sequence $10 \times \pi/2 - t_d - \pi/2 -$ aquisition (acq.).[9,19] An initial pulse train, consisting of ten $\pi/2$ pulses separated by 80 μs, was used to destroy any longitudinal magnetization M_z prior to recording its temperature and frequency dependent recovery as a function of the delay time t_d. Rotating-frame ^{7}Li NMR SLRϱ rates $1/T_{1\varrho} = R_{1\varrho}$ were recorded with the spin-lock technique, $\pi/2\,p(t_{lock}) -$ acq.[15,16,19,25–28] The corresponding (angular) locking frequency ω_1 was chosen to be as low as possible. Here, $\omega_1/2\pi \approx 10$ kHz was used and the duration of the locking pulse t_{lock} was varied from 100 μs to 100 ms. Note that the recycle delay for the SLRϱ experiments was set to at least $5 \times 1/R_1$ in order to guarantee full longitudinal relaxation between each scan. Both R_1 and $R_{1\varrho}$ were obtained by parameterizing the magnetic transients $M_z(t_d)$ and $M_\varrho(t_{lock})$, respectively, by stretched exponentials (see below): $M_z(t_d) \propto 1 - \exp[-(t/T_1)^\gamma]$ and $M_\varrho(t_{lock}) \propto \exp[-(t_{lock}/T_{1\varrho})^{\gamma_\varrho}]$, respectively.

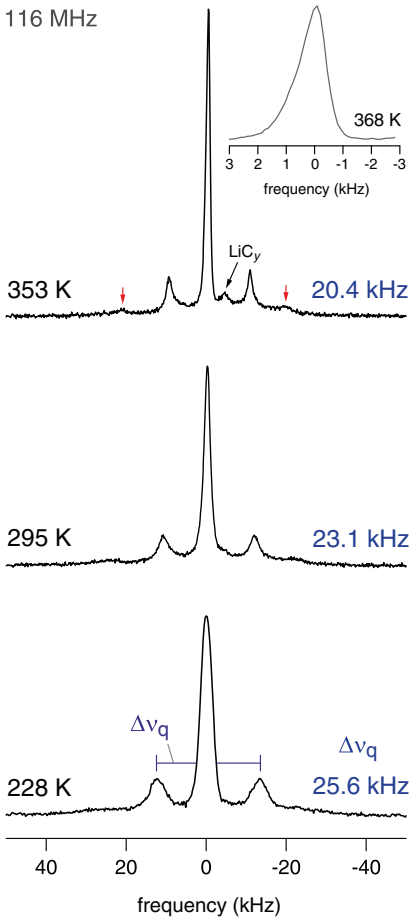

FIG. 2. (Color online) Static ^{7}Li NMR spectra of polycrystalline LiC_6 (116 MHz) recorded at the temperatures indicated. With increasing T homonuclear dipole-dipole interactions are averaged owing to Li^+ hopping which results in narrowing of the linewidths. The quadrupole coupling constant $C_q = 2\Delta\nu_q$ decreases with increasing temperature. The slight anisotropy of the central line (see inset) is due to the layered structure of the sample.

In addition, temperature-variable ^{7}Li NMR spin-spin relaxation (SSR) rates $1/T_2 = R_2$ were recorded by taking advantage of a (two-pulse) solid-echo pulse sequence,[19] that had been optimized for spin-3/2 nuclei such as ^{7}Li. t_{echo} in $\pi/2 - t_{echo} - (64^\circ) -$ acq. denotes the variable interpulse delay. The transients obtained can be satisfactorily described with single exponentials. Static ^{7}Li NMR spectra were either obtained after Fourier transformation (FT) of the free induction decay, which were recorded by nonselective irradiation with a single $\pi/2$ pulse, or by FT of the solid echo beginning from the top of the signal.

III. RESULTS AND DISCUSSION

A. NMR spectra and motional narrowing

Before discussing our SLR NMR results in detail, we call the reader's attention to the static ^{7}Li NMR spectra shown in Fig. 2 which were recorded at different temperatures T. Let us first discuss the central line of the spectrum which is also determined by a distinct powder pattern because of electric

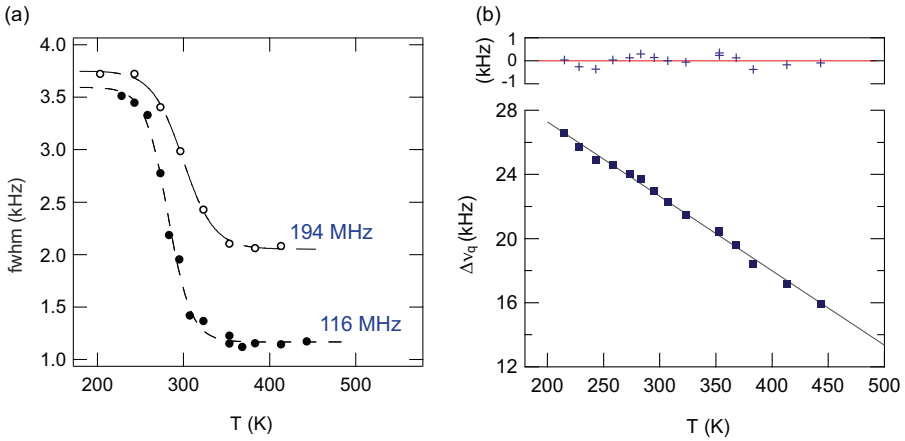

FIG. 3. (Color online) (a) Motional narrowing of the ^{7}Li NMR central line of polycrystalline LiC_6. Linewidths (FWHM, full width at half maximum) were recorded at 116 and 194 MHz. Most likely, the field-dependent final width in the regime of extreme narrowing reflects both the effect of chemical shift anisotropy and, more importantly, the influence of local magnetic field gradients on the spin-spin-relaxation time; see also Ref. 29. (b) Temperature dependence of $\Delta\nu_q$; the upper graph shows the deviations from the linear fit used to describe $\Delta\nu_q(T)$.

quadrupolar interactions (see below). At sufficiently low T, Li^+ translational motion is slow compared to the spectral width determined by the central transition. This results in dipolarly broadened NMR spectra. Motion-induced averaging of dipolar interactions causes line narrowing at elevated T [see Fig. 3(a)]. Expectedly, its overall width (full width at half maximum) in the rigid-lattice regime slightly depends on the strength B_0 of the external magnetic field applied [Fig. 3(a)]. The relatively low, absolute value is compatible with lithium ions lying in planes with six nearest Li neighbors at a distance of approximately 4.3 Å. With increasing T mainly Li-Li dipolar interactions are averaged due to diffusive motion of the spins. From the motional narrowing (MN) curve an activation energy for Li hopping can be roughly estimated with the relation introduced by Waugh and Fedin. Line narrowing sets in at $T_n \approx 260$ K which translates into $E_{a,\,MN}/\text{meV} \approx 1.62 \times T_n/\text{K} \mathrel{\hat{=}} 0.42$ eV. This value is comparable with the one deduced from the low-T flank of the NMR relaxation rate peaks analyzed below; see also Ref. 30. An analysis according to the Abragam formalism[31] yields an even lower activation energy ($\leqslant$0.2 eV). Possible shortcomings of such analyses have recently been outlined in the study of Faske *et al.* and Storek *et al.*[32,33]

At high temperatures the central line reveals a slight anisotropic broadening which reflects the Li ions exposed to the layer structure of LiC_6. Furthermore, in this high-T range, the NMR linewidths of the two-pulse spectra are presumably affected by internal inhomogeneous magnetic fields[29] that arise from the nonzero susceptibility of the LiC_6 particles (see also below, Sec. III B2).

The spectrum recorded at 353 K (see Fig. 2) revealed a small amount of impurities as indicated by the arrow. Fortunately, such a small amount has negligible influence on the SLR NMR rates recorded. The signal with low intensity, that becomes visible at elevated temperatures only, might be ascribed to stage-n graphite intercalation compounds (GICs) such as LiC_{18}, LiC_{27}, or LiC_{36}.[34] These might be formed because of Li loss during preparation. Small amounts of the stage-2 GIC LiC_{12}, as found by XRPD (see above), could hardly be detected by NMR. In particular, LiC_{12} should be distinguishable by its different quadrupole powder pattern characterized by a smaller coupling constant[34] (see also below). Note that the spectra shown in Fig. 2 are plotted such that the central lines show up at $\nu = 0$ kHz. When referenced to an aqueous solution of LiCl (0.1 M), the NMR shift, i.e., the isotropic Knight shift, turns out to be about 41.6 ppm. This is in perfect agreement with results reported and discussed in the literature[14] for LiC_6 (about 42.6 ppm),[34] previously.

Owing to the interaction of the quadrupole moment of ^{7}Li (spin-quantum number 3/2) with a nonvanishing electric field gradient (EFG) at the nuclear site,[31,35,36] the NMR spectra are composed of satellite intensities forming a well-defined quadrupole powder pattern. Since the Li sites are electrically equivalent, a single pattern is observed. From the inner singularities (the outer ones are marked in Fig. 2 by vertically drawn arrows) the site-specific quadrupole coupling constant $C_q = 2\Delta\nu_q$ can be estimated; see the NMR spectrum recorded at 228 K (Fig. 2). Assuming axial symmetry ($\eta = 0$), as expected from the crystal structure, the quadrupole splitting $\Delta\nu_q$ is given by $\Delta\nu_q = |e^2qQ/(2h)|[3\cos^2(\theta) - 1]$ where θ denotes the angle between the c axis and the external magnetic field (in the principal axis system). e is the elemental charge, eq represents the EFG at the Li site, Q is the quadrupole moment of ^{7}Li, and h denotes Planck's constant. At the position of the 90° singularities we obtain $\Delta\nu_q = |e^2qQ/(2h)|$ leading to $2\Delta\nu_q = |e^2qQ/h| = C_q$. This yields 46.2 kHz for the quadrupole coupling constant at 295 K. Note once again that the values given in Fig. 2, and those shown as a function of T in Fig. 3 as well, were obtained for an axially oriented EFG with respect to the principal axis system. The absolute values are consistent with those from ^{7}Li-NMR and ^{8}Li-β-NMR measurements in the literature.[34,37] As an example, Letellier *et al.*[34] found $\Delta\nu_q = 22.6$ kHz at ambient temperature which is in good agreement with our value (23.1 kHz). Using an oriented sample, Roth *et al.*[38] report a value of 22 kHz; in an early work of Conard *et al.*[39] a splitting of 24 kHz is found. LiC_{12}, LiC_{18}, LiC_{27}, and LiC_{36} show smaller quadrupole splittings $\Delta\nu_q$ ranging from 17 to 19 kHz.[34]

It is worth noting that the decrease of the quadrupole splitting $\Delta\nu_q$ with increasing T cannot simply be ascribed to changes of the lattice parameters. Owing to the narrower temperature range covered we were not able to reveal the $T^{3/2}$ dependence found by β-NMR on an oriented LiC_6 sample.[37] Here, $\Delta\nu_q$ (200 K $< T <$ 450 K) changes linearly with T.

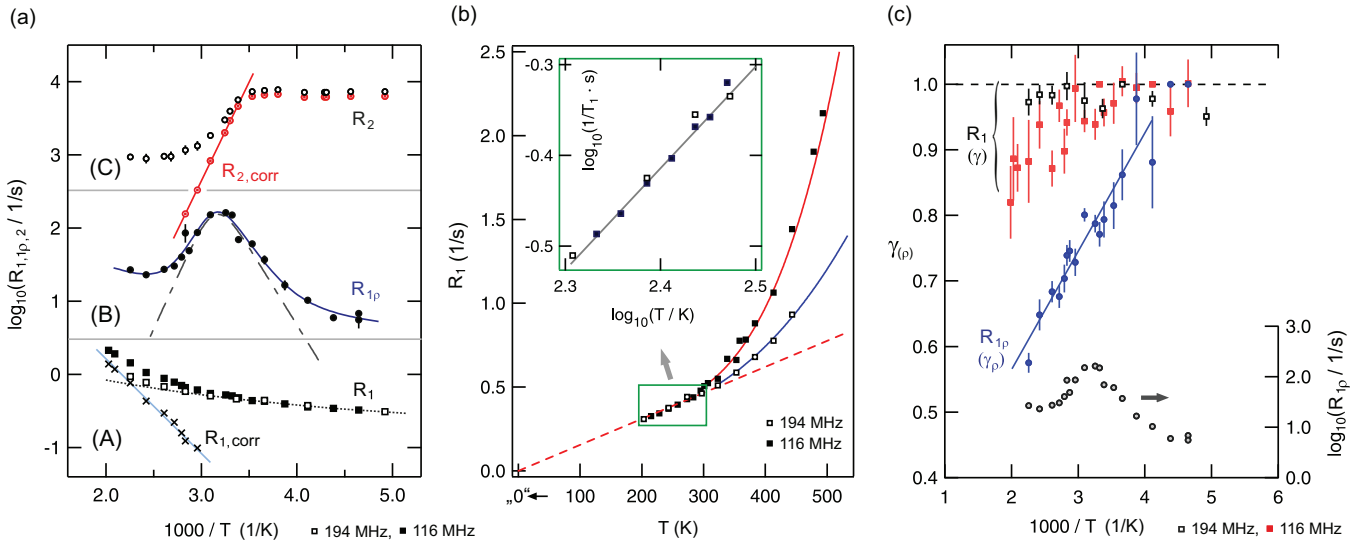

FIG. 4. (Color online) (a) Arrhenius plot illustrating the temperature dependence of the ^{7}Li NMR relaxation rates R_1 (A) and $R_{1\varrho}$ (B) measured at 116 and 194 MHz, respectively; R_2 (C) rates were recorded at 116 MHz. (b) R_1 of LiC_6 plotted as R_1 vs T and $\log_{10} R_1$ vs $\log_{10} T$ (inset). (c) Temperature dependence of the stretching factors γ obtained from the various temperature-variable NMR relaxation transients; exemplarily, selected transients M_ϱ are depicted in Fig. 5(b). For comparison, $R_{1\varrho}(1/T)$ is also shown. See text for further explanations.

B. Diffusion-induced relaxation NMR

1. *^{7}Li SLR NMR in the laboratory and rotating frame of reference*

In the Arrhenius presentation of Fig. 4(a) an overview of the ^{7}Li NMR relaxation rates measured is given. At first we will briefly discuss the SLR NMR rates recorded at 116 MHz and 194 MHz, i.e., in the laboratory frame of reference. At low temperatures R_1 seems to be independent of the Larmor frequency applied. Combined with a linear dependence of R_1 on temperature, this is expected for SLR being mainly induced by coupling of the Li spins with conduction electrons. Indeed, a power-law fit

$$R_1 \propto T^{\kappa}, \tag{1}$$

indicated by the dotted line shown in Fig. 4(a), yields $\kappa = 1.1(1)$. This can be even better illustrated by plotting R_1 vs T: The dashed line in Fig. 4(b) represents ideal linear behavior according to $R_1 = s'T^{\kappa}$ with $\kappa = 1$. The inset uses the representation $\log_{10} R_1$ vs $\log_{10} T$ to calculate κ in the low-temperature regime with a linear fit. The latter yields $s' = 7.9(3) \times 10^{-4}$ s^{-1} K^{-1} and $\kappa = 1.12(4)$ (cf. the power-law analysis shown above). The product T_1T turns out to be approximately 650 ± 15 s · K, which is in very good agreement with the ^{7}Li NMR result reported by Estrade *et al.*[14] (600 ± 120 s · K).

Above 300 K the rates R_1 increasingly deviate from $R_1 = S_0T$ which points to the influence of other relaxation mechanisms owing to Li^+ hopping processes or (anharmonic) lattice vibrations. A two-phonon Raman process would give $R_1 \propto T^2$ at temperatures T larger or similar to the Debye temperature Θ. In order to separate such background effects from diffusion-induced processes, we extrapolated the power-law fit of Fig. 4(a) to higher temperatures and subtracted the rates from the overall ones measured; i.e.,

$$R_{1,\,\mathrm{corr}} = R_1 - R_{1,\,\mathrm{e}} \tag{2}$$

with $R_{1,\,\mathrm{e}} \approx S_0T^{\kappa}$. If we assume that the background-corrected rates obtained are mainly influenced by Li hopping, an activation energy can be roughly estimated. Note that the rates were recorded in the regime $\omega_0\tau \gg 1$; i.e., the activation energy E_{a,T_1} should be characteristic of short-range (or localized) Li motions in LiC_6. These might include translational processes in LiC_6 with a short jump distance.[5] Here, we obtain 0.25(2) eV which is very similar to the result previously estimated from NMR line narrowing.[14]

Ion dynamics proceeding on a longer length scale, however, can only be probed when the so-called high-T flank of the diffusion-induced rate peak is reached. In the present case, this needs very high temperatures. Fortunately, the spin-lock technique can be used which is *per se* sensitive to slower Li motions covering a longer time scale. Therefore, we recorded diffusion-induced SLR NMR rate peaks at frequencies ω_1 on the order of some kHz instead of using ω_0 with values in the MHz range. Doing so, by formally replacing ω_0 with ω_1 the SLR NMR rate peak shifts towards lower temperature so that both the maximum and the high-T flank become accessible. The corresponding rates $R_{1\varrho}$, which have been extracted from the stretched magnetization transients recorded, are shown in Fig. 4(a) as a function of the inverse temperature. At low temperatures, that is, below 250 K, they are increasingly governed by nondiffusive background effects. Note that the ratio $R_{1\varrho}/R_1$ turns out to be approximately 1.5 orders of magnitude. Thus, besides interactions of the Li spins with conduction electrons in the case of R_1 measurements (see above), the low-T $R_{1\varrho}$ rates seem to be influenced by additional processes (see below). For comparison, the corresponding stretching factors of the various transients measured are shown in Fig. 4(c). In Fig. 5 selected magnetization transients of the $R_{1\varrho}$ NMR measurements are shown.

Finally, with increasing T the overall rates $R_{1\varrho}$ pass through a maximum located at $T = 314$ K. At even higher

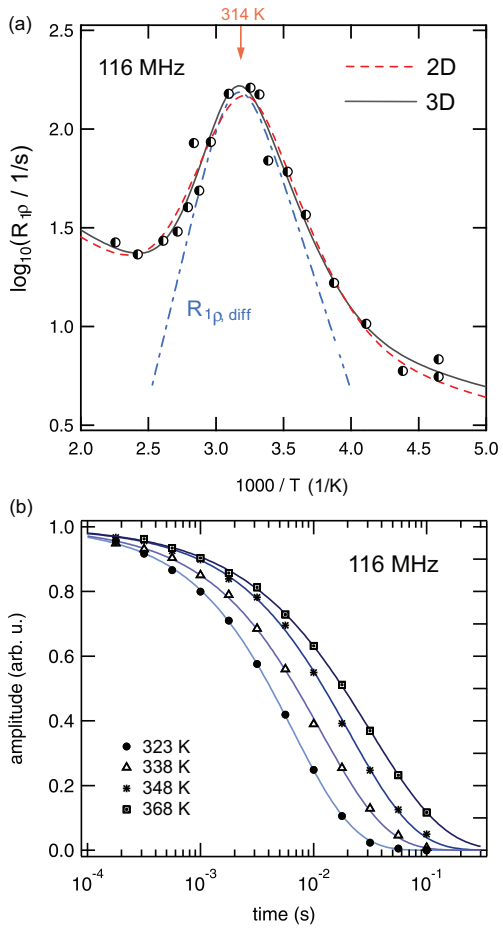

FIG. 5. (Color online) (a) ^{7}Li SLRρ NMR rates of polycrystalline LiC_6 (see Fig. 4), plotted in an Arrhenius diagram. For comparison with the fit according to Eqs. (3) and (4) (solid line), the dashed line represents the 2D fit by means of Eq. (6). The dashed-dotted line shows the purely Li^+ diffusion-induced contribution when the rates are analyzed in terms of a modified BPP-type spectral density function yielding 0.57(2) eV and $\beta = 1.7(2)$. (b) Selected temperature-variable magnetization transients $M_\varrho(t_{\rm lock})$ containing the ^{7}Li SLR NMR rates in the rotating frame of reference. The transients illustrate the behavior of M_ϱ on the high-T flank of the diffusion-induced rate peak shown above. Solid lines show fits with stretched exponentials $M_\varrho(t_{\rm lock}) \propto \exp[-(t_{\rm lock}/T_{1\varrho})^{\gamma_\varrho}]$; in this T range the stretching factor γ_ϱ, also shown in Fig. 4(c), scatters around 0.7 [see Fig. 4(c)].

temperatures, i.e., when $R_{1\varrho}$ decreases, the nondiffusive relaxation background shows up again. In order to separate unwanted background effects from diffusion-induced contributions, the overall rates $R_{1\varrho}$ were, in the first place, approximated with a sum of a modified BPP-type relaxation function and a power-law expression:

$$R_{1\varrho}^{\rm 3D} = R_{1\varrho,\,\rm diff}^{\rm 3D} + R_{1\varrho,\,\rm bgr} = C_\varrho\big(J(2\omega_1) + \tfrac{5}{3}J(\omega_0) + \tfrac{2}{3}J(2\omega_0)\big) + BT^{\kappa'} \quad (3)$$

with $J(\omega_{1(0)})$ being here a Lorentzian-shaped spectral density function according to

$$J(\alpha\cdot\omega_{1(0)})_{\alpha=1,2} = C'\tau_{\rm c}/[1+(\alpha\cdot\omega_{1(0)}\tau_{\rm c})^{\beta}]. \quad (4)$$

Note that the correlation rate $\tau_{\rm c}^{-1}$ is on the order of the jump rate τ^{-1}. In many cases it can be described by an Arrhenius relation containing the pre-exponential factor τ_0^{-1} and the activation energy $E_{\rm a}$ determining long-range Li diffusion

$$\tau_{\rm c}^{-1} \approx \tau^{-1} = \tau_0^{-1}\exp(-E_{\rm a}/k_{\rm B}T); \quad (5)$$

$k_{\rm B}$ denotes Boltzmann's constant. Here, the best fit yields $\kappa' = 2.0(4)$, thus indicating that lattice vibrations become the main origin of background relaxation (see above). The parameter β reflects any asymmetry of the rate peak $R_{1\varrho}(1/T)$ which may arise from correlation effects such as structural disorder and/or Coulomb interactions.[20,21] In general, uncorrelated motion should result in a symmetric NMR rate peak; any correlation effects, for comparison, are expected to reduce the slope on the low-T side compared to the situation in the limit $\omega_1\tau \ll 1$, that is, the high-T regime. In the present case we found $\beta = 1.7(2)$; thus, the diffusion-induced rate peak, indicated by the dashed-dotted line in Fig. 4(a), is slightly asymmetric.

The activation energy $E_{\rm a}$ turned out to be 0.57(2) eV; the prefactor τ_0^{-1} is approximately 1.6×10^{14} s^{-1}. The latter is in very good agreement with values typically expected for phonon frequencies. Moreover, $E_{\rm a} \approx 0.57$ eV is consistent with the prediction of Freiländer *et al.*[7] The value obtained from Eq. (3) also equals the activation energy which can be directly obtained from the high-T side of the rate peak. Moreover, in the limit $\omega_1\tau \gg 1$, where $J(\omega_1,\tau) \propto \omega^{-\beta}\tau^{1-\beta}$ holds, the corresponding slope yields $E_{\rm a,low} = 0.42(2)$ eV. In the present case, $E_{\rm a,low}$ and $E_{\rm a}$ obey the relation $E_{\rm a,low} = (\beta-1)E_{\rm a}$. Note that the same result is obtained when Eq. (3) is restricted to the first term: $R_{1\varrho,\,\rm diff} \propto J(2\omega_1)$.

It is worth noting that $J(\omega)$ in Eq. (4) represents a spectral density function which describes diffusive motion in three dimensions (3D). Frequency-dependent β-NMR measurements,[7,8] however, indicate a low-dimensional diffusion process in LiC_6. Additionally, at temperatures higher than 630 K, a 2D motional process was claimed based on QENS measurements.[5] Therefore, we also tried to analyze our SLR NMR data with a semiempirical spectral density function for 2D diffusion. In concrete terms, we used the expression by Richards[40,41] which is based on a function introduced by Avogadro and Villa taking account of a logarithmic frequency dependence in the high-temperature limit $\omega_{0(1)}\tau_{\rm c} \ll 1$.[42,43] Following Küchler *et al.*,[44] who first incorporated the effect of correlation via the parameter β also for 2D diffusion, it reads

$$R_{1\varrho}^{\rm 2D} = R_{1\varrho,\,\rm diff}^{\rm 2D} + R_{1\varrho,\,\rm bgr} \approx C'_\varrho\tau_{\rm c}\ln[1+1/(2\omega_1\tau_{\rm c})^{\beta}] + B'T^{\kappa''}. \quad (6)$$

This ansatz worked well for other layer-structured materials showing 2D diffusion.[10,12,13,18] The fit, indicated in Fig. 5 by the dashed line, yields $B \approx B'$ and $\kappa' \approx \kappa''$. Moreover, $E_{\rm a}^{\rm 2D}$ is given by approximately 0.62 eV and, thus, at least comparable to the result obtained by Eqs. (3) and (4). However, in the present case, the prefactor τ_0^{-1} turns out to be unusually high; it would be approximately 1.8×10^{16} s^{-1}. This is by about two orders of magnitude larger than that obtained from the modified-BPP fit used to describe the temperature dependence of the NMR rates (*vide supra*). Hence, based on the results obtained it seems that the semiempirical Richards model (represented by the dashed line in Fig. 5) is less appropriate to

describe Li dynamics in LiC_6. Certainly, this fact might also be explained by nonnegligible Li hopping processes taking place via defects perpendicular to the layers, that is, channel-like diffusion, influencing the NMR response of a pure 2D process.

2. ^{7}*Li NMR spin-spin relaxation*

The results obtained from SLR NMR are corroborated by the analysis of complementary spin-spin relaxation (SSR) data. In agreement with the results of Eqs. (3) and (4), temperature-variable SSR measurement yield an activation energy of 0.53(2) eV. This value can be extracted from the rates measured as follows. Below 285 K, that is, in the so-called rigid lattice regime, R_2^{-1} is almost independent of temperature and amounts to approximately 125 μs. Owing to averaging of dipole-dipole interactions, because of increasing of the Li^+ hopping, the rates significantly start to decrease indicating long-range Li translational motion. Interestingly, at 400 K they reach a plateau value characterized by $R_{2,\mathrm{high}}^{-1} \approx 1$ ms. This feature is very similar to the one observed by McDowell *et al.*[29] previously in the 2D H^+ ion conductor $ZrBe_2H_{1.4}$ (ZBH). In ZBH the deviation is ascribed to long-range H motion in the presence of a magnetic field gradient which is due to the nonzero magnetic susceptibility of the metal hydride. The mean-field gradient in ZBH is directly proportional to the magnitude B_0 of the external magnetic field applied. As a result, the lower the Larmor frequency used the farther the beginning of the plateau is shifted towards higher temperature resulting in a decrease of $R_{2,\mathrm{high}}$. Hence, the residual NMR (central) linewidth in the regime of extreme motional narrowing is expected to be smaller for measurements carried out at 116 MHz compared to those performed at 194 MHz [see Fig. 3(a)].

Subtracting $R_{2,\mathrm{high}}$ from the overall rates measured yields $R_{2,\mathrm{corr}}$. From the linear fit shown in Fig. 4(a) the above-mentioned activation energy [0.53(2) eV] can be deduced. Lastly, with the help of both $R_{1\varrho}$ and R_2 measurements it is possible to probe Li diffusion in LiC_6 at temperatures ranging from 270 K to 360 K. This regime coincides with the operating range for most battery applications.

C. Li jump rates and self-diffusion coefficients

Considering the maximum of the $R_{1\varrho}(1/T)$ peak probed, it is possible to precisely determine the mean Li jump rate irrespective of the spectral density function J chosen to parametrize the data. At $T = 314$ K, that is the temperature where the peak shows up [see Fig. 5(a)], for SLR NMR in the rotating frame of reference the condition $\omega_1\tau_c \approx 0.5$ holds.[9] Identifying τ_c with the motional residence time of an Li spin and inserting $\omega_1 = 2\pi \times 10(1)$ kHz, we obtain $\tau_c \approx \tau = 8$ μs. According to the Einstein-Smoluchowki equation,[46]

$$D_{d\mathrm{D}} = a^2/(2d \cdot \tau), \tag{7}$$

this corresponds to $D_{2\mathrm{D}}(314\mathrm{K}) \approx 1.9 \times 10^{-11}$ cm^2 s^{-1} and $D_{3\mathrm{D}}(314\ \mathrm{K}) \approx 1.3 \times 10^{-11}$ cm^2 s^{-1}. Here, we used $a \approx 3$ Å as a good approximation for a mean jump distance and calculated the diffusion coefficient for both spatially restricted and nonrestricted motion, i.e., for $d = 2$ or $d = 3$, whereby d represents the dimensionality of the diffusion process.

In Fig. 6(a) the jump rate determined by means of the Li^+ diffusion-induced $R_{1\varrho}(1/T)$ rate peak is shown in an Arrhenius plot and compared with those values which can be estimated from (analogous) ^{8}Li β-NMR measurements of Freiländer *et al.*[7] Although ^{8}Li NMR was carried out on oriented (HOPG) LiC_6 samples good agreement is found. For comparison, the solid line represents an Arrhenius line characterized by an activation energy of 0.55 eV, which represents the mean value when the results from $R_{1\varrho}$ and R_2 are considered. The gray area indicates the temperature range covered by Li^+ diffusion-induced $R_{1\varrho}$ measurements. From the Arrhenius line indicated a prefactor τ_0^{-1} can be estimated ($\approx 1 \times 10^{14}$ s^{-1}) which is consistent with that obtained from the analysis of the $R_{1\varrho}(1/T)$ NMR peak with a BPP-type expression (*vide supra*).

Besides $R_{1\varrho}$ measurements also R_2 (and motional line narrowing as well) is suitable to estimate Li jump rates. At the temperature where the rates R_2 start to decrease [$T \approx 294$ K; see Fig. 4(a)] the Li jump rate is expected to be on the order of $\tau^{-1} \approx 2\pi R_{20}$ with $R_{20}^{-1} = T_{20} = 140$ μs being the rigid-lattice SLR NMR rate. This yields $\tau = 22$ μs. Even slower motions can be estimated from the onset of motional line narrowing; in the present case NMR central lines significantly start to decrease in linewidth at $T \approx 250$ K. Roughly spoken, this is expected when τ reaches values on the order of a few ms. Additionally, the inflexion point ($T_{\mathrm{infl.}} \approx 275$ K at 116 MHz) of the whole motional narrowing (MN) curve (see above, Fig. 3) can be used to estimate τ according to $\tau^{-1}(T_{\mathrm{infl.}}) \approx 2\pi\nu_0$ with ν_0 being the rigid-lattice linewidth (≈3.5 kHz). For comparison, the values estimated from SSR NMR and MN are also included in Fig. 6(a).

It is worth noting that in the presence of a broad distribution of jump rates [note that such a feature would also be reflected in a deviation of β from BPP-type behavior ($\beta = 2$)], the NMR line narrowing would be predominantly influenced by that fraction of ions diffusing faster compared to others. Hence, as indicated above, the interpretation of MN NMR data can easily lead to an overestimation of the mean lithium jump rate and an underestimation of the activation energy; see, e.g., Refs. 32 and 33. For comparison, activation barriers ranging from 0.1 and 0.3 eV have been calculated for different types of interstitialcy diffusion mechanisms in LiC_6.[22]

Finally, considering the rates shown in Fig. 6(a), at room temperature (293 K) the Li jump rate turns out to be 4.5×10^4 s^{-1}. This corresponds to a self-diffusion coefficient on the order of 5×10^{-12} cm^2 s^{-1} at 293 K. Decreasing the temperature from 293 to 268 K (−5 °C), Li self-diffusivity is slowed down by a factor of 10. Such key figures are crucial for the safe and efficient operation of graphite-based ion batteries. In particular, at freezing temperatures the performance of a battery is then additionally limited and controlled to a large extent by slow Li diffusion within the host material. It is noteworthy that room-temperature self-diffusion coefficients ranging from 10^{-16} m^2 s^{-1} to 10^{-15} m^2 s^{-1}, as found for LiC_6 here, are comparable to those recently obtained by NMR also for layer-structured cathode materials such as $Li_{x\approx 0.7}TiS_2$.[10] Thus, regarding Li *self-diffusion* in fully intercalated stage-1 LiC_6, Li ion mobility does not exceed that of conventional cathode materials.

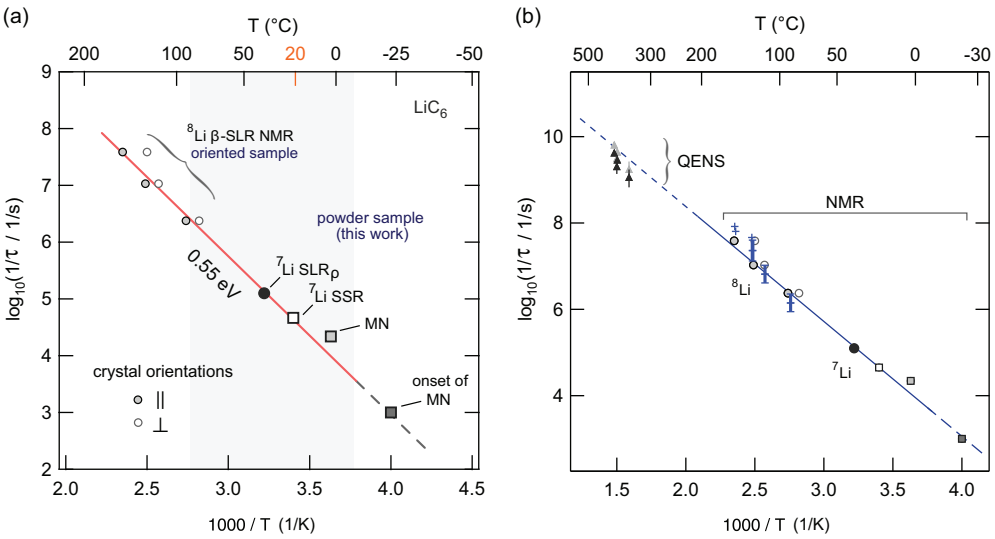

FIG. 6. (Color online) (a) Arrhenius plot of Li jump rates in LiC_6 deduced from various NMR techniques being sensitive to translational ion jumps on quite different time scales, here, covering up to five decades. SLR NMR rate peaks provide a relatively theory-independent determination of jump rates. The rates determined by β-NMR were deduced from Ref. 7. See text for further explanation. (b) Comparison of the rates shown in (a) with those obtained from QENS (Ref. 5). The diffusion coefficients from QENS reported by Magerl *et al.* (Ref. 5) have been roughly converted into jump rates τ^{-1} (triangles in black) via the Einstein-Smoluchowski equation [see Eq. (7)] assuming, as suggested in Ref. 5, 2D diffusion and a relatively long jump distance a of approximately 4.26 Å. Using $a \approx 3$ Å, which is close to the average of possible jump distances in LiC_6, yields the rates shown by gray triangles. $a = 2.5$ Å, which is the jump distance for an interstitial migration mechanism (Refs. 22 and 45), yields an even better agreement. The crosses represent jump rates from β-NMR presented in Ref. 8.

Strictly speaking, the results presented here should not be mixed with *chemical* diffusion coefficients which have been experimentally probed via (solid-state) electrochemical macroscopic method as well as calculated (4×10^{-12} m^2 s^{-1}, $E_a \approx 0.4$ eV) recently for 2D (in-plane) Li^+ motion in LiC_6.[47] Interestingly, the results of the theoretical work by Toyoura *et al.*[45] on ordered LiC_6 agree well with the present findings. Activation barriers for Li migration, which were calculated separately for the vacancy and interstitial Li migration process, turned out to be approximately 0.5 eV; see also Ref. 22. The corresponding (in-plane) diffusion coefficients are 10^{-14} m^2 s^{-1} and 10^{-15} m^2 s^{-1}, respectively. Apart from this good agreement, the present results are in line with those from earlier experimental studies; see, e.g., Ref. 48 for an overview of Li (chemical) diffusion coefficients determined for various carbon anode materials. Note that by the application of NMR spectroscopy we were able to study Li ion dynamics separately from electron dynamics in mixed conducting LiC_6. While the latter influences the SLR NMR rates recorded at low temperatures, with increasing T diffusive motions significantly govern spin-lattice relaxation while other interactions relatively lose ground. These show up once again at temperatures higher than 400 K.

As a last comparison, in Fig. 6(b) data from the QENS study of Magerl *et al.*,[5] pointing to an in-plane 2D jump-type diffusion mechanism, are included. The self-diffusion coefficients deduced from QENS have been roughly converted into jump rates according to Eq. (7). Here, we used both $a \approx 4.26$ Å as found by QENS for the 2D diffusion process and $a \approx 3$ Å, which is a good approximation for the average of possible jump distances. Considering the error limits and the narrow temperature range covered by the earlier study,[5] in our opinion, a relatively good agreement is found with the results obtained from NMR. The solid line is to guide the eye and refers to an Arrhenius law with $E_a = 0.54$ eV and $\tau_0^{-1} = 5 \times 10^{13}$ s^{-1} which is very similar to that shown in Fig. 6(a). To sum up, over a relatively broad dynamic range a single Arrhenius relation seems to be appropriate to describe Li diffusion in ordered LiC_6.

IV. CONCLUSIONS AND OUTLOOK

Spin-lattice relaxation NMR using the stable isotope ^{7}Li was applied to probe room-temperature Li dynamic parameters in polycrystalline, mixed conducting LiC_6 being the most widely used anode material. As deduced from atomic-scale NMR measurements Li hopping in the bulk is characterized by an activation energy of approximately 0.55 eV and an Li self-diffusion coefficient of 10^{-15} m^2 s^{-1} (295 K), thus, comparable to Li self-diffusivity in layer-structured transition metal sulfides and oxides serving as positive electrodes in lithium-ion batteries.

The results obtained from the different NMR techniques employed are in good agreement with previous studies[7,8] using ^{8}Li β-NMR to probe diffusion parameters at elevated temperatures. Most importantly, the jump rates can be well approximated with a *single* Arrhenius law which is determined by an activation energy of approximately 0.55 eV and a pre-factor on the order of typical phonon frequencies, viz., 10^{14} s^{-1}. On that note the present study updates our knowledge on Li self-diffusion in LiC_6. It is noteworthy that the activation energy probed by NMR is in fair agreement with calculated barrier heights (≈0.5 eV) by Toyoura *et al.*[45] for both the in-plane vacancy and interstitial Li migration mechanism. Even the

chemical diffusion coefficients reported by Toyoura *et al.*[45] (viz., 10^{-14} m^2 s^{-1} and 10^{-15} m^2 s^{-1} for the interstitial and vacancy mechanism, respectively) agree with the present findings.

Considering solely ^{7}Li NMR rates, it is difficult to judge whether the diffusion process probed is strictly governed by 2D diffusion. The present results are in very good agreement with those probed by orientation-dependent and frequency-dependent SLR ^{8}Li β-NMR measurements on highly oriented pyrolytic graphite. The β-NMR results indeed gave strong evidence for low-dimensional lithium diffusion.[7,8] Fair agreement is also found with results from QENS probing in-plane diffusion in the ordered phase of LiC_6.[5] Recent theoretical investigations also strongly point to high lithium-ion diffusivity in the direction parallel to the graphene layers and to much slower interlayer hopping, that is, motion across the basal plane.[47]

However, though there are convincing reasons to claim even microscopic Li diffusion as purely low-dimensional in LiC_6, the semiempirical SLR NMR model introduced by Richards for 2D motion seem to be less adequate to satisfactorily describe the temperature dependence of the ^{7}Li NMR $R_{1\varrho}(1/T)$ rate peak probed here. The applicability of a modified BPP-type relaxation model, see, e.g., the previous work by Küchler *et al.*,[44] might indicate a small, but nonnegligible, influence of interlayer hopping process on the diffusion-induced SLR NMR rates.

To shed further light on the Li dynamics in LiC_6, the application of NMR techniques being able to directly record motional correlation functions might be beneficial. For instance, considering the temperature range below 300 K, this should be possible via the generation of Jeener-Broekaert NMR echoes[49] with the so-called spin-alignment echo (SAE) technique.[50–53] In general, SAE (or stimulated echo) NMR is sensitive to extremely slow translational and rotational jump processes.[54–60]

ACKNOWLEDGMENTS

We thank our colleagues at the TU Graz and at the Leibniz University Hannover for valuable discussions. Financial support by the Deutsche Forschungsgemeinschaft (DFG) is highly appreciated (DFG Research Unit 1277, Grant No. WI3600/2-2 and 4-1 and Grant No. HE1574/13-2), and by the Austrian Federal Ministry of Economy, Family, and Youth and the Austrian National Foundation for Research, Technology, and Development is greatly appreciated.

*The authors were equally involved in experimental work, data analysis, and project planning. Corresponding author: julia.langer@tugraz.at

†See also for correspondence: viktor.epp@tugraz.at

‡See also for correspondence: wilkening@tugraz.at

[1] M. S. Whittingham, Chem. Rev. **104**, 4271 (2004).

[2] J. M. Tarascon and M. Armand, Nature (London) **414**, 359 (2001).

[3] M. Wakihara and O. Yamamoto, eds., *Lithium Ion Batteries* (Wiley-VCH, Weinheim, 1998).

[4] M. Winter and J. O. Besenhard, Electrochem. Acta **45**, 31 (1999).

[5] A. Magerl, H. Zabel, and I. S. Anderson, Phys. Rev. Lett. **55**, 222 (1985).

[6] T. Springer and R. E. Lechner, in *Diffusion in Condensed Matter—Methods, Materials, Models*, 2nd ed, edited by P. Heitjans and J. Kärger (Springer, Berlin, 2005), Chap. 3, pp. 91–164.

[7] P. Freiländer, P. Heitjans, H. Ackermann, B. Bader, G. Kiese, A. Schirmer, H.-J. Stöckmann, C. V. der Marel, A. Magerl, and H. Zabel, Z. Phys. Chem. **151**, 93 (1987).

[8] A. Schirmer and P. Heitjans, Z. Naturforsch. **50a**, 643 (1995).

[9] P. Heitjans, A. Schirmer, and S. Indris, in *Diffusion in Condensed Matter*, edited by P. Heitjans and J. Kärger (Springer, Berlin, 2005), Chap. 9, p. 367.

[10] M. Wilkening and P. Heitjans, Phys. Rev. B **77**, 024311 (2008).

[11] M. Wilkening, A. Kuhn, and P. Heitjans, Phys. Rev. B **78**, 054303 (2008).

[12] V. Epp and M. Wilkening, Phys. Rev. B **82**, 020301 (2010).

[13] V. Epp, O. Gün, H.-J. Deiseroth, and M. Wilkening, Phys. Chem. Chem. Phys. **15**, 7123 (2013).

[14] H. Estrade, J. Conard, P. Lauginie, P. Heitjans, F. Fujara, W. Buttler, G. Kiese, H. Ackermann, and D. Guérard, Physica B **99**, 531 (1980).

[15] D. Ailion and C. P. Slichter, Phys. Rev. Lett. **12**, 168 (1964).

[16] C. P. Slichter and D. Ailion, Phys. Rev. **135**, A1099 (1964).

[17] M. Wilkening, W. Iwaniak, J. Heine, V. Epp, A. Kleinert, M. Behrens, G. Nuspl, W. Bensch, and P. Heitjans, Phys. Chem. Chem. Phys. **9**, 6199 (2007).

[18] V. Epp, S. Nakhal, M. Lerch, and M. Wilkening, J. Phys.: Condens. Matter **25**, 195402 (2013).

[19] E. Fukushima and S. B. W. Roeder, *Experimental Pulse NMR: A Nuts and Bolts Approach* (Addison-Wesley Pub. Co., Advanced Book Program, Reading, MA, 1981).

[20] M. Meyer, P. Maass, and A. Bunde, Phys. Rev. Lett. **71**, 573 (1993).

[21] A. Bunde, W. Dieterich, P. Maass, and M. Meyer, in *Diffusion in Condensed Matter—Methods, Materials, Models*, 2nd ed, edited by P. Heitjans and J. Kärger (Springer, Berlin, 2005), Chap. 20, pp. 813–856.

[22] K. Toyoura, Y. Koyama, A. Kuwabara, and I. Tanaka, J. Phys. Chem. C **114**, 2375 (2010).

[23] A. Herold, Synth. Met. **23**, 27 (1988).

[24] D. Guérard and A. Hérold, Carbon **13**, 337 (1975).

[25] D. C. Ailion and C. P. Slichter, Phys. Rev. **137**, A235 (1965).

[26] D. C. Look and I. J. Lowe, J. Chem. Phys. **44**, 2995 (1966).

[27] T. J. Rowland and F. Y. Fradin, Phys. Rev. **182**, 760 (1969).

[28] D. Wolf, Phys. Rev. B **10**, 2724 (1974).

[29] A. F. McDowell, C. F. Mendelsohn, M. S. Conradi, R. C. Bowman, and A. J. Maeland, Phys. Rev. B **51**, 6336 (1995).

[30] M. Wilkening, D. Bork, S. Indris, and P. Heitjans, Phys. Chem. Chem. Phys. **4**, 3246 (2002).

[31] A. Abragam, *The Principles of Nuclear Magnetism* (Clarendon, Oxford, 1961).

[32] S. Faske, H. Eckert, and M. Vogel, Phys. Rev. B **77**, 104301 (2008).

[33]M. Storek, R. Böhmer, S. W. Martin, D. Larink, and H. Eckert, J. Chem. Phys. **137**, 124507 (2012).
[34]M. Letellier, F. Chevallier, and F. Béguin, J. Phys. Chem. Solids **67**, 1228 (2006).
[35]P. Diehl, E. Fluck, H. Günther, R. Kosfeld, and J. Seelig, eds., *NMR—Basic Principles and Progress*, Vol. 30 (Springer, Berlin, 1994).
[36]D. Freude and J. Haase, in *NMR–Basic Principles and Progress*, edited by P. Barker and H. Pfeiffer, Vol. 29 (Springer, Berlin, 1993).
[37]P. Freiländer, P. Heitjans, H. Ackermann, B. Bader, G. Kiese, A. Schirmer, and H.-J. Stöckmann, Z. Naturforsch. A **41**, 109 (1986).
[38]G. Roth, K. Lüders, P. Pfluger, and H.-J. Güntherodt, Solid State Commun. **39**, 423 (1981).
[39]J. Conard and H. Estrade, Mat. Sci. Eng. **31**, 173 (1977).
[40]P. M. Richards, Solid State Commun. **25**, 1019 (1978).
[41]P. M. Richards, in *Topics in Current Physics*, edited by M. B. Salamon, Vol. 15 (Springer, Berlin, 1979).
[42]A. Avogadro and M. Villa, J. Chem. Phys. **66**, 2359 (1977).
[43]C. A. Sholl, J. Phys. C **14**, 447 (1981).
[44]W. Küchler, P. Heitjans, A. Payer, and R. Schöllhorn, Solid State Ion. **70/71**, 434 (1994).
[45]K. Toyoura, Y. Koyama, A. Kuwabara, F. Oba, and I. Tanaka, Phys. Rev. B **78**, 214303 (2008).
[46]H. Mehrer, *Diffusion in Solids* (Springer, Berlin, 2006).
[47]K. Persson, V. A. Sethuraman, L. J. Hardwick, Y. Hinuma, Y. S. Meng, A. van der Ven, V. Srinivasan, R. Kostecki, and G. Ceder, J. Phys. Chem. Lett. **1**, 1176 (2010).
[48]M. Park, X. Zhang, M. Chung, G. B. Less, and A. M. Sastry, J. Power Sources **195**, 7904 (2010).
[49]J. Jeener and P. Broekaert, Phys. Rev. **157**, 232 (1967).
[50]R. Böhmer, T. Jörg, F. Qi, and A. Titze, Chem. Phys. Lett. **316**, 419 (2000).
[51]F. Qi, T. Jörg, and R. Böhmer, Solid State Nucl. Magn. Res. **22**, 484 (2002).
[52]M. Wilkening, J. Heine, C. Lyness, A. R. Armstrong, and P. G. Bruce, Phys. Rev. B **80**, 064302 (2009).
[53]M. Wilkening, W. Küchler, and P. Heitjans, Phys. Rev. Lett. **97**, 065901 (2006).
[54]X.-P. Tang, R. Busch, W. L. Johnson, and Y. Wu, Phys. Rev. Lett. **81**, 5358 (1998).
[55]M. Lausch and H. W. Spiess, J. Magn. Reson. **54**, 466 (1983).
[56]H. W. Spiess, J. Chem. Phys. **72**, 6755 (1980).
[57]G. Fleischer and F. Fujara, in *NMR—Basic Principles and Progress*, edited by P. Diehl, E. Fluck, H. Günther, R. Kosfeld, and J. Seelig, Vol. 30 (Springer, Berlin, 1994).
[58]F. Fujara, S. Wefing, and H. Spiess, J. Chem. Phys. **84**, 4579 (1986).
[59]T. Dries, F. Fujara, M. Kiebel, E. Rössler,, and H. Silescu, J. Chem. Phys. **88**, 2139 (1988).
[60]M. Wilkening and P. Heitjans, Solid State Ion. **177**, 3031 (2006).

3.2 Ultraslow Li Ion Conductors

In many technical applications, *e.g.*, electrochemical systems such as fuel cells or secondary Li ion batteries, ion transport is the limiting, rate-determining factor for conversion and storage of energy. When working with doped materials, *e.g.*, in semiconductor systems, low, or rather no diffusivity of the guest species is advantageous. The same holds for blanket materials used in nuclear fusion technology, where a controlled mediation of tritium release is needed. For this purpose, lithium metalates such as Li_2TiO_3, Li_2ZrO_3 or Li_2SnO_3 are required due to their slow Li conductivity. So beside the need to advance in the field of materials exhibiting high Li mobility, as it is necessary for the application as solid-electrolytes, it is also of interest to understand the Li self-diffusion parameters in materials with low Li diffusivity. Lithium metalates such as $LiNbO_3$, $LiTaO_3$, Li_2TiO_3 or Li_2ZrO_3 are a few examples of interesting model systems that have been extensively studied via microscopic and macroscopic characterization techniques. In the next two contributions (**M2**, **M3**) Li diffusion is studied in Li_2SnO_3.

Another model system, single crystalline $LiAlO_2$, is studied in **P3** by means of electrical conductivity measurements and dynamic mechanical analysis (DMA). Li relaxation rates were derived from both techniques and directly converted into diffusion coefficients via the Einstein-Smoluchowski equation (*cf.* equation (2.9)). In the past, mechanical detection of ionic motion has been successfully applied to mixed-ion conducting glassy systems [22,108,109]. To our knowledge there are no reports on comparative studies of electrical and mechanical relaxation characterizing long-range Li ion motion in single crystalline Li ion conductors so far.

3.2.1 Li^+ Exchange and Long-range Dynamics in Li_2SnO_3

In the first part **M2**, we take a closer look at local Li environments and Li exchange pathways between the *three* crystallographically distinct sites. Despite the simple, monoclinic-type structure composed of alternating Li and $LiSn_2$ layers, we found a rather complex and interesting diffusion behavior which can be described to be of heterogeneous nature due to the defect structure induced by the mechanochemical synthesis procedure. Slow Li exchange was investigated via 2D EXSY NMR (*cf.* section 2.3.2) The appearance of off-diagonal intensities indicates chemical exchange between the respective sites during a certain mixing time t_m. If this experiment is recorded at various mixing times, site-specific jump rates can be determined. Since the pioneering work of Xu *et al.* [72] on diamagnetic Li_4SiO_4, most 2D EXSY studies focused on *paramagnetic* Li ion conductors. In the case of paramagnetic materials we find short spin-lattice relaxation times and large hyperfine shifts due to Fermi contact interaction; which is why 1D

and 2D MAS experiments are much easier to carry out. The distinct Li positions can therefore be more easily resolved than in *diamagnetic* structures like Li_2SnO_3. Still, we were able to resolve three distinct Li sites within a spectral range of 1 ppm via variable-temperature ^{6}Li MAS NMR and quantify exchange rates via the application of the selective 1D inversion NMR technique. Together with the 2D EXSY NMR experiments, the results point towards a preferred Li hopping perpendicular to the *ab*-plane, which is governed by the vacancy distribution in the $LiSn_2$-layer. Studies such as the one presented in here are very rare.

In the second paper manuscript **M3**, we studied the elementary steps of slow Li self-diffusion on an extended hopping timescale down to the Hz range, taking advantage of NMR spin-lattice relaxation measurements in the laboratory and rotating frame of reference along with SAE NMR. Damping of the echo amplitude is mediated by slow Li jump processes. In contrast to conventional SLR techniques, SAE provides direct access to hopping rates as the echo decay rate $1/\tau_{SAE}$ corresponds to the correlation rate, *i.e.* the mean Li jump rate of one Li atom. Only with the help of this technique a self-diffusion coefficient in the order of 10^{-20} m^2s^{-1} can be accessed for ultra-slow ionic motion at room temperature. Activation energy and jump rates deduced from SAE corroborate the SLR measurements. In contrast to long-range dynamics probed by SAE, SLR measurements are sensitive only to short-range motion. A good agreement between the values for dynamical parameters points to similar diffusion mechanisms on a microscopic and macroscopic length scale. Furthermore, a strong dependence of τ_{SAE} on the echo evolution time underlines the heterogeneous dynamics, which was also found in the previously presented ^{6}Li MAS NMR experiments. Overall both studies draw a comprehensive picture of complex, heterogeneous dynamics with preferred diffusion pathways. However, all the geometrically different pathways exhibit similar activation energies for Li diffusion.

M2: (pp. 85–111)

An unexpected pathway — ^{6}Li exchange NMR points to vacancy-driven out-of-plane Li ion hopping in crystalline Li_2SnO_3

J. Langer, D. L. Smiley, A. D. Bain, G. R. Goward and M. Wilkening

An unexpected pathway — ^{6}Li exchange NMR points to vacancy-driven out-of-plane Li ion hopping in crystalline Li_2SnO_3

J. Langer*,†, D. L. Smiley‡, A. D. Bain‡, G. R. Goward‡, M. Wilkening†

† Institute for Chemistry and Technology of Materials (NAWI Graz) Graz University of Technology, 8010 Graz, Austria;
DFG Research Unit 1277, Graz University of Technology, 8010 Graz, Austria

‡ Department of Chemistry and Chemical Biology, McMaster University, Hamilton, Ontario L8S 4M1, Canada

Abstract

The development and engineering of new materials for modern electrochemical energy storage systems requires an in-depth understanding of Li ion dynamics, not only on the macroscopic length scale, but also from an atomic-scale point of view. Hence, the study of suitable model systems is indispensable if we want to understand the complexity of non-model systems already applied, *e.g.*, as active materials in rechargeable batteries. Here, Li_2SnO_3 served as such a model system to enlighten the elementary steps of ion hopping between the three magnetically distinct Li sites. Via high-resolution 1D and 2D NMR we were able to probe the favored exchange pathway. Both 1D and 2D NMR point to non-uniform ion dynamics and two independent exchange processes perpendicular to the *ab*-plane, *viz*. between the sites 4*e* (Li(3)) and 8*f* (Li(1)) as well as 4*e* and 4*d* (Li(2)). ^{6}Li selective inversion NMR confirmed extremely slow Li exchange and yielded hopping rates in the order of 3 s^{-1} for 4*e*-8*f*, and 0.7 s^{-1} for 4*e*-4*d*. Altogether, the findings give evidence for a 3-site, 2-exchange model describing Li hopping along the c-axis rather than in the Li-rich *ab*-plane as one would expect at first glance. This unexpected result can, however, be understood when the site preference of Li vacancies is considered. Recent theoretical calculations have predicted the preferred for-

mation of Li vacancies at the Li(3) sites. This allows for localized Li ion exchange involving Li(3); thus, perfectly corroborating the present findings by ^{6}Li MAS NMR.

keywords: solid-state NMR, oxides, diffusion mechanisms, Li migration pathways, slow motions

1. Introduction

The study of Li ion dynamics is of fundamental interest in the various sub-disciplines of materials research. Besides hydrogen, Li^+ is the lightest and, thus, most mobile cation. Fast Li ion conductors are of particular interest in Li-based energy storage systems such as rechargeable Li ion batteries, solid-state lithium batteries as well as lithium-oxygen or lithium-sulfur batteries.[1–6] On the other hand, slow ion conductors are needed, for example, in semiconductor or nuclear fusion research where Li metalates, such as Li_2TiO_3, Li_2ZrO_3 or Li_2SnO_3, serve as promising candidates to realize suitable blanket materials:[7,8] Li is involved in the conversion of neutrons and tritium breeding as the tritium effusion rate is linked to Li ion diffusion.[9]

From a fundamental point of view it is necessary to gain a profound picture of the underlying Li ion exchange mechanism in order to purposefully develop new Li ion conductors.[5,10–12] Understanding diffusion dynamics requires not only to study macroscopic properties but also to reveal what is behind long range ion transport, *i.e.*, to identify the key elementary steps of Li^+ hopping.[12–15] In ideal cases they can be probed in great detail by nuclear magnetic resonance (NMR) spectroscopy which offers a large portfolio of techniques being able to measure (bulk) jump rates covering a broad time and length scale.[10,15–21]

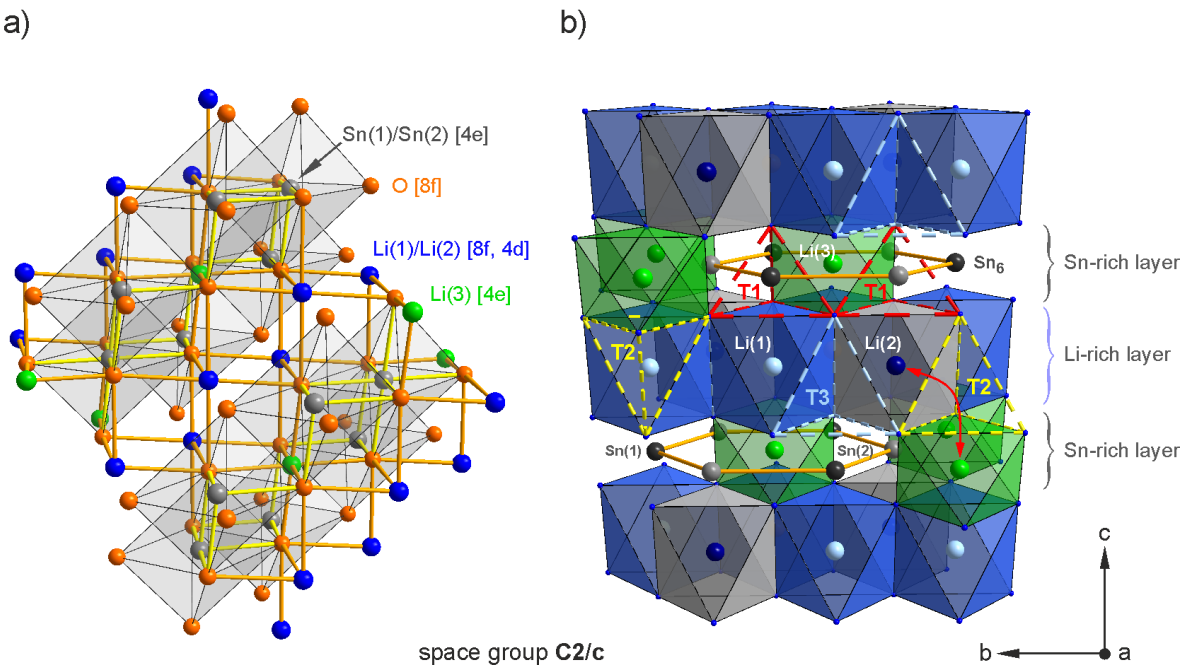

Figure 1. a) Crystal structure of monoclinic Li_2SnO_3 (C2/c). In b) the three distinct Li sites and the two magnetically inequivalent Sn sites are highlighted. Pure Li layers constituted by Li(1) on 8*f* and Li(2) on 4*d* sites alternate with $LiSn_2$ layers, where Li(3), along with Sn(1) and Sn(2) ions are located on 4*e*. Li and Sn atoms are octahedrally coordinated by oxygen (*cf.* a) and b)). The LiO_6-polyhedra share common edges and build a 3D network for Li^+ self-diffusion. Li ions may hop between the regularly occupied positions via the empty tetrahedral sites T1, T2, and T3 (see b)); see text for further discussion of the possible Li hopping pathways that differ because of the size of the tetrahedral sites and the repulsive interactions with neighboring SnO_6 octahedra.

In particular, the study of diffusion mechanisms also includes the investigation of extremely slow ion dynamics via exchange spectroscopy and stimulated echo NMR, for instance.[10,12,22] Considering recent studies on this topic, Li ion dynamics has already been studied for Li_2TiO_3 and Li_2ZrO_3 via both ^6Li and ^7Li NMR as well as broadband conductivity spectroscopy (CS).[23–27] These materials are structurally similar to Li_2SnO_3 as they all crystallize in the same monoclinic space group C2/c, *i.e.*, in a pseudo NaCl-type lattice (see Fig. 1).[28,29] In Li_2ZrO_3 there are two

crystallographic inequivalent Li positions while the β-modification of Li_2TiO_3 shows three distinct Li sites; the same is true for Li_2SnO_3. So far, the corresponding three Li NMR lines have not been resolved by NMR. In a recent study by Salager *et al.* focusing on $Li_2Ru_{1-y}SnyO_3$-type positive electrode materials, the ^{7}Li MAS NMR spectrum of the end member Li_2SnO_3, which was recorded at 17.6 T, showed two sharp signals with relative intensities of 28 % and 72 %; the latter was anticipated to be composed of two NMR lines with very similar chemical shifts.[30]

The Li jump rates measured for the analogous compounds Li_2ZrO_3 and the Li_2TiO_3 are very low; values are in the order of 60 jumps per hour for the metazirconate[27] (310 K), and amount to be approximately 60 jumps per second for the metatitanate[24] (350 K). Li ion exchange in Li_2TiO_3 is anticipated to occur in the *ab*-plane and along the *c*-axis, provided suitable nearby vacancies are available.[23,24] Slow, long-range Li diffusion processes were investigated by Ruprecht *et al.* via CS and ^{7}Li spin-alignment echo NMR; depending on the length scale used to acquire the data activation energies of ca. 0.8 eV and 0.47 eV, respectively, were obtained.[23]

Despite of the prior investigations on lithium metalates, there is, so far, no detailed picture of Li ion motion or of the preferred Li^+ diffusion pathways in Li_2SnO_3. Site-specific Li^+ hopping can be made visible via 1D and 2D ^{6}Li MAS NMR exchange spectroscopy (EXSY).[31–35] In order to obtain quantitative results regarding exchange rates and local energy barriers this often results in extremely time-consuming measurements lasting many days or even weeks. In particular, this is the case when diamagnetic materials with very long longitudinal NMR relaxation rates have to be studied.[27] Therefore, as an alternative, 1D selective inversion NMR provides a more time-saving means to collect information on Li ion exchange processes.[36–38] Here, in combination with 1D and 2D ^{6}Li NMR experiments this greatly helped us getting to the bottom of ion dynamics in polycrystalline Li_2SnO_3. By using MAS NMR at fast spinning speeds we were able to resolve the three magnetically inequivalent sites in the oxide, and, in the absence of Li motion, to accurately determine the individual site occupancies. Our 2D MAS EXSY NMR experiments shed light on the nature of the relevant (local) Li ion exchange

processes; the data obtained provides a valuable basis for the more complete analysis via 1D (shaped-pulse) selective inversion NMR, which is presented in the last section of this study.

2. Experimental

Sample preparation and characterization

Li_2SnO_3 was prepared by mechanochemical treatment of stoichiometric amounts of SnO_2 and Li_2CO_3 via a conventional solid state reaction route[39]. In a first step the powders were ground at 600 rpm for 15 hours in a high-energy planetary ball mill (Fritsch Pulverisette 7, premium line). The mixture was then calcined at 1073 K for six hours. Afterwards the powder was pressed into pellets and then sintered for 12 h at 1273 K in air, yielding transparent crystallites. Phase analysis of the powder via X-ray diffraction (XRD) was carried out on a Bruker D8 Advance diffractometer with Bragg-Brentano geometry using Cu K_α radiation.

1D NMR / 2D EXSY NMR

Variable-temperature ^{6}Li 1D as well as 2D MAS NMR spectra were recorded on an Avance III solid-state NMR 500-MHz spectrometer connected to a cryomagnet with a nominal field of 11.7 T; that corresponds to a ^{6}Li resonance frequency of ν_0 = 74 MHz. A standard Bruker 2.5 mm H/X probe was used; the rotation frequency was 30 kHz. Cooling of the sample was achieved via evaporating liquid nitrogen by means of a heat exchange coil. The 1D NMR spectra were recorded in a single-pulse excitation experiment; they were referenced to solid lithium acetate ($\delta = -0.1$ ppm) serving as secondary reference. The primary reference was an 1M aqueous solution of lithium chloride (δ = 0 ppm). Typically, a solid pulse of 3.2 µs length and recycle delays between 360 s and 3600 s were used to ensure full longitudinal relaxation. In all experiments temperatures were calibrated using the ^{79}Br resonance in KBr as a chemical shift thermometer.[40]

^{119}Sn spectra were acquired at room temperature using a high-performance Bruker Avance II 900-MHz spectrometer with a nominal field of 21.1 T (ν_0 = 336 MHz). The 1D MAS spectra

recorded at ultra-high magnetic field were acquired in a one-pulse experiment employing a pulse length of 3 μs and a recycle delay of 60 s. Experiments were carried out at various spinning rates, *viz*. 0 kHz, 3 kHz, 5 kHz, 10 kHz, 20 kHz and 30 kHz; the corresponding spectra were referenced to solid $SrSnO_3$, which resonates at − 640 ppm.[41] The spinning sideband manifolds were analyzed with the DMFit software[42] in order to determine chemical shift anisotropy (CSA) parameters.

A NOESY pulse sequence was employed to record the ^{6}Li 2D NMR spectra at mixing times (t_m) of 0.1 and 1 s. The sample was spun at an MAS speed of 30 kHz using ambient bearing gas. For the spectrum with t_m = 1s we employed time domains (TD) of 128 data points (dp) in the F1 direction and 1024 points in the F2 direction. The 2D NMR spectrum at t_m = 0.1s was recorded with TD(F1) = 32 dp, and TD(F2) = 512 dp. Acquisition of the spectra was performed in both experiments using dwell times of 250 μs, a recycle delay of 120 s, and 32 scans. Since the NMR spin-lattice relaxation time T_1 is much larger than the time period determined by t_m, that is, $T_1 \gg \tau$, a saturation comb, consisting of up to 16 closely spaced 90° pulses, was used allowing relaxation delays shorter than $5 \times T_1$.

1D selective inversion NMR

One-dimensional selective inversion experiments under MAS conditions were also performed on a Bruker Avance III spectrometer operating at a ^{6}Li Larmor frequency of 74 MHz; the rotational speed was 30 kHz. A Bruker 2.5 mm triple resonance probe was used in all experiments. Cooling of the sample was achieved via fresh evaporation of liquid nitrogen using a heat exchange coil. The 1D NMR spectra were obtained using a one-pulse experiment with a (90°) solid pulse of 5 μs and recycle delays ranging from 160 s to 300 s; the spectra were referenced to a solution of 1M ^{6}Li-enriched LiCl (δ = 0 ppm). ^{6}Li NMR selective inversion recovery spectra were acquired using a 180° – τ_{mix} – 90° sequence, where a long, soft 180° Gaussian-shaped pulse[43] was 25 ms in length with a soft pulse power of 0.0154 W. The mixing time τ_{mix} was varied across a series of experiments; it was chosen to range from 0.05 μs to 100 s. A hard 5

µs pulse was used to acquire the final signal. Temperatures were calibrated with $Sm_2Sn_2O_7$ as described elsewhere.[44] Deconvolution and integration of the pseudo-2D data sets was done with a Mathematica notebook developed by D. Brouwer (Redeemer University, Canada). Each integral was normalized to the integration value of the slice collected at the longest mixing time for the inverted site. The data was analyzed using the CIFIT program developed by A. D. Bain.[45] The program uses the observed areas for all sites in the NMR spectrum as a function of mixing time in order to determine a set of parameters: lithium ion jump rates (k), the spin–lattice relaxation times (T_1) in the absence of chemical exchange, as well as the difference in magnetization between initial ($M_i(0)$) and equilibrium ($M_i(\infty)$) conditions. CIFIT utilizes a rate matrix that describes the relaxation of spins under the influence of chemical exchange, as described in greater detail elsewhere.[45,46] The program adjusts the free parameters using a Levenberg–Marquardt algorithm until the sum of the squares of the differences between the experimental and calculated data is minimized.

3. Results and Discussion

Structural characterization via XRD and ^{6}Li NMR

According to the structure refinement of Hodeau and Marezio[29] Li_2SnO_3 crystallizes with distorted NaCl-type structure having monoclinic symmetry (C2/c). Oxygen forms a distorted cubic close-packed network where fully occupied Li layers with Li(1) and Li(2) in 8*f* and 4*d* position alternate with $LiSn_2$ layers. In these layers the Li ions Li(3) and the two crystallograhically inequivalent Sn ions, Sn(1) and Sn(2), share the octahedral 4*e* position (see Fig. 1). It is known that the layers can show complex stacking disorders along the *c*-axis.[28,29,47] At temperatures being equal or higher than 1273 K a high-*T* (HT) phase of Li_2SnO_3 forms. The corresponding XRD powder pattern is used as a reference which is compared with our sample in Fig. 2. Since we observed additional line broadening of the XRD reflections we cannot rule out some stacking faults along the *c*-axis.[47]

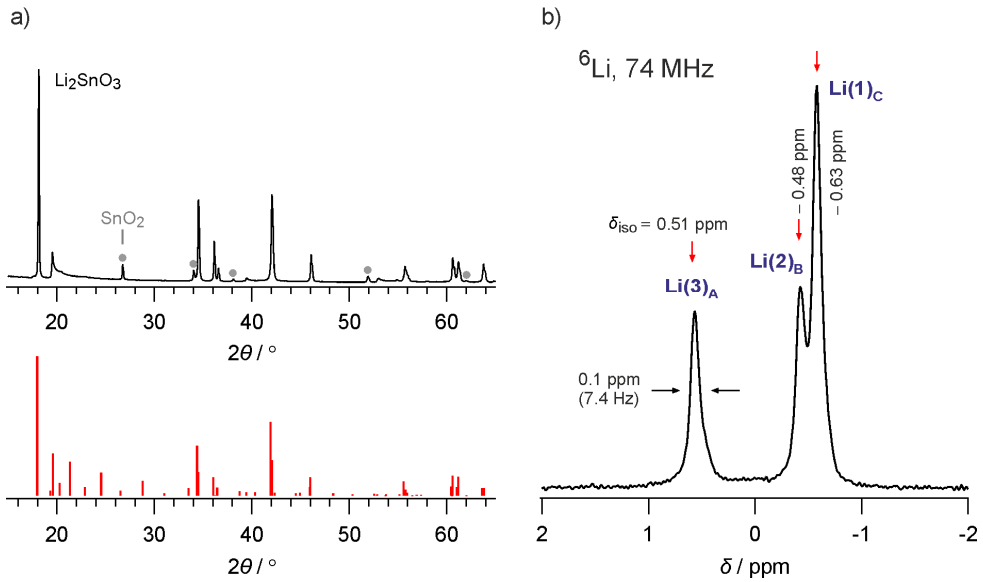

Figure 2.: a) XRD powder pattern of Li_2SnO_3 after annealing at 1273 K (shown in black). Reflections marked with triangles can be assigned to a small amount of (Li-free) SnO_2. The Li_2SnO_3-reference (ICSD-35235) is shown in red. b) the corresponding ^{6}Li MAS NMR spectrum (B_0 = 11.7 T); in order to avoid the effect of Li exchange on the three lines observed it was recorded at sufficiently low T , *i.e.*, at 285 K.

According to the crystal structure of Li_2SnO_3 there should be two slightly different crystallographic positions for Sn (*cf.* Fig. 1); the two Sn ions share the 4*e* position but differ in lattice parameters *y/b* and *z/c*, respectively. Even by the use of high-field ^{119}Sn MAS NMR at 21.1 T we were, however, not able to resolve the two lines. Instead a single resonance, as can be seen in Fig. 3, is seen even if we raise the spinning frequency up to 30 kHz. Nevertheless by recording ^{119}Sn NMR spectra at various spinning speeds we were able to gain information on the (average) local tin environment, which is reflected by simulating the isotropic chemical shift δ_{iso}, the anisotropy η_{CS} and axiality Δ, the "reduced anisotropy", of the chemical shift anisotropy (CSA) tensor. The latter is defined by the relation $\Delta = \delta_{zz} - \delta_{iso}$. The anisotropy parameter indicates by how much the line shape deviates from that of an axially symmetric tensor. In Fig. 3

our static ^{119}Sn NMR spectrum is characterized by η_{CS} = 0.36; Δ lies between 44.7 and 47.5 ppm. The ^{119}Sn NMR spectra recorded at high spinning speeds point to δ_{iso} = – 445 ppm.

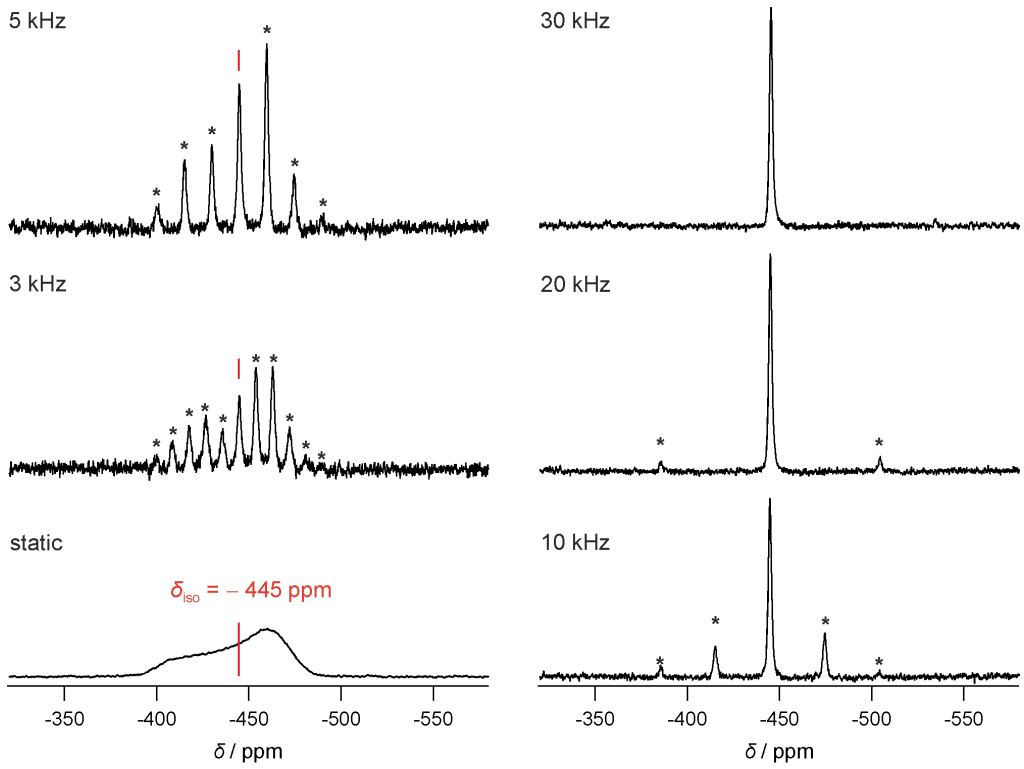

Figure 3. ^{119}Sn NMR spectra (ν_0 = 336 MHz) of HT-Li_2SnO_3 recorded at different MAS frequencies (3 – 30 kHz) and an ultra-high magnetic field B_0 of 21.1 T. Asterisks denote spinning sidebands. For comparison, the static NMR spectrum is also shown.

Variable-temperature 1D ^{6}Li MAS NMR spectra

The structure of Li_2SnO_3 provides three crystallographically and, thus, magnetically inequivalent Li sites, which are each characterized by site-specific NMR chemical shift values. The ran-

dom distribution of Li and Sn cations might lead to a distribution of chemical shifts according to the small variations of local structures.

All three Li sites have an octahedral coordination where $Li(1)O_6$ and $Li(2)O_6$, being connected by sharing common edges (see Fig. 1), have very similar nearest-neighbor distances. Therefore, they are expected to exhibit very similar ^{6}Li NMR chemical shifts. Indeed, the 1D ^{6}Li MAS NMR spectrum recorded at 11.7 T and sufficiently low *T* (see Figs. 2 and 4) is composed of three well-resolved lines labeled as $Li(3)_A$, $Li(2)_B$ and $Li(1)_C$. In earlier studies it was not possible to resolve three NMR lines corresponding to the different Li environments.[30] In accordance with a CASTEP simulation of chemical shift parameters, signal $Li(3)_A$ (0.51 ppm, 285 K) is assigned to Li(3), while the crystallograhically more similar sites Li(2) and Li(1) appear at chemical shift values of − 0.48 and − 0.63 ppm (285 K). In Li_2SnO_3 with ideal stoichiometry Li(1) constitutes 50% of the total number of Li ions present, and 25% are distributed each among the Li(2) and Li(3) sites. In fact, at 285 K, the ratio of the corresponding areas is 0.93 : 0.96 : 2, which is in very good agreement with the distribution expected. As can be easily shown by static, variable-temperature ^{7}Li NMR line shape studies, at 285 K, which characterizes the rigid-lattice regime, Li ion diffusivity is extremely slow.[48] At such low temperatures the average Li^+ jump rate is much lower than the spectral separation of the NMR lines $Li(3)_A$ and $Li(1)_C$. For that reason the ^{6}Li MAS NMR spectrum is unaffected by any Li ion exchange processes meaning that the areas under the lines are expected to approximately reflect the population of the three distinct Li sites.

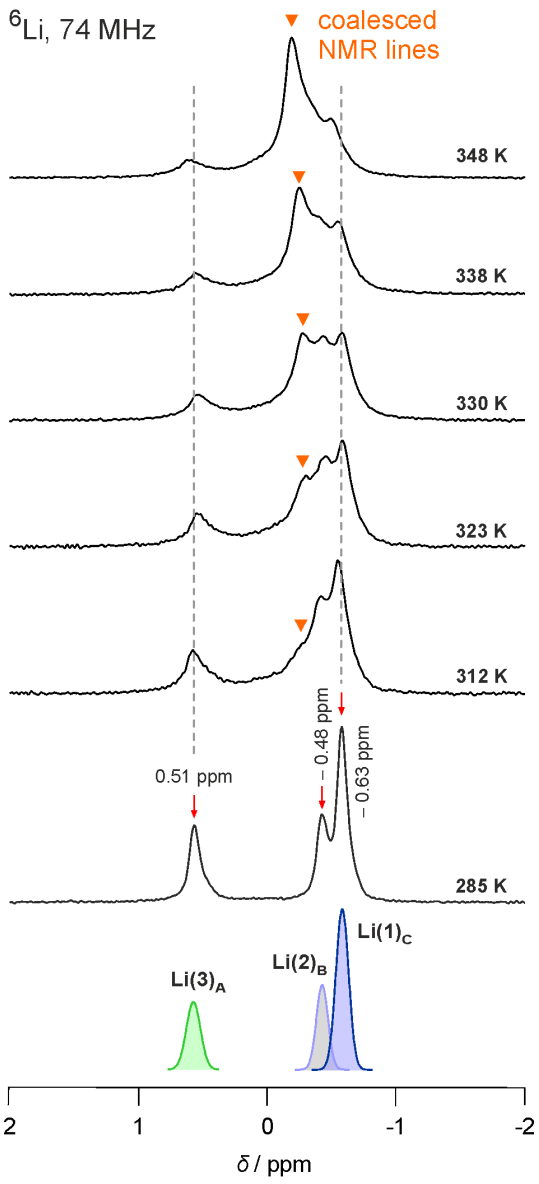

Figure 4. Evolution of the ^{6}Li MAS NMR spectra (ν_0 = 74 MHz) of Li_2SnO_3 with increasing temperature. Areas of the NMR lines Li(3)$_A$, Li(2)$_B$, Li(1)$_C$ corresponding to the spectrum recorded at 285 K are illustrated at the bottom. The triangles indicate the effect of coalescence due to Li(3)-Li(1) exchange. See text for further discussion.

At T = 312 K a "shoulder" emerges in the 1D ^{6}Li NMR spectrum that is located at ca. – 0.2 ppm; it significantly gains in intensity when temperature is increased to 348 K. Simultaneously, the intensities of lines $Li(3)_A$ and $Li(1)_C$ decrease considerably. Importantly, signal $Li(2)_B$ remains almost affected by any coalescence as compared to the lines assigned to Li(1) and Li(3). This points towards enhanced Li ion exchange between the Li(1) and Li(3) sites. Li(1)-Li(3) exchange means that local Li ion hopping perpendicular to the *ab*-plane is more frequently as compared to jumping between the sites Li(1) and Li(2) (see Fig. 1). Because the spectral separation of the lines Li(1) and Li(3) is ca. 84 Hz, we estimate that the corresponding hopping rate of the Li(1)-Li(3) exchange is in the same order of magnitude. On the other hand, the Li(2) ions seem to be less involved in Li^+ self-diffusivity, at least if we consider the regime of slow ion dynamics.

At this stage, any exchange processes between Li(1) and Li(2), as well as Li(2) and Li(3), cannot be excluded. The 1D NMR data, however, give evidence that ion hopping between Li(1) and Li(3) is energetically favored. This is an unexpected result since Li(1) is located in the Li-rich layer and Li(3) is the site which is sixfold coordinated by Sn in the Li-Sn layer. Before we will discuss the relevant hopping pathways that connect the three Li sites via the various tetrahedral voids in Li_2SnO_3 (see Fig. 1), we should take a closer look at the evolution of the 1D spectra with temperature, *i.e.*, the coalescence of the NMR lines.

The position of the line affected by coalescence is directly linked to the occupancies of the sites involved. As the population of Li(1) is double of Li(2) and Li(3) it is shifted towards signal $Li(1)_C$, *i.e.*, negative ppm values. The shift of the resulting line assuming full coalescence can be calculated according to: $\delta_{coal} = f_1 \cdot \delta_1 + f_2 \cdot \delta_2 + f_3 \cdot \delta_3$ with $f_{1,2,3}$ representing the individual (normalized) populations ($f_1 + f_2 + f_3 = 1$) and $\delta_{1,2,3}$ the corresponding site-specific chemical shifts unaffected by any exchange processes. Fast exchange between all three sites would result in $\delta_{coal} = -0.31$ ppm. In our 1D spectrum we find $\delta_{coal,\,exp} = -0.19$ ppm (348 K). This value would be in good agreement with a calculated value of $\delta_{coal} = -0.15$ ppm which is obtained if we assume Li ion exchange mainly between Li(1) and Li(3).

Interestingly, the resonance lines do not fully coalesce even if the temperature is raised to

348 K. The fact that coalescence of the NMR lines covers a broad temperature range might be interpreted as heterogeneous Li ion dynamics in Li_2SnO_3, controlled by the low number density of vacant Li sites present. For some of the Li ions a spatially heterogeneous distribution of Li vacancies might result in a limited capability to jump between next neighboring sites; efficient exchange is only possible in those regions with a sufficiently large number of vacancies accumulated. As will be discussed below, recent calculations have shown that Li vacancies will form preferably on the Li(3) sites. This preference is expected to make out the main hopping exchange process (see below).

In the extreme a heterogeneous ion dynamics might be due to a clustering effect of vacancies. Such a behavior could stem from the mechanochemical synthesis procedure where the high mechanical impact forces lead to defect-rich structures.[49–52] Even if annealed at high temperatures, at which defects are usually cured, such regions might leave its fingerprints – although much less pronounced – in the crystalline product obtained finally. Slight deviations from ideal stoichiometry could greatly influence the dynamic parameters.

Partial and very slow Li diffusion was also deduced from results of a combined ^{6}Li and ^{7}Li NMR study on isostructural Li_2TiO_3.[24] Heterogeneous ion dynamics was attributed to a slight deviation in Li stoichiometry sensitively influencing the vacancy concentration. Worth mentioning, molecular dynamics (MD) simulations have shown that diffusion in both the *ab*-plane and along the *c*-axis is equally probable in Li_2TiO_3, the exact diffusion properties, however, depend on the location of any Li vacancies formed.[24]

For the sake of completeness, we could definitely rule out the possibility of structural rearrangements, *e.g.*, polyhedra distortion or formation of new, even amorphous, phases during our NMR measurements that have been restricted to temperatures well below 400 K. *In-situ* XRD data shows no evidence of any reversible or irreversible structural transformation occurring in this temperature range.[48]

2D ^{6}Li EXSY NMR

In order to refine the picture seen via 1D MAS NMR, we used 2D EXSY NMR to visualize Li exchange in contour plots. 2D EXSY NMR is perfectly suited to directly study exchange processes via the analysis of cross-signals (off-diagonal) intensities. Off-diagonal intensities in the corresponding contour plots result when jumps between magnetically inequivalent sites occur during the mixing time t_m chosen. In perfect agreement with our ^{6}Li 1D NMR spectra Li exchange between $Li(3)_A$ and $Li(1)_C$ is clearly seen already at a short mixing time of only 100 µs. In addition to ^{6}Li NMR, we were able to reveal further cross-peak intensities indicating a second site exchange process between $Li(3)_A$ and $Li(2)_B$. The corresponding signal is even more pronounced when a mixing time of 1 s was applied. This definitely proves that the exchange rate associated is much lower. Since the signals $Li(2)_B$ and $Li(1)_C$ are close to each other on the ppm scale ($\delta_2 = -0.48$ ppm, $\delta_1 = -0.63$ ppm,), signal overlapping masks Li ion exchange between the neighboring Li(2) and Li(1) sites in the Li-rich layer. The fact that no coalescence of lines $Li(2)_B$ and $Li(1)_C$ is seen points to a very slow diffusion process as compared to Li(3)-Li(1) and Li(3)-Li(2), respectively. In summary, 2D EXSY nicely corroborates the findings from 1D NMR; furthermore, it definitely refines the picture derived from the line shape analyses by revealing that overall coalescence is due to two individual two-site hopping processes whereby the Li(3)-Li(1) exchange is faster than that describing hopping between Li(3) and Li(2).

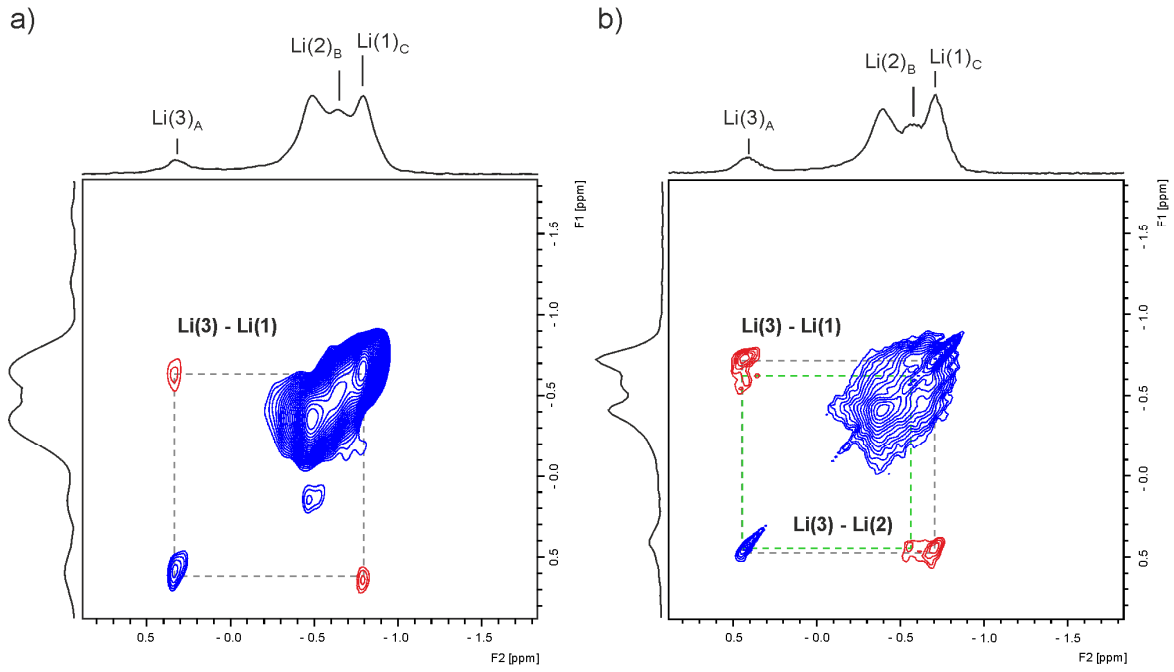

Figure 5. 2D ^{6}Li NMR exchange spectra (ν_0 = 74 MHz, T = 323 K) recorded at two different mixing times t_m: a) 0.1 s and b) 1 s. Off-diagonal cross-signals (in red) indicate Li ion hopping perpendicular to the *ab*-plane in Li_2SnO_3. In-plane exchange via Li(1) and Li(2) is hardly seen because of the small spectra distance of the corresponding NMR lines which is only 0.15 ppm (11 Hz) at 285 K, see Fig. 2.

The site-preferences of local Li ion hopping, as derived from 2D EXSY NMR, might be understood by considering the crystal structure and local environment of the three Li sites: exchange between filled and vacant sites is possible through several tetrahedral sites, labeled as T1, T2, and T3 in Fig. 1. The tetrahedra, which differ in size and the number of Sn atoms in their direct neighborhood, connect the LiO_6-octahedra by face sharing. While Li(1)-Li(2) exchange is possible via T3; Li(1) (and Li(2)) ions can reach the Li(3) position via T1 and T2. To understand the Li(1)-Li(3) exchange probed in the present study, either Li(1) or Li(3) should offer an increased probability to accommodate Li vacancies. Indeed, recent calculations by Brant *et al.* have shown that it is energetically favorable to create vacancies at the 4*e* (Li(3)) sites compared with the formation at the 8*f* (Li(1)) or 4*d* (Li(2)) sites by 0.1 eV.[53] These findings

perfectly agree with the Li deficiency, 0.93 instead of 1, found for the Li(3) and Li(2) sites as reflected by the ratio of the corresponding areas in the 1D NMR spectrum recorded at 285 K (see above). Thus, if we assume a vacant Li(3) site in the honeycomb $[SnO_3]^{2-}$ layer, we have to look for a possible Li jump pathway connecting the sites Li(3) and Li(1). Li(1) can leave its position via T2, then entering the $Li(3)O_6$ octahedron perpendicular to the plane defined by the Sn_6 hexagon while passing the face F2 with an area of 4.05 $Å^2$ (see Fig. 6 and the red arrow shown in Fig. 1).

T2 is rather symmetric with relatively long O-O distances ranging from 3.06 Å to 3.34 Å. Each empty Li(3) position can be reached via two T2 tetrahedra. Alternatively, Li(1) may use the T1 tetrahedron as another pathway to reach Li(3) via the face F1 (Fig. 6). T1 as well as F1 (3.51 $Å^2$) are, however, smaller; the O-O distances of T1 range from 2.73 to 3.06 Å. Additionally, T1 shares two faces with SnO_6 octahedra (Fig. 6). Thus, repulsive Li-Sn interactions make this an energetically unfavorable pathway. For Li(2) the same T2-pathway exists; thus, from simple geometric considerations the Li(1)-Li(3) as well as Li(2)-Li(3) exchange via T2 seems to represent the most probable local exchange pathways. Li ion exchange is, however, driven by the existence of Li(3) vacancies in the Sn-rich layer. Assuming Li(3) vacancies is in line with the NMR results from our 1D and 2D experiments. As has been pointed out by Brant *et al.* the preference to form vacancies at the 4e sites changes when going from the oxide to the sulfide, Li_2SnS_3. In Li_2SnS_3 vacancies at 8*f* and 4*d* are more stable by – 0.3 eV.[53]

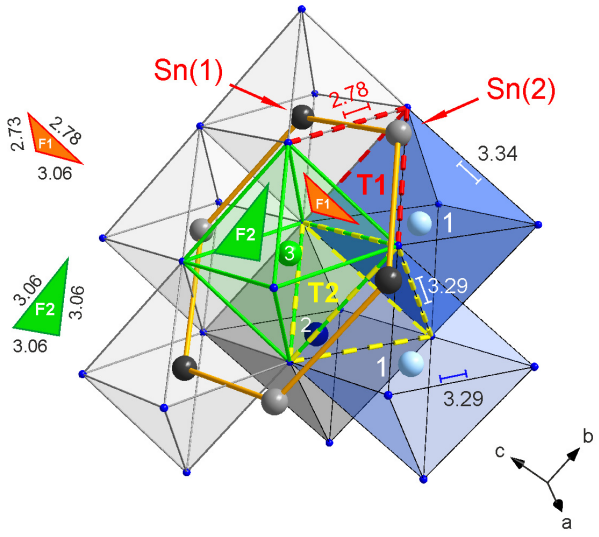

Figure 6. Li ion jump pathways connecting the Li(3) site with the sites Li(1) and Li(2) via empty tetrahedral voids in Li_2SnO_3. Values given denote oxygen-oxygen distances in angstrom. Li(1) and Li(2) may reach the vacant Li(3) site via T2 and T1. The T2 tetrahedron is larger than T1. At the same time it is less influenced by repulsive interactions with neighboring SnO_6 octahedra which share common faces with T1.

Obviously, in Li_2SnO_3 the position Li(3) is prone to accommodate Li vacancies resulting in Li exchange perpendicular to the *ab*-plane while in-plane Li(2)-Li(3) exchange is much less frequent. This observation is at least valid for the regime of ultraslow Li hopping, *i.e.*, temperatures below 330 K.

1D selective inversion ^{6}Li MAS NMR

Slow chemical exchange processes, relative to (longitudinal) spin-lattice relaxation, can also be studied with the help of 1D selective inversion MAS NMR spectroscopy.[36–38,54] Via selective inversion measurements we tried to quantify the Li(1)-Li(3) and Li(2)-Li(3) exchange made visible through 2D EXSY NMR. Following the selective inversion of the magnetization of the Li

spins at a particular site, the return to the condition of thermal equilibrium is monitored as a function of a variable delay time. Signal recovery is governed by *(i)* the ion exchange rate with the non-inverted spins as well as *(ii)* by inherent spin-lattice relaxation governed by the rate $1/T_1$. The magnetization buildup changes as a function of temperature and, thus, provides a mean to determine ion hopping rates and activation energies. Additionally, $1/T_1$ rates are measured independently and are included in the fitting procedure.

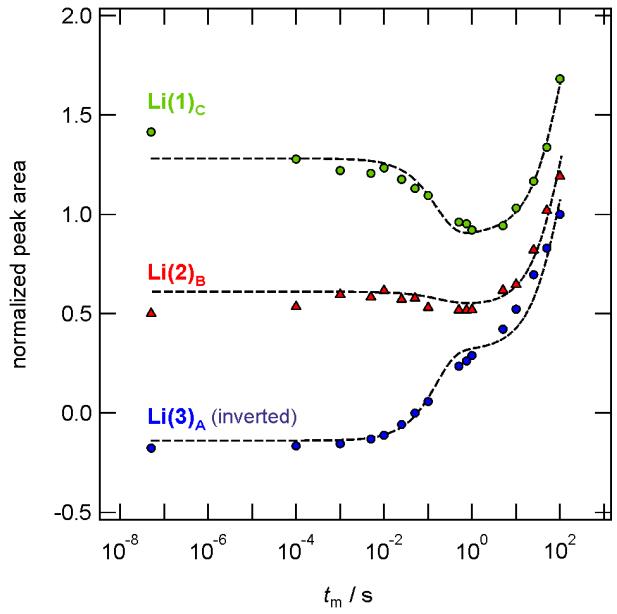

Figure 7. Results from 1D selective inversion ^{6}Li MAS NMR (ν_0 = 74 MHz): transient curves of the inverted ($Li(3)_A$) and non-inverted sites ($Li(2)_B$ and $Li(1)_C$) following a selective inversion of resonance $Li(3)_A$ at 285 K. For reasons of better visibility the *x*-coordinate is plotted in logarithmic scale. The solid lines show the results of the fitting procedure using the CIFIT program.

In our present study we look at two individual Li jump processes between three sites using the CIFIT program[45,46] to analyze the experimental ^{6}Li NMR data. While signal $Li(3)_A$ can be selectively inverted with a long, soft Gaussian-shaped pulse, the lines $Li(2)_B$ and $Li(1)_C$ cannot be inverted individually. The two lines are separated by only 0.15 ppm which leads to signifi-

cant overlapping of the resonances. Upon inversion of site $Li(3)_A$ the transient magnetizations of sites $Li(2)_B$ and $Li(1)_C$ are plotted in Fig. 7. The curves are used to extract the $Li(3)_A$-$Li(2)_B$ and $Li(3)_A$-$Li(1)_C$ rate constants. Importantly, the depth of the transient well increases when exchange with the inverted site becomes more rapid before any ^{6}Li NMR spin-lattice relaxation processes take over. In order to better visualize the data we have plotted the time axis of Fig. 7 in logarithmic scale. The magnetization buildup curve of signal $Li(3)_A$ clearly shows that the return to equilibrium is governed by longitudinal relaxation. For transient $Li(1)_C$ we find a pronounced attenuation of the magnetization which is due to ion hopping between the sites $Li(3)_A$ and $Li(1)_C$. Interestingly, for $Li(2)_B$ we can only observe a small change of the magnetization transient indicating slower cation exchange between the sites $Li(3)_A$ and $Li(2)_B$. Note that at 285 K no coalescence of the three NMR lines is observed (see above) and the inversion of signal $Li(3)_A$ is experimentally reasonable. With increasing *T*, however, coalescence effects make it difficult to precisely monitor the areas under the resonances as a function of mixing time t_m. Hence, we are limited to a quite narrow temperature range which does not allow for reliable *T*-dependent measurements to extract an activation energy. These are much better accessible via time-domain NMR methods.[48]

At 285 K, however, we could extract some quantitative information of the jump processes. The corresponding exchange rates amount to $k_{3\text{-}1} = 3\ s^{-1}$ (4*e*-8*f*) and $k_{3\text{-}2} = 0.7\ s^{-1}$ (4*e*-4*d*), respectively. As expected, the exchange rates at 285 K are much lower than 84 Hz as estimated from our 1D ^{6}Li NMR spectra discussed above. In good agreement with 2D EXSY NMR the Li(3)-Li(1) exchange process is the dominant one, whereas hopping between Li(3) and Li(2) is indeed characterized by a lower rate. Similarly to 2D EXSY NMR, ion hopping in the 2D plane between neighboring Li(2) and Li(1) sites cannot be ruled out though it could not be resolved in the selective inversion experiments carried out. The absence of significant coalescence in 1D ^{6}Li NMR, however, indicates that in-plane Li exchange is less important than out-of-plane hopping. Obviously, the latter is driven by vacant Li(3) sites in Li_2SnO_3 making the hopping pathway including the T2 tetrahedra the preferred one, as is illustrated in Fig. 6.

(1) Tarascon, J.-M.; Armand, M. Issues and Challenges Facing Rechargeable Lithium Batteries. *Nature* **2001**, *414* (6861), 359–367.

(2) Winter, M.; Besenhard, J. O.; Spahr, M. E.; Novak, P. Insertion Electrode Materials for Rechargeable Lithium Batteries. *Adv. Mater.* **1998**, *10* (10), 725–763.

(3) Choi, N.-S.; Chen, Z.; Freunberger, S. A.; Ji, X.; Sun, Y.-K.; Amine, K.; Yushin, G.; Nazar, L. F.; Cho, J.; Bruce, P. G. Challenges Facing Lithium Batteries and Electrical Double-Layer Capacitors. *Angew. Chemie Int. Ed.* **2012**, *51* (40), 9994–10024.

(4) Ellis, B. L.; Lee, K. T.; Nazar, L. F. Positive Electrode Materials for Li-Ion and Li-Batteries. *Chem. Mater.* **2010**, *22* (3), 691–714.

(5) Knauth, P. Inorganic Solid Li Ion Conductors: An Overview. *Solid State Ionics* **2009**, *180* (14–16), 911–916.

(6) Cao, C.; Li, Z.; Wang, X.-L.; Zhao, X.; Han, W.-Q. Recent Advances in Inorganic Solid Electrolytes for Lithium Batteries. *Front. Energy Res.* **2014**, *2* (25).

(7) Van der Laan, J. G.; Kawamura, H.; Roux, N.; Yamaki, D. Ceramic Breeder Research and Development: Progress and Focus. *J. Nucl. Mater.* **2000**, *283–287, P* (0), 99–109.

(8) Roux, N.; Avon, J.; Floreancing, A.; Mougin, J.; Rasneur, B.; Ravel, S. Low-Temperature Tritium Releasing Ceramics as Potential Materials for the ITER Breeding Blanket. *J. Nucl. Mater.* **1996**, *233–237, P* (0), 1431–1435.

(9) Ohno, H.; Konishi, S.; Nagasaki, T.; Kurasawa, T.; Katsuta, H.; Watanabe, H. Correlation Behavior of Lithium and Tritium in Some Solid Breeder Materials. *J. Nucl. Mater.* **1985**, *133–134* (0), 181–185.

(10) Wilkening, M.; Heitjans, P. From Micro to Macro: Access to Long-Range Li^+ Diffusion Parameters in Solids via Microscopic $^{6,7}Li$ Spin-Alignment Echo NMR Spectroscopy. *ChemPhysChem* **2012**, *13* (1), 53–65.

(11) Tang, X. P.; Geyer, U.; Busch, R.; Johnson, W. L.; Wu, Y. Diffusion Mechanisms in Metallic Supercooled Liquids and Glasses. *Nature* **1999**, *402* (6758), 160–162.

(12) Wilkening, M.; Heitjans, P. Li Jump Process in H-$Li_{0.7}TiS_2$ Studied by Two-Time ^7Li Spin-Alignment Echo NMR and Comparison with Results on Two-Dimensional Diffusion from Nuclear Magnetic Relaxation. *Phys. Rev. B* **2008**, *77* (2), 024311.

(13) Wilkening, M.; Küchler, W.; Heitjans, P. From Ultraslow to Fast Lithium Diffusion in the 2D Ion Conductor $Li_{0.7}TiS_2$ Probed Directly by Stimulated-Echo NMR and Nuclear Magnetic Relaxation. *Phys. Rev. Lett.* **2006**, *97* (6), 65901.

(14) Langer, J.; Epp, V.; Heitjans, P.; Mautner, F. A.; Wilkening, M. Lithium Motion in the Anode Material LiC_6 as Seen via Time-Domain ^{7}Li NMR. *Phys. Rev. B* **2013**, *88* (9), 094304.

(15) Kuhn, A.; Narayanan, S.; Spencer, L.; Goward, G.; Thangadurai, V.; Wilkening, M. Li Self-Diffusion in Garnet-Type $Li_7La_3Zr_2O_{12}$ as Probed Directly by Diffusion-Induced ^{7}Li Spin-Lattice Relaxation NMR Spectroscopy. *Phys. Rev. B* **2011**, *83* (9), 94302.

(16) Böhmer, R.; Jeffrey, K. R.; Vogel, M. Solid-State Li NMR with Applications to the Translational Dynamics in Ion Conductors. *Prog. Nucl. Magn. Reson. Spectrosc.* **2007**, *50* (2-3), 87–174.

(17) Stanje, B.; Epp, V.; Nakhal, S.; Lerch, M.; Wilkening, M. Li Ion Dynamics along the Inner Surfaces of Layer-Structured 2H–Li_xNbS_2. *ACS Appl. Mater. Interfaces* **2015**, *7* (7), 4089–4099.

(18) Dunst, A.; Epp, V.; Hanzu, I.; Freunberger, S. A.; Wilkening, M. Short-Range Li Diffusion vs. Long-Range Ionic Conduction in Nanocrystalline Lithium Peroxide Li_2O_2-the Discharge Product in Lithium-Air Batteries. *Energy Environ. Sci.* **2014**, *7* (8), 2739–2752.

(19) Heitjans, P.; Schirmer, A.; Indris, S. NMR and B-NMR Studies of Diffusion in Interface-Dominated and Disordered Solids. In *Diffusion in Condensed Matter*; Heitjans, P., Kärger, J., Eds.; Springer: Berlin, 2005; pp 367–415.

(20) Epp, V.; Wilkening, M. Li-Ion Dynamics in Solids as Seen Via Relaxation NMR. In *Handbook of Solid State Batteries*; Dudney, N. J., West, W. C., Nanda, J., Eds.; Materials and Energy; World Scientific: New Jersey, Hong Kong, 2015; Vol. 6, pp 133–190.

(21) Epp, V.; Guen, O.; Deiseroth, H.-J.; Wilkening, M. Highly Mobile Ions: Low-Temperature NMR Directly Probes Extremely Fast Li^+ Hopping in Argyrodite-Type Li_6PS_5Br. *J. Phys. Chem. Lett.* **2013**, *4* (13), 2118–2123.

(22) Ruprecht, B.; Billetter, H.; Ruschewitz, U.; Wilkening, M. Ultra-Slow Li Ion Dynamics in Li_2C_2-on the Similarities of Results from ^{7}Li Spin-Alignment Echo NMR and Impedance Spectroscopy. *J. Phys. Condens. Matter* **2010**, *22* (24), 245901.

(23) Ruprecht, B.; Wilkening, M.; Uecker, R.; Heitjans, P. Extremely Slow Li Ion Dynamics in Monoclinic Li_2TiO_3-Probing Macroscopic Jump Diffusion via ^{7}Li NMR Stimulated Echoes. *Phys. Chem. Chem. Phys.* **2012**, *14* (34), 11974–11980.

(24) Vijayakumar, M.; Kerisit, S.; Yang, Z.; Graff, G. L.; Liu, J.; Sears, J. A.; Burton, S. D.; Rosso, K. M.; Hu, J. Combined ^{6,7}Li NMR and Molecular Dynamics Study of Li Diffusion in Li_2TiO_3. *J. Phys. Chem. C* **2009**, *113* (46), 20108–20116.

(25) Baklanova, Y. V.; Arapova, I. Y.; Shein, I. R.; Maksimova, L. G.; Mikhalev, K. N.; Denisova, T. a. Charge Distribution and Mobility of Lithium Ions in Li_2TiO_3 from ^{6,7}Li NMR Data. *J. Struct. Chem.* **2013**, *54* (1), 111–118.

(26) Baklanova, Y. V; Arapova, I. Y.; Buzlukov, A. L.; Gerashenko, A. P.; Verkhovskii, S. V; Mikhalev, K. N.; Denisova, T. A.; Shein, I. R.; Maksimova, L. G. Localization of Vacancies and Mobility of Lithium Ions in Li_2ZrO_3 as Obtained by ^{6,7}Li NMR. *J. Solid State Chem.* **2013**, *208* (0), 43–49.

(27) Bottke, P.; Freude, D.; Wilkening, M. Ultraslow Li Exchange Processes in Diamagnetic Li_2ZrO_3 As Monitored by EXSY NMR. *J. Phys. Chem. C* **2013**, *117* (16), 8114–8119.

(28) Kreuzburg, G.; Stewner, F.; Hoppe, R. Die Kristallstruktur von Li_2SnO_3. *Zeitschrift für Anorg. und Allg. Chemie* **1971**, *379* (3), 242–254.

(29) Hodeau, J. L.; Marezio, M.; Santoro, A.; Roth, R. S. Neutron Profile Refinement of the Structures of Li_2SnO_3 and Li_2ZrO_3. *J. Solid State Chem.* **1982**, *45* (2), 170–179.

(30) Salager, E.; Sarou-Kanian, V.; Sathiya, M.; Tang, M.; Leriche, J.-B.; Melin, P.; Wang, Z.; Vezin, H.; Bessada, C.; Deschamps, M.; et al. Solid-State NMR of the Family of Positive Electrode Materials $Li_2Ru_{1-y}Sn_yO_3$ for Lithium-Ion Batteries. *Chem. Mater.* **2014**, *26* (24), 7009–7019.

(31) Jeener, J.; Meier, B. H.; Bachmann, P.; Ernst, R. R. Investigation of Exchange Processes by Two-dimensional NMR Spectroscopy. *J. Chem. Phys.* **1979**, *71* (11), 4546-4533.

(32) Abel, E. W.; Coston, T. P. J.; Orrell, K. G.; Šik, V.; Stephenson, D. Two-Dimensional NMR Exchange Spectroscopy. Quantitative Treatment of Multisite Exchanging Systems. *J. Magn. Reson.* **1986**, *70* (1), 34–53.

(33) Verhoeven, V. W. J.; de Schepper, I. M.; Nachtegaal, G.; Kentgens, A. P. M.; Kelder, E. M.; Schoonman, J.; Mulder, F. M. Lithium Dynamics in $LiMn_2O_4$ Probed Directly by Two-Dimensional ^{7}Li NMR. *Phys. Rev. Lett.* **2001**, *86* (19), 4314–4317.

(34) Wilkening, M.; Romanova, E. E.; Nakhal, S.; Weber, D.; Lerch, M.; Heitjans, P. Time-Resolved and Site-Specific Insights into Migration Pathways of Li^+ in α-Li_3VF_6 by ^{6}Li 2D Exchange MAS NMR. *J. Phys. Chem. C* **2010**, *114* (44), 19083–19088.

(35) Grey, C. P.; Dupré, N. NMR Studies of Cathode Materials for Lithium-Ion Rechargeable Batteries. *Chem. Rev.* **2004**, *104* (10), 4493–4512.

(36) Davis, L. J. M.; He, X. J.; Bain, A. D.; Goward, G. R. Studies of Lithium Ion Dynamics in Paramagnetic Cathode Materials Using ^{6}Li 1D Selective Inversion Methods. *Solid State Nucl. Magn. Reson.* **2012**, *42*, 26–32.

(37) Davis, L. J. M.; Ellis, B. L.; Ramesh, T. N.; Nazar, L. F.; Bain, A. D.; Goward, G. R. ^{6}Li 1D EXSY NMR Spectroscopy: A New Tool for Studying Lithium Dynamics in Paramagnetic Materials Applied to Monoclinic Li_2VPO_4F. *J. Phys. Chem. C* **2011**, *115* (45), 22603–22608.

(38) Smiley, D. L.; Davis, L. J. M.; Goward, G. R. An Improved Understanding of Li+ Hopping Pathways and Rates in $Li_3Fe_2(PO_4)_3$ Using Selective Inversion ^{6}Li NMR Spectroscopy. *J. Phys. Chem. C* **2013**, *117* (46), 24181–24188.

(39) Zhang, D. W.; Zhang, S. Q.; Jin, Y.; Yi, T. H.; Xie, S.; Chen, C. H. Li_2SnO_3 Derived Secondary Li–Sn Alloy Electrode for Lithium-Ion Batteries. *J. Alloys Compd.* **2006**, *415* (1–2), 229–233.

(40) Thurber, K. R.; Tycko, R. Measurement of Sample Temperatures under Magic-Angle Spinning from the Chemical Shift and Spin-Lattice Relaxation Rate of ^{79}Br in KBr Powder. *J. Magn. Reson.* **2009**, *196* (1), 84–87.

(41) Sebald, A.; Merwin, L. H.; Dollase, W. A.; Seifert, F. A Multinuclear, High-Resolution Solid-State NMR Study of Sorensenite ($Na_4SnBe_2(Si_3O_9)\cdot 2H_2O$) and Comparison with Wollastonite and Pectolite. *Phys. Chem. Miner.* **1990**, *17* (1), 9–16.

(42) Massiot, D.; Fayon, F.; Capron, M.; King, I.; Le Calvé, S.; Alonso, B.; Durand, J.-O.; Bujoli, B.; Gan, Z.; Hoatson, G. Modelling One- and Two-Dimensional Solid-State NMR Spectra. *Magn. Reson. Chem.* **2002**, *40* (1), 70–76.

(43) Bauer, C.; Freeman, R.; Frenkiel, T.; Keeler, J.; Shaka, A. J. Gaussian Pulses. *J. Magn. Reson.* **1984**, *58* (3), 442–457.

(44) Grey, C. P.; Cheetham, A. K.; Dobson, C. M. Temperature-Dependent Solid-State ^{119}Sn-MAS NMR of $Nd_2Sn_2O_7$, $Sm_2Sn_2O_7$, and $Y_{1.8}Sm_{0.2}Sn_2O_7$. Three Sensitive Chemical-Shift Thermometers. *J. Magn. Reson. Ser. A* **1993**, *101* (3), 299–306.

(45) Bain, A. D.; Cramer, J. A. Slow Chemical Exchange in an Eight-Coordinated Bicentered Ruthenium Complex Studied by One-Dimensional Methods. Data Fitting and Error Analysis. *J. Magn. Reson. Ser. A* **1996**, *118* (1), 21–27.

(46) Bain, A. D. Chemical Exchange in NMR. *Prog. Nucl. Magn. Reson. Spectrosc.* **2003**, *43* (3-4), 63–103.

(47) Tarakina, N. V.; Denisova, T. A.; Maksimova, L. G.; Baklanova, Y. V.; Tyutyunnik, A. P.; Berger, I. F.; Zubkov, V. G.; Van Tendeloo, G. Investigation of Stacking Disorder in Li_2SnO_3. *Zeitschrift für Krist. Suppl.* **2009**, *2009* (30), 375–380.

(48) Langer, J.; Wilkening, M. To Be Published.

(49) Sepelak, V.; Duvel, A.; Wilkening, M.; Becker, K.-D.; Heitjans, P. Mechanochemical Reactions and Syntheses of Oxides. *Chem. Soc. Rev.* **2013**, *42* (18), 7507–7520.

(50) Wilkening, M.; Epp, V.; Feldhoff, A.; Heitjans, P. Tuning the Li Diffusivity of Poor Ionic Conductors by Mechanical Treatment: High Li Conductivity of Strongly Defective $LiTaO_3$ Nanoparticles. *J. Phys. Chem. C* **2008**, *112* (25), 9291–9300.

(51) Preishuber-Pflügl, F.; Epp, V.; Nakhal, S.; Lerch, M.; Wilkening, M. Defect-Enhanced F^- Ion Conductivity in Layer-Structured Nanocrystalline $BaSnF_4$ Prepared by High-Energy Ball Milling Combined with Soft Annealing. *Phys. status solidi* **2015**, *12* (1-2), 10–14.

(52) Wohlmuth, D.; Epp, V.; Bottke, P.; Hanzu, I.; Bitschnau, B.; Letofsky-Papst, I.; Kriechbaum, M.; Amenitsch, H.; Hofer, F.; Wilkening, M. Order vs. Disorder-a Huge Increase in Ionic Conductivity of Nanocrystalline $LiAlO_2$ Embedded in an Amorphous-like Matrix of Lithium Aluminate. *J. Mater. Chem. A* **2014**, *2* (47), 20295–20306.

(53) Brant, J. A.; Massi, D. M.; Holzwarth, N. A. W.; MacNeil, J. H.; Douvalis, A. P.; Bakas, T.; Martin, S. W.; Gross, M. D.; Aitken, J. A. Fast Lithium Ion Conduction in Li_2SnS_3: Synthesis, Physicochemical Characterization, and Electronic Structure. *Chem. Mater.* **2015**, *27* (1), 189–196.

(54) Davis, L. J. M.; Goward, G. R. Differentiating Lithium Ion Hopping Rates in Vanadium Phosphate versus Vanadium Fluorophosphate Structures Using 1D ^{6}Li Selective Inversion NMR. *J. Phys. Chem. C* **2013**, *117* (16), 7981–7992.

M3: (pp.115–134)

Long-range Li^+ diffusion in Li_2SnO_3 studied by two-time ^7Li spin-alignment echo NMR and ^7Li NMR relaxometry

J. Langer and M. Wilkening

Long-range Li^+ diffusion in Li_2SnO_3 studied by two-time ^7Li spin-alignment echo NMR and ^7Li NMR relaxometry

J. Langer*,[1] and M. Wilkening†,[2]

† Institute for Chemistry and Technology of Materials (NAWI Graz) Graz University of Technology, 8010 Graz, Austria;DFG Research Unit 1277, Graz University of Technology, 8010 Graz, Austria

Abstract

A deeper understanding of atomic-scale Li hopping in solid Li ion conductors requires the study of ion dynamics on a broad time scale. Here, we report a complementary study, applying ^7Li spin-lattice relaxation (SLR) nuclear magnetic resonance (NMR) techniques together with spin-alignment echo (SAE) NMR to study slow Li^+ self-diffusion in monoclinic Li_2SnO_3. SLR NMR in the laboratory and rotating frame of reference probe fast ion hopping in the MHz and kHz regime and provide information on short-range diffusion involving available Li vacancies within the crystal structure. Long-range Li motion in low-conducting lithium stannate is studied via ^7Li SAE NMR, providing direct access to Li jump rates and a mean self-diffusion coefficient D. Damping of the echo amplitude $S_2(t_m, t_p)$ recorded as a function of the mixing time t_m, and fixed evolution time t_p, is induced by slow Li jump processes. The corresponding activation energy E_a = 0.46 eV can be deduced from the Arrhenius-type behavior of the echo decay rates τ_{SAE}, corroborating the dynamical parameters derived from SLR NMR. Furthermore, we investigated the influence of dipole-dipole interaction on the SAE experiment by t_m-dependent experiments carried out at $t_p > 20$ μs as well as by t_p-dependent measurements at short mixing times. Dipolar contributions to the echo decay are already present at t_p = 20 μs; they start to dominate with increasing t_p and t_m. Furthermore, the strong t_p-dependence of τ_{SAE} points towards heterogeneous dynamics which is likely to be caused by a slightly disordered structure.

Introduction

Solid lithium ion conductors have attracted a great deal of scientific and industrial attention in the last decades. In particular, their application in lithium-ion batteries, *viz.* as solid electrolytes, anode and cathode materials, demands a thorough understanding of ion transport characteristics related to structural properties and solid-state synthesis. Knowledge about lithium *self-diffusion* parameters does not only play a vital role in the engineering of modern battery materials, but is also of fundamental interest in physical chemistry and materials science. Moreover, the study of model systems with well-defined structural properties provides a basis for the understanding of application-oriented non-model systems. In the present study, the slow Li ion conductor Li_2SnO_3 serves as such a model substance to investigate Li ion diffusion from an atomic-scale point of view. With the help of a microscopic technique, such as solid-state nuclear magnetic resonance spectroscopy it is possible to probe long- and short-range ion motion, and gain information on the timescale and geometry of diffusion.[1–3] Recently, we studied polycrystalline lithium stannate with respect to site-specific Li exchange processes and diffusion pathways using one- (1D) and two-dimensional (2D) ^{6}Li NMR spectroscopy.[4] In accordance with the monoclinic crystal structure it was possible to resolve three magnetically inequivalent Li sites and two individual exchange processes on the second timescale.

The structure consists of pure Li layers with Li(1) and Li(2) residing on the *8f* and *4d* positions alternating with $LiSn_2$ layers with Li(3) on the *4e* position along the c-axis. As confirmed by ^{6}Li 2D exchange and 1D selective inversion NMR preferred Li exchange occurs along the *c*-axis between Li(1) and Li(3) with an exchange rate $k_{1\text{-}3} = 3\ s^{-1}$ while Li hopping between Li(2) and Li(3) is less favored with $k_{2\text{-}3} = 0.7\ s^{-1}$. Interestingly these findings are corroborated by a recent study of Aitken *et al.*[5], and Vijayakumar *et al.*[6] for isostructural Li_2TiO_3, where the formation of vacancies on the *4e* position is energetically favored compared to *8f* and *4d* sites. However, in contrast to its structure, the dynamical behavior tends to be rather complex: We observed heterogeneous dynamics where a fraction of Li ions remains immobile in the temperature range covered by variable-temperature (VT) ^{6}Li MAS NMR. As a result of the high crystallinity of the material, the amount of vacancies, being necessary for Li hopping, is small. Ultimately, part of the Li ions are trapped on their positions, while a mobile fraction is able to diffuse along the *c*-axis. At higher *T*, that is, above 348 K, we might observe a more homogeneous behavior

with increased Li^+ or vacancy mobility. These questions can be answered with the help of static NMR measurements along with advanced techniques, *i.e.* SLR NMR and SAE NMR, where we can look further into the heterogeneous dynamics of micro- and macroscopic diffusion in Li_2SnO_3, covering jump rates ranging from $10^{-5}\,s^{-1}$ up to $10^{10}\,s^{-1}$.

Both SAE NMR and high-resolution 2D magic-angle-spinning (MAS) NMR are sensitive to ultraslow Li motion, measuring jump rates up to of a few jumps per minute.[7] With 2D MAS NMR *site-specific* jump rates can be probed, however with the prerequisite that the individual sites can be each resolved. This can be particularly challenging when investigating amorphous or disordered materials. In the case of polycrystalline Li_2SnO_3, the site-specific resonances lie within a range of 1.5 ppm, including a coalescence peak that masks the "residual" peaks representing the "immobile" Li ions at elevated temperatures. Additionally, resonance peaks marking Li(1) and Li(2) are only 0.15 ppm apart and partly overlap, even at low temperatures. Thus it makes it challenging to investigate hopping between these sites in the *ab*-plane. However, note that from a structural point of view exchange between Li(1) and Li(2) cannot be excluded. Also, compared to SAE measurements, 2D exchange experiments tend to be more time consuming, with the measurement duration being influenced by long T_1 relaxation times.

Quantitative information on Li jump activation energies and jump rates, as well as on the dimensionality of diffusion, can be accessed with ^{6,7}Li spin-lattice ($T_{1(\rho)}$) and spin-spin relaxation (SSR) measurements (T_2) or ^{8}Li β-NMR, if performed as a function of temperature and frequency. Spin-lattice relaxation rates $R_1 = 1/T_1$ are displayed in an Arrhenius representation as log R_1 versus inverse temperature $1/T$. In the ideal case a rate peak is probed which allows the determination of a characteristic jump rate τ^{-1} at the rate maximum, as $\omega_0\tau \approx 1$. In the low-T regime ($\omega_0\tau \ggg 1$) local, short-range hopping is probed while the flank of the rate peak is influenced by correlation effects due to structural disorder or coulombic interactions. The high-T flank, on the other hand, is changed by dimensionality effects, as it is the case for anisotropic 2D or 1D diffusion. A totally symmetric rate peak is only obtained for isotropic (3D) uncorrelated Li motion. All these artefacts reduce the respective slopes of the high- and low-T flank, which results in 'apparent' values being lower than the actual energy barriers. Note that an accurate determination of E_a necessitates mathematical models such as the ones proposed by Bloembergen-Purcell-Pound (BPP) for 3D[8] or Richards for 2D diffusion[9]. These models, partly semiempirical, take into account both correlation and dimensionality effects.

But even in the case of fast ion conductors, the complete R_1 rate peak can, in many cases, only be probed at high temperatures (up to 1000 K), which is particularly problematic for the investigation of heat-sensitive materials. This problem can be overcome by basically applying resonance frequencies in the kHz range. Then the rate peak is shifted towards lower temperatures allowing for the detection of the complete $R_{1\rho}$ rate peak. Also, changes in the diffusion mechanism can be observed, as *per se* this method is sensitive to much slower Li dynamics as SLR measurements carried out in the laboratory frame of reference. Nonetheless, as in the case of R_1 a self-contained interpretation of the data requires specific relaxation models.

Overall, SAE NMR completely differs from SLR measurements: Li jump rates can be directly extracted from a two-time correlation function, without needing a mathematical model. In principle, the SAE technique bases on the interaction of the quadrupole coupling constant δ_q with the electric field gradient (EFG) at the nuclear site, which is caused by the electric charge distribution in its neighborhood. As a result the Zeeman frequency is altered leading to quadrupole frequencies ω_q labeling electrically inequivalent Li sites. Consequently, during diffusion Li ions experience temporal fluctuations of the EFG, *i.e.* different ω_q, which, if monitored as a function of time yield dynamic information on Li ion hopping. SAE experiments are performed using the three-pulse sequence of Jeener-Broekart:[10]

$$\beta_1(\phi_1) - t_p - \beta_2(\phi_2) - t_m - \beta_3(\phi_3) - t_{acq.} \tag{1}$$

with $\beta_1 = 90°$ and $\beta_2 = \beta_3 = 45°$. ϕ_i denotes the different pulse phases while t_p and t_m describe the respective evolution and mixing time of the experiment. In order to study the timescale of Li dynamics spin-alignment echos are recorded as a function of the mixing time. The echo amplitude decays if the nuclei are exposed to different ω_q, marking successful jumps between inequivalent Li sites. By correlating the quadrupole frequencies before and after a certain mixing time interval we obtain a two-time correlation function enabling a direct, model-free access to Li jump rates:

$$S_2(t_p, t_m, t) = \frac{9}{20}\left\langle \sin\left[\omega_q(t_m = 0)t_p\right]\sin\left[\omega_q(t_m)t\right]\right\rangle \tag{2}$$

with $\langle \ldots \rangle$ describing the powder average. The spin-alignment decay can be parametrized with a simple exponential function (though experimentally often described with stretched exponentials), containing the decay rate τ_{SAE}^{-1} that can be, in the ideal case, identified with the correlation rate, *i.e.* the mean Li

jump rate τ^{-1}. Note that correlation times are unaffected by changes of the quadrupole coupling constants due to temperature and independent of the magnetic field of the experiment. Using the Einstein-Smoluchowski equation the jump rate can be directly transformed into a self-diffusion coefficient $D = a^2 / 2d\tau$. This is in contrast to SLR measurements where the motional correlation rate equals the Li jump rate only at the rate maximum for which the condition $\omega_0 \tau_c \approx 1$ holds. Only at the peak maximum a direct transformation into the self-diffusion coefficient is possible without applying a relaxation model to convert the SLR NMR rates into jump rates.

The coefficient *a* in $D = a^2 / 2d\tau$ represents the mean jump distance while *d* takes the dimensionality of the diffusion mechanism into account. The self-diffusion coefficient derived from SAE measurements is often found to show similar values as those obtained from SLR maxima or from impedance spectroscopic studies.

Therefore, in our study, we studied slow Li^+ hopping motion with conventional static SLR NMR in the laboratory and rotating frame of reference as well as with complementary Li-stimulated echo NMR. The latter give direct access to the timescales of ultraslow Li motion and, thus, Li self-diffusion coefficients near room temperature. Furthermore, by performing both t_m- and t_p-dependent SAE experiments we can investigate the interplay of homonuclear dipole-dipole interactions with the quadrupolar alignment states.

Experimental

Monoclinic HT-Li_2SnO_3 was synthesized according to a procedure described elsewhere. For the ^{7}Li NMR measurements the transparent powder was fire-sealed in a Duran glass ampoule (4 mm in diameter, 3 cm in length) under vacuum.

Variable-temperature measurements were performed on a Bruker Avance III spectrometer connected to a shimmed cryomagnet with a nominal field of 7.0 T. All ^{7}Li NMR experiments were conducted with a commercial high-temperature probe (Bruker) between 217 K and 593 K, which was monitored and adjusted using a Eurotherm temperature controller in connection with a type T thermocouple. Spin-lattice relaxation rates R_1 were recorded at a Larmor frequency ω_0 = 116 MHz by means of a

saturation recovery pulse sequence $10 \times \pi/2 - t_d$ - $\pi/2$.[11,12] Hereby a closely spaced comb consisting of ten ($\pi/2$) pulses destroys any initial longitudinal magnetization, ensuring $M_z = 0$ at $t = 0$. After a variable delay time t_d the recovery of $M_z(t)$ is probed with a single $\pi/2$ pulse.

Relaxometry measurements in the rotating frame of reference (SLRρ) yielding $R_{1\rho}$ employ a spin-locking technique as described in greater detail elsewhere.[13–15] In principle, an initial $\pi/2$ pulse is followed by an angular locking pulse along the Y' axis of the rotating frame, locking the spins in the effective locking field B_1. Here, the decay of the magnetization M_ρ is monitored as a function of the duration t_{lock} of the locking pulse ranging from 46 µs to 1 s. The locking frequency ω_1 lies in the kHz order and was chosen as low as possible ($\omega_1 = 20$ kHz). As $\omega_1 \ll \omega_0$, SLRρ measurements are much more sensitive towards slower Li motion than SLR NMR in the laboratory frame of reference. Both R_1 and $R_{1\rho}$ were obtained by parametrizing the magnetization transients $M_z(t_d)$ and $M_\rho(t_{lock})$ with stretched exponentials, *i.e.* $M_z(t_d) \propto 1 - \exp\left[-(t_d / T_1)^\gamma\right]$ and $M_\rho(t_{lock}) \propto \exp\left[-(t_{lock} / T_{1\rho})^{\gamma'}\right]$, respectively.

Additionally, spin-spin relaxation rates $R_2 = 1/T_2$ were obtained by the (two-pulse) solid-echo technique 90° - t_{echo} – 64° - acq. with t_{echo} denoting the variable interpulse delay.[16]

Spin-alignment echos were measured applying the three-pulse Jeener-Broekart sequence[10,17] (see above) as a function of the mixing time (10 µs $\leq t_m \leq$ 10s) at various fixed evolution times (t_p = 20 µs; 50 µs; 100 µs; 200 µs) or as a function of the evolution time (20 µs $\leq t_p \leq$ 356 µs) at t_m = 10 µs, covering a broad temperature range from 231 K to 513 K.

Static ^{7}Li spectra were obtained after Fourier transformation of the free induction decay (FID) recorded in a one-pulse experiment, typically applying $\pi/2$ pulse lengths between 2.5 and 3.0 µs. Note that, for the echo spectra, only the top of the solid echo was Fourier transformed. For all types of experiments a sufficiently long recycle delay of $5 \times T_1$ ensured full longitudinal relaxation between each scan. Also, appropriate phase cycling helped to eliminate unwanted coherences and decrease the effect of pulse imperfections.

Results and Discussion

^{7}Li spectra and motional narrowing

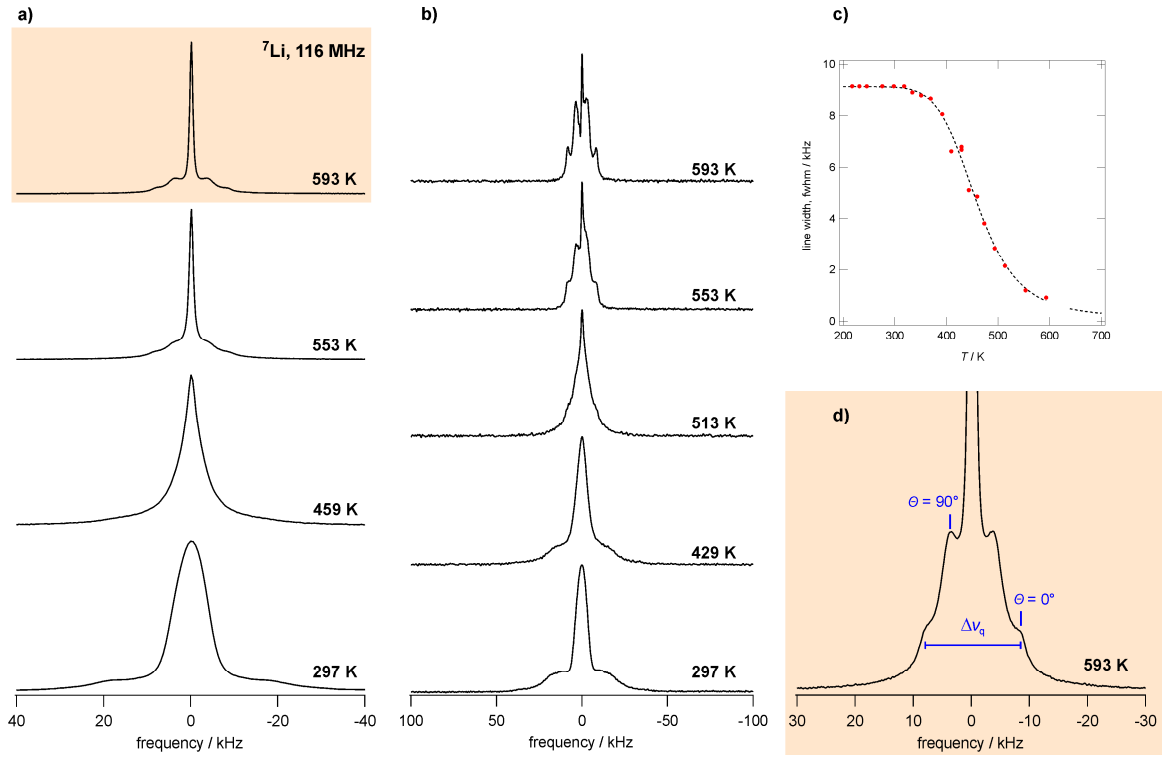

Figure 1: a) Static ^{7}Li one-pulse spectra as a function of temperature, b) ^{7}Li SAE spectra recorded at ν_0 = 116 MHz showing apronounced quadrupole foot; evolution of a distinct quadrupolar powder pattern with increasing temperature, c) motional narrowing curve of the static ^{7}Li line width (full width at half maximum (fwhm), d) magnification of the quadrupole foot for the ^{7}Li spectrum recorded at 593 K.

Temperature-dependent ^{7}Li NMR spectra can probe local electronic and local magnetic structures and draw a first picture of Li diffusivity in lithium stannate. In the so-called rigid lattice regime Li diffusion is too slow to directly affect the spectral line width. As can be seen in Fig. 1c the linewidth (full width at half maximum FWHM) remains almost constant between 217 K and 318 K. Spectra recorded in this regime exhibit a dipolarly broadened Gaussian line shape with a very broad quadrupolar contribution (Fig. 1a). The linewidth decreases with increasing temperature as dipole-dipole interactions are averaged due to the onset of Li motion while the satellite intensity decreases. In this intermediate region

we observed an inhomogeneous narrowing of the central line which points towards a distribution of Li jump rates. A distribution of jump rates is caused by heterogeneous Li dynamics as has already been reported for this material.[18] At $T \geq 553$ K spectra are characterized by the appearance of a distinct quadrupole powder pattern which originates from the interaction of the quadrupole moment with a non-zero electric field gradient (EFG) at the nuclear site. This interaction alters the Zeeman-levels leading to several spin-transitions.[19] The observed pattern for Li_2SnO_3 shows one set of singularities (*cf.* Fig. 1d). From the spectral distance $\Delta\nu_Q$ between the outer singularities a quadrupole coupling constant of $C_q(^7Li, 593\ K) = 16$ kHz can be deduced. As we can find three electrically inequivalent, yet structurally very similar sites, this single C_q can be regarded as a mean value for all three Li positions.

In our stimulated-echo spectra (*cf.* Fig. 1b) the quadrupolar satellites are enhanced and appear in a more structured fashion. Even at short evolution times of $t_p = 20$ µs we observe a sharp central line, which is due to dipole-dipole interaction on top of a broad quadrupole-induced signal. The central line narrows with increasing temperature, along with the broad quadrupolar satellites, representing the superposition of the three different quadrupole powder patterns. At $T = 513$ K a pronounced pattern starts to emerge, yielding a mean $C_q = 16$ kHz at 593 K, in accordance with the ^{7}Li spectra obtained after single-pulse excitation.

If the linewidth (FWHM) $\Delta\nu$ is monitored as a function of T we can estimate a mean Li jump rate and jump activation energy from the diffusion-initialized (motional) narrowing (see Fig. 1c). At the inflection point of the so-called motional narrowing curve the jump rate $\tau_{MN}^{-1} = 2\pi \times \nu_{RL}$ (ν_{RL} denotes the rigid-lattice linewidth) lies in the order of 10^4 jumps per second. If the curve is approximated with the model proposed by Hendrickson & Bray[20] a hopping activation energy of 0.45 eV can be deduced. Note that these values have to be taken as rough estimations. In order to get a more accurate access to dynamical parameters SLR NMR techniques and SAE NMR probe Li diffusivity over a broad time and length scale.

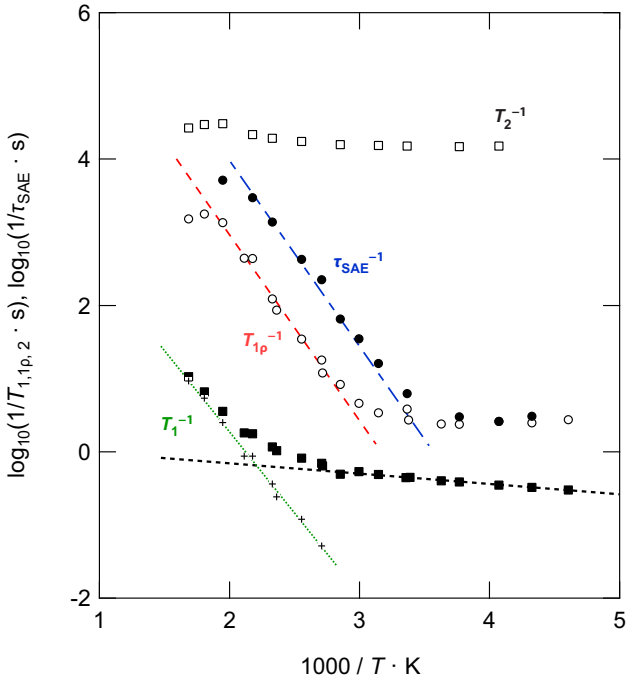

Figure 2: Arrhenius-type plot illustrating the temperature dependence of ^{7}Li spin-lattice relaxation rates using ν_0 = 116 MHz (T_1^{-1}) and ν_{lock} = 20 kHz ($T_{1\rho}^{-1}$), together with SAE echo decay rates τ_{MN}^{-1} and spin-spin relaxation rates (T_2^{-1}) at B_0 = 7.0 T. The colored dashed lines represent linear fits yielding the respective jump activation energy E_a. See text for further explanations.

Spin-lattice relaxation: T_1 and $T_{1\rho}$

Figure 2 shows an Arrhenius-plot of NMR relaxation rates determined in the laboratory and rotating frame of reference together with transversal relaxation rates and SAE decay rates. SLR measurements in the laboratory frame of reference probe Li motion on the MHz time scale, *i. e.* ν_0 = 116 MHz for the ^{7}Li nucleus. At $T \leq$ 369 K, where $\omega_0 \tau \ggg 1$ is met, the relaxation rates are almost temperature-independent. Here, R_1 is additionally influenced by background effects that add up to purely diffusion-induced relaxation rates $R_{1,diff}$, thus: $R_1 = R_{1,diff} + R_{1,bgr.}$ Background relaxation rates $R_{1,bgr}$ can be approximated with a power-law fit $R_{1,bgr} \propto T^{\kappa}$, e.g. $\kappa = 1$ if the relaxation mechanism is governed by coupling with conduction electrons, or $\kappa = 2$ for a phononic relaxation mechanism dependent on the Debye-temperature. Localized Li jumps or spin-fluctuations with paramagnetic impurities can also contribute to the non-diffusive rates. In order to obtain $R_{1,bgr}$ we extrapolated a power-law fit, with $\kappa = 1.7(1)$, to higher T and

then subtracted the rates from the overall rates R_1 yielding $R_{1,diff}$ assuming that $R_{1,diff}$ is solely induced by Li motion.[21] $R_{1,diff}$ increases linearly which allows the determination of an Arrhenius-activated jump activation energy E_A = 0.44(1) eV from the slope of the low-temperature flank d($R_{1,diff}$) / d(T^{-1}). Note that in this temperature regime localized, short-range Li hopping is probed, comparable to the dynamic parameters probed by motional narrowing.

In order to investigate Li diffusion on a broader length-scale it is necessary to probe the high-temperature flank of the SLR rate peak which can be achieved via spin-lattice relaxation measurements in the rotating frame of reference. This technique is sensitive to slower Li motion by using so-called spin-locking frequencies in the kHz-regime which shifting the SLR rate peak towards lower temperatures. At low temperatures $R_{1\rho}$ is temperature-independent as it is governed by non-diffusive background relaxation mechanisms. As can be seen in figure 2 the rates increase gradually until T = 555 K, possibly marking a rate maximum where the motional correlation rate τ_c^{-1} is in the order of the Li jump rate τ^{-1} and $\omega_1 \tau_c \approx 0.5$ is fulfilled. The "preliminary" rate maximum allows us to estimate a Li self-diffusion coefficient $D = 3.8 \times 10^{-15}$ m^{2}s^{-1} at 555 K. Using locking frequencies of ω_1 = 20 kHz we are looking at a Li jump rate in the order of 2.5×10^5 s^{-1} and an activation energy of 0.45(2) eV deduced from the low-T flank. This value is consistent with our results from the T_1 measurements and can be regarded as evidence that the same diffusion process was probed with both techniques. It emphasizes our previous findings of Li_2SnO_3 being a slow Li ion conductor.

Spin-spin relaxation: T_2

In addition to SLR measurements probing Li motion via the decay of the longitudinal magnetization, the decay of the transversal magnetization is caused by spin-spin relaxation. The decay of the corresponding magnetization transients follows a single-exponential behavior: $M(xy)' = M_0 \exp(-t / T_2)$. Rates were recorded over a broad temperature range from 246 K to 593 K. Up until 391 K we observed a temperature-independent behavior with T_2 being in the order of 7×10^{-5} s. Note that in this regime Li mobility is very low, with residence times smaller than 10^{-4} s, as can be deduced from the rigid-lattice line width of ν_{RL} (*vide supra*). In general, the transversal relaxation process is slowed down by fast Li diffusion, where local magnetic fields are averaged over time. The resulting decrease of R_2 is Arrhenius-activated and allows an estimation of the Li diffusion energy E_A.

Here, the transversal relaxation rates slightly increase up to $T = 593$ K whereas Li jump rates have not yet reached the order of the inverse rigid lattice line width, causing in R_2 to decrease. These findings corroborate T_1 measurements where the diffusion-induced relaxation rate peak is found at $T \gg 593$ K, where the jump rate is in the order of the motional correlation rate: $\omega_0 \tau_c \approx 1$.

Spin alignment echo NMR

Spin-alignment echo NMR extends the timescale of our portfolio of microscopic NMR techniques. Along with 2D exchange NMR methods quantitative information can be obtained on ultra-slow Li dynamics, up to the order of a few jumps per minute.[7]

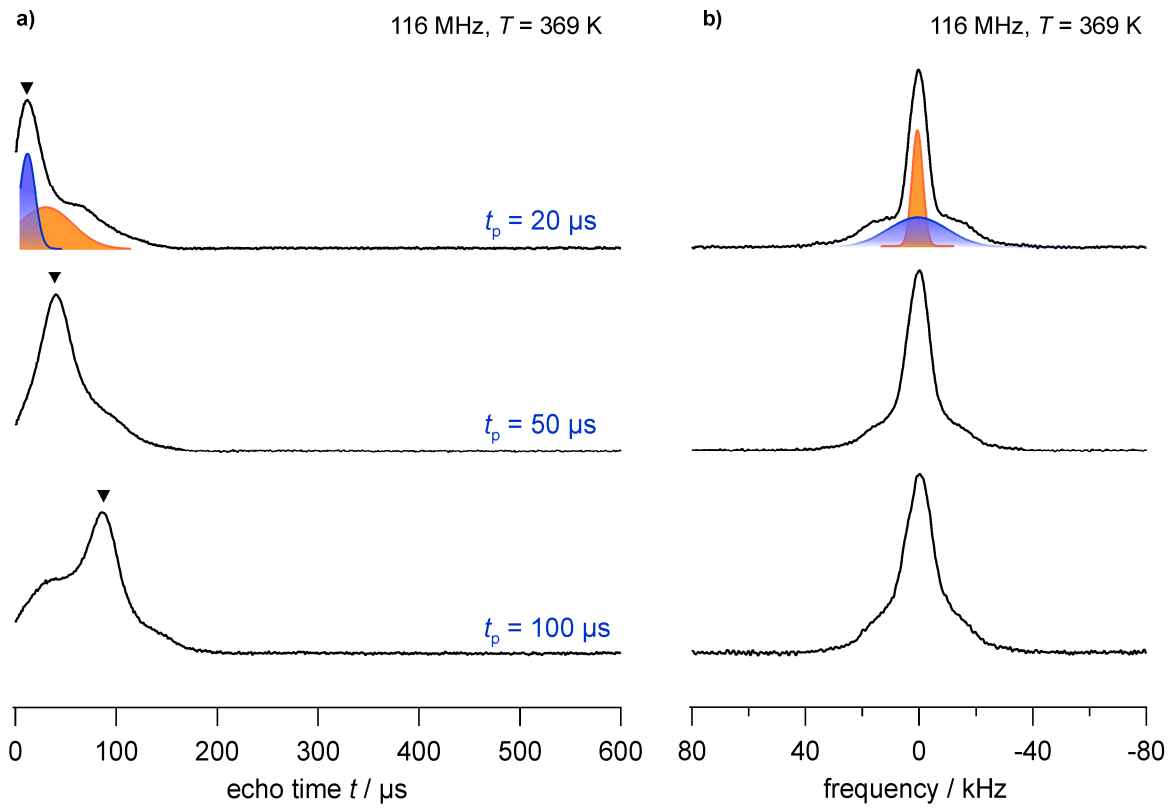

Figure 3: a) ^{7}Li NMR spin-alignment echoes recorded with the Jeener-Broekart pulse sequence choosing a mixing time of $t_m = 10$ µs. Echoes are composed of a broad dipolar echo (shown in orange) and a sharply decaying quadrupole intensity (in blue); Fourier transformation starting from the top of the echo (as indicated by the black triangles) lead to the corresponding echo spectra as shown in b).

Information on the timescale of the Li motion process is obtained by varying the mixing time t_m, while the variation of t_p tunes the sensitivity of the SAE experiment and gives information on the geometry of the process. Increasing the evolution time enables us to increase the resolution between Li sites with similar EFG. Normally t_p is chosen to be as short as possible in order to suppress strong homonuclear dipole-dipole interaction of the ^{7}Li nuclei and obtain a pure quadrupolar response. Figure 3a shows spin-alignment echoes recorded at various evolution times. The spin-alignment (quadrupolar) echo, starting to appear at $t = t_p$, is superimposed by a broad dipolar echo (*cf.* Qi *et al.*[22]). Note that at short evolution times the quadrupolar echo can be more easily distinguished from the broad contribution. With increasing t_p the intensities of both contributions decrease individually with the dipolar response predominating at t_p = 100 µs. To be precise, note that the echo appears at $t' = t_p + t_a$ with t_a reflecting receiver dead-time effects and the influence of rf pulses. The influence of t_a gets smaller with t_p; for t_p = 20 µs we find t_a = 12 µs, while for $t_p \geq 50$ µs t_a amounts for 10 µs. The dependence of the position of the quadrupolar echo as a function of the mixing time is discussed in more detail for ^{6}Li SAE NMR studies by Wilkening *et al.*[23]

Corresponding SAE spectra (*cf.* Fig. 3b) are obtained after Fourier transformation starting from the top of the echo, yielding two-component spectra composed of a sharp dipolar central transition on top of a quadrupolarly broadened contribution. The latter represents a superposition of three distinct quadrupole powder patterns of the electrically inequivalent Li sites in Li_2SnO_3.[4] With increasing t_p the spectra are increasingly governed by dipole-dipole interactions. Note that, for longer evolution times, additional peak broadening after Fourier transformation is due to intensity loss.

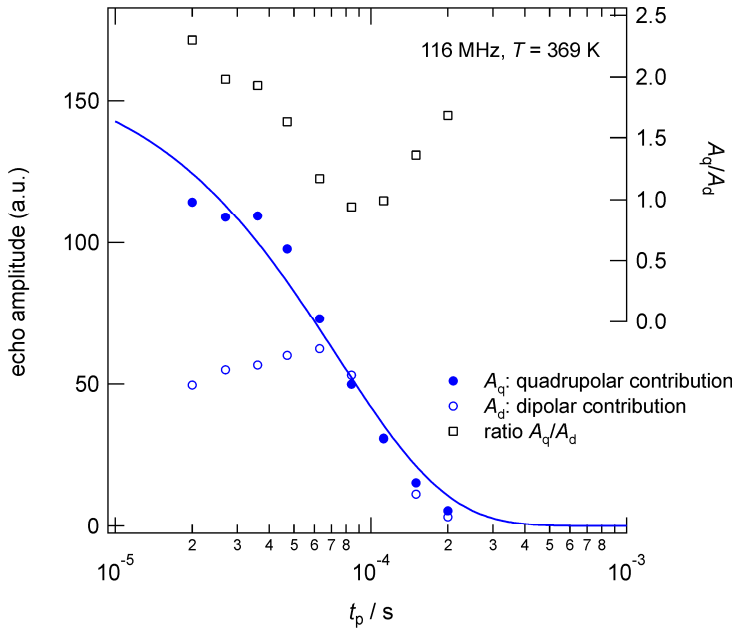

Figure 4: Echo amplitudes of quadrupolar (A_q) and dipolar contributions (A_d) to the ^{7}Li spin-alignment-echo (shown in Fig. 3a) as a function of the evolution time t_p. The solid line represents an exponential fit yielding a transverse SAE decay rate $T_{2,q}$. For comparison the ratio A_q/A_d is shown at the top of the graph.

If the echo amplitude is recorded as a function of the evolution time at a fixed mixing time ($t_m \rightarrow 0$) a separation of dipolar contributions to the spin-alignment signals can usually be achieved for $t_m \rightarrow 0$ and short t_p.[22,24–26] As can be seen in Figure 4, the echo amplitudes A_q and A_d change as a function of the preparation time, owing to transverse dephasing of the Li spins. In fact, an exponential fit of A_q yields a transverse SAE decay rate $T_{2,q} = 74(8)$ µs (at $T = 369$ K) which corroborates nicely our T_2 measurements, where spin-spin relaxation times T_2 were in the order of 70 µs. As expected, the longer the preparation time, the more dipolar information is stored with an amplitude maximum at $t_p = 63$ µs. At $t_p > 63$ µs the dipolar echo decreases, similarly to the spin-alignment echo, with $T_{2,d} = 60(10)$ µs (at $T = 369$ K), as deduced from an exponential fit. The ratio A_q/A_d turns out to be ca. 1 at $t_p = 112$ µs. At larger preparation times it increases before it gradually increases at sufficiently long preparation times.

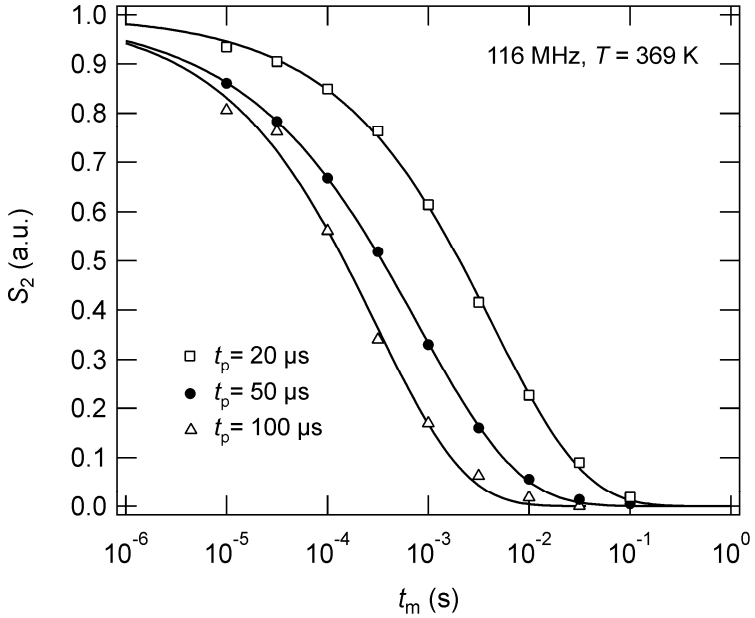

Figure 5: ^{7}Li SAE two-time correlation functions for a fixed evolution time and variation of the mixing time. The corresponding correlation rates, which were obtained from a (stretched) exponential fit (solid lines), are shown in the Arrhenius representation below (see Figure 6)

In order to study the influence of the generation of dipolar order onto τ_{SAE} we recorded echo decay curves S_2 at various mixing times of t_p = 20 µs; t_p = 50 µs, t_p = 100 µs as a function of temperature and mixing time t_m. Figure 5 shows the corresponding decay curves at a temperature of 369 K. Accordingly, the echo decay times $\tau(t_p)$ can also be directly obtained by parametrizing the S_2-transients with a stretched exponential function. Here, the echo decay times $\tau(t_p)$, recorded at 369 K (Fig. 5) decrease by a factor of 14 in the range 20 µs $\leq t_p \leq$ 100 µs. At lower temperatures, *e.g.* at 296 K, we even found a much larger t_p-dependence as $\tau(t_p)$ changes by a factor of 349 in the same evolution time range. If $\tau(t_p)^{-1}$ is monitored as a function of temperature in an Arrhenius-type plot (*cf.* Fig. 6, full circles) this strong dependence on the evolution time is evident in the low-T regime, where the difference spans several decades. With increasing temperature this dependence grows continuously weaker; rates seem to coincide at $T \geq$ 513 K. The fact that $\tau(t_p)$ only weakly depends on t_p at elevated temperatures can be related to an increase of the "Li jump angle", as has been reported by Qi for glassy β-spodumene.[25] In this material the disorder of Si^{4+} and Al^{3+} within the SiO_4 and AlO_3 tetrahedra leads to disordered EFGs; as a result Li motion occurs along the EFG-primary axes at both at large and small angles, *i.e.* these small-angle motions lead to a strong t_p-dependence of the echo decay times at lower temperatures.[27]

Also similarly, in the case of Li_2SnO_3, disorder in the ionic structure might cause this behavior.[4] If the nuclei interact with multiple, yet very similar EFG, as it is likely for Li_2SnO_3 with three electrically similar sites,[4] $\tau(t_p)$ is strongly influenced by the evolution time.

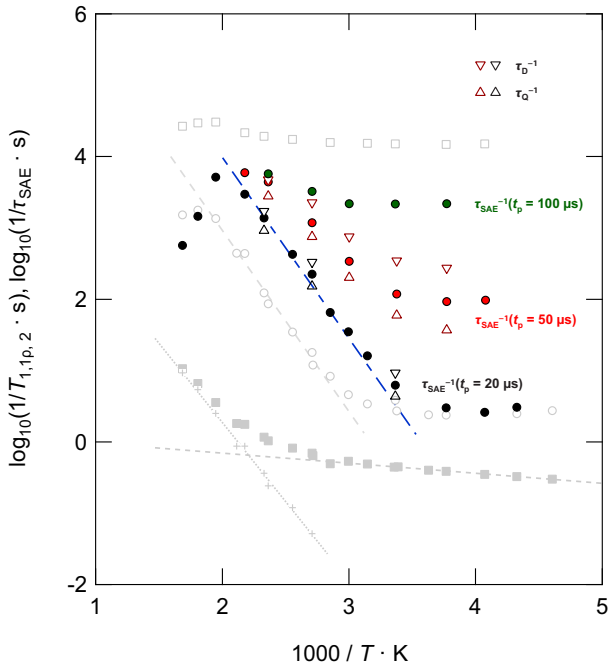

Figure 6: Arrhenius representation of the echo decay rates τ_{SAE} recorded at different sets of t_p, as a function of temperature. If the preparation time is chosen as short as possible (t_p = 20 µs) the echo decay rates represent the respective Li jump rates which allow the determination of a mean E_a from a linear fit. (See text for further information). The empty triangles represent the individual dipolar and quadrupolar decay rates τ_D^{-1} and τ_Q^{-1}.

In another approach dipolar and quadrupolar contributions can be extracted via the respective ^{7}Li SAE peak areas, which were obtained after Fourier transformation starting from the top of the echo. The peak areas of the central intensities and SAE powder pattern were fitted with Gaussians; and from the transients, *i.e.* peak areas as a function of the mixing time, characteristic quadrupolar $\tau_Q(t_p)^{-1}$ and dipolar $\tau_D(t_p)^{-1}$ decay rates were determined for t_p = 20 µs and t_p = 50 µs , as represented by the empty triangles in Fig. 6. It can be seen that echo decay rates $\tau(t_p)^{-1}$ determined directly via integration of the echo decay (at $t = t_p$) as a function of t_m, pose a mean value taking both spin-alignment and dipolar order

into account. At a short evolution time of t_p = 20 µs both $\tau_Q(t_p)^{-1}$ and $\tau_D(t_p)^{-1}$ are in the same order in the temperature range 295 K ≤ T ≤ 429 K; *i.e.* $\tau_Q(t_p)^{-1} \approx \tau_D(t_p)^{-1} \approx \tau(t_p)^{-1}$. If t_p is increased, the echo decay is more and more predominated by homonuclear dipole-dipole contributions, which, decay faster than the "pure" S_{2q} and the mean S_2, *e.g.* at T = 295 K: $\tau_D(t_p$ = 50 µs) = 0.0029 s and $\tau_Q(t_p$ = 50 µs) = 0.017 s. Interestingly, with increasing T dipole-dipole and quadrupolar interaction are averaged, as a result of the onset of Li motion, and $\tau_Q(t_p) \approx \tau_D(t_p)$.

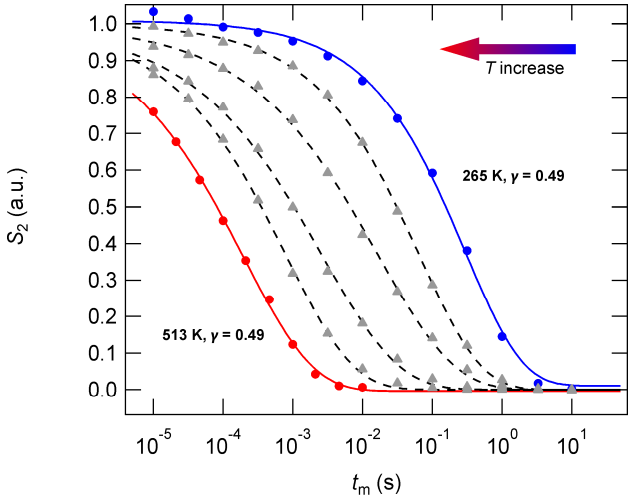

Figure 7: Two-time correlation functions S_2 (t_p = 20 µs), parametrized by stretched exponentials containing τ_{SAE} and the stretching factor γ at different temperature values.

Ultimately, by variation of t_m (at t_p = 20 µs) we can monitor the timescale of successful Li jumps between electrically inequivalent Li sites. In figure 7 echo decay curves S_2 (t_p, t_m, t = t_p) are shown as a function of temperature from which the Li jump rates $1/\tau_{SAE}$ can be extracted. The echo amplitudes were read out starting from the top of the echo (t = t_p) and can be parametrized with stretched exponentials: $S_2(t_m) = (1 - S_\infty)\exp\left(-(t_m / \tau_{SAE})^{\gamma}\right)$, with S_∞ denoting the final-state correlation factor and stretching factors γ ranging between 0.53 (T = 265 K) and 0.39 (T = 513 K), as shown in Figure 7. It can be also observed that S_2 decreases towards a final value of 0 (S_2 = S_0 = 0), *i. e.* the decay of the echo caused by relaxation process, being characteristic for a single isotropic motion process. The obtained decay rates are plotted as a function of 1000/T in the Arrhenius representation shown in Figure 6. In the low-T range between 231 K and 297 K τ_{SAE} lies in the order of 0.3 to 0.4 s coinciding with SLR_ρ back-

ground rates. At higher T rates follow Arrhenius behavior: $\tau_{SAE} \propto \exp(-E_a/(k_B T))$ yielding a hopping energy of $E_a = 0.46(2)$ eV, as deduced from the linear fit.

The consistency of this E_a value with what was obtained in SLR ($E_a = 0.44(1)$ eV) and SLR_ρ ($E_a = 0.45(2)$ eV) NMR points to a sole diffusion process which can be probed over a range of ten decades. Taking into account our ^{6}Li NMR studies on the same material, where we could distinguish between three distinct sites and two diffusion processes[18]; this activation energy can be regarded as a mean value for all the hopping processes present in the material. Considering the structural similarity of the sites it seems highly plausible that the jumping processes between these three sites can be activated with similar E_a in the range of 0.44(2) – 0.45(2) eV. Also, with SAE NMR we can directly access a characteristic Li self-diffusion coefficient at room temperature, transforming the corresponding $1/\tau_{SAE}$ via the Einstein-Smoluchowski equation *(vide supra)*. Assuming three-dimensional isotropic diffusion we can deduce $D \approx 9 \times 10^{-20}$ m^{2}s^{-1} at $T = 297$ K, typical for a slow Li ion conductor, similarly to what has been previously reported for isostructural β-Li_2TiO_3.[28] Compared to $D_\rho = 3.8 \times 10^{-15}$ m^{2}s^{-1}, as deduced from the "preliminary" $R_{1\rho}$ maximum at 555 K, the corresponding D_{SAE} yields a somewhat lower value of 3.5×10^{-16} m^{2}s^{-1}. The value of D_ρ might be additionally influenced by such artefacts as correlation effects local fields, hereby altering ν_{lock}.

Conclusion/Summary

Li_2SnO_3 serves as an interesting model system to study Li^+ dynamics with the help of ^{7}Li relaxation NMR and spin-alignment echo NMR which is capable of probing long-range diffusion parameters from a microscopic point of view. Results from relaxometry measurements both yield a similar activation energy of ≈ 0.4 eV. The high-T flank of the rate peak could not be probed with either method, which is why theses values characterize short-range Li motion. Additionally R_1 and $R_{1\rho}$ can be influenced by correlation effects which alter the slope of the rate peak on the low-T side. As SLR in the rotating frame of reference is sensitive to lower Li jump rates in the kHz range, the corresponding rate peak is usually shifted towards lower temperatures, indicating a rate maximum around $T = 555$ K, *i.e.* the Li jump rate is in the order of 2.5×10^5 s^{-1}.

In contrast to SLR in the laboratory and rotating frame of reference the jump rate is directly included in the measured (two-time) correlation function measured via SAE NMR. Importantly, this allows us to *directly* determine a Li *self-diffusion* coefficient at room temperature ($T = 297$ K): $D \approx 9 \times 10^{-20}$ m^{2}s^{-1}

for Li_2SnO_3. Interestingly, the long-range Li motion probed by SAE is activated with an E_a = 0.44(2) eV, in accordance with results from the relaxometry measurements. These findings strongly indicate that we find a similar diffusion mechanism for short- and long-range Li ion dynamics.

Additional experiments, *viz.* recording spin-alignment echoes at t_p > 20 μs and the variation of the evolution time at fixed mixing times (so-called "cross-measurements"), were conducted to study the influence of dipolar contributions to the measured echoes, spectra and decay rates. Increasing the preparation time allows for a better resolution of quadrupolar and dipolar contributions, which is reflected by the corresponding echo decay rates $\tau_Q(t_p)^{-1}$ and $\tau_D(t_p)^{-1}$, differing by one order of magnitude at 297 K for t_p = 50 μs. Here, $\tau(t_p)^{-1}$ (and thus $\tau_Q(t_p)^{-1}$ and $\tau_D(t_p)^{-1}$) also strongly depend on the temperature which is due to the interaction of the nuclei with very similar EFG, *viz.* the three electrically similar Li sites in Li_2SnO_3. This temperature-dependence, which grows weaker with elevated temperature, can also be traced back to ionic disorder in the crystal structure.

Finally, by monitoring the respective echo intensities as a function of the preparation time, a transversal relaxation rate $T_{2,q}$ = 74(8) μs is obtained, in agreement with "classical" spin-spin relaxation measurements.

Overall, together with our previous ^{6}Li MAS NMR study[4], we were able to obtain a detailed picture of the complex dynamics, involving distinct and preferred diffusion pathways, which are nonetheless characterized by similar dynamical parameters, *i.e.* activation energies and Li jump rates.

Acknowledgment

J. L. and M. W. thank the DFG Research Unit 1277 (grant no.: WI3600 4-2) for financial support. J. L. is grateful to V. Epp for numerous discussions.

References

1 P. Heitjans, A. Schirmer and S. Indris, in *Diffusion in Condensed Matter*, eds. P. Heitjans and J. Kärger, Springer, Berlin, 2005, pp. 367–415.

2 P. Heitjans, S. Indris and M. Wilkening, in *Diffusion Fundamentals*, eds. J. Kärger, F. Grinberg and P. Heitjans, Leipziger Universitätsverlag, Leipzig, 2005, pp. 226–245.

3 R. Böhmer, K. R. Jeffrey and M. Vogel, *Prog. Nucl. Magn. Reson. Spectrosc.*, 2007, **50**, 87–174.

4 J. Langer, *J. Phys. Chem. C*, 2015, submitted.

5 J. A. Brant, D. M. Massi, N. A. W. Holzwarth, J. H. MacNeil, A. P. Douvalis, T. Bakas, S. W. Martin, M. D. Gross and J. A. Aitken, *Chem. Mater.*, 2015, **27**, 189–196.

6 M. Vijayakumar, S. Kerisit, Z. Yang, G. L. Graff, J. Liu, J. A. Sears, S. D. Burton, K. M. Rosso and J. Hu, *J. Phys. Chem. C*, 2009, **113**, 20108–20116.

7 P. Bottke, D. Freude and M. Wilkening, *J. Phys. Chem. C*, 2013, **117**, 8114–8119.

8 N. Bloembergen, E. M. Purcell and R. V Pound, *Phys. Rev.*, 1948, **73**, 679–712.

9 P. M. Richards, *Solid State Commun.*, 1978, **25**, 1019–1021.

10 J. Jeener and P. Broekaert, *Phys. Rev.*, 1967, **157**, 232–240.

11 D. Ailion and C. P. Slichter, *Phys. Rev. Lett.*, 1964, **12**, 168–171.

12 C. Brinkmann, S. Faske, B. Koch and M. Vogel, *Zeitschrift für Phys. Chemie*, 2010, **224**, 1535–1553.

13 Redfield A, *Phys. Rev.*, 1955, **98**, 1787–1809.

14 D. C. Ailion and C. P. Slichter, *Phys. Rev.*, 1965, **137**, A235–A245.

15 D. C. Look and I. J. Lowe, *J. Chem. Phys.*, 1966, **44**.

16 E. Fukushima and S. B. W. Roeder, *Experimental Pulse NMR: A Nuts and Bolts Approach*, Addison-Wesley Pub. Co., Reading, MA, Advanced B., 1981.

17 R. Böhmer, *J. Magn. Reson.*, 2000, **147**, 78–88.

18 J. Langer and M. Wilkening, *to be Publ.*

19 A. Abragam, *The Principle of Nuclear Magnetism*, Clarendon Press: Oxford, U.K., 1961.

20 J. R. Hendrickson and P. J. Bray, *J. Magn. Reson.*, 1973, **9**, 341–357.

21 P. M. Richards, in *Topics in Current Physics, Physics of Superionic Conductors*, Springer, Berlin, Heidelberg, 1979, p. 141.

22 F. Qi, G. Diezemann, H. Böhm, J. Lambert and R. Böhmer, *J. Magn. Reson.*, 2004, **169**, 225–239.

23 M. Wilkening, A. Kuhn and P. Heitjans, *Phys. Rev. B*, 2008, **78**, 54303.

24 F. Qi, T. Jörg and R. Böhmer, *Solid State Nucl. Magn. Reson.*, 2002, **22**, 484–500.

25 F. Qi, Johannes Gutenberg-Universiät Mainz, 2003.

26 X.-P. Tang and Y. Wu, *J. Magn. Reson.*, 1998, **133**, 155–165.

27 R. Böhmer, G. Diezemann, G. Hinze and E. Rössler, *Prog. Nucl. Magn. Reson. Spectrosc.*, 2001, **39**, 191–267.

28 B. Ruprecht, M. Wilkening, R. Uecker and P. Heitjans, *Phys. Chem. Chem. Phys.*, 2012, **14**, 11974–11980.

P3: (pp. 137–144)

3.2.2 Mechanical detection of ultraslow, Debye-like Li-ion motions in $LiAlO_2$ single crystals

J.Langer, D. Wohlmuth, A. Kovalčik, V. Epp, F. Stelzer, and M. Wilkening
Ann. Phys. **527**, 523 (2015)

Excursus: Dynamical Mechanical Analysis *vs.* Electrical Conductivity Measurements
In principle dynamical mechanical analysis is based on the inelastic relaxation of the sample after being subjected to mechanical stress. Usually a rectangular piece of the material (with the geometry depending on the operating mode) is fixed between clamps. For the DMA studies presented below a single cantilever clamp system was used with a cantilever oscillating at various frequencies, thus exciting the sample at the same time with a dynamic force. Consequently, this results in an internal friction (or mechanical loss) that is given by the ratio:

$$\tan\delta = \frac{E''}{E'}$$

with E'' denoting the loss modulus and E' as the storage modulus. This loss factor describes ionic displacements (if $\tan\delta < 0$) in the sample. By plotting $\tan\delta$ as a function of temperature, a characteristic mechanical loss peak is obtained. The temperature at the peak maximum is used to obtain the mechanical relaxation rate.

In order to relate mechanical loss spectra with Li ion motion we estimated the temperature for a certain *motional correlation rate* τ^{-1} *e.g.* 1 Hz from conductivity measurements. Here, the solid-state diffusion coefficient D_σ derived from a DC conductivity isotherm can be related with a *motional correlation rate* via the Einstein-Smoluchowski relation, similar to NMR relaxation measurements:

$$\tau^{-1} = \frac{6}{l^2} \cdot D_\sigma$$

with l as the jump distance of the Li ion and $D_\sigma = D^{\mathrm{T}}$ (assuming a correlation factor of 1). In this manner we can relate a motional correlation rate, *i.e.* Li jump rate, of 1 Hz to D_σ and the corresponding temperature value. A Li jump rate of 1 Hz should be accessible by mechanical relaxation if we perform the measurement of $\tan\delta$ at a fixed oscillation frequency of 1 Hz. If the mechanical loss is caused by Li self-diffusion, the mechanical loss peak should appear at the temperature value, derived from D_σ (for a jump rate of 1 Hz).

Ann. Phys. (Berlin) **527**, No. 7–8, 523–530 (2015) / DOI 10.1002/andp.201500205

annalen der physik

Mechanical detection of ultraslow, Debye-like Li-ion motions in $LiAlO_2$ single crystals

Julia Langer[1,2,*], *Dominik Wohlmuth*[1], *Adriana Kovalcik*[1], *Viktor Epp*[1,2], *Franz Stelzer*[1], *and Martin Wilkening*[1,2,**]

Received 31 May 2015, revised 14 July 2015, accepted 16 July 2015
Published online 5 August 2015

Single crystalline $LiAlO_2$ is known as a very poor ion conductor. Thus, in its crystalline form it unequivocally disqualifies itself from being a powerful solid electrolyte in modern energy storage systems. On the other hand, its interesting crystal structure proves beneficial to sharpen our understanding of Li ion dynamics in solids which in return might influence application-oriented research. $LiAlO_2$ allows us to apply and test techniques that are sensitive to extremely slow Li ion dynamics. This helps us clarifying their diffusion behaviour from a fundamental point of view. Here, we combined two techniques to follow Li ion translational hopping in $LiAlO_2$ that can be described by the same physical formalism: dynamic *mechanical* relaxation and *electrical* relaxation, *i.e.*, ionic conductivity measurements. Via both methods we were able to track the same transport mechanism in $LiAlO_2$. Moreover, this enabled us to directly probe extremely slow Li exchange rates at temperatures slightly above 430 K. The results were compared with recent insights from nuclear magnetic resonance spectroscopy. Altogether, an Arrhenius-type Li diffusion process with an activation energy of ca. 1.12 eV was revealed over a large dynamic range covering 10 orders of magnitude, *i.e.*, spanning a dynamic range from the nano-second time scale down to the second time scale.

1 Introduction

The fundamental study of diffusion processes [1, 2], particularly that of oxygen anions and lithium cations, builds the basis for the development of modern electrochemical energy storage systems that meet today's market demands. To deepen our understanding of diffusion processes in general, model substances need to be studied with complementary techniques preferably over a large dynamic range. This will help us to correlate dynamic properties, including particularly the elemental steps of ion hopping in solid electrolytes [3], with structural motifs.

γ-$LiAlO_2$ serves as such a model substance. It is known to be a very poor ion conductor. Therefore, the oxide, which is practically an electronic insulator, is considered to act as advanced tritium breeding blanket material. The γ-modification of $LiAlO_2$ crystallizes with the space group $P4_32_12$; the Li ions reside in the tetrahedral voids (4a). The LiO_4 tetrahedra, as well as the AlO_4 ones, are connected by corner sharing; presumably, this arrangement is responsible for the extremely low Li^+ diffusivity observed. An illustration of the crystal structure is shown in Fig. 1. At room temperature the solid-state diffusion coefficient is expected to be in the order of 10^{-26} $m^2\,s^{-1}$; this roughly corresponds to an Li ion conductivity well below 10^{-15} $S\,cm^{-1}$ which is at the limits of being detectable by impedance spectrometers. A colossal increase of Li ion conductivity by 7 orders of magnitude has recently been observed for nanostructured, disordered $LiAlO_2$ that has been prepared from the coarse grained starting material by high-energy ball milling [4]. During mechanical treatment the oxide mainly becomes amorphous; partly, it is transformed into the δ-form being a high-pressure modification.

Here, we applied electrical conductivity measurements performed over a broad frequency and temperature range to characterize long-range ion transport in γ-$LiAlO_2$ single crystals. At low temperatures we used dynamic mechanical analysis (DMA) [5–9] to probe lithium relaxation rates. Both techniques yield consistent results.

* See also for correspondence E-mail: julia.langer@tugraz.at
** Corresponding author E-mail: wilkening@tugraz.at
[1] Christian Doppler Laboratory for Lithium Batteries, and Institute for Chemistry and Technology of Materials, Graz University of Technology (NAWI Graz), Stremayrgasse 9, 8010 Graz, Austria
[2] DFG Research Unit "Mobility of Lithium Ions in Solids", Graz University of Technology, Stremayrgasse 9, 8010 Graz, Austria

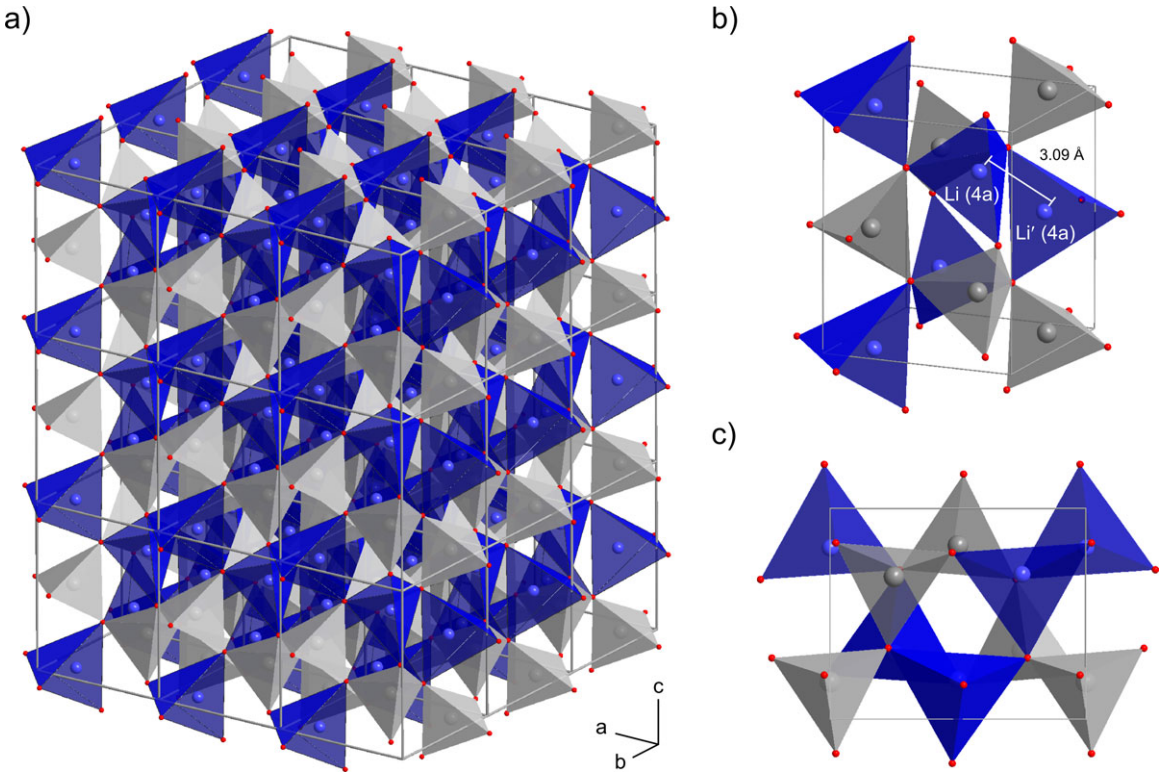

Figure 1 Crystal structure of $LiAlO_2$: a) $3 \times 3 \times 3$ supercell, b) unit cell illustrating the connection of the LiO_4 tetrahedra by corner sharing; c) view along the *a*-axis.

A comparison is possible after the DC conductivity values have been converted into solid-state diffusion coefficients via the Nernst-Einstein relation. Considering the conductivity isotherms, they give strong evidence for an overall mean relaxation process that is characterized by an activation energy of 1.12 eV. Obviously, the same motional process is also seen by DMA. This nicely corroborates a previous study by Indris et al. using ^{7}Li NMR spectroscopy [10].

2 Experiment

The $LiAlO_2$ single crystals studied in the present work were obtained commercially from Crystal GmbH. The glass-like, transparent rectangles were pulled along the [100] orientation and polished on one side.

For the broadband conductivity analysis squares with an edge length of 1 cm and a thickness of 0.93 cm were prepared. To ensure electrical contact, Au electrodes of about 100 nm thickness were applied with a sputter coater (Leica EM SCD050) in custom vacuum equipment. Impedance measurements were carried out according to a two-terminal AC method with a Novocontrol Concept 80 broadband analyzer (Alpha-AN, Novocontrol). The analyzer was connected to a BDS 1200 cell in combination with an active ZGS cell interface from Novocontrol; this setup allowed temperature-variable 2-electrode measurements.

The temperature was automatically controlled with a nitrogen-purged QUATRO cryosystem (Novocontrol). In order to create a highly constant nitrogen gas flow the cryo-system is working with a heating element that builds up a specified pressure in a liquid nitrogen dewar. After being heated by a gas jet, the freshly evaporated nitrogen flows directly through the sample cell that is mounted in the cryostat. This setup allows very stable system operation with an accuracy better than $\pm$ 0.1 K.

In the case of high temperature conductivity measurements the Concept 80 analyzer was used and connected to a Novotherm-HT 1600 cell. The HT 1600 cell is designed to record impedance measurements from ambient to 1870 K. The temperature resolution was 0.1 K; high-temperature measurements were carried out in controlled nitrogen atmosphere. The cells were operated with WinDETA control software via an IEEE 488 (GPIB) interface; for the HT 1600 cell a ZG4 test interface was used. Altogether the whole setup with the two cells, the

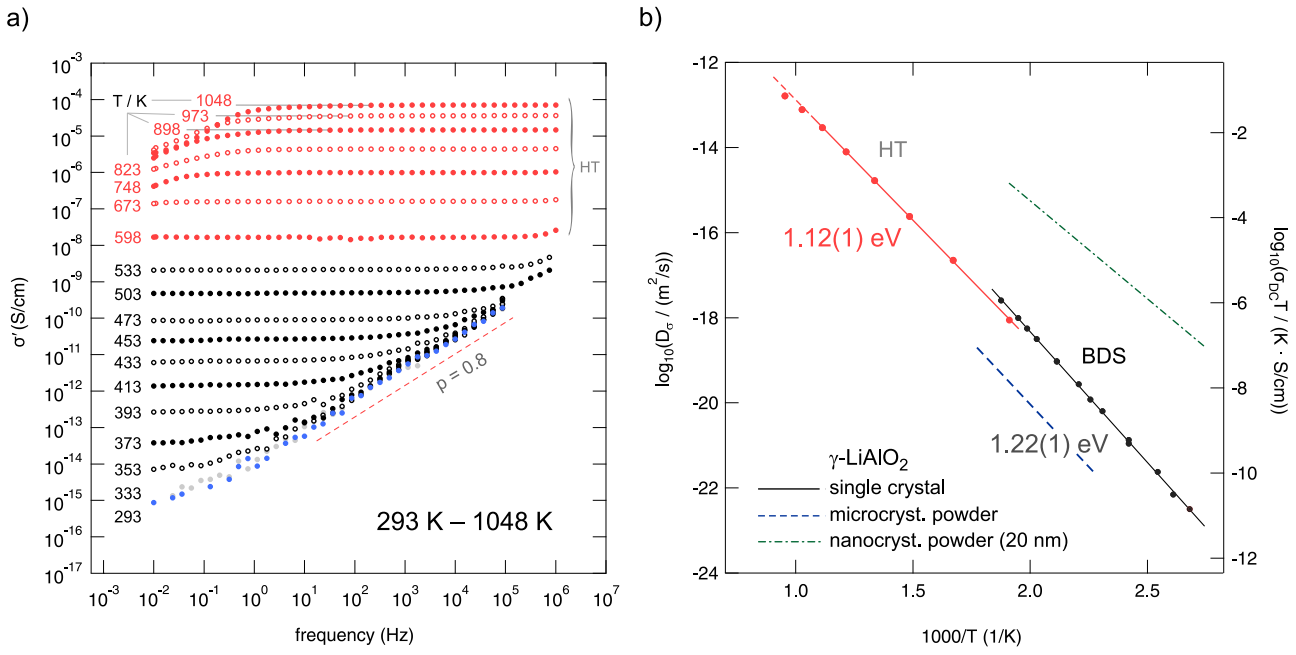

Figure 2 a) Conductivity isotherms (real part of the complex conductivity σ' *vs* frequency ν) recorded at temperatures ranging from 293 K to 1048 K. The frequency range covered was 10^{-2} Hz – 10^{6}. Above 595 K the spectra were acquired with the HT 1600 impedance cell. Below 340 K the isotherms do not depend on temperature any longer; σ' follows a power law according to $\sigma' \propto \nu^{0.8}$. b) Right axis: Arrhenius plot of the DC conductivity values ($\sigma'(\nu \rightarrow 0) \equiv \sigma_{DC}$); data is shown as $\log_{10}(\sigma_{DC}T)$ *vs* 1000/*T*. Left axis: Temperature dependence of the solid-state diffusion coefficient D_σ that is obtained after conversion of σ_{DC} with the help of the Nernst-Einstein equation (see text.) Solid lines represent linear fits yielding activation energies, depending on the *T*-range and cell used, of 1.22 eV and 1.12 eV, respectively. For comparison, ion conductivities of a microcrystalline and a nanocrystalline powder sample are also shown, see Ref. [4]. Obviously, ion transport in powder samples is additionally slowed down by blocking grain boundary effects.

BDS cell and the HT cell, is able to record impedances and permittivities at frequencies ranging from few μHz up to 20 MHz at temperatures ranging from 170 K to 1870 K.

Dynamic mechanical analysis (DMA), see especially [5], was performed on a DMA Q800 (TA Instruments, USA) using a single cantilever clamp system. Several calibrations were done before the DMA analyses that include electronic, force, and dynamic calibration as well as adjustment of the position and calibration of the cantilever clamp system using a precise steel standard with the following dimensions 35.54 × 12.77 × 3.20 mm.

We measured the mechanical loss factor $\tan\delta = E''/E'$, where E'' is the loss modulus and E' is the storage modulus. For the experiments rectangular pieces of $LiAlO_2$ in the size of about 17.3 × 10.03 × 0.93 mm were used. The DMA Q800 was operated in a frequency/strain mode, using a single cantilever clamp system at various oscillation frequencies ranging from 0.5 to 50 Hz. We used an amplitude of 15 μm. The temperature of each experiment was varied from 290 K to 570 K; the heating rate used was 3 K/min. Measurements were carried out under air atmosphere. The temperatures T at the maxima of the $\tan\delta$ loss peaks recorded at the individual frequencies were used to estimate mechanical relaxation rates.

3 Results and discussion

3.1 Conductivity measurements

Conductivity isotherms (σ' *vs* ν) of the $LiAlO_2$ specimens, which were recorded over a broad temperature range (293 K – 1048 K) and frequency regime (10^{-2} – 10^{6} Hz), are shown in Fig. 2. At very low temperatures, see, *e.g.*, the isotherms at 293 K and 333 K, σ', which is the real part of the complex conductivity, is independent of T. Its variation with increasing frequency follows a power law $\sigma' \propto \nu^{p}$; where the exponent p is 0.8. Such a frequency dependence is often found in this T range, even for structurally disordered ionic materials. $p \rightarrow 1$ would be the characteristic result corresponding to a frequency independent ϵ'' being the imaginary part of the complex permittivity $\hat{\epsilon}$. This behaviour is frequently termed *nearly*

constant loss (NCL); NCL-type behaviour is often related to strictly localized, that is, caged ion dynamics [11]. With increasing temperature the isotherms change and reveal a distinct frequency independent plateau showing up at low frequencies; the associated conductivity can be identified with the DC value. At 433 K, for instance, the isotherm is composed of the DC plateau and a transition regime, that is, a dispersive part, which passes into the $\sigma' \propto \nu^{0.8}$ behaviour with increasing ν. With increasing T the DC plateau starts to dominate the spectra, see, *e.g.*, the isotherm at 673 K. When Li ion transport reaches sufficiently high conductivities the charge carriers pile up in front of the ion blocking electrodes. This polarisation effect manifests itself in a decrease of σ' at sufficiently high T and low frequency. The isotherm at 1048 K is composed of a DC plateau and a polarisation regime determining σ' below 1 Hz.

By reading off the DC conductivity values of the isotherms recorded, an Arrhenius plot can be constructed that is shown in Fig. 2b). Solid lines show fits with an Arrhenius law.

$$\sigma_{DC}\, T = A \exp\left(-E_{a,\,DC}/(k_B T)\right). \tag{1}$$

k_B denotes Boltzmann's constant. It is important to note that the two cells used yield slightly different conductivity values around 500 K. Within the precision of our measurements we can say that the activation energy $E_{a,DC}$ of long-range Li ion transport in $LiAlO_2$ single crystals ranges between 1.22 and 1.12 eV. In order to estimate the corresponding diffusion coefficients we used the Nernst-Einstein equation (eq. (2)) to transform σ_{DC} into D_σ values.

$$D_\sigma = \frac{\sigma_{DC} k_B T}{N q^2}, \tag{2}$$

Here, q denotes the charge of the Li ions and N represents the number density of charge carriers (2.39×10^{28} m^{-3}). At about 400 K the solid-state diffusion coefficient is in the order of 10^{-22} m^2 s^{-1} clearly pointing out the low Li ion diffusivity of $LiAlO_2$ single crystals.

For comparison, Fig. 2 also includes data on a microcrystalline powder sample of γ-$LiAlO_2$, see [4]. Ion conductivities were derived from a pellet that was prepared by cold pressing. The fact that its ionic conductivity is lower than that in single crystalline $LiAlO_2$ points to ion blocking grain boundaries governing through-going ion migration. High-energy ball milling, however, overcomes this barrier by transforming the oxide into a mixture of nanocrystalline $LiAlO_2$ (20 nm in diameter) embedded in an amorphous matrix of lithium aluminium oxide. The nanostructured material shows a much higher ion conductivity than that found for the single crystalline form [4], *cf.* Fig. 2.

3.2 Variable-temperature DMA measurements – comparison with the response from electrical conductivity

Our results using DMA are shown in Fig. 3 that displays the mechanical loss spectra recorded. In order to find out whether the loss peaks can be attributed to Li ion dynamics we estimated the temperature at which the motional correlation rate is in the order of 1 Hz. Using the solid-state diffusion coefficients estimated from σ_{DC}, we can determine the order of magnitude of the underlying Li jump rate in γ-$LiAlO_2$. According to the Einstein-Smoluchowski equation [12, 13] the self-diffusion coefficient, D_{SD} is given by

$$D_{SD} = \ell^2/(6\tau) \tag{3}$$

where ℓ denotes the jump distance of the moving ion, and $1/\tau$ the jump rate.

Finally, the self-diffusion coefficient D_{SD} is linked to D_σ via the relations $D_{tracer} = H_r D_\sigma$ and $D_{tracer} = f D_{SD}$ where D_{tracer} is the so-called tracer diffusion coefficient [1]. H_r and f represent the Haven ratio and the correlation factor, respectively, connecting D_{tracer} with D_{SD}. Altogether this yields

$$D_{tracer} = H_r \frac{\sigma_{DC} k_B T}{N q^2} = f\ell^2/(6\tau) \tag{4}$$

which gives

$$\tau^{-1} = (H_r/f)\frac{6 k_B T}{N q^2 \ell^2} \cdot \sigma_{DC} = (H_r/f)\frac{6}{\ell^2} \cdot D_\sigma \tag{5}$$

directly relating the motional correlation rate τ^{-1}, which is available by nuclear magnetic resonance (NMR) [14–17], for example, with σ_{DC}. Assuming $H_r \approx 1$ and uncorrelated motion ($f = 1$) the ratio H_r/f is of the order of unity, thus, eq. (5) simplifies to

$$\tau^{-1} = \frac{6}{\ell^2} \cdot D_\sigma \tag{6}$$

Besides NMR, values in the order of τ^{-1} should also be accessible by mechanical relaxation. Using eq. (6) a diffusion coefficient in the order of 10^{-20} m^2 s^{-1}, which describes Li diffusion in $LiAlO_2$ at ca. 445 K, corresponds to a jump rate being in the order of 1 Hz. This estimation uses a mean jump distance $\ell \approx 3.1$ Å which represents the shortest Li-Li distance in $LiAlO_2$ (see Fig. 1). Thus,

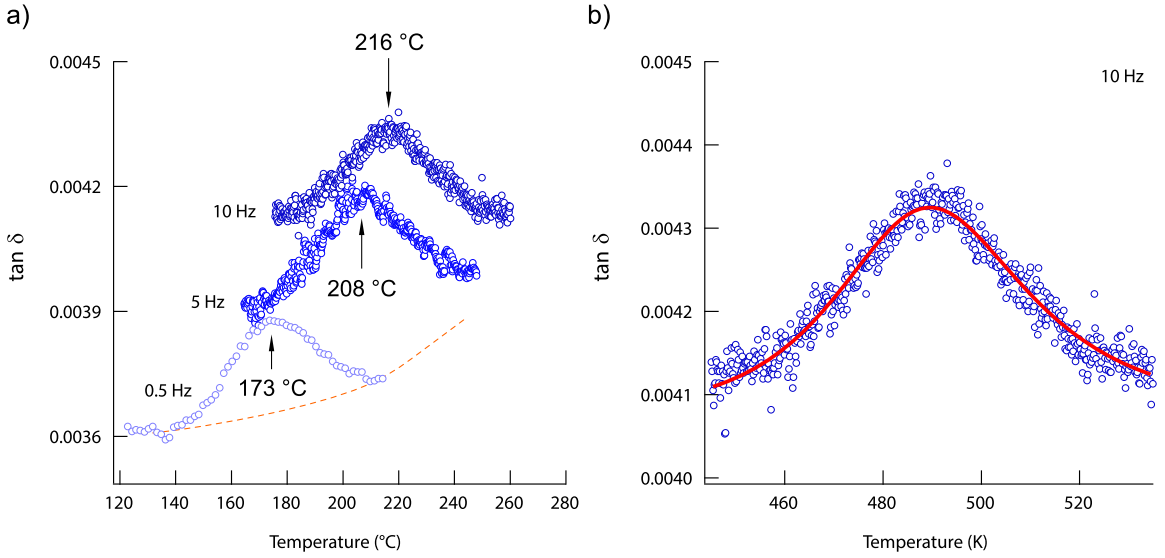

Figure 3 a) Mechanical loss spectra (tan δ vs T) of a $LiAlO_2$ single crystal recorded at 0.5 Hz, 5 Hz and 10 Hz. Intensities are well below tan δ = 0.005. Arrows point to the maxima of the spectra. The dashed line indicates background effects that let the peak at 0.5 Hz appear somewhat asymmetric. Symmetric peaks are seen when background effects do not gain the upper hand. b) Mechanical loss spectrum of $LiAlO_2$ recorded at 10 Hz; the solid line represents a fit according to eq. (10). The parameters a and b turned out to be $a = b = 1$ indicating Debye behaviour that relies on a single exponential relaxation function.

$\tan\delta$ of a DMA measurement carried out at a fixed frequency of $\nu = 1$ Hz is expected to pass through a peak at temperatures well above 400 K — and indeed this is observed in the present case (see Fig. 3).

In DMA the relevant dynamic force $\hat{F}$, having the amplitude F_0, that is applied to excite the sample with an angular frequency $\omega = 2\pi\nu$ is given by

$$\hat{F} = F_0 \exp(i(\omega t + \delta)) \tag{7}$$

δ represents the phase. Young's modulus $\hat{E}$ is defined as

$$\hat{E} = \frac{\hat{F}}{\hat{x}}\frac{1}{k} = E'/iE'' \tag{8}$$

with $\hat{x}$ being the dynamic displacement of the sample, $\hat{x} = x_0 \exp(i\omega t)$, and k representing a constant that depends on the thickness t_1 of the sample, its width w and the distance d between the two metal supports: $k = w/4 \times (t_1/d)^3$. The mechanical loss, $\tan\delta$, (or internal friction) is given by the ratio

$$\tan\delta = \frac{E''}{E'}, \tag{9}$$

as mentioned above. Usually we expect $\tan\delta$ values smaller than 0.4 if they origin from ionic displacements. Care has to be taken to reduce background effects resulting from friction between the sample and the metal supports.

In Fig. 3 the mechanical loss $\tan\delta$ of our DMA measurements is shown as a function of temperature for three excitation frequencies ranging from 0.5 to 10 Hz. In our case $\tan\delta$ values are significantly smaller than 0.005. Hence, it is by far not easy to detect the loss peaks of interests that are due to ion hopping in $LiAlO_2$ single crystals. Fortunately, the DMA Q800 instrument is able to record $\tan\delta$ values with a sensitivity of 10^{-4} using a resolution of 10^{-5}. Proper calibration and positioning is needed as well as the use of an adequate clamp system, here a single cantilever system, that is compatible to the sample geometry and stiffness. Moreover, a precise sample geometry and perfect surface morphology helps reduce background effects. Despite the difficulty with such effects, which seem to increase with increasing excitation frequency, in Fig. 3 a) distinct $\tan\delta$ peaks are visible in the T region expected for Li ion dynamics. For instance, while at $\nu = 0.5$ Hz the loss peak shows up at $T = 446$ K, it is shifted toward higher T (489 K, $\nu = 10$ Hz) if we increase ν by a factor of 20.

We used a double power law to analyze the mechanical loss data. The following function, see especially the study by Almond and West, [18], contains the fitting parameter a and b which are allowed to take values ranging from 0 to 1:

$$\tan\delta(\omega, T) \propto \frac{1}{(\omega\tau)^{-a} + (\omega\tau)^{b}} \tag{10}$$

Original Paper

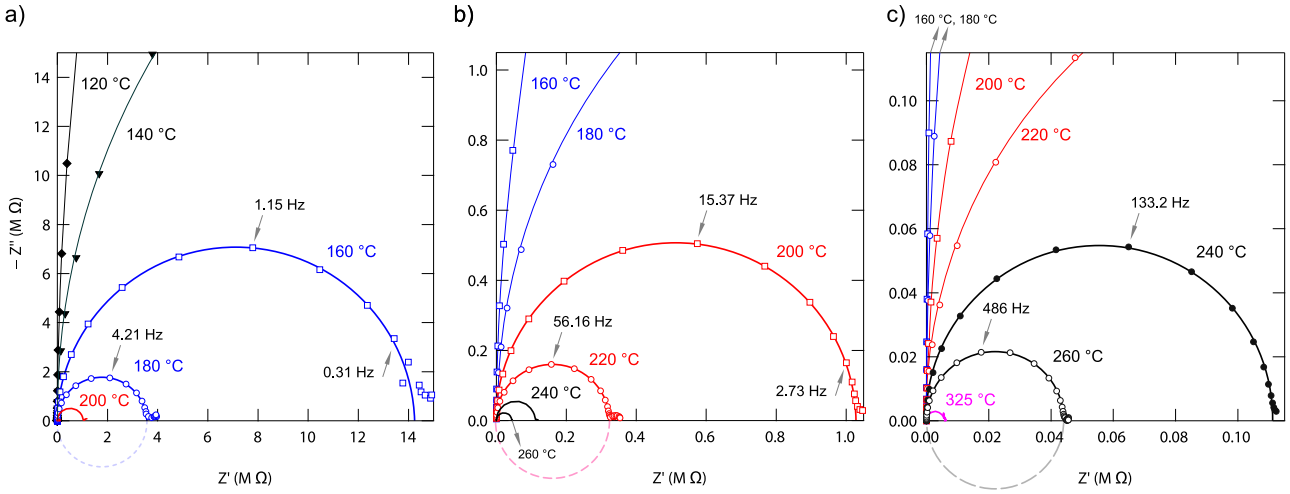

Figure 4 a) to c) Complex plane plots (imaginary part of $\hat{Z}$, $-Z''$, plotted vs the real part Z') of the impedance data recorded for the $LiAlO_2$ single crystals. Non-depressed circles can be used to approximate the data showing that, in accordance with an almost frequency independent σ', Debye behaviour governs ion transport in the T range and frequency regime investigated. The dashed lines represent circles whose center coincides with the Z'-axis.

with the relaxation time τ given via

$$\tau = \tau_0 \exp\left(E_{a,\,ML}/(k_B T)\right) \tag{11}$$

Eq. (10) can also be written in the form

$$\tan\delta(\omega, T) \propto \frac{(\omega\tau)^a}{1+(\omega\tau)^{a+b}} \tag{12}$$

In our case the data can be best represented by choosing $a = b = 1$; this results in pure Debye behaviour. This is also seen in Fig. 4 when we consider the complex plane representation of the complex impedance $\hat{Z}$. The main electrical response that also governs the conductivity spectra, *cf.* the DC plateaus in Fig. 2, can be approximated with a non-depressed semicircle whose center lies on the Z'-axis, see also [19].

Debye-like behaviour is also expected to yield electrical modulus spectra that are characterized by a width at half maximum of 1.14 decades. The complex modulus is related to $\hat{\sigma}$ via the complex permittivity $\hat{\epsilon}$ according to $\hat{M} = 1/\hat{\epsilon}$ with $\hat{\epsilon} = \hat{\sigma}/(i\omega\epsilon_0)$; ϵ_0 denotes the permittivity in vacuum. In Fig. 5 selected modulus spectra $M''(\nu)$ are shown that are scaled such that the spectrum recorded at 393 K served as a reference.

Reading off the relaxation rates at the frequencies where M'' passes through the maxima yields rates that roughly follow Arrhenius behaviour with an activation energy ranging from 1.02 (393 K to 413 K) to 1.12 eV (> 600 K), depending on the temperature range. This is close to the result found by analyzing $\sigma_{DC}(1/T)$ (see above), particularly if we consider higher temperatures. As an

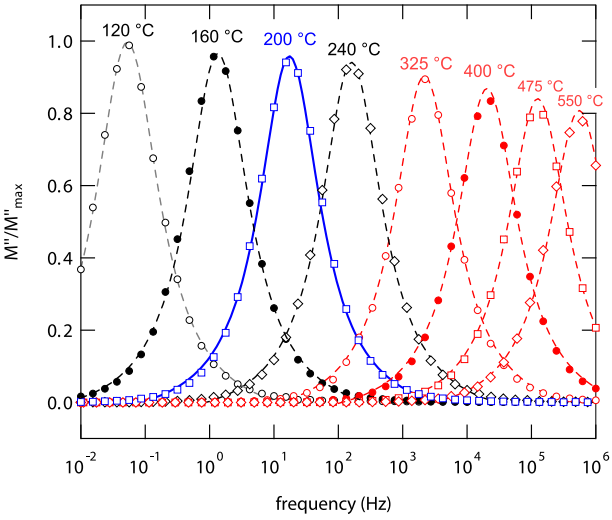

Figure 5 Electric modulus spectra of the $LiAlO_2$ single crystals studied. The shape of the peaks does not change significantly with increasing temperature. Lines are drawn as guides to the eye. The width at half maximum, viz. 1.14 decades, is close to that expected for pure Debye behaviour. M''_{max} is the amplitude of M'' at 393 K.

example, at ca. 473 K the modulus peak shows up at approximately $\nu = 20$ Hz. This electrical relaxation frequency is, within a factor of 4-5, in agreement with the mechanical one of DMA; note that loss peaks are seen at approximately 480 K at 5 Hz (see Fig. 3). Coming back to the shape of the $\tan\delta$ loss peaks of Fig. 3 (see, for instance, b)) the fits according to eq. (10) yield activation energies of $E_{a,ML} = 1.2(1)$ eV and pre-factors in the

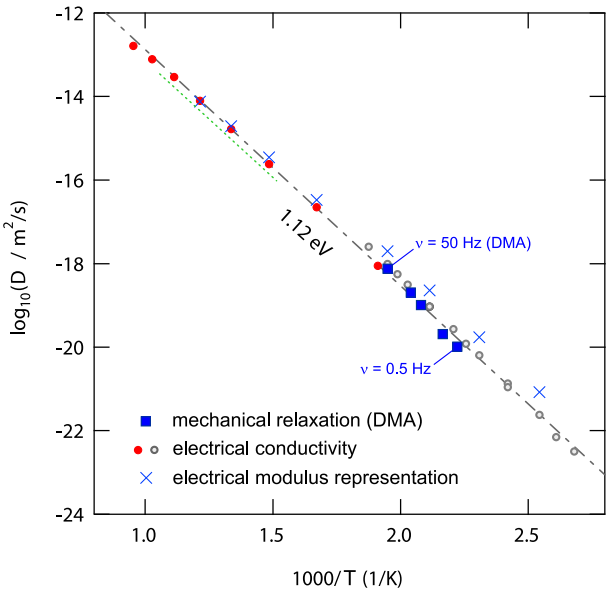

Figure 6 Arrhenius plot of the diffusion coefficients obtained from electrical and mechanical measurements. The dashed-dotted line is an overall fit that includes all of the data points. It yields 1.12 eV as a mean value over the temperature range studied. The dotted line indicates the position of the diffusion coefficients derived from simulations of variable-temperature 1D ^{7}Li NMR spectroscopy [10].

order of $\tau_0 \approx 4.5 \times 10^{-15}$ s. The latter value falls into the range of phonon frequencies underpinning the reliability of the data derived from DMA. $E_{a,\,ML}$ is in good agreement with the results from conductivity spectroscopy.

For a quantitative comparison, we treated the mechanical relaxation times τ as Li residence times and converted them into diffusion coefficients using eq. (3). By choosing $\ell = 3.1$ Å (see above) the coefficients obtained are in good agreement with those of electrical relaxation. For comparison, in Fig. 6 the rates of the modulus peaks are also included; they have been transformed into D values according to the same procedure.

The dashed-dotted line in Fig. 6 represents an Arrhenius line considering all of the data points; it yields an overall activation energy of 1.12 eV. Recently, almost the same value (1.14 eV) has been reported by some of us for microcrystalline $LiAlO_2$. Heitjans and co-workers [10] studied the orientation dependence of Li ion transport in $LiAlO_2$ single crystals: along the [001] direction 1.26 eV was found, along the [110] direction ion transport is reported to be governed by 1.14 eV; the data refer to temperatures ranging from 423 K to 623 K. The activation energy from diffusion-induced ^{7}Li NMR relaxometry, which was restricted to temperatures lower than 1000 K, is ca. 0.72 eV [10]. Konishi and Ohno reported on a similar value previously (0.77 eV) [19]. This value refers to the so-called low-T flank of a relaxation rate peak. Most likely, it is influenced by correlation effects. The deviation was interpreted as an indication for a vacancy diffusion mechanism being relevant for long-range ion transport in $LiAlO_2$. Interestingly, via the examination of variable-temperature, static 1D ^{7}Li NMR spectra (293 K to 1023 K) the authors analyzed the change of quadrupole intensities with temperature; Heitjans and co-workers were able to deduce an activation energy of 1.12 eV [10] that agrees remarkably well with that of our experiments.

The most recent results by Wiedemann et al. [20], which were extracted from preliminary neutron diffraction studies at high temperatures on $LiAlO_2$ single crystals, give evidence for the temporary involvement of distorted octahedral voids connecting two regular Li positions. Possible through-going migration pathways point to activation energies ranging from 1.25 to 1.7 eV. This includes Li migration along the hexangular-like channels along the ⟨100⟩ direction as well as the quadrangular-like channels along the [001] direction [20].

Of course, ion diffusion might be influenced by impurity ions giving rise to extrinsic regions in conductivity spectroscopy with lower mean activation barriers. Note that for the intrinsic region activation energies ranging from 1.26 eV [19] to 1.47 eV [21] were reported. In the study of Konishi and Ohno the extrinsic to intrinsic transition was detected at ca. 1040 K. Below that temperature an activation energy of 0.81 eV was found; this is comparable to the value which was reported by Matsuo et al. (0.79 eV) [21]. The fact that our activation energy is in agreement with the intrinsic one underlines the high purity of the crystals used.

4 Summary

Li ion dynamics in γ-$LiAlO_2$ single crystals was investigated by both electrical and mechanical excitation. The material served as a model system to study ion dynamics with no partial occupancies on the Li sites. Conductivity isotherms and impedance data analyzed in complex plane plots reveal Debye-like electrical relaxation behaviour that is characterized by an activation energy of ca. 1.12 eV. Around 500 K the solid-state diffusion coefficients derived from DC conductivities agree well with those estimated from dynamic mechanical analyses. Characteristic mechanical loss peaks, which also point to Debye behaviour, show up between 446 K and 489 K if frequencies ranging from 0.5 to 10 Hz are used to record tan δ values.

Our results nicely agree with those recently found by the evaluation of quadrupole satellites of ^{7}Li NMR

spectra being sensitive to local electric field fluctuations at the nuclear sites. In summary, a single, Debye-like Li diffusion process was probed covering a dynamic range of ca. 10 orders of magnitude. It illustrates extremely slow Li exchange at ambient temperature that is presumably due to (i) the highly regular arrangement of Li ions in tetrahedral coordination, (ii) the low number density of vacant sites in the Li sublattice and, finally, (iii) the unfavorable connection of the LiO_4 polyhedra in $LiAlO_2$, *i.e.*, via corner-sharing.

Acknowledgements. We thank our colleagues at the TU Graz for valuable discussions. Financial support by the Deutsche Forschungsgemeinschaft (DFG Research Unit 1277, grant no. WI3600/2-2 and 4-1) as well as by the Austrian Federal Ministry of Science, Research and Economy, and the Austrian National Foundation for Research, Technology and Development (CD-Laboratory of Lithium Batteries: Ageing Effects, Technology and New Materials) is greatly appreciated.

Key words. Slow Li-Ion Dynamics, Mechanical Relaxation, Conductivity Spectroscopy, Lithium Aluminium Oxide.

References

[1] H. Mehrer, Diffusion in Solids (Springer, Berlin, 2006).
[2] P. Heitjans, A. Schirmer, and S. Indris, in: Diffusion in Condensed Matter – Methods, Materials, Models, edited by P. Heitjans and J. Kärger, 2nd edition (Springer, Berlin, 2005), chap. 9, pp. 369–415.
[3] P. Knauth, Solid State Ion., **180**, 911 (2009).
[4] D. Wohlmuth, V. Epp, P. Bottke, I. Hanzu, B. Bitschnau, I. Letofsky-Papst, M. Kriechbaum, H. Amenitsch, F. Hofer, and M. Wilkening, J. Mater. Chem. A, **2**, 20295 (2014).
[5] B. Roling and M. D. Ingram, Solid State Ion., **105**, 48 (1998).
[6] B. Roling and M. D. Ingram, Phys. Rev. B, **57**, 14192 (1998).
[7] B. Roling, A. Happe, M. D. Ingram, and K. Funke, J. Phys. Chem. B, **103**, 4122 (1999).
[8] M. D. Ingram and B. Roling, J. Non-Cryst. Solids, **265**, 113 (2000).
[9] M. D. Ingram and B. Roling, J. Phys.: Condens. Matter, **15**, S1595 (2003).
[10] S. Indris, P. Heitjans, R. Uecker, and B. Roling, J. Phys. Chem. C, **16**, 14243 (2012).
[11] K. Funke, C. Cramer, and D. Wilmer, in: Diffusion in Condensed Matter – Methods, Materials, Models, edited by P. Heitjans and J. Kärger, 2nd edition (Springer, Berlin, 2005), chap. 21, pp. 857–893.
[12] A. Einstein, Ann. Phys. (Berlin), **17**, 549 (1905).
[13] M. Smoluchowski, Ann. Phys. (Berlin), **21**, 756 (1906).
[14] J. Langer, V. Epp, P. Heitjans, F. A. Mautner, and M. Wilkening, Phys. Rev. B **88**, 094304 (2013).
[15] A. Dunst, V. Epp, I. Hanzu, S. A. Freunberger, and M. Wilkening, Energy Environ. Sci., **7**, 2739 (2014).
[16] V. Epp, O. Gün, H. J. Deiseroth, and M. Wilkening, J. Phys. Chem. Lett., **4**(13), 2118 (2013).
[17] A. Kuhn, S. Narayanan, L. Spencer, G. Goward, V. Thangadurai, and M. Wilkening, Phys. Rev. B, **83**, 094302 (2011).
[18] D. P. Almond and A. R. West, Solid State Ion., **26**, 265 (1988).
[19] S. Konishi and H. Ohno, J. Am. Ceram. Soc., **67**, 418 (1984).
[20] D. Wiedemann, S. Nakhal, S. Zander, and M. Lerch, Z. Anorg. Allg. Chem., **640**(11), 2342 (2014).
[21] T. Matsuo, H. Ohno, K. Noda, S. Konishi, H. Yoshida, and H. Watanabe, J. Chem. Soc., Faraday Trans. 2, **79**(8), 1205 (1983).

3.3 Garnet-type solid electrolytes

In the last years extensive experimental effort has been directed towards the development and application of solid electrolytes in all-solid-state batteries, in order to enhance performance, durability and safety of the electrochemical system. The prerequisites, high ionic bulk conductivity and a large electrochemical window were met for garnet-type Li ion conductors [110]. Murugan and co-workers reported of cubic $Li_7La_3Zr_2O_{12}$ (LLZO) which exhibited a high conductivity value of 3×10^{-4} S cm^{-1} and chemical stability against Li metal[111].

Since this breakthrough in the field of solid-state batteries, a lot of scientific effort has gone into the understanding the origin of the high ionic conductivity in LLZO and into further improvement by supervalent doping (*e.g.*, Al^{3+} for 3 Li^+). In fact, by doping with Al, LLZO can be stabilized in the cubic polymorph at room temperature, which exhibits a higher conductivity than tetragonal LLZO. Doping of LLZO with Al or Ga takes place on the Li sub-lattice; hence, it considerably influences lithium ion dynamics. In the garnet structure, Al seems to preferentially occupy tetrahedrally coordinated 24*d* and 96*h* lattice sites [112] (see Fig. 1 in **P4**). The 24*d* site represent a "junction" in the Li pathway, which was reported to result in a blocking effect and decreased Li mobility, if this site is occupied by dopant atoms. The situation could be different if 96*h* lattice sites (distorted tetrahedrally coordinated) are occupied, which, according to Rettenwander *et al* [113], can be achieved if Ga is used as a dopant. Due to its position right below Al in the periodic table Ga should show a similar crystal chemical behavior and can also stabilize the cubic LLZO-phase. However, at the same time the local structure changes by the preferred occupation of 96*h* sites by Ga cation. In order understand these surprising site occupation preferences and the influence of Ga doping on Li ion dynamics, mixed-doped Al,Ga-LLZO garnets were provided by D. Rettenwander (Universität Salzburg, Austria) and studied with high-resolution ^{71}Ga and ^{27}Al NMR at 21.1 T. NMR studies were performed in the frame of a research stay in the group of Prof. G. Goward (Hamilton, Canada), and in collaboration with the National Ultrahigh-Field NMR Facility for Solids (Ottawa, Canada). The corresponding publication **P4** is presented below. Interestingly, our studies did not corroborate previous findings of Ga solely occupying 96*h* sites. For Ga, a similar site occupation preference was found as for Al-, *viz.* substitution of Li ions on both 96*h* and 24*d* position. Thus, the change in Li dynamics is hypthesized to result from the change in lattice constants, rather than from a site preference of the dopants or a blocking effect for the 24*d* position. In this context a brief description on quadrupole Ga NMR in solid Li ion conductors is found as an introduction to our study.

P4: (pp. 149–156)

Site occupation of Ga and Al in stabilized cubic $Li_{7-3(x+y)}Ga_xAl_yLa_3Zr_2O_{12}$ garnets as deduced from ^{27}Al and ^{71}Ga MAS NMR at ultrahigh magnetic fields

D. Rettenwander, J. Langer, W. Schmidt, C. Arrer, K. J. Harris, V. Terskikh, G. R. Goward, M. Wilkening, and G. Amthauer, Chem. Mater. **27**, 3135 (2015)

***Excursus*:** Solid-state Ga NMR in crystalline solids[114]

Compared to other nuclei of group III such as ^{11}B or ^{27}Al, Ga NMR remains relatively undeveloped. Both isotopes ^{69}Ga and ^{71}Ga are NMR-active nuclei, both with a spin angular momentum $I = 3/2$. ^{71}Ga has a natural abundance of 40%, with a gyromagnetic ratio $\gamma = 8.2 \times 10^7$ rad T^{-1} s^{-1} and an electric quadrupole moment $Q = 1.07 \times 10^{-29}$ m^2 similar to that of ^{27}Al. However, the quadrupole splitting is about three times larger, given the same strength of the EFG, as it is a spin-3/2 nucleus. Consequently, this results in large quadrupolar broadenings of the first and second order, hence much broader line shapes are obtained for $^{69,71}Ga$ compared to ^{11}B or ^{27}Al. Note that ^{69}Ga has a larger quadrupole momentum $Q = 1.68 \times 10^{-29}$ m^2 and thus even larger quadrupole coupling constant C_Q. As the second-order quadrupolar line broadening is proportional to q_{zz}/ν_0 (with q_{zz} denoting the principle z-component of the EFG and ν_0 as the Larmor frequency), ^{69}Ga lines are thus three times broader than ^{71}Ga line shapes, although it has a higher natural abundance (60%). With the help of magic-angle spinning, first order quadrupolar interactions affecting the central transition can be removed. However, line broadening due to second-order effects result in non-symmetric broad line shapes. (For more detailed information see section 2.3.2) Due to lattice strain and local disorder, *e.g.* as in the case of LLZO, perfect tetrahedrally and octahedrally symmetric environments (asymmetry parameter $\eta_Q = 0$) for the Ga nucleus are distorted, which results in even larger EFG at the site. This is reflected in the ^{71}Ga NMR line shapes recorded for Al-,Ga-doped LLZO presented in **P4**. Here, both a sharp and a broad Ga line is observed representing two distinct, more and less distorted, tetrahedrally-coordinated Ga sites. However local disorder has to be taken into account, which complicates peak assignment by the magnitude and value of C_Q and η_Q.

CHEMISTRY OF MATERIALS

Article

pubs.acs.org/cm

Site Occupation of Ga and Al in Stabilized Cubic $Li_{7-3(x+y)}Ga_xAl_yLa_3Zr_2O_{12}$ Garnets As Deduced from ^{27}Al and ^{71}Ga MAS NMR at Ultrahigh Magnetic Fields

Daniel Rettenwander,*[,†,⊥] Julia Langer,*[,‡,⊥] Walter Schmidt,[‡] Christian Arrer,[†] Kristopher J. Harris,[#] Victor Terskikh,[§] Gillian R. Goward,[#] Martin Wilkening,[‡] and Georg Amthauer[†]

[†]Department of Materials Research and Physics, University of Salzburg, 5020 Salzburg, Austria

[‡]Christian Doppler Laboratory for Lithium Batteries, Institute for Chemistry and Technology of Materials, DFG Research Unit 1277 "molife", Graz University of Technology (NAWI Graz), 8010 Graz, Austria

[#]Department of Chemistry & Chemical Biology, McMaster University, Hamilton, Ontario L8S 4M1, Canada

[§]Department of Chemistry, University of Ottawa, Ottawa, Ontario K1N 6N5, Canada

Supporting Information

ABSTRACT: Li-containing garnets, which are stabilized in their cubic modification by doping with Al or Ga, show very high Li-ion conductivities. This property qualifies them to be used as solid electrolytes in advanced all-solid-state batteries. The relation between local structures and dynamic properties, however, is still not fully understood. Here, cubic mixed-doped $Li_{7-3(x+y)}Ga_xAl_yLa_3Zr_2O_{12}$ garnet solid solutions with different portions of Al and Ga were synthesized. It turned out that the solubility of Ga is higher than that of Al; the evaluation of 42 different doping compositions indicated an increase of the lattice parameter a_0 with increasing Ga content. ^{71}Ga MAS NMR spectra recorded at 21.1 T revealed two ^{71}Ga NMR resonances, corresponding to Ga occupying both the 24*d* (243 ppm) and 96*h* sites (193 ppm). This behavior, which has been observed for the first time in this study, is very similar to that of Al. The ^{71}Ga NMR line at 193 ppm observed here remained invisible in previous NMR studies that were carried out at lower magnetic fields. The invisibility at lower field is because of large second-order quadrupolar broadening that has a lower effect on the ^{71}Ga NMR spectra at higher magnetic field. Most importantly, the similarity in site preference of Al and Ga found here inevitably raises a question about the significance of a blocking effect on long-range Li-ion transport. It weakens the assumption that the site preference of dopants is responsible for the higher Li diffusivity of Ga-doped samples compared to the Al-doped analogues. Concerning Li-ion dynamics, our ^{7}Li NMR line shape measurements indicate that the change in lattice constant a_0 with increasing doping level seems to have a larger influence on Li-ion dynamics than the Al:Ga ratio.

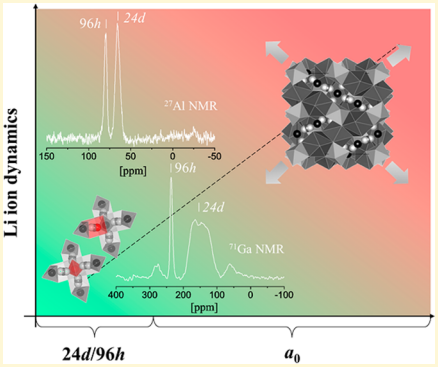

1. INTRODUCTION

Since the initial study by Murugan et al. in 2007, $Li_7La_3Zr_2O_{12}$ (LLZO) garnet has received much scientific attention as a fast Li-ion conductor.[1] Superior chemical and thermal stability, and electrochemical inertness in a wide potential window, particularly its stability against Li metal, make LLZO an excellent candidate to be used as solid electrolyte in both Li-ion and Li oxygen batteries.

The garnet-based structure occurs in at least two structural modifications, viz., a low-temperature tetragonal phase (space group $I4_1/acd$) and a non-quenchable high-temperature cubic phase (space group $Ia\bar{3}d$); the latter is shown in Figure 1.[2,3] Li-ion conductivity of the cubic polymorph is 2 orders of magnitude higher (10^{-3}–10^{-4} S cm^{-1}) compared to that of the tetragonal polymorph (10^{-6} S cm^{-1}). Fortunately, the cubic phase can be stabilized at room temperature (RT) by replacing Li with supervalent dopants (e.g., $Al^{3+} \leftrightarrow 3Li^+$), as has been previously demonstrated in many investigations.[4,5] Consequently, attention has been directed to other dopant cations, such as gallium. In the periodic table, Ga is located directly below Al; hence, it should show a crystal-chemical behavior similar to that of Al. Indeed, the successful stabilization of cubic garnet-type LLZO via the incorporation of Ga has been reported recently.[6−9]

Much experimental as well as theoretical effort has been undertaken to collect information on the local coordination as well as the site preferences of the dopants in LLZO. Some of our group have shown that Al preferentially occupies the tetrahedrally coordinated 24*d* sites as well as the distorted four-fold-coordinated 96*h* sites in LLZO.[10] For Ga, on the other hand, recent ^{71}Ga NMR studies indicated that only a single site (viz., the 96*h* site) is occupied by the dopant, irrespective of the

Received: February 22, 2015
Revised: March 30, 2015
Published: April 2, 2015

DOI: 10.1021/acs.chemmater.5b00684
Chem. Mater. 2015, 27, 3135−3142

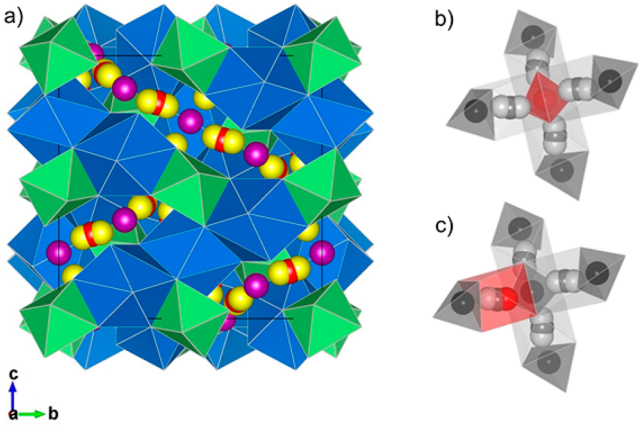

Figure 1. (a) Crystal structure of cubic LLZO ($Ia\bar{3}d$). Blue dodecahedra (24*c*) are occupied by La^{3+}, green octahedra (16*a*) by Zr^{4+}. The Li ions are distributed over three sites, viz., tetrahedrally coordinated (24*d*) sites represented by purple spheres, octahedrally coordinated (48*g*) sites represented by red spheres, and distorted four-fold-coordinated (96*h*) sites represented by yellow spheres. The figures on the right show the polyhedra of the main Li pathway. Red spheres/polyhedra indicate the occupation of one of the vacant sites, 24*d* (b) and 96*h* (c), by a dopant.

amount of Ga introduced.[7] Since the 24*d* site forms a junction between the loops of the Li-ion pathways in LLZO, the occupation of this site is suspected to act as a blockade for the mobile Li ions; this might be in contrast to the situation when only the 96*h* sites are occupied (see Figure 1).

Consequently, provided there is a significant site preference for Al and Ga, one might expect a measurable influence on Li-ion transport properties of LLZO, as discussed by Allen et al.[11]

In order to test this assumption, we synthesized mixed-doped LLZO:(Ga,Al) with varying portions of Al and Ga. Here, a series of $Li_{7-3(x+y)}Ga_xAl_yLa_3Zr_2O_{12}$ garnet solid solutions with intended mole fractions of x Ga and y Al, with $x, y \in \{0.0, 0.1, ..., 0.8 \wedge x + y \leq 0.8\}$ per formula unit (pfu) were synthesized by a conventional high-temperature sintering method.[12] For the sake of simplicity, samples are given with the following formulas:

$$Li_{6.4}Ga_{0.2-y}Al_yLa_3Zr_2O_{12} \rightarrow Ga_{0.2-y}Al_y, \quad \text{with } y = 0.0-0.2$$

$$Li_{6.1}Ga_{0.3-y}Al_yLa_3Zr_2O_{12} \rightarrow Ga_{0.3-y}Al_y, \quad \text{with } y = 0.0-0.3$$

$$Li_{5.8}Ga_{0.4-y}Al_yLa_3Zr_2O_{12} \rightarrow Ga_{0.4-y}Al_y, \quad \text{with } y = 0.0-0.4$$

$$Li_{5.5}Ga_{0.5-y}Al_yLa_3Zr_2O_{12} \rightarrow Ga_{0.5-y}Al_y, \quad \text{with } y = 0.0-0.5$$

$$Li_{5.2}Ga_{0.6-y}Al_yLa_3Zr_2O_{12} \rightarrow Ga_{0.6-y}Al_y, \quad \text{with } y = 0.0-0.6$$

$$Li_{4.9}Ga_{0.7-y}Al_yLa_3Zr_2O_{12} \rightarrow Ga_{0.7-y}Al_y, \quad \text{with } y = 0.0-0.7$$

$$Li_{4.6}Ga_{0.8-y}Al_yLa_3Zr_2O_{12} \rightarrow Ga_{0.8-y}Al_y, \quad \text{with } y = 0.0-0.8$$

Thereafter, the samples were investigated by X-ray powder diffraction (XRPD), scanning electron microscopy (SEM), and ^{27}Al (spin-quantum number $I = 5/2$) and ^{71}Ga ($I = 3/2$) magic angle spinning (MAS) nuclear magnetic resonance (NMR) spectroscopy. The latter was used to probe local magnetic and electronic structures. Finally, the Li-ion dynamics was studied by ^{7}Li ($I = 3/2$) NMR spectroscopy.

2. EXPERIMENTAL SECTION

Syntheses. The starting materials were Li_2CO_3 (99%, Merck), La_2O_3 (99.99%, Aldrich), ZrO_2 (99.0%, Aldrich), Ga_2O_3 (99.0%, Aldrich), and Al_2O_3 (99.0%, Aldrich).The well-ground powder was first calcinated at 900 °C and then reground, pelletized, and sintered at 1050 °C for 16 h. A small fragment taken from the middle of the sintered pellets was ground and used for the XRPD and NMR investigations. For SEM analysis, polycrystalline chips from the pellets were embedded in epoxy holders, and then the surface was ground and polished using diamond paste.

XRPD. Diffraction patterns were recorded with a Siemens D8 diffractometer using Cu Kα radiation. This was done to characterize the synthetic products in terms of all phases present and to determine the symmetry and unit-cell dimension of the garnet. Data were collected between 10° and 80° 2θ. The lattice parameter a_0 and the average grain size were obtained by Rietveld refinement using the program Topas V2.1 (Bruker).

SEM. Images were taken using a Zeiss Ultra Plus device. In particular, we put emphasis on the investigation of the phase composition and the chemical homogeneity, i.e., the distribution, of La, Zr, and Al, using a back-scattered electrons (BSE) detector and energy-dispersive spectroscopy (EDS) measurements, respectively.

Solid-State NMR. ^{27}Al and ^{71}Ga MAS NMR spectra, including the multiple quantum (MQ) MAS spectra, were acquired at RT using a high-performance Bruker Avance II 900-MHz spectrometer. The spectrometer is connected to a cryomagnet with a nominal field of 21.1 T; it is installed at the Canadian National Ultrahigh-Field NMR Facility. The value of 21.1 T corresponds to Larmor frequencies $\omega_0/2\pi$ = 234.5 MHz for ^{27}Al and 274.5 MHz for ^{71}Ga. All experiments were performed under MAS conditions at spinning rates of 25 kHz (^{27}Al), 31.25 kHz (^{27}Al triple quantum (3Q) MAS), and 30 kHz (^{71}Ga), using a Bruker 2.5 mm H/X probe. Chemical shift values, δ_{iso}, were referenced to 1 M aqueous solutions of $Al(NO_3)_3$ and $Ga(NO_3)_3$. The one-dimensional MAS spectra were recorded via single pulse excitation; very short pulse lengths of 1.0 μs (^{27}Al) and 0.5 μs (^{71}Ga) were used. For the ^{27}Al and ^{71}Ga measurements, the recycle delay was set to 0.5 s in both cases. The NMR acquisition conditions were tested to ensure quantitative spectra. ^{27}Al MAS NMR spectra were recorded with 640 scans, while ^{71}Ga spectra were acquired with 16k scans ($Ga_{0.4}Al_{0.0}$, $Ga_{0.3}Al_{0.1}$, $Ga_{0.2}Al_{0.2}$) or 32k scans ($Ga_{0.1}Al_{0.3}$).

^{27}Al 3QMAS NMR spectra were acquired using a standard three-pulse sequence with a Z-filter. The spectra were rotor-synchronized in the F1 dimension, and a relaxation delay of 2.5 s was used with 192 ($Ga_{0.0}Al_{0.4}$) or 288 ($Ga_{0.2}Al_{0.2}$) scans per each of the 128 td1 increments. The DMFit software was used to simulate the NMR line shapes and to determine chemical shift values as well as to estimate the corresponding coupling constants and asymmetry parameters.

Variable-temperature ^{7}Li NMR line shapes were recorded under non-MAS conditions at 11.7 T (193.4 MHz) using a Bruker Avance III spectrometer in combination with a commercial Bruker probe for broadband applications. Typically, the 90° pulse length was approximately 2 μs; we used a solid-echo pulse sequence to record the spectra.

DOI: 10.1021/acs.chemmater.5b00684
Chem. Mater. 2015, 27, 3135−3142

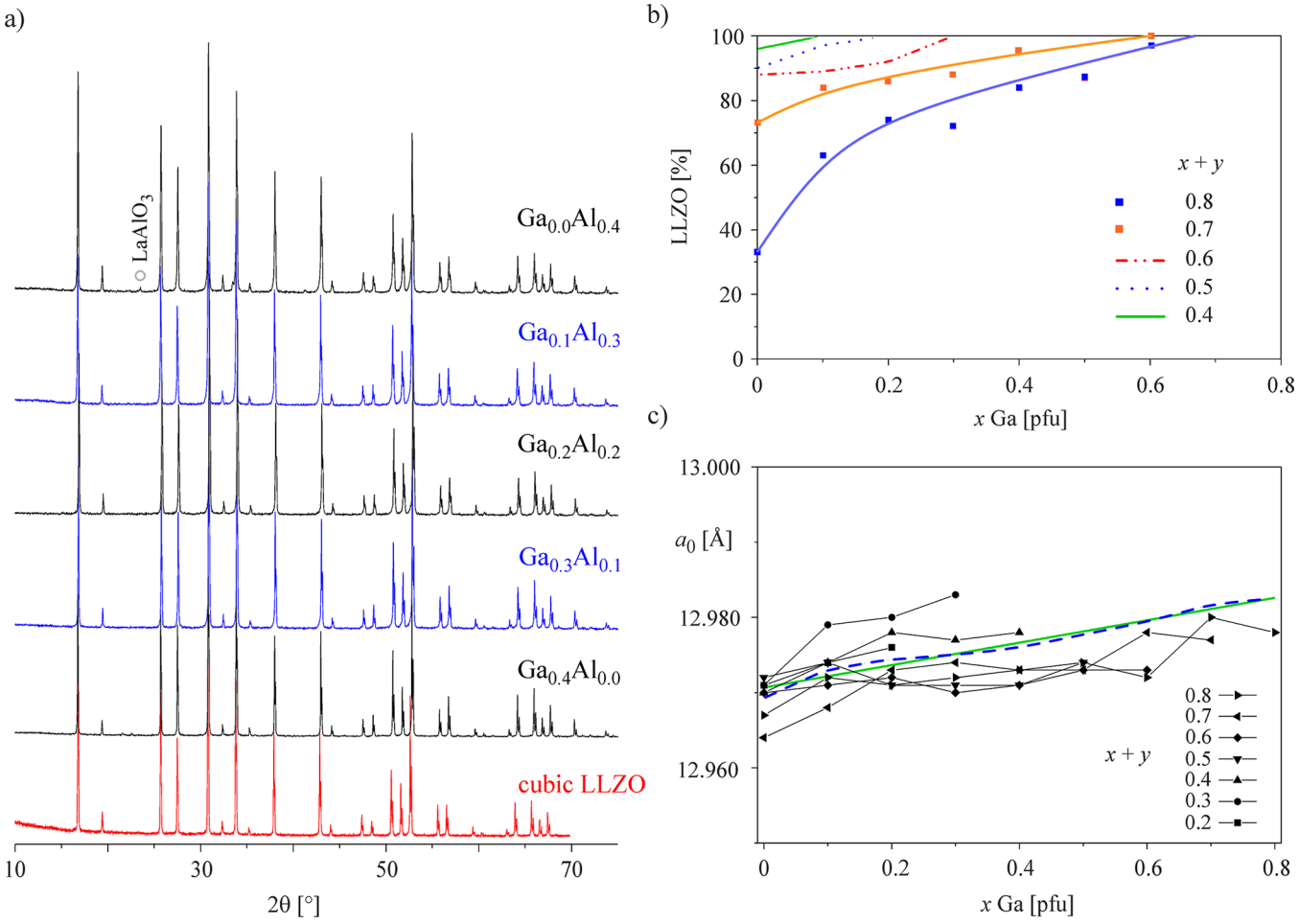

Figure 2. (a) XRPD patterns of $Ga_{0.4-y}Al_y$ with x = 0.0, 0.1, 0.2, 0.3, and 0.4. The diffraction pattern of cubic LLZO (red) is shown for comparison. (b) Portion of LLZO in the synthesis as a function of the Ga content. The lines, serving as guides to the eye, correspond to different solid solutions. Above these lines, phases other than LLZO are present. These extra phases are given in Table S1 in the Supporting Information. (c) Unit-cell parameter a_0 of Ga_xAl_y garnets as a function of Ga content. The dashed line represents the average of the multiple curves; the solid line is a linear fit of the multiple averaged curves.

3. RESULTS AND DISCUSSION

Phase Composition As Seen via XRPD. The XRPD patterns of $Ga_{0.4-y}Al_y$ are shown in Figure 2, together with the pattern of cubic LLZO.[5] For the patterns of all other solid solutions, we refer to Figure S1 in the Supporting Information.

Phase compositions were evaluated by Rietveld analysis, with the corresponding results summarized in Table S1. These data are also illustrated in Figure 2b, showing the portion of LLZO in the syntheses as a function of Ga content. The solid solutions synthesized exhibit reflections clearly showing cubic symmetry. There are no indications of any phases formed other than LLZO for $Ga_{0.4-y}Al_y$ with $y < 0.4$. The sample with $y = 0.4$ shows a low-intensity single reflection representing <1 wt % $LaAlO_3$. This impurity phase is also seen by ^{27}Al MAS NMR in the sample with $y = 0.3$; in that case it seems to be X-ray amorphous. The other samples are phase pure, independent of the intended portion of dopants. In all solid solutions with $x + y > 0.5$, the number and the amount of extra phases increase with the portion of Al. Typically, these extra phases are $LaAlO_3$, $Li_2Zr_2O_3$, and $La_2Zr_2O_7$; the more Al is present, the more easily those phases are formed. More details about the samples are given in the Supporting Information. The evaluation of the LLZO portion in the syntheses, as shown in Figure 2b, gives evidence for a lower incorporation limit of Al as compared to Ga. By increasing the Al portion (y) in $Ga_{x-y}Al_y$, with $x \leq 0.8$, the amount and the number of extra phases rise simultaneously. Phase-pure Ga-doped LLZO can be synthesized up to $x = 0.8$; this is in contrast to Al-doped LLZO, for which the incorporation limit turns out to be approximately 0.3 pfu.

Lattice Parameter (XRPD). The unit-cell constant, a_0, was evaluated by Rietveld analysis. Results are summarized in Table S1 and illustrated in Figure 2c. There is no indication that a_0 follows a general trend for the singly doped solid solution ($Ga_xAl_{0.0}$ and $Ga_{0.0}Al_y$). Our findings are in agreement with previous studies on Ga-doped LLZO, where the lattice parameter a_0 does not change systematically or significantly with the amount of dopants.[7,8] This is probably related to the aliovalent doping mechanism, where three Li^+ ions are substituted by one Ga^{3+}, and to the variation in site occupation. Interestingly, the a_0 value increases with the Ga portion by approximately 0.015 Å/Ga pfu. In our study, the Li content remains constant, but Al is continuously replaced by Ga within each series. Thus, in this case, the larger ionic radius of Ga seems to be responsible for the slight increase in a_0 observed.

Phase Stability and Solubility of Al and Ga. So far, efforts have been made to investigate the solubility of Al and Ga in LLZO and their influence on phase behavior. A detailed study on the role of the amount of Al and Li in cubic LLZO

DOI: 10.1021/acs.chemmater.5b00684
Chem. Mater. 2015, 27, 3135−3142

was presented by Rangasamy et al.[13] Those authors showed that the Al content has to be above a critical concentration of 0.20 pfu to stabilize the cubic garnet phase. Otherwise, if the Al content is above 0.39 pfu, two phases will form, cubic LLZO and $LaAlO_3$. Because Ga is located directly below Al in the periodic table, one may suspect Ga to have effects similar to those of Al on the stabilization of the cubic phase. Indeed, phase-pure cubic LLZO garnet can be obtained with a Ga content ranging from 0.16 to 0.72 pfu.[7]

Here, we were able to show that mixed doping with Al and Ga stabilizes the cubic phase in the same way as known for doping with a single element. It turned out that the solubility of Ga is higher than that of Al. Furthermore, the amount of extra phases increases with increasing Al portion. Most likely, the reason for the lower incorporation limit of Al compared to Ga can be related to the larger difference between the radii of Li ($r[4]$ = 0.59 Å; $r[6]$ = 0.74 Å) and Al ($r[4]$ = 0.39 Å; $r[6]$ = 0.53 Å) compared to the difference between Li and Ga ($r[4]$ = 0.47 Å; $r[6]$ = 0.62 Å).[14] According to Goldschmidt's rule, the maximum change in ionic radii should be below approximately 15% to fully substitute a given cation in solid solutions. Consequently, owing to the smaller radii of Al in different coordination spheres, one might expect a lower incorporation limit for Al ions than for Ga ions. Recently, the preparation of Al-doped LLZO samples with up to 1.78 Al pfu, namely $Li_{6.36}Al_{1.78}La_{2.27}Zr_{1.38}O_{12}$, has been tried via mechanosynthesis combined with calcination.[15] Here, 1.78 Al pfu means that 6.36 + 1.78 = 8.14 Al^{3+} cations are distributed over the Li sites (24*d*, 48*g*, and 96*h*). Because of repulsive Li^+−Li^+ and Li^+−Al^{3+} interactions, no more than 60 out of 168 available Li sites per unit cell (= 7.5 Li pfu) can be occupied by Li that is distributed among the available sites 24*d*, 48*g*, and 96*h*. This estimation is based on the assumption that, if a Li ion is located on a 24*d* site, Li ions in the immediate neighborhood will be displaced to a 96*h* void next to an empty 24*d* position. The value of 7.5 Li pfu is in agreement with the upper incorporation limit found experimentally by Rangasamy et al.[13]

Additional Al ions, however, might also be found in side products such as $LiAlO_2$ or $LaAlO_3$, as mentioned above.[12] If present in an amorphous form, they are expected to be invisible by X-ray diffraction but detectable by NMR spectroscopy. Due to signals overlapping in ^{27}Al MAS NMR, however, it can be difficult to detect such phases. As an example, δ_{iso} of crystalline or X-ray amorphous $LiAlO_2$ (the γ- or δ-form) shows up at ca. 82 ppm, which falls into the same ppm range of ^{27}Al on 96*h* in LLZO.[16] In ref 15, some of the ^{27}Al MAS NMR resonances at around 80 ppm, which should be interpreted as a single site in Al-LLZO, broaden with increasing Al content; in some cases a shoulder located at 82 ppm is visible for large Al portions. This feature might be attributed to the increasing formation of side products such $LiAlO_2$. Amorphous extra phases may work as a sintering aid and assist in connecting the LLZO particles, thus enabling long-range ion transport because of reduced ion-blocking effects stemming from low-conducting grain boundary regions.[8] Note that, in analogy to the Al-doped oxides, the formation of crystalline $LiGaO_2$ has also been observed during the synthesis of Ga-bearing garnets.[8]

Element Distribution (EDS Mapping). For illustration, Al and Ga incorporation and distribution were evaluated for a representative sample, $Ga_{0.2}Al_{0.2}$, by using BSE and EDS mapping (see Figure 3). The grains formed are smaller than 10 μm in diameter and are partly connected to each other. The element mapping of those grains clearly indicates that Al and Ga are successfully incorporated and homogeneously distributed throughout the garnet structure.

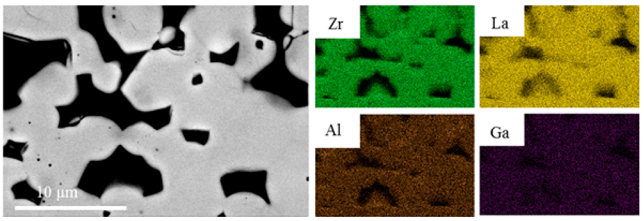

Figure 3. (Left) BSE image and (right) EDS element mapping of a representative sample, namely $Li_{5.8}Ga_{0.2}Al_{0.2}La_3Zr_2O_{12}$. The intensity of the color does not correspond to the amount of the element measured.

^{27}Al and ^{71}Ga MAS NMR. Selected NMR spectra of samples with the composition $Ga_{0.4-y}Al_y$, with y = 0.1, 0.2, 0.3, and 0.4, are shown in Figure 4. The position and the shape of the lines were evaluated with DMFit software; the results are summarized in Table 1.

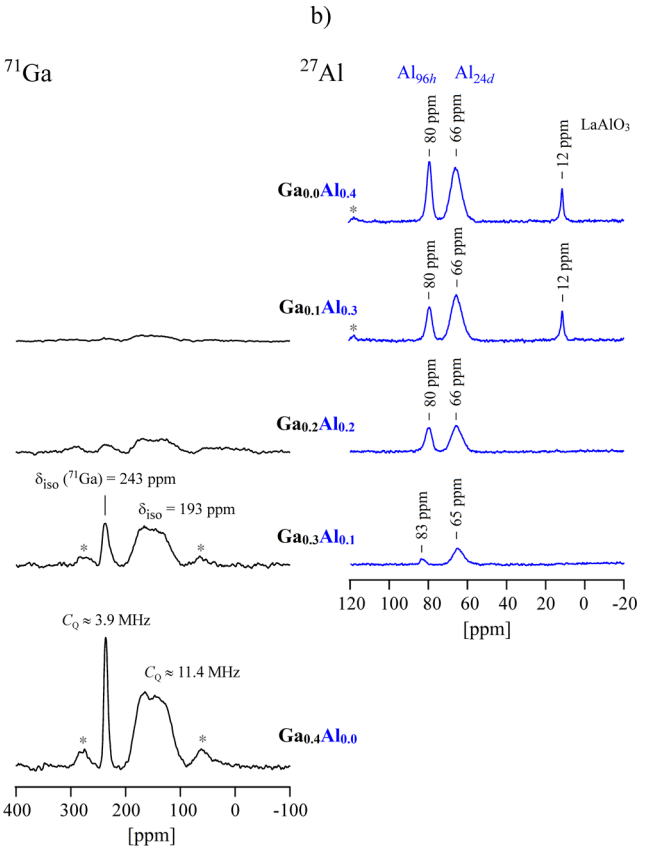

Figure 4. (a) ^{71}Ga (black) and (b) ^{27}Al (blue) MAS NMR spectra of $Li_{5.8}Ga_{0.4-y}Al_yLa_3Zr_2O_{12}$ garnets recorded at 21.1 T. Asterisks denote spinning side bands. See text for further details.

^{71}Ga (I = 3/2, natural abundance 39.6%) and ^{27}Al (I = 5/2, natural abundance 100.0%) are quadrupolar nuclei; the corresponding interaction of their quadrupole moments ($Q_{^{71}Ga}$ = 1.07 × 10^{-29} m^2 and $Q_{^{27}Al}$ = 1.466 × 10^{-29} m^2) with surrounding electric field gradients results in specific shapes of the NMR lines that depend on the interplay of the magnitude of the external magnetic field applied and the underlying coupling constant and asymmetry parameters characterizing the

DOI: 10.1021/acs.chemmater.5b00684
Chem. Mater. 2015, 27, 3135−3142

Table 1. NMR Parameters of $Li_{7-3(x+y)}Ga_xAl_yLa_3Zr_2O_{12}$ As Obtained by ^{27}Al and ^{71}Ga MAS NMR as Well as Static ^7Li NMR

sample	NMR	δ_{iso} (ppm)	C_Q (MHz)	assignment	fwhm[a] (Hz)
$Ga_{0.0}Al_{0.4}$	^{27}Al	65.9		24*d*	
		79.5		96*h*	5700
		11.7		$LaAlO_3$	
$Ga_{0.1}Al_{0.4}$	^{27}Al	65.9		24*d*	
		79.5		96*h*	
		11.6		$LaAlO_3$	5700
	^{71}Ga	–[b]		24*d*	
		–[b]		96*h*	
$Ga_{0.2}Al_{0.2}$	^{27}Al	65.5		24*d*	
		79.8		96*h*	4500
	^{71}Ga	–[b]		24*d*	
		–[b]		96*h*	
$Ga_{0.3}Al_{0.1}$	^{27}Al	65.2		24*d*	
		83.1		96*h*	3000
	^{71}Ga	193	11.1	24*d*	
		243	4.9	96*h*	
$Ga_{0.4}Al_{0.0}$	^{71}Ga	193	11.4	24*d*	2200
		243	3.9	96*h*	

[a]Full width at half-maximum, line widths as obtained from static ^7Li NMR line shape measurements at ambient temperature. [b]Signal observed but not simulated due to insufficient S/N.

interaction. While first-order electric quadrupole interactions are largely eliminated by sufficiently fast spinning, MAS is unable to remove the second-order effects.

^{27}Al NMR spectra of Al-doped LLZO have already been extensively analyzed in the past; see, e.g., refs 5 and 10. In accordance with previous reports, our ^{27}Al MAS NMR spectra of mixed LLZO show two characteristic resonances at ca. 66 ppm and ca. 81 ppm, irrespective of the amount of Al inserted. For the samples with high Al content, an additional resonance at 12 ppm was found; it reflects octahedrally coordinated Al ions in $LaAlO_3$, which is a known extra phase that forms during the synthesis of Al-doped LLZO.[5] As mentioned above, $LaAlO_3$ was also observed in XRPD for samples with high Al content. Since in our case the magnetic field interaction at B_0 = 21.1 T is much stronger than the quadrupole interactions, our ^{27}Al MAS NMR spectra benefit from a better resolution, resulting in sharp signals with almost isotropic line shapes. For this reason, the ^{27}Al NMR parameters C_Q and η_Q cannot be simulated well with DMFit; however, the apparent chemical shift values can be measured.

Here, also considering our recent study,[10] we assign the chemical shifts at 66 and 81 ppm (see Table 1) to Al ions residing on the 24*d* and 96*h* sites, respectively.[10] This assignment is in agreement with recent studies by other groups, focusing on the site preference of Al in LLZO; the resonance near 66 ppm has consistently been interpreted to reflect Al ions on the 24*d* position.[4,5,15,17] In one of those studies, the resonance was extraordinarily broad and, therefore, was interpreted as a superposition of two resonances assigned to two different 24*d* sites of LLZO phases, which had not yet reached thermodynamic equilibrium.[17]

In most of the published ^{27}Al MAS NMR spectra of LLZO, a second resonance shows up at approximately 80 ppm, being carefully assigned to the distorted, four-fold-coordinated 96*h* position. Because of the asymmetric line shape of this resonance, the signal was suspected to be a superposition of more than one NMR lines showing up in the region from 75 to 85 ppm. These results were afterward re-interpreted using DFT methods.[10]

In order to resolve potentially overlapping lines, we studied $Ga_{0.2}Al_{0.2}$ and $Ga_{0.0}Al_{0.4}$ with the help of ^{27}Al 3QMAS NMR (Figure 5). This technique increases the resolution of the

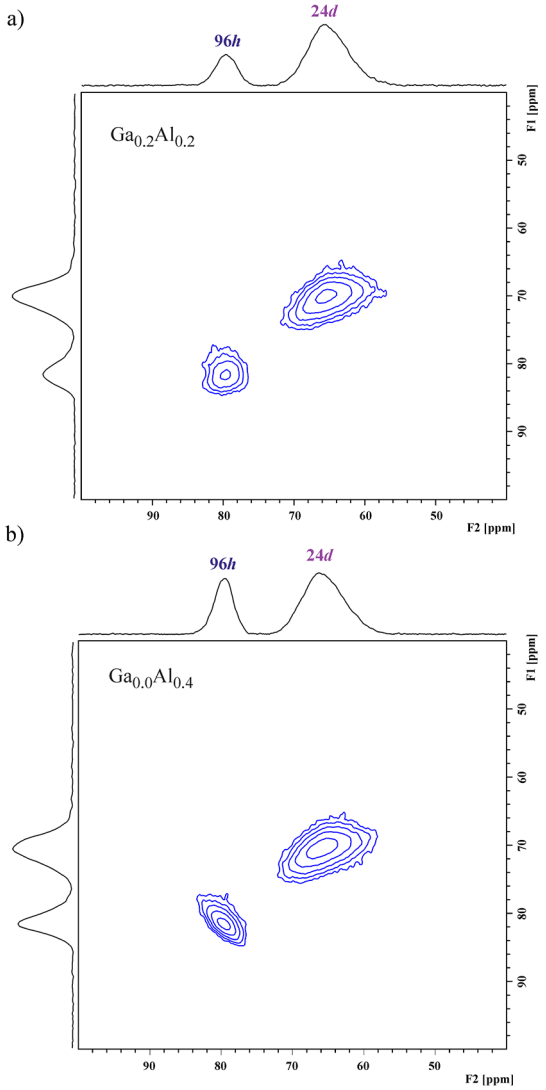

Figure 5. ^{27}Al 3QMAS NMR spectra of (a) $Ga_{0.2}Al_{0.2}$ and (b) $Ga_{0.0}Al_{0.4}$ recorded at 21.1 T and a spinning speed of 31.25 kHz.

spectra that are influenced by non-negligible second-order quadrupolar interactions which cannot be averaged by MAS, as mentioned above.

The ^{27}Al 3QMAS spectra of $Ga_{0.2}Al_{0.2}$ and $Ga_{0.0}Al_{0.4}$ essentially prove that the line broadening is not caused by distinct overlapping sites. However, it is worth noting that the diagonal streaking in the 2D projection indicates a certain distribution of chemical shifts reflecting a small amount of disorder or strain in the sample. This feature is even more pronounced in the ^{27}Al 3QMAS spectrum of $Ga_{0.0}Al_{0.4}$ for the

DOI: 10.1021/acs.chemmater.5b00684
Chem. Mater. 2015, 27, 3135−3142

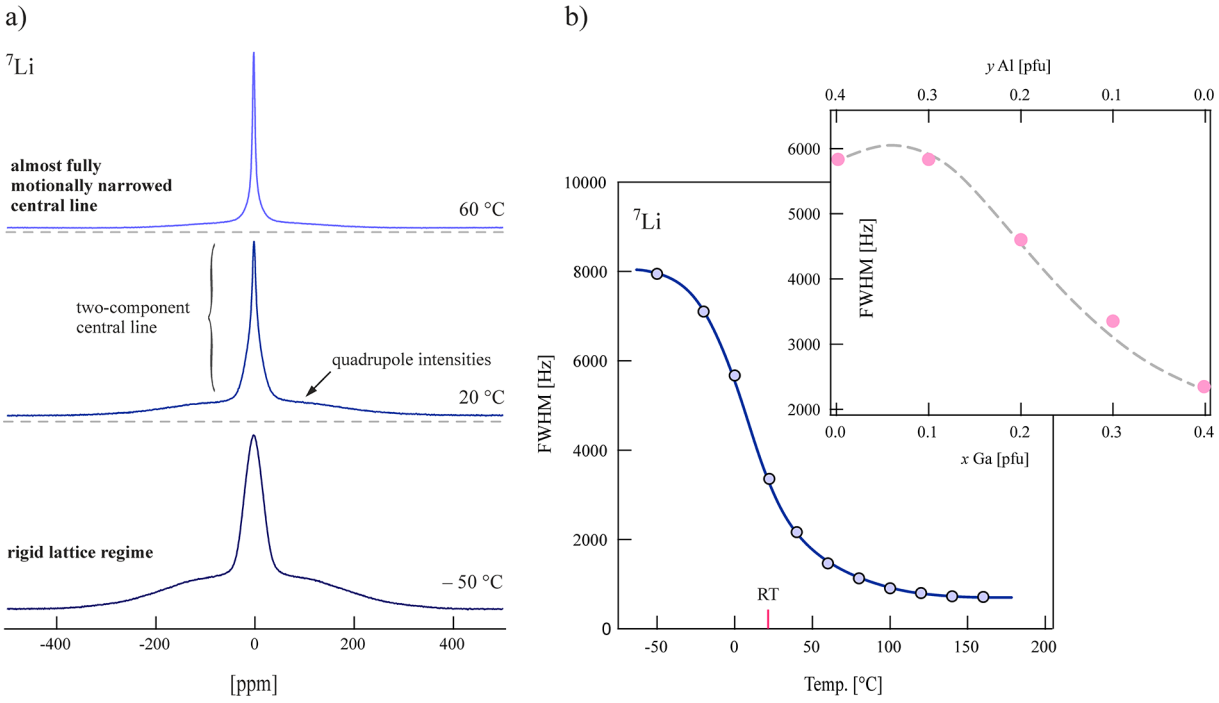

Figure 6. (a) ^{7}Li NMR line shape measurements and motional narrowing (non-rotating samples) of a sample with a Ga content of $x = 0.4$, recorded via a solid-echo pulse sequence at 194.3 MHz. At low temperatures the NMR line consists of a dipolarly broadened central line and a so-called quadrupole foot. The central line narrows with increasing temperature, indicating rapid Li exchange between the available crystallographic Li positions. (b) Motional narrowing of the ^{7}Li NMR line width (blue). Extreme narrowing is reached at temperatures slightly higher than 100 °C. (Inset) ^{7}Li NMR line width, determined at ambient temperature, as a function of the Ga:Al ratio of the garnets studied (full width at half-maximum). The solid line in (b) and the dashed line in the inset serve to guide the eye.

resonance at 81 ppm reflecting the distorted 96*h* site (see Figure 5). Thus, in agreement with previous works, the two signals observed reflect Al ions residing on only two distinct sites, viz., 24*d* and 96*h* voids, respectively.

Assignment for the ^{71}Ga MAS NMR resonances is not as well established in the literature as the ^{27}Al assignments. All previous publications have observed a single ^{71}Ga NMR resonance from doped LLZO, though the characteristics of the site break up into two distinct cases.[6,7,9] One publication, focusing on the complete solid solution of Ga-doped LLZO, with Ga contents up to 0.84 pfu, showed a single site with a large chemical shift (δ_{iso} = 244(2) ppm), a small quadrupole interaction (C_Q = 4.0(2) MHz), and an EFG tensor that deviates from axial symmetry (η_Q = 0.46(3)).[7] A different study revealed a single Ga site with a smaller chemical shift (δ_{iso} = 207(10) ppm), a larger C_Q (12.7(3) ppm), and an EFG tensor that is essentially axially symmetric (η_Q = 0.05(05)).[9] These characteristics mimic the two four-fold-coordinated dopant sites in the ^{27}Al system discussed above, as would be expected for two elements in the same group of the periodic table.[5]

It is, therefore, relatively straightforward to assign the higher chemical shift peak to Ga ions in the 96*h* site and the lower chemical shift peak to 24*d* dopant ions. This assignment is the only reasonable one, given that the local symmetry (S_4) at the 24*d* site enforces axial symmetry on the EFG tensor (η_Q = 0). However, we do note that local disorder (that may break this symmetry) probably varies somewhat with the preparation route; hence, some samples may display 24*d* site peaks that are better represented by a range of parameters rather than a single η = 0 site. Here, the ^{71}Ga NMR signal of the 24*d* site can be best simulated with $\eta_Q < 0.3$ (see below).

^{71}Ga MAS NMR spectra of the $Ga_{0.4}Al_{0.0}$ and $Ga_{0.3}Al_{0.1}$ samples recorded at 21.1 T (see Figure 4) clearly show both sites that were observed individually in different samples. The signal at high chemical shift, δ_{iso} = 243(1) ppm, is narrow under the ultrahigh magnetic field applied, though an upper limit of 4.4 MHz can still be placed on C_Q. The lower chemical shift site, δ_{iso} = 193(1) ppm, is estimated to have C_Q = 11.3(1) MHz, and an upper limit of 0.5 can be placed on η using line shape simulations. These parameters are in close agreement with the published ^{71}Ga values and mimic the ^{27}Al NMR results as well; therefore, we assign the 243 ppm peak to the 96*h* site, and the 193 ppm peak to the 24*d* site.

It is quite interesting that previous ^{71}Ga NMR studies of doped LLZO all reported that only one of the two sites was observed.[6,7,9] Howard et al. and Rettenwander et al. analyzed Ga-doped LLZO at an applied field of 9.4 T with relatively slow sample spinning and observed only the narrow 96*h* line.[6,7] On the other hand, Bernuy-Lopez et al. recently investigated LLZO doped with up to 0.3 Ga pfu at 11.75 T and fast sample spinning; they observed only the broad 24*d* signal.[9] While the broad 96*h* signal may have been obscured by the lower magnetic field and slower spinning rates applied in the first two of these studies, there is little doubt that the narrow peak from the 96*h* site would easily have been observed in the study by Bernuy-Lopez et al. if Ga populated this site in the material. The observation of both sites in the same material presented here provides the first evidence that Ga can populate both the 96*h* and 24*d* sites in the same doped LLZO. These data provide vital information on the structure and are important for developing the model of Li-ion dynamics of in the system.

Site Preferences of Al and Ga in Dopant-Stabilized LLZO. If we assume that the area under the NMR line is

DOI: 10.1021/acs.chemmater.5b00684
Chem. Mater. 2015, 27, 3135–3142

roughly proportional to the amount of the measured nuclei, the site distribution can be evaluated according to, e.g.,

$$24d \text{ pfu } [i, j] = \frac{A_{1i}}{\sum_{i=1}^{n} A_{1i}} c_1 + \frac{A_{2j}}{\sum_{j=1}^{m} A_{2j}} c_2$$

where i is the ith resonance of nucleus 1, A_{1i} denotes the area under the line i, and c_1 is the intended dopant concentration of nucleus 1, etc. The resulting site occupancies 24*d*:96*h* are quite similar and range from 0.2:0.1 ($Ga_{0.0}Al_{0.4}$, $Ga_{0.1}Al_{0.4}$) to 0.3:0.1 ($Ga_{0.2}Al_{0.2}$, $Ga_{0.3}Al_{0.1}$, $Ga_{0.4}Al_{0.0}$). Comparing the NMR spectra of the samples with a low amount of Ga incorporated (see Figure 4), there might be a tendency that, at first, the 96*h* position is preferentially occupied by Ga as compared to the 24*d* site. Considering the ^{27}Al MAS NMR spectrum of $Ga_{0.3}Al_{0.1}$, the Al ions seem to prefer to occupy the 24*d* sites at first. However, we found a rather similar site preference for Al and Ga; the dopant distribution among the available sites in LLZO may, of course, depend on the synthesis conditions chosen. This might also serve to explain differences in interpretation, where Bernuy-Lopez et al. reported that only the 24*d* site is occupied by Ga ions.[9]

Li-Ion Dynamics As Seen by ^{7}Li NMR. Narrowing of the ^{7}Li NMR central line with temperature, which is caused by thermally activated Li motion, is shown in Figure 6. If we look at the change of the line width as a function of Ga content at ambient temperature (Table 1), we observe a decrease of the ^{7}Li NMR line width with increasing Ga content. $Ga_{0.4}Al_{0.0}$ shows the highest Li-ion diffusivity found in this series. The regime of extreme narrowing is reached at temperatures slightly higher than 100 °C, this being an indication for high diffusivity in $Ga_{0.4}Al_{0.0}$.

The corresponding ^{7}Li (I = 3/2) NMR line shapes recorded under non-rotating conditions are composed of a central line and quadrupole intensities. Dipole−dipole as well as electric quadrupole interactions are increasingly averaged due to sufficiently fast Li exchange among the available crystallographic Li positions (see Figure 6).

The central line reveals heterogeneous line narrowing, pointing to complex ion dynamics. From a dynamic point of view, we have to deal with a relatively large distribution of jump rates. At sufficiently low temperatures, some of the Li ions distributed among the available sites in LLZO seem to be less mobile than others, meaning not all of them have access to the same fast diffusion pathway at the same time. This feature has also been found for Al-doped LLZO by some of our group recently;[4] it is also known for glassy ion conductors.[18] The fact that here the broad quadrupole powder pattern is affected by thermally activated Li hopping processes at temperatures as low as 20 °C indicates extremely rapid Li exchange (see below).

One might also think to interpret the overall line shape found in the motional narrowing regime as a result of the spin physics of spin-3/2 quadrupole nuclei that would lead to biexponential relaxation transients. In our case, however, the corresponding NMR spin−lattice and spin−spin relaxation transients do not show multiple components; instead, they can be well fitted with a single exponential function. Additionally, regarding the ^{7}Li NMR line shapes well above 60 °C, a single Lorentzian-shaped, motionally narrowed line shows up; hence, it is no longer possible to separate the two contributions. Thus, most likely the complex line shape observed in the line narrowing regime does indeed reflect heterogeneous dynamics.

Li jump rates can be estimated from NMR line narrowing. The inflection point of the motional narrowing curve of the NMR central line (see Figure 6b) is at 283 K. At this temperature the corresponding Li jump rate, $1/\tau$, can be roughly estimated according to $1/\tau = \nu_{rl}2\pi$, where ν_{rl} denotes the rigid lattice line width;[19] here we have ν_{rl} = 8 kHz. This leads to $1/\tau$ (283 K) $\approx 5 \times 10^4$ s^{-1}. Using an activation energy of 0.35 eV, which is commonly found for Al-doped, highly conducting LLZO,[4] this gives, at RT (300 K), a mean residence time between two successful hops in the order of 1−10 μs. This finding is consistent with the expected high room-temperature Li-ion conductivity of dopant-stabilized garnets, which typically ranges from 10^{-3} to 10^{-4} S/cm (see above).[4]

A possible influence of dopant cations on ionic conductivity was first proposed by Allen et al.[11] They discussed a possible blocking effect of dopants located at the Li-ion sublattice in garnets. In particular, the 24*d* site might act as a blockade for through-going ion diffusion, as already noted above. Allen et al. investigated garnets of the composition $Li_{6.75}La_3Zr_{1.75}Ta_{0.25}O_{12}$, with and without doping, using Al or Ga. The undoped garnet showed the highest total Li-ion conductivity, $\sigma_{total} = 8.7 \times 10^{-4}$ S cm^{-1} at RT, and the activation energy E_a = 0.22 eV. These values were compared to those of the Al-doped and the Ga-doped garnets, characterized by $\sigma_{total} = 3.7 \times 10^{-4}$ and 4.1×10^{-4} S cm^{-1}, with E_a = 0.30 and 0.27 eV, respectively.[11] The ionic conductivity of the undoped sample is reported to be twice that of the doped samples. The doped samples showed similar electrochemical performances. The lattice parameters of the doped and undoped samples are reported to be a_0 = 12.96 and 12.95 Å, respectively.[11]

In our opinion, the increase of σ_{total} observed and the slight decrease of E_a found for the undoped sample could also be related to the total amount of Li present or to the change in lattice constant a_0. Evidence for the latter is given in an earlier study by Murugan et al.,[20] who investigated the influence of the lattice parameter on Li-ion conductivity. Those authors were able to show that the partial substitution of La by divalent cations (e.g., Ba, Mg, Ca, and Sr) as well as by the use of higher sintering temperatures leads to an increase of a_0. This increase is accompanied by an increase of σ_{total} and a decrease of the E_a, as well as an increasing grain boundary resistance, R_{gb}. As an example, $Li_6SrLa_2Ta_2O_{12}$ and $Li_6BaLa_2Ta_2O_{12}$ are characterized by $\sigma_{total} = 3.05 \times 10^{-5}$ and 9.28×10^{-5} S cm^{-1}, as well as a_0 = 12.83 and 12.97 Å, respectively. This means that an increase in a_0 of 0.014 Å already leads to an increase of the ion conductivity by a factor of 2; this is similar to what Allen et al. have observed.[11]

In our study, we found a decrease in the ^{7}Li line width (fwhm) as a function of the Ga content; see the inset of Figure 6b. Since the RT line width can be regarded as a qualitative measure of translational Li-ion dynamics, it means that more Ga has been incorporated the higher the Li-ion diffusivity. Because (i) the Li content remains constant and (ii) no significant site preference of the dopants Al and Ga was found in NMR, we tend to connect the increase in Li-ion dynamics, as seen by the change in ^{7}Li NMR line widths, with the increase of a_0 rather than attributing this finding to the blocking effect of trivalent cations located on 24*d* sites.

■ ASSOCIATED CONTENT

Supporting Information

Table S1, summarizing unit cell parameters; XRPD analyses of phase composition; and Figure S1, showing XRPD patterns of

DOI: 10.1021/acs.chemmater.5b00684
Chem. Mater. 2015, 27, 3135−3142

the compounds studied. This material is available free of charge via the Internet at http://pubs.acs.org.

AUTHOR INFORMATION

Corresponding Authors

*E-mail: daniel.rettenwander@sbg.ac.at.
*E-mail: julia.langer@tugraz.at.

Author Contributions

⊥D.R. and J.L. contributed equally to this work.

Funding

The research was supported by Austrian Science Fund (FWF), project no. P25702. Further support was received from the Austrian Federal Ministry of Science, Research and Economy, and the Austrian National Foundation for Research, Technology and Development.

Notes

The authors declare no competing financial interest.

ACKNOWLEDGMENTS

D.R. thanks Peter R. Slater (Birmingham, UK) and Juan M. López del Amo (Miñano, Spain) for providing their NMR spectra. M.W. and W.S. thank the Austrian Federal Ministry of Science, Research and Economy, and the Austrian National Foundation for Research, Technology and Development for financial support. M.W. and J.L. thank the DFG Research Unit 1277 for additional financial support. Access to the 21.1 T NMR spectrometer was provided by the National Ultrahigh-Field NMR Facility for Solids (Ottawa, Canada), a national research facility funded by a consortium of Canadian universities, supported by the National Research Council Canada and Bruker BioSpin, and managed by the University of Ottawa (http://nmr900.ca).

REFERENCES

(1) Murugan, R.; Thangadurai, V.; Weppner, W. *Angew. Chem.* **2007**, *119*, 7925.
(2) Awaka, J.; Kijima, N.; Hayakawa, H.; Akimoto, J. *J. Solid State Chem.* **2009**, *182*, 2046.
(3) Awaka, J.; Takashima, A.; Hayakawa, H.; Kijima, N.; Idemoto, Y.; Akimoto, J. *Key Eng. Mater.* **2011**, *485*, 99.
(4) Buschmann, H.; Dölle, J.; Berendts, S.; Kuhn, A.; Bottke, P.; Wilkening, M.; Heitjans, P.; Senyshyn, A.; Ehrenberg, H.; Lotnyk, A.; Duppel, V.; Kienle, L.; Janek, J. *Phys. Chem. Chem. Phys.* **2011**, *13*, 19378.
(5) Geiger, C. A.; Alekseev, E.; Lazic, B.; Fisch, M.; Armbruster, T.; Langner, R.; Fechtelkord, M.; Kim, N.; Pettke, T.; Weppner, W. *Inorg. Chem.* **2011**, *50*, 1089.
(6) Howard, M. A.; Clemens, O.; Kendrick, E.; Knight, K. S.; Apperly, P. A.; Anderson, P. A.; Slater, P. R. *Dalton Trans.* **2012**, *41*, 12048.
(7) Rettenwander, D.; Geiger, C. A.; Tribus, M.; Tropper, P.; Amthauer, G. *Inorg. Chem.* **2014**, *53*, 6264.
(8) El Shinawi, H.; Janek, J. *J. Power Sources* **2013**, *225*, 13−19.
(9) Bernuy-Lopez, C.; Manalastas, W., Jr.; Lopez del Amo, J. M.; Aguadero, A.; Aguesse, F.; Kilner, J. A. *Chem. Mater.* **2014**, *26*, 3610.
(10) Rettenwander, D.; Blaha, P.; Laskowski, R.; Schwarz, K.; Bottke, P.; Wilkening, M.; Geiger, C. A.; Amthauer, G. *Chem. Mater.* **2014**, *26*, 2617.
(11) Allen, J. L.; Wolfenstine, J.; Rangasamy, E.; Sakamoto, J. *J. Power Sources* **2012**, *206*, 315.
(12) Vosegaard, T.; Massiot, D.; Gautier, N.; Jakobsen, H. J. *Inorg. Chem.* **1997**, *36*, 2449.
(13) Rangasamy, E.; Wolfenstine, J.; Sakamoto, J. *Solid State Ionics* **2012**, *206*, 28.
(14) Shannon, R. D.; Prewitt, C. T. *Acta Crystallogr.* **1969**, *B25*, 925.
(15) Düvel, A.; Kuhn, A.; Robben, L.; Wilkening, M.; Heitjans, P. *J. Phys. Chem. C* **2012**, *116*, 15192.
(16) Wohlmuth, D.; Epp, V.; Bottke, P.; Hanzu, I.; Bitschnau, B.; Letofsky-Papst, I.; Kriechbaum, M.; Amenitsch, H.; Hofer, F.; Wilkening, M. *J. Mater. Chem. A* **2014**, *2*, 20295.
(17) Hubaud, A. A.; Schroeder, D. J.; Key, B.; Ingram, B. J.; Dogan, F.; Vaughey, J. T. *J. Mater. Chem. A* **2013**, *1*, 8813.
(18) Faske, S.; Eckert, H.; Vogel, M. *Phys. Rev. B* **2008**, *77*, 104301.
(19) Wilkening, M.; Kuhn, A.; Heitjans, P. *Phys. Rev. B* **2008**, *78*, 054303.
(20) Murugan, R.; Thangadurai, V.; Weppner, W. *J. Electrochem. Soc.* **2008**, *155*, A90.

DOI: 10.1021/acs.chemmater.5b00684
Chem. Mater. 2015, 27, 3135−3142

4. Conclusion and Outlook

During the course of this PhD work different classes of materials have been investigated, *viz.* (i) layered structures: $Li_{0.17}SnS_2$ and LiC_6, (ii) ultraslow ionic conductors: Li_2SnO_3 and $LiAlO_2$, (iii) garnet-type ion conductors: $Li_{7-3(x+y)}Ga_xAl_yLa_3Zr_2O_{12}$. Here, the contribution of material synthesis, as in the case of lithium stannate Li_2SnO_3, or the study of applied systems such as electrochemical cells was minor. The main focus was placed on material characterization, or in a more concrete sense, the fundamental study of Li ion diffusion mechanisms and dynamical parameters. In order to understand the complexity of Li diffusion, methods that probe ionic motion from a microscopic and macroscopic point of view were employed. Along with conductivity measurements and dynamic mechanical relaxation analysis we employed a large portfolio of NMR techniques and were able to access Li self-diffusion parameters and diffusion pathways under the influence of morphology, crystallinity and structural disorder on a sub-Hz to GHz time scale.

$Li_{0.17}SnS_2$. Low-dimensional Li ion dynamics were studied in $Li_{0.17}SnS_2$ for three different morphologies: *micro-* and *nanocrystalline* and another *defect-enriched nano-sized* sample. Uncorrelated Li motion in the SnS_2 interlayer region was successfully probed for micro-$Li_{0.17}SnS_2$. However, Li diffusion in both samples of nano-$Li_{0.17}SnS_2$ proved to be more complex: Due to the influence of amorphous or defect-rich interfacial regions broad SLRρ rate maxima were, mainly governed by correlation effects and local jumps. These findings were corroborated by ^{7}Li NMR line shape analysis of nanocrystalline $Li_{0.17}SnS_2$ exhibiting a two-component NMR line. ^{7}Li NMR spectra show both fast and slow diffusing ions in the crystalline grains and in large interfacial areas of nanocrystalline $Li_{0.17}SnS_2$.

Furthermore, the influence of thermal annealing was studied for the *microcrystalline* sample. The diffusion-induced SLRρ rate peak surprisingly pointed towards two distinct diffusion processes, taking into account that only interlayer sites should be occupied for an intercalation degree of $x = 0.17$ in Li_xSnS_2. After thermal annealing the rate peak shifts and is then mainly dominated by the slower of the two processes. Most likely this irreversible change in diffusion behavior can be ascribed to a temperature-induced redistribution of the Li ions caused by an be inhomogeneous distribution directly after chemical intercalation.

In this context, structural characterization of $Li_{0.17}SnS_2$ with neutron diffraction would help to elucidate the Li site occupancy and Li distribution within the SnS_2 host material, possibly leading to a better understanding of the underlying diffusion mechanism. Additionally frequency-dependent NMR measurements could provide more information on the anisotropic Li motion in $Li_{0.17}SnS_2$, similarly to ^{7}Li NMR studies on Li_xNbS_2.[92,93]

LiC_6. For the stage-1 graphite intercalation compound, a diffusion-induced SLRρ rate peak (in the rotating frame) indicates a self-diffusion coefficient of $D_{2D} \approx 1.9 \times 10^{-11}$ m^2 s^{-1} for restricted (2D) and $D_{3D} \approx 1.3 \times 10^{-11}$ m^2 s^{-1} for non-restricted motion (3D) at 314 K . Considering an activation energy of 0.55 eV, this corresponds to $D \approx 10^{-15}$ m^2 s^{-1} at room temperature (T = 295 K), which is lower than expected for a widely used negative electrode material. Both spin lattice relaxation in the laboratory and rotating frame are, to a great deal, influenced by non-diffusive background relaxation, which can be traced back to the strong coupling of Li spins with the conducting electrons of the graphite. This could also be the reason why the realization of frequency-dependent NMR proved to be difficult. Locking frequencies higher than 10 kHz could not be applied as the magnitude of the corresponding locking pulses was were too high to be handled by the spectrometer. Interestingly, analysis of the rate peak points towards a non-negligible influence of diffusion perpendicular to the *ab*-plane, as it can be best approximated with a modified-BPP model. Overall, a uniform Arrhenius-activated dynamics can be deduced by taking previous NMR relaxation measurements into account. In order to shed further light onto long-range diffusion in LiC_6 spin-alignment echo NMR measurements have already been carried out and are currently under preparation for publication. Preliminary results show macroscopic diffusion proceeding via the same mechanism as probed by spin-locking NMR on a shorter length scale.

Li_2SnO_3. Being isostructural to Li_2TiO_3 and Li_2ZrO_3 diamagnetic lithium stannate fulfills the expectations of a slow Li ion conductor with a RT self-diffusion coefficient in the order of 10^{-20} m^{2}s^{-1} as probed by stimulated-echo and spin-lattice relaxation NMR. However, it proves to be an interesting model system for the study of two preferred exchange processes in a structure with three distinct Li sites. This can only be understood with the help of 1D and 2D ^{6}Li MAS NMR. Surprisingly, Li exchange occurs along the crystallographic *c*-axis, with a structural disorder possibly influencing the distribution and density of vacancies to a certain extent. A heterogeneous diffusion behavior is corroborated by the results from static ^{7}Li SLR and SAE NMR experiments. The XRD pattern of Li_2SnO_3 synthesized via high-energy ball milling indicates a considerable influence of stacking faults of the alternating Li and $LiSn_2$- layers. A complicated analysis of the structural data with specialized software was not undertaken in the

framework of this study, but could prove to be beneficial in elucidating the diffusion pathways proposed by ^{6,7}Li NMR.

$LiAlO_2$. Following the comparative studies of mechanical *vs.* electrical relaxation in mixed-conducting glasses by Roling *et al.* [108,109], Debye-like Li dynamics were detected by both dynamic mechanical analysis and DC conductivity measurements and is characterized by an activation energy of 1.12 eV. In particular, at high temperatures around 500 K, self-diffusion coefficients from the mechanical analyses are in good agreement with the conductivity data. By comparing the data to ^{7}Li NMR results from literature, a single type of diffusion process can be probed over a large dynamic range of about 10 orders of magnitude. Overall, it was shown that the same Li transport mechanism can be accessed for a slow-conducting, highly ordered single crystal, via both methods. This opens up the window for the fundamental study of Li ion motion in highly-ordered systems with no partial Li occupancies. However, extremely small loss factors, as obtained for $LiAlO_2$, might limit the applicability. Besides, an adequate clamp system and sample geometry seems to be crucial for the detection of the loss peak. This is indicated by preliminary tests on single-crystalline $LiNbO_3$ samples.

$Li_{7-3(x+y)}Ga_xAl_yLa_3Zr_2O_{12}$. The aim of this study was understanding the enhanced Li dynamics of cubic Al-, Ga-doped garnets compared to garnets doped with Al only. In the context of previous studies a prevalent occupation of the 96*h* site of Ga was associated with a blocking effect by Al occupying 24*d* sites in the Li sub-lattice. However via high-resolution ^{27}Al and ^{71}Ga NMR at 21 T we discovered a similar site preference for both ions, *i.e.*, occupation of 24*d* and 96*h* sites. Consequently, together with detailed analysis of the XRD data, a change in the lattice constant might be seen as the origin of higher Li conductivity upon incorporation of Ga ions with ionic radii larger than those of Al. This study confirms that there is yet no uniform explanation found for the difference in influencing Li mobility between Al and Ga used as dopants. Further, comparison with literature data reported for the same structure is challenging as slight structural differences, resulting from varying synthesis conditions, seem to have a great impact of preferred occupancies and their correlation with Li diffusion.

A. Supplemental Material

Supplement Issue:

On the Site Occupation of Ga and Al in Stabilized Cubic $Li_{7-3(x+y)}Ga_xAl_yLa_3Zr_2O_{12}$ Garnets as Deduced from Al and Ga MAS NMR at Ultrahigh Magnetic Fields

Daniel Rettenwander*[†], Julia Langer[‡], Walter Schmidt[‡], Christian Arrer[†], Kris Harris, [#] Victor Terskikh,[§] Gillian Goward,[#] Martin Wilkening[‡], Georg Amthauer[†]

[†]Department of Materials Research and Physics, University of Salzburg, 5020 Salzburg, Austria

[‡]Christian Doppler Laboratory for Lithium Batteries, Institute for Chemistry and Technology of Materials, Graz University of Technology, 8010 Graz, Austria

[#]Department of Chemistry & Chemical Biology, McMaster University, Hamilton, Ontario L8S 4M1, Canada

[§]National Ultrahigh-Field NMR Facility for Solids, Ottawa, Ontario K1A 0R6, Canada

KEYWORDS Li-oxide garnet, Al, Ga, LLZO, ion conductor, NMR, ultrahigh magnetic fields

Table S1. Unit-Cell Parameter of $Li_{7-3(x+y)}Ga_xAl_yLa_3Zr_2O_{12}$ with x, y ∈ {0.0, 0.1, …,0.8 ∧ $x + y \leq 0.8$} and the Amount of Phases in the Different Syntheses Obtained by Rietveld Refinement.[a]

sample	a_0 [Å]	LLZO [%]	$LaAlO_3$ [%]	$Li_2Zr_2O_3$ [%]	$La_2Zr_2O_7$ [%]
$Ga_{0.8}Al_{0.0}$	12.978	100	-	-	-
$Ga_{0.7}Al_{0.1}$	12.980	100	-	-	-
$Ga_{0.6}Al_{0.2}$	12.972	97	3	-	-
$Ga_{0.5}Al_{0.3}$	12.974	87	2	-	-
$Ga_{0.4}Al_{0.4}$	12.973	84	10	3	2
$Ga_{0.3}Al_{0.5}$	12.972	72	12	3	12
$Ga_{0.2}Al_{0.6}$	12.971	74	12	5	4
$Ga_{0.1}Al_{0.7}$	12.972	63	22	8	7
$Ga_{0.0}Al_{0.8}$	12.967	33	58	-	9
$Ga_{0.7}Al_{0.0}$	12.977	100	-	-	-
$Ga_{0.6}Al_{0.1}$	12.978	100	-	-	-
$Ga_{0.5}Al_{0.2}$	12.973	87	2	-	11
$Ga_{0.4}Al_{0.3}$	12.973	96	2	-	2
$Ga_{0.3}Al_{0.4}$	12.974	88	4	2	6
$Ga_{0.2}Al_{0.5}$	12.973	86	5	5	4
$Ga_{0.1}Al_{0.6}$	12.968	84	6	9	1
$Ga_{0.0}Al_{0.7}$	12.964	73	7	4	16
$Ga_{0.6}Al_{0.0}$	12.973	100	-	-	-
$Ga_{0.5}Al_{0.1}$	12.973	100	-	-	-
$Ga_{0.4}Al_{0.2}$	12.971	100	-	-	-
$Ga_{0.3}Al_{0.3}$	12.970	100	-	-	-
$Ga_{0.2}Al_{0.4}$	12.972	92	6	2	-
$Ga_{0.1}Al_{0.5}$	12.971	89	8	3	-
$Ga_{0.0}Al_{0.6}$	12.970	88	8	4	-
$Ga_{0.5}Al_{0.0}$	12.974	100	-	-	-
$Ga_{0.4}Al_{0.1}$	12.971	100	-	-	-
$Ga_{0.3}Al_{0.2}$	12.971	100	-	-	-
$Ga_{0.2}Al_{0.3}$	12.971	100	-	-	-
$Ga_{0.1}Al_{0.4}$	12.974	97	3		-
$Ga_{0.0}Al_{0.5}$	12.972	90	7	3	-
$Ga_{0.4}Al_{0.0}$	12.978	100	-	-	-
$Ga_{0.3}Al_{0.1}$	12.977	100	-	-	-
$Ga_{0.2}Al_{0.2}$	12.978	100	-	-	-
$Ga_{0.1}Al_{0.3}$	12.974	100	-	-	-
$Ga_{0.0}Al_{0.4}$	12.970	100	<1	-	-
$Ga_{0.3}Al_{0.0}$	12.983	100	-	-	-
$Ga_{0.2}Al_{0.1}$	12.980	100	-	-	-
$Ga_{0.1}Al_{0.2}$	12.979	100	-	-	-
$Ga_{0.0}Al_{0.3}$	12.971	100	-	-	-
$Ga_{0.2}Al_{0.0}$	12.976	100	-	-	-
$Ga_{0.1}Al_{0.1}$	12.974	100	-	-	-
$Ga_{0.0}Al_{0.2}$	12.971	100	-	-	-

[a]Errors of the obtained values are insignificant and therefore not shown.

Phase Composition (XRPD).

$Ga_{5-y}Al_y$: Garnet solid solutions with a total dopant content of 0.5 are cubic in symmetry (see Figure 5). With an Al content of y = 0.4 one additional phase, 3 % $AlLaO_3$, occurs. At an Al content of y = 0.5 3 % $AlLaO_3$, and 7 % $Li_2Zr_2O_3$ are present in the sample. The presence of extra Al phases in the sample for $y \geq 0.3$ indicates to an upper incorporation limit of Al close to 0.3 Al pfu.

$Ga_{6-y}Al_y$: Samples with a total dopant concentration of 0.6 exhibit reflections indicating only cubic symmetry up to $y < 0.4$ (see Figure 6). At an Al content of y = 0.4 6 % $LaAlO_3$, and 2 % $Li_2Zr_2O_3$ arise in the synthesis. Increasing the Al content to y = 0.5 leads to extra phases, 8 % $LaAlO_3$, and 3 % $Li_2Zr_2O_3$ and with y = 0.6 8 % $LaAlO_3$, and 4 % $Li_2Zr_2O_3$ are present in the sample, respectively.

$Ga_{7-y}Al_y$ garnets are single phase up to $y < 0.2$. With an increasing Al content the amount of extra phases increase simultaneously. With y = 0.2 2 % $LaAlO_3$ appear. With y = 0.3 and 0.4 two additional phases occur; for y = 0.3 2 % $AlLaO_3$, and 11 % $La_2Zr_2O_7$ and for y = 0.4 4 % $LaAlO_3$, and 2 % $La_2Zr_2O_7$. Samples with y = 0.5, 0.6, and 0.7 contain three extra phases; we find for y = 0.5 5 % $AlLaO_3$, 5 % Li_2ZrO_3 and 4 % $La_2Zr_2O_7$, for y = 0.6 6 % $AlLaO_3$, 9 % Li_2ZrO_3 and 1 % $La_2Zr_2O_7$, and for y = 0.7 7 % $AlLaO_3$, 4 % Li_2ZrO_3 and 16 % $La_2Zr_2O_7$.

$Ga_{8-y}Al_y$: LLZO with a total dopant content of 0.8 are single phase up to $y < 0.2$. Probably small amounts of extra phases < 1 wt-% are present in those samples. The increase of the Al portion leads to an increase of the amount of extra phases. At an Al content of y = 0.2 3 % $AlLaO_3$ and with y = 0.3, 2 %.$AlLaO_3$ occur, respectively. If y = 0.4—07 three additional phases arise; for y = 0.5 10 % $AlLaO_3$, and 11 % $La_2Zr_2O_7$ and for y = 0.4 4 % $AlLaO_3$, and 2 % $La_2Zr_2O_7$. In samples with y = 0.5, 0.6 and 0.7 three extra phases occurs; we find for y = 0.5 5 % $AlLaO_3$, 5 % Li_2ZrO_3 and 4 % $La_2Zr_2O_7$, for y = 0.6 6 % $AlLaO_3$, 9 % Li_2ZrO_3 and 1 % $La_2Zr_2O_7$, and for y = 0.7 7 % $AlLaO_3$, 4 % Li_2ZrO_3 and 16 % $La_2Zr_2O_7$.

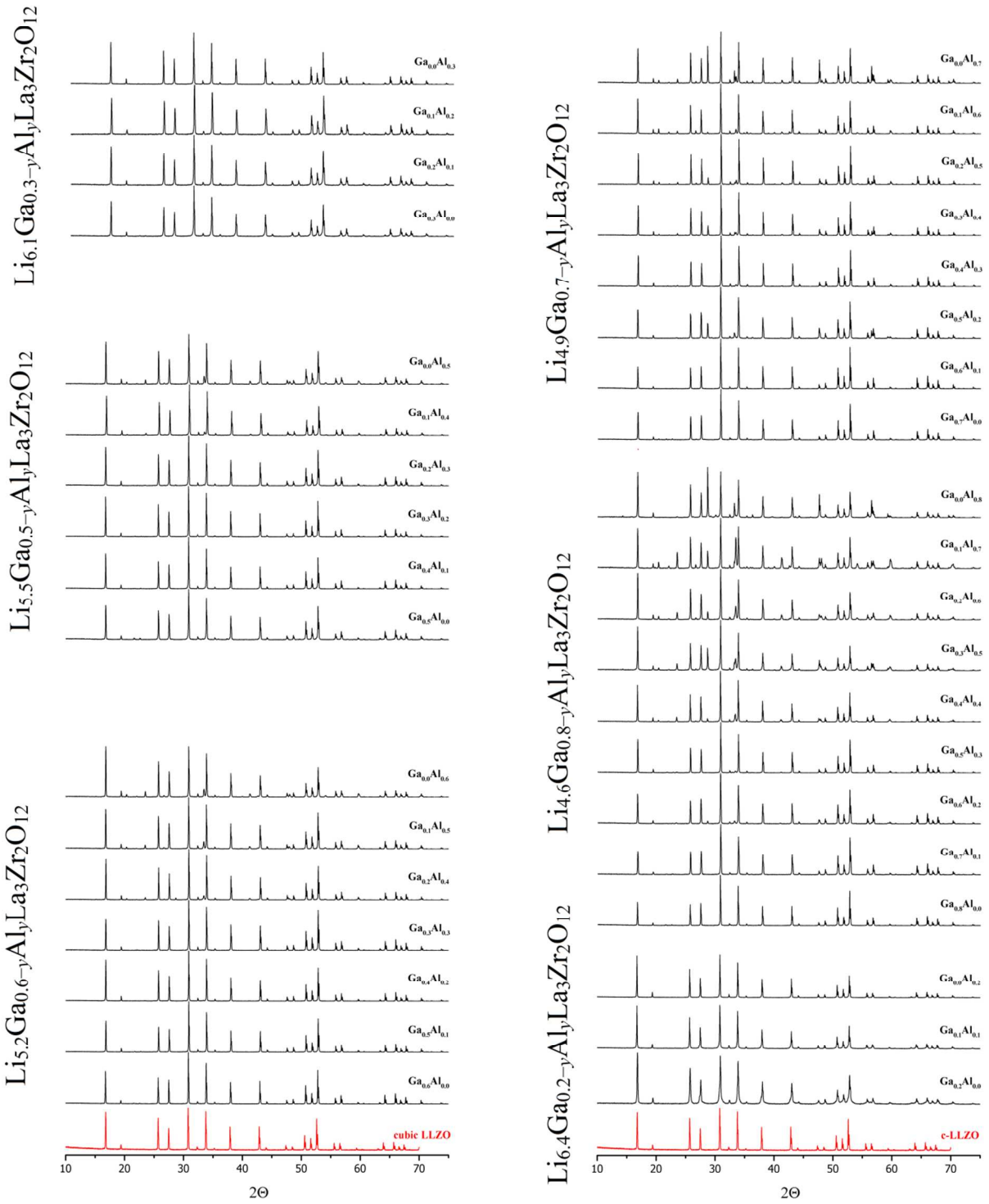

Figure S1. XRPD pattern of $Li_{6.4}Ga_{0.2-y}Al_yLa_3Zr_2O_{12}$, $Li_{6.1}Ga_{0.3-y}Al_yLa_3Zr_2O_{12}$, $Li_{5.5}Ga_{0.5-y}Al_yLa_3Zr_2O_{12}$, $Li_{5.2}Ga_{0.6-y}Al_yLa_3Zr_2O_{12}$, $Li_{4.9}Ga_{0.7-y}Al_yLa_3Zr_2O_{12}$, and $Li_{4.6}Ga_{0.8-y}Al_yLa_3Zr_2O_{12}$. The diffraction pattern of cubic LLZO (red) is shown for comparison.

B. Experimental

B.1. Apparatus

B.1.1. Solid-State NMR Setup

NMR measurements were primarily carried out on two configurations of Bruker Avance III solid-state NMR spectrometesr of the wide-bore (WB) type. An Avance III 300 spectrometer is connected to a shimmed cryomagnet with a nominal field of 7 T, which corresponds to a ^{6}Li resonance frequency of 44 MHz, or 116 MHz for ^{7}Li. The second configuration involves an Avance III 500 spectrometer together with an 11 T magnet, consequently with $\nu_0(^{6}\mathrm{Li})$ = 74 MHz, and $\nu_0(^{7}\mathrm{Li})$ = 194 MHz. Another configuration involved a standard-bore (SB) Avance III operating at 11 T. For high-field NMR measurements a 21 T magnet in conjunction with a Bruker Avance II spectrometer (SB) provided resonance frequencies of $\nu_0(^{6}\mathrm{Li})$ = 132 MHz, $\nu_0(^{27}\mathrm{Al})$ = 132 MHz, $\nu_0(^{71}\mathrm{Ga})$ = 275 MHz. The different types of probe heads that were used for static and MAS experiments are all commercially available "standard" Bruker probes.

For static measurements a broadband Teflon probe can be employed between temperatures of about 180 K and 450 K while a ceramic probe is designed for operation in the high-temperature range up to 620 K. Both probes are equipped with a Eurotherm temperature controller in connection with type T thermocouples.

High-resolution magic-angle spinning NMR on both the Avance III-500 and Avance II was conducted by using 2.5 mm Bruker-type broadband probeheads (WB, SB), which allow a maximum spinning rate of 35 kHz.

For static measurements powder-samples were fire sealed under vacuum, using glass ampoules typically of 3-4 cm length and 4 mm of diameter. Characterization via magic-angle-spinning NMR was performed with the powder sample packed into zirconia rotors with 2.5mm diameter.

B.1.2. Impedance Spectroscopy Setup

For conductivity measurements of single-crystalline $LiAlO_2$ the samples were prepared as squares with a side length of 1 cm and a thickness of 0.93 cm. Electrical contacts were applied as Au electrodes (about 100 nm thickness) with a sputter coater (Leica EM SCD050). A detailed description of the measurement setup is given in P3 (section 3.2.2).

B.1.3. Software

The following software was used for acquisition, processing, analysis and presentation of the data found in this thesis.

Topspin 3.1 (Bruker Biospin GmbH): Acquisition of NMR experiments on Bruker Avance III spectrometers, along with phase correction and Fourier transformation of the NMR spectra.

WinDeta 5.73 (Novocontrol Technologies GmbH & Co. KG): Execution of impedance spectroscopy measurements along with data export.

DMFIT Program: Conversion of Bruker files into ASCII format; fitting of solid-state NMR spectra.

Diamond 3.2: Visualization of crystallographic structures.

IGOR Pro 6.3.7: Processing and analysis of data; creating graphics.

CIFIT[56]**:** Fitting of data obtained from selective inversion NMR experiments. (See also: www.chemistry.mcmaster.ca/bain/cifman.pdf)

Corel Draw X4: Processing and editing of graphics for presentation and publication.

Microsoft Office 2010: Text processing (Word, Excel).

Mendeley Desktop 1.15: Management of references.

B.2. NMR pulse sequences

Saturation Recovery Pulse Sequence

This pulse sequence is used to measure spin-lattice relaxation rates in the laboratory frame of reference (*cf.* Figure 13). Initially a saturation train of ten pulses $\beta_1 = \pi/2$ is used to destroy the longitudinal magnetization M_z. The recovery of M_z is monitored as a function of the varying delay time t_d by a detection pulse $\beta_2 = \pi/2$. The amplitude of the resulting FID is proportional to M_z. Thus, the recovery of M_z can be approximated by stretched exponentials.

$$M_z(t_d) = M_{z,\mathrm{eq}}\left[1 - \exp(-\left[t_d / T_1\right]^{\gamma})\right]$$

$M_{z\mathrm{eq}}$ denotes the equilibrium magnetization and γ the stretching factor. In order to ensure full relaxation between each scan the recycle delay is set to $5 \times T_1$. 1D spectra can be obtained by Fourier transformation of an FID as long as a sufficiently long delay time is provided.

Spin-Lock Pulse Sequence

In the rotating frame of reference $T_{1\rho}$ is recorded via the spin-locking technique [59–62,115], as shown in Figure 13. At first a pulse $\beta_1 = \pi/2$ tips the equilibrium magnetization $M_{\rho\mathrm{eq}}$ into the *x,y*-plane where it is spin-locked in the field B_1. This is achieved by applying a locking pulse β_2 for the varying duration t_{lock} of the pulse. If the locking field is switched off we find the magnetization in the field B_1 relaxing towards zero, which is also reflected in the resulting FID. The magnetization transients are also parametrized via stretched exponentials.

$$M_{\rho}(t_{\mathrm{d}}) = M_{\rho,\mathrm{eq}}\left[\exp(-\left[t_{\mathrm{d}} / T_{1\rho}\right]^{\gamma})\right]$$

As for SLR in the lab frame of reference the recycle delay is set to $5 \times T_1$.

Solid-echo pulse sequence

The solid echo pulse sequence records the transversal relaxation (T_2) as depicted in . After rotating the magnetization into the *x,y*-plane the spins start to dephase due to spin-spin relaxation during the preparation (evolution) time t_{p}. This is followed by a refocusing pulse $\beta_2 = 64°$ and an echo appearing at $t = 2t_{\mathrm{p}}$. Due to this sequence quadrupolar contributions are more emphasized in the appearing echo. The magnetization decay is measured as a function of t_{p} starting from the top of the echo. Usually these transients can be described by a single exponential function.

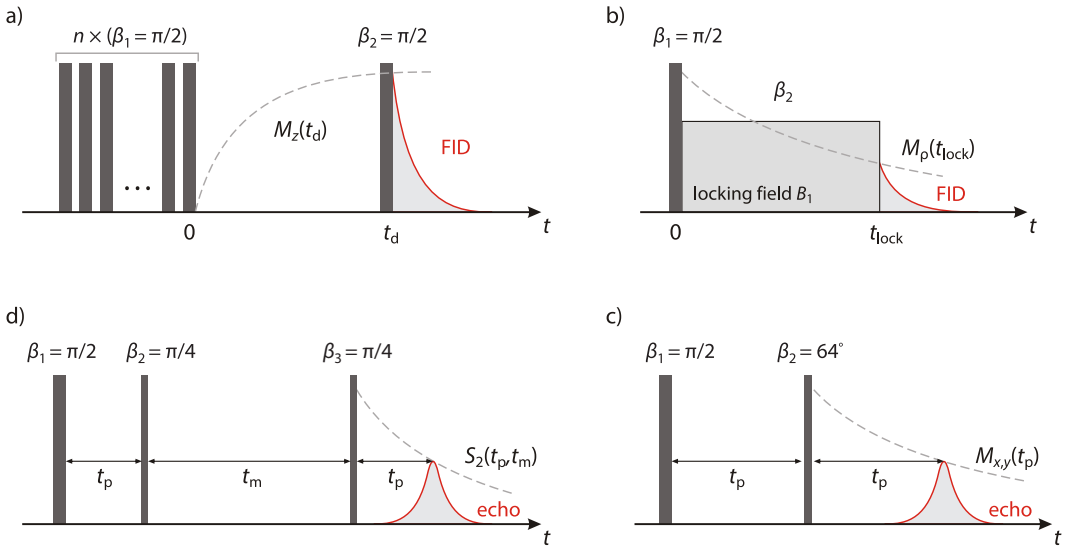

Figure 13: a) Saturation recovery sequence used to record spin-lattice relaxation rates in the laboratory frame of reference. b) The spin-locking technique applying resonance frequencies in the kHz range. c) Solid-echo sequence for recording R_2 and solid-echo spectra. d) Spin-alignment echoes are generated with a Jeener-Broekart pulse sequence. (See text for further information.) For all types of NMR experiments proper phase cycling was applied in order to eliminate inaccurate pulse lengths and phases. More information on the phase cycling of these experiments is given in Ref. [11,33]

$$M_{x,y}(t_p) = M_{x,y}^{eq}\left[\exp(-[2t_p / T_2])\right]$$

^{7}Li NMR SAE Pulse Sequence

Spin-alingment echoes are recorded with a Jeener-Broekart pulse sequence, as already described in 2.3.4, and depicted in Figure 13. If single-spin motional correlation functions are measured the preparation time is usually set to a value of 10 μs ≤ t_p ≤ 20 μs. The echo amplitude S_2 (t_p, t_m) is damped due to diffusive motion with the resulting decay curves described by stretched exponentials (*cf.* equation (2.94). Relaxation processes and spin-diffusion can lead to a second decay step in the curve.

2D EXSY (NOESY) pulse sequence and 1D selective inversion pulse sequence

Here, the reader is referred to the introductory chapter 2.3.2, which provides a detailed description on MAS exchange spectroscopy and a graphical representation in Figure 6.

C. Publications

C.1. Journal articles

Diffusion-induced ^{7}Li NMR relaxation of layer-structured tin disulphide – Li diffusion along the buried interfaces in $Li_{0.17}SnS_2$
J. Langer, V. Epp, M. Sternad, and M. Wilkening, Solid State Ionics **276**, 56 (2015).

Mechanical detection of ultraslow, Debye-like Li-ion motions in $LiAlO_2$ single crystals
J. Langer, D. Wohlmuth, A. Kovalčik, V. Epp, F. Stelzer, and M. Wilkening, Ann. Phys. **527**, 523 (2015).

Site Occupation of Ga and Al in Stabilized Cubic $Li_{7-3(x+y)}Ga_xAl_yLa_3Zr_2O_{12}$ Garnets as deduced from ^{27}Al and ^{71}Ga MAS NMR at Ultrahigh Magnetic Fields
D. Rettenwander, J. Langer, W. Schmidt, C. Arrer, K. J. Harris, V. Terskikh, G. R. Goward, M. Wilkening, and G. Amthauer, Chem. Mater. **27**, 3135 (2015).

Lithium motion in the anode material LiC_6 as seen via time-domain ^{7}Li NMR
J. Langer, V. Epp, P. Heitjans, F. A. Mautner, and M. Wilkening, Phys. Rev. B **88**, 094304 (2013).

C.2. Oral presentations

Elucidating Li ion dynamics and diffusion pathways in Li_2SnO_3 – A comparative $^{6,7}Li$ NMR study
J. Langer, P. Bottke, and M. Wilkening
20th International Conference on Solid State Ionics (SSI-20), Keystone (US), June 14-19, 2015.

Lithium ion dynamics in micro- and nanocrystalline layer-structured insertion materials as seen via ^{7}Li nuclear magnetic resonance
J. Langer, V. Epp, and M. Wilkening
E-MRS Spring Meeting, Lille (FRA), May 26-30, 2014.

Solid-state NMR studies on micro- and nanocrystalline two-dimensional Li-ion conductors
J. Langer, V. Epp, P. Bottke, I. Hanzu, and M. Wilkening
19th International Conference on Solid State Ionics (SSI-19), Kyoto (JPN), June 2-7, 2013.

C.3. Poster presentations

Combined $^{6,7}Li$ NMR study of slow Li diffusion in monoclinic Li_2SnO_3
J. Langer and M. Wilkening
15th European Conference on Solid State Chemistry (ECSSC), Vienna (AUT), August 23-26, 2015.

Li diffusion in layer-structured nanocrystalline dichalcogenides as probed by NMR spectroscopy
J. Langer, V. Epp, and M. Wilkening
ZFM-Summer School 2012: "Functional Solids", Celle (GER), July 22-27, 2012.

D. Bibliography

1. C. B. Field, V. R. Barros, D. J. Dokken, K. J. Mach, M. D. Mastrandrea, T. E. Bilir, M. Chatterjee, K. L. Ebi, Y. O. Estrada, R. C. Genova, B. Girma, E. S. Kissel, A. N. Levy, S. MacCracken, P. R. Mastrandrea, and L. L. White, editors , *Climate Change 2014: Impacts, Adaption and Vulnerability: Part A Global and Sectoral Aspects.* (Cambridge University Press, 2014).

2. O. Edenhofer, R. Pichs-Madruga, Y. Sokona, J. Minx, E. Farahani, S. Kadner, K. Seyboth, A. Adler, I. Baum, S. Brunner, P. Eickemeier, B. Kriemann, J. Savolainen, S. Schlömer, C. von Stechow, and T. Zwickel, editors , *Climate Change 2014: Mitigation of Climate Change* (Cambridge University Press, 2014).

3. International Electrotechnical Commission (IEC), White Paper: *Electrical Energy Storage* (2015).

4. J. B. Bates, N. J. Dudney, B. Neudecker, A. Ueda, and C. D. Evans, Solid State Ionics **135**, 33 (2000).

5. J. Maier, Nat Mater **4**, 805 (2005).

6. P. Heitjans and M. Wilkening, MRS Bull. **34**, 915 (2009).

7. M. Wilkening, V. Epp, A. Feldhoff, and P. Heitjans, J. Phys. Chem. C **112**, 9291 (2008).

8. M. Wilkening and P. Heitjans, ChemPhysChem **13**, 53 (2012).

9. R. Böhmer and F. Qi, Solid State Nucl. Magn. Reson. **31**, 28 (2007).

10. R. Böhmer, J. Magn. Reson. **147**, 78 (2000).

11. M. Wilkening, Ultralangsame Ionenbewegungen in Festkörpern, Universität Hannover, 2005.

12. H. Mehrer, *Diffusion in Solids: Fundamentals, Methods, Materials, Diffusion-Controlled Processes* (Springer, Berlin, New York, 2007).

13. G. E. Murch, in *Phase Transform. Mater.*, edited by G. Kostorz (WILEY-VCH Verlag GmbH, Weinheim, 2001), pp. 171–238.

14. A. Einstein, Ann. Phys. **322**, 549 (1905).

15. A. Einstein, Ann. Phys. **324**, 371 (1906).

16. M. von Smoluchowski, Ann. Phys. **326**, 756 (1906).

17. A. R. West, *Solid State Chemistry* (Wiley, Chichester, UK, 1984).

18. H. Mehrer and F. Wenwer, in *Diffus. Met.* (Vieweg, 1998).

19. M. Achimovičová, K. Lucenildo da Silva, N. Daneu, A. Rečnik, S. Indris, H. Hain, M. Scheuermann, H. Hahn, and V. Šepelák, J. Mater. Chem. **21**, 5873 (2011).

20. P. Stilbs, Prog. Nucl. Magn. Reson. Spectrosc. **19**, 1 (1987).

21. J. R. M. Donald, editor , *Impedance Spectroscopy* (Wiley, New York, 1987).

22. C. Martiny, S. Murugavel, B. Roling, F. Natrup, H. Bracht, and M. D. Ingram, Glas. Technol. **43C**, 309 (2002).

23. P. Heitjans, Solid State Ionics **18**, 50 (1986).

24. P. Heitjans, S. Indris, and M. Wilkening, in *Diffus. Fundam.*, edited by J. Kärger, F. Grinberg, and P. Heitjans (Leipziger Universitätsverlag, Leipzig, 2005), pp. 226–245.

25. P. Heitjans, A. Schirmer, and S. Indris, in *Diffus. Condens. Matter*, edited by P. Heitjans and J. Kärger (Springer, Berlin, 2005), pp. 367–415.

26. T. Springer and R. E. Lechner, in *Diffus. Condens. Matter - Methods, Mater. Model.*, edited by P. Heitjans and J. Kärger, 2nd ed. (Springer, Berlin, 2005), pp. 91–164.

27. D. Haarer and H. W. Spiess, editors , *Spektroskopie Amorpher Und Kristalliner Festkörper* (Steinkopf, Darmstadt, 1995).

28. A. Abragam, *The Principle of Nuclear Magnetism* (Clarendon Press: Oxford, U.K., 1961).

29. C. P. Slichter, *Principles of Nuclear Magnetic Resonance*, 3rd ed. (Springer-Verlag, Berlin, New York, 1990).

30. M. H. Levitt, *Spin Dynamics: Basics of Nuclear Magnetic Resonance*, 2001st ed. (John Wiley & Sons, Ltd., Chichester, UK, 2001).

31. M. J. Duer, *Introduction to Solid-State NMR Spectroscopy* (Blackwell Science Ltd., Malden, MA, 2004).

32. H. Friebolin, *Basic One- and Two-Dimensional NMR Spectroscopy*, 5th ed. (WILEY-VCH Verlag, Weinheim, 2011).

33. V. Epp, Lithium Diffusivity in Fast Solid-State Ion Conductors, Technische Universität Graz, 2014.

34. B. Ruprecht, Langsamer Li-Transport in Lithiumübergangsmetalloxiden Untersucht Mit NMR- Und Impedanzspektroskopischen Methoden, Universität Hannover, 2012.

35. F. Qi, 2H- Und 7Li-NMR-Untersuchungen Zur Dynamik an Ionenleitern, Johannes Gutenberg-Universiät Mainz, 2003.

36. W. Küchler, Kernspinresonanz-Untersuchungen Zur Diffusion von Li in Der Schichtstrukturierten Und Der Kubischen Interkalationsverbindung LixTiS2, Universität Hannover, 1992.

37. J. Keeler, *Understanding NMR Spectroscopy* (John Wiley & Sons, Ltd., Chichester, UK, 2010).

38. J. Fitzgerald, in *ACS Symp. Ser. No.717* (ACS, Washington, DC, 1999).

39. A. Medek, J. S. Harwood, and L. Frydman, J. Am. Chem. Soc. **117**, 12779 (1995).

40. L. Frydman, in *Encycl. Nucl. Magn. Reson.*, edited by D. M. Grant and R. K. Harris (John Wiley & Sons, Ltd., Chichester, UK, 2002), pp. 262–274.

41. L. Frydman and J. S. Harwood, J. Am. Chem. Soc. **117**, 5367 (1995).

42. J.-P. Amoureux, C. Fernandez, and L. Frydman, Chem. Phys. Lett. **259**, 347 (1996).

43. J.-P. Amoureux, Solid State Nucl. Magn. Reson. **2**, 83 (1993).

44. J.-P. Amoureux and C. Fernandez, Solid State Nucl. Magn. Reson. **10**, 211 (1998).

45. V. Kappes, Impedanz- Und NMR-Spektroskopische Untersuchungen an Wasserhaltigen Alumosilikatgläsern, Universität Hannover, 2002.

46. A. D. Bain, Prog. Nucl. Magn. Reson. Spectrosc. **43**, 63 (2003).

47. P. Bottke, Zur Lithium-Selbstdiffusion in Kristallinen Festkörpern, Technische Universität Graz, 2015.

48. K. G. Orrell, V. Šik, and D. Stephenson, Prog. Nucl. Magn. Reson. Spectrosc. **22**, 141 (1990).

49. C. L. Perrin and T. J. Dwyer, Chem. Rev. **90**, 935 (1990).

50. L. J. M. Davis, B. L. Ellis, T. N. Ramesh, L. F. Nazar, A. D. Bain, and G. R. Goward, J. Phys. Chem. C **115**, 22603 (2011).

51. L. J. M. Davis, X. J. He, A. D. Bain, and G. R. Goward, Solid State Nucl. Magn. Reson. **42**, 26 (2012).

52. L. J. M. Davis and G. R. Goward, J. Phys. Chem. C **117**, 7981 (2013).

53. D. L. Smiley, L. J. M. Davis, and G. R. Goward, J. Phys. Chem. C **117**, 24181 (2013).

54. A. D. Bain and J. A. Cramer, J. Magn. Reson. Ser. A **118**, 21 (1996).

55. C. Bauer, R. Freeman, T. Frenkiel, J. Keeler, and A. J. Shaka, J. Magn. Reson. **58**, 442 (1984).

56. A. D. Bain and D. A. Fletcher, Mol. Phys. **95**, 1091 (1998).

57. J. J. Led and H. Gesmar, J. Magn. Reson. **49**, 444 (1982).

58. D. L. Smiley, M. Z. Tessaro, X. He, and G. R. Goward, J. Phys. Chem. C **119**, 16468 (2015).

59. C. P. Slichter and D. Ailion, Phys. Rev. **135**, 1099 (1964).

60. D. C. Ailion and C. P. Slichter, Phys. Rev. **137**, A235 (1965).

61. D. C. Look and I. J. Lowe, J. Chem. Phys. **44**, (1966).

62. D. Ailion and C. P. Slichter, Phys. Rev. Lett. **12**, 168 (1964).

63. S. W. Kelly and C. A. Sholl, J. Phys. Condens. Matter **4**, 3317 (1992).

64. N. Bloembergen, E. M. Purcell, and R. V Pound, Phys. Rev. **73**, 679 (1948).

65. P. Heitjans, A. Korblein, H. Ackermann, D. Dubbers, F. Fujara, and H.-J. Stockmann, J. Phys. F Met. Phys. **15**, 41 (1985).

66. A. Bunde, W. Dieterich, P. Maass, and M. Meyer, in *Diffus. Condens. Matter*, edited by P. Heitjans and J. Kärger (Springer, Berlin, 2005), pp. 813–856.

67. P. M. Richards, Solid State Commun. **25**, 1019 (1978).

68. W. Küchler, P. Heitjans, A. Payer, and R. Schöllhorn, Solid State Ionics **70–71, Par**, 434 (1994).

69. H. W. Spiess, J. Chem. Phys. **72**, 6755 (1980).

70. M. Lausch and H. W. Spiess, J. Magn. Res. **54**, 466 (1983).

71. X.-P. Tang and Y. Wu, J. Magn. Reson. **133**, 155 (1998).

72. Z. Xu and J. F. Stebbins, Science (80-.). 1332 (1995).

73. V. W. J. Verhoeven, I. M. de Schepper, G. Nachtegaal, A. P. M. Kentgens, E. M. Kelder, J. Schoonman, and F. M. Mulder, Phys. Rev. Lett. **86**, 4314 (2001).

74. L. S. Cahill, R. P. Chapman, J. F. Britten, and G. R. Goward, J. Phys. Chem. B **110**, 7171 (2006).

75. J. Jeener and P. Broekaert, Phys. Rev. **157**, 232 (1967).

76. A. Kuhn, V. Epp, G. Schmidt, S. Narayanan, V. Thangadurai, and M. Wilkening, J. Phys. Condens. Matter **24**, 035901 (2012).

77. V. Epp, O. Gün, H.-J. Deiseroth, and M. Wilkening, Phys. Chem. Chem. Phys. **15**, 7123 (2013).

78. G. Fleischer and F. Fujara, in *Nucl. Magn. Reson.* (Springer, Berlin, 1994), p. 159.

79. F. Qi, G. Diezemann, H. Böhm, J. Lambert, and R. Böhmer, J. Magn. Reson. **169**, 225 (2004).

80. F. Qi, T. Jörg, and R. Böhmer, Solid State Nucl. Magn. Reson. **22**, 484 (2002).

81. D. Wohlmuth, V. Epp, P. Bottke, I. Hanzu, B. Bitschnau, I. Letofsky-Papst, M. Kriechbaum, H. Amenitsch, F. Hofer, and M. Wilkening, J. Mater. Chem. A **2**, 20295 (2014).

82. S. Indris, P. Heitjans, R. Uecker, and B. Roling, J. Phys. Chem. C **116**, 14243 (2012).

83. S. Indris, P. Heitjans, R. Uecker, and T. Bredow, Phys. Rev. B **74**, 245120 (2006).

84. M. Bouroushian, *Electrochemistry of Metal Chalcogenides* (Springer-Verlag, Berlin, Heidelberg, 2010).

85. M. S. Whittingham, Chem. Rev. **104**, 4271 (2004).

86. M. Wilkening, W. Küchler, and P. Heitjans, Phys. Rev. Lett. **97**, 65901 (2006).

87. R. Winter and P. Heitjans, Fourth Int. Conf. Nanostructured Mater. **12**, 883 (1999).

88. R. Winter and P. Heitjans, J. Phys. Chem. B **105**, 6108 (2001).

89. R. Winter and P. Heitjans, J. Non. Cryst. Solids **293-295**, 19 (2001).

90. M. Wilkening and P. Heitjans, Defect Diffus. Forum Vols . 237-240 **240**, 1182 (2005).

91. W. Bensch, T. Bredow, H. Ebert, P. Heitjans, S. Indris, S. Mankovsky, and M. Wilkening, Prog. Solid State Chem. **37**, 206 (2009).

92. V. Epp, S. Nakhal, M. Lerch, and M. Wilkening, J. Phys. Condens. Matter **25**, 195402 (2013).

93. B. Stanje, V. Epp, S. Nakhal, M. Lerch, and M. Wilkening, ACS Appl. Mater. Interfaces **7**, 4089 (2015).

94. T. Pietrass, F. Taulelle, P. Lavela, J. Olivier-Fourcade, J. Jumas, and S. Steuernagel, J. Phys. Chem. B **101**, 6715 (1997).

95. I. Lefebvre-Devos, J. Olivier-Fourcade, J. C. Jumas, and P. Lavela, Phys. Rev. B **61**, 3110 (2000).

96. M. Wilkening, S. Indris, and P. Heitjans, Phys. Chem. Chem. Phys. **5**, 2225 (2003).

97. D. Billaud, F. X. Henry, and P. Willmann, J. Power Sources **54**, 383 (1995).

98. D. Aurbach, B. Markovsky, I. Weissman, E. Levi, and Y. Ein-Eli, Electrochim. Acta **45**, 67 (1999).

99. J.-M. Tarascon and M. Armand, Nature **414**, 359 (2001).

100. J. R. Dahn, Phys. Rev. B **44**, 9170 (1991).

101. M. S. Dresselhaus and G. Dresselhaus, Adv. Phys. **51**, 1 (2002).

102. A. Magerl, H. Zabel, and I. S. Anderson, Phys. Rev. Lett. **55**, 222 (1985).

103. P. Freiländer, P. Heitjans, H. Ackermann, G. Kiese, H. Stöckmann, and C. Van Der Marel, Zeitschrift Für Phys. Chemie **151**, 93 (1987).

104. N. Itou, H. Toyoda, K. Morita, and H. Sugai, J. Nucl. Mater. **290–293**, 281 (2001).

105. K. Toyoura, Y. Koyama, A. Kuwabara, and I. Tanaka, J. Phys. Chem. C **114**, 2375 (2010).

106. K. Persson, V. A. Sethuraman, L. J. Hardwick, Y. Hinuma, Y. S. Meng, A. van der Ven, V. Srinivasan, R. Kostecki, and G. Ceder, J. Phys. Chem. Lett. **1**, 1176 (2010).

107. S. Thinius, M. M. Islam, P. Heitjans, and T. Bredow, J. Phys. Chem. C **118**, 2273 (2014).

108. B. Roling and M. Ingram, Phys. Rev. B **57**, 14192 (1998).

109. B. Roling, Curr. Opin. Solid State Mater. Sci. **5**, 203 (2001).

110. S. Stramare, V. Thangadurai, and and W. Weppner, Chem. Mater. **15**, 3974 (2003).

111. R. Murugan, V. Thangadurai, and W. Weppner, Angew. Chemie Int. Ed. **46**, 7778 (2007).

112. D. Rettenwander, P. Blaha, R. Laskowski, K. Schwarz, P. Bottke, M. Wilkening, C. A. Geiger, and G. Amthauer, Chem. Mater. **26**, 2617 (2014).

113. D. Rettenwander, C. A. Geiger, M. Tribus, P. Tropper, and G. Amthauer, Inorg. Chem. **53**, 6264 (2014).

114. J. T. Ash and P. J. Grandinetti, Magn. Reson. Chem. **44**, 823 (2006).

115. D. Wolf, Phys. Rev. B **10**, 2710 (1974).

E. Acknowledgment

Many thanks go to Prof. Dr. Martin Wilkening for giving me the opportunity to pursue my PhD work under his supervision. I highly appreciate that I was given the chance to present my scientific work on many conferences abroad and could visit the research group of Prof. Dr. Gillian Goward in Hamilton (Canada). In particular I'd like to thank Prof. Wilkening for his encouraging words in stressful times and always having an open ear for questions.

I am very grateful to all fellow members of the Wilkening-group (AGW) for creating a great working atmosphere. A special thanks goes to Dr. Viktor Epp for introducing me to most of the NMR measurement techniques, providing help with troubleshooting, many fruitful discussions, as well as for reading and improving my thesis. Also, I'm very glad to have had such a fun time with Viktor Epp, Dominik Wohlmuth and Andreas Dunst who all shared a small office with me.

Many other people have contributed to this work with their collaboration, scientific input and helpful discussions: Dr. Patrick Bottke in particular for help with MAS NMR measurements; Dr. Franz Mautner and Dr. Brigitte Bitschnau for the sample characterization via x-ray diffraction; Prof. Dr. Gillian Goward, Prof. Dr. Alex Bain, Dr. Victor Terskikh, Dr. Kristopher Harris, Danielle Smiley and Zoe Reeve for their help, support and warm welcome during my research stay in Canada; Prof. Dr. Wolfgang Tremel for the synthesis of the micro- and nanocrystalline SnS_2 samples and Dr. Daniel Rettenwander for the preparation of the Al-, Ga-doped LLZO samples. Also, I'm grateful to the Research Unit 1277 (molife) for financially supporting my research stay abroad.

A very special thank you goes to Doris Höglinger, not only for reading my thesis and a lot of moral support in the final stage of the writing process, but also for being a such a good friend since high school.

Most of all I am indebted to my family, who always wondered what I did all the time. Thank you so much for your love, support, patience and open ears during my years of study!